Miscellaneous Paper GL-94-49
September 1994

US Army Corps
of Engineers
Waterways Experiment
Station

AD-A285 745

Task IV: Groundshock-Induced Hydrogeologic Response

Volume II: Hydrologic Response of Deep Based Systems to Blast Loading

by Scott E. Blouin, Kwang J. Kim,
Applied Research Associates, Inc.

DTIC
OCT 2 1994
G

411412 94-32946 223A

Approved For Public Release; Distribution Is Unlimited

DTIC

94 1

Prepared for U.S. Air Force Ballistic Missile Office

The contents of this report are not to be used for advertising, publication, or promotional purposes. Citation of trade names does not constitute an official endorsement or approval of the use of such commercial products.

PRINTED ON RECYCLED PAPER

Miscellaneous Paper GL-94-49
September 1994

Task IV: Groundshock-Induced Hydrogeologic Response

Volume II: Hydrologic Response of Deep Based Systems to Blast Loading

by Scott E. Blouin, Kwang J. Kim

Applied Research Associates, Inc.
New England Division
South Royaltion, VT 05068

Final Report

Approved for public release; distribution is unlimited

Prepared for U.S. Air Force Ballistic Missile Office
Norton Air Force Base

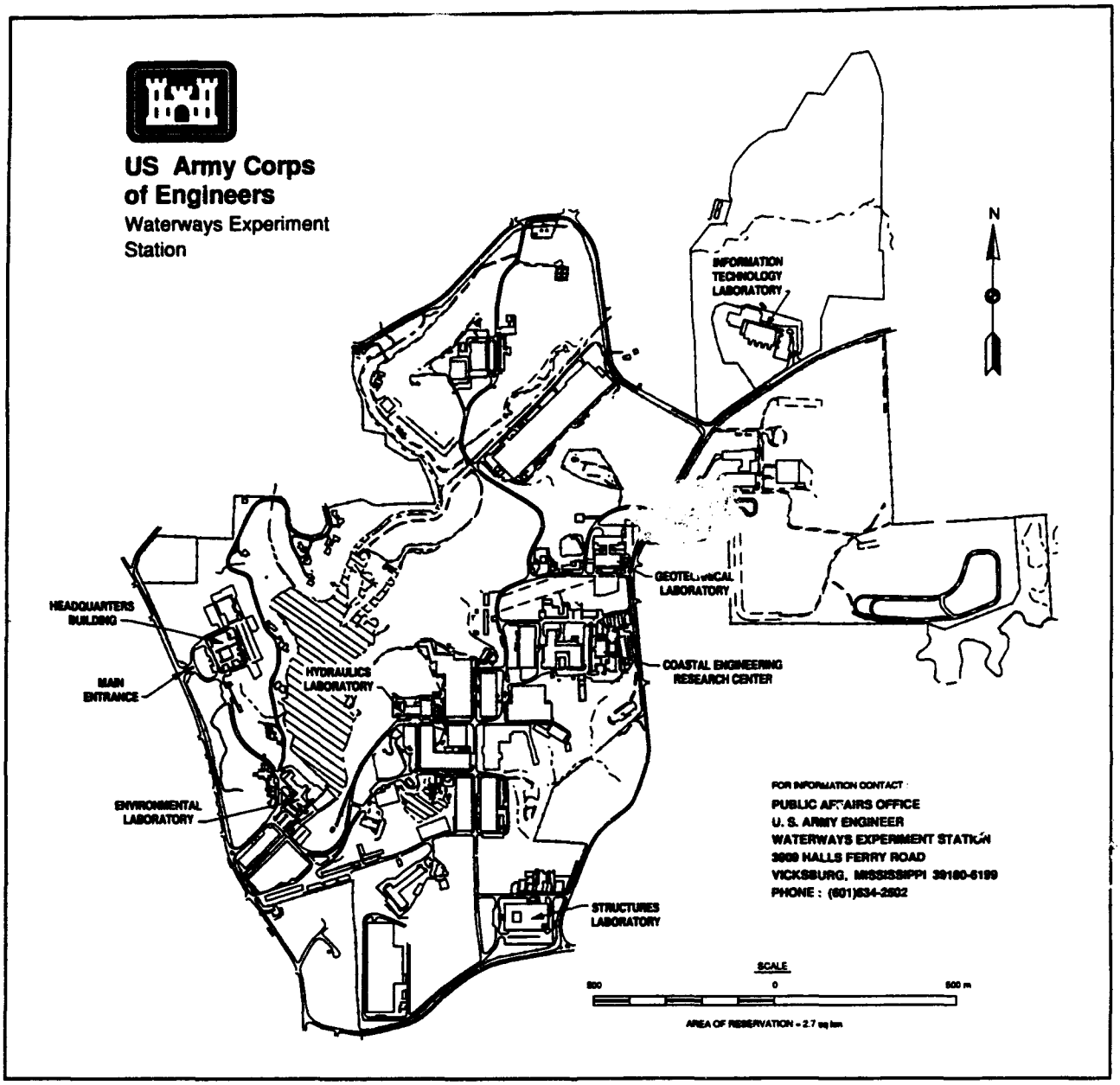

Waterways Experiment Station Cataloging-in-Publication Data

Blouin, Scott.
Task IV : groundshock-induced hydrogeologic response. Volume II, Hydrologic response of deep based systems to blast loading / by Scott E. Blouin, Kwang J. Kim ; prepared for U.S. Air Force Ballistic Missile Office.
219 p. : ill. ; 28 cm. -- (Miscellaneous paper ; GL-94-49 v. 2)
Includes bibliographic references.
1. Guided missile silos -- Protection. 2. Blast effect -- Environmental aspects. 3. Pore water. 4. Hydraulic fracturing. I. Kim, Kwang Jin, 1949- II. United States. Army. Corps of Engineers. III. U.S. Army Engineer Waterways Experiment Station. IV. Geotechnical Laboratory (U.S.) V. United States. Air Force. Ballistic Missile Office. VI. Title. VII. Title: Groundshock-induced hydrogeologic response. VIII. Title: Hydrologic response of deep based systems to blast loading. IX. Series: Miscellaneous paper (U.S. Army Engineer Waterways Experiment Station) ; GL-94-49 v. 2.
TA7 W34m no.GL-94-49 v. 2

TABLE OF CONTENTS

Section		Page
1	Overview, Conclusions and Recommendations	2
2	Geologic and Hydrologic Setting, Ranier Mesa	9
3	Occurrence of Water During and After Mining	23
4	Inflow of Water Following Underground Tests	47
5	CONSL Code Description	67
6	Development of Residual Stresses	74
7	Parametric Evaluation of Flow and Pressure Dissipation	93
8	ONETON Numerical Simulation	137
References		145
Appendix A:	Undrained Isotropic Compression of Saturated Porous Media in Plane Strain	A1
Appendix B:	Flow Due to Volume Change in Saturated Porous Materials	B1
Appendix C:	Finite Element Formulation of Consolidation	C1
Appendix D:	CONSL Code Listing	D1
SF 298		

SECTION 1

OVERVIEW, CONCLUSIONS AND RECOMMENDATIONS

OVERVIEW

Deep based facilities will almost surely be deployed well beneath the water table. In addition to the usual problems with inflow of water during construction, such facilities may be subjected to additional water problems resulting from the high intensity dynamic loadings expected during a nuclear attack. At the Nevada Test Site (NTS) test structures adjacent to contained nuclear bursts have sustained only minimal structural damage from the dynamic stresses and ground motions, but have been completely flooded with ground water mobilized by the blast. Similar occurrences at key locations on a deep based strategic system would defeat the system even though it survived the dynamic threat.

This study identifies the principal mechanisms responsible for explosively generated inflow of water and makes preliminary estimates of the potential magnitude of this problem at a typical deep basing site as exemplified by Generic Mountain C. A summary of hydrologic response data from NTS underground nuclear and high explosive (HE) tests beneath Rainier Mesa is used to identify similar response mechanisms which would threaten deep based facilities subjected to surface or shallow buried nuclear bursts. Two phase one dimensional axisymmetric code calculations are used to assess the potential threat from explosively generated inflow of water at Generic Mountain C. Flow rates, flow volumes and pore pressure dissipation for a wide

variety of rock types ranging from the impermeable tuffs of Rainier Mesa to the permeable sandstones of Generic Mountain C are calculated using the CONSL two phase code.

The NTS data base is summarized and highlighted in Sections 2, 3 and 4. Section 2 describes the unique geologic and hydrologic regime of Rainier Mesa, with its high porosity, very low permeability altered tuff and variable perched water table. Section 3 summarizes the most significant and best documented instances of inflows encountered during construction of, and exploration for, the E, N and T tunnel complexes beneath Rainier Mesa. Inflow data from exploration and construction activities are instructive in identifying potential water sources and in describing interconnectivity and extent of water bearing fractures. The fourth section presents data illustrating the two explosive induced water producing mechanisms identified at NTS. The subsection on the MIGHTY EPIC event describes the mobilization of fracture water by a contained nuclear detonation and documents the flooding of test structures and access drifts which occurred on that event. The subsection on the ONETON HE contained burst describes the production of water from the residual stress field produced by cavity expansion. The residual stresses squeezed water from the pores of the rock over a period of many days. Migration of the pore water away from the higher stress regions near the explosively formed cavity was accompanied by pore collapse and a slow decrease in residual stress.

Sections 5 through 8 investigate the mobilization of pore water by residual stresses and pore pressures and use parametric two phase flow calculations to estimate the magnitude of potential flow due to this flow mechanism for a deep based system beneath Generic Mountain C. Section 5 and Appendices A through D describe the CONSL code used in the parametric calculations.

Section 6 describes mechanisms by which residual stresses and pore pressures are developed from both contained and surface bursts in or on saturated rock. The parametric flow calculations are presented in Section 7 for a broad range of rock types encompassing the NTS tuff and the rocks making up Generic Mountain C. Sensitivity studies of flow volume as a function of changes in rock properties are also presented. Finally, a calculation of flow on the ONETON event using measured residual stresses and rock properties is presented in Section 8 and compared to the ONETON data. The agreement between the calculation and the data validates the calculational procedures and strengthens the concerns raised by the calculations of Generic Mountain C in Section 7.

CONCLUSIONS

- Post shot water has been produced by two mechanisms at NTS.

  — Complete flooding of test structures occurred on the MIGHTY EPIC nuclear event. Flooding was caused by fracture water mobilized by the dynamic stresses and ground motions (including block motion). Water entered the structures through relatively minor tears in the steel liners.

  — Flooding of the instrumentation drift on the ONETON HE event resulted from interstitial pore water being driven out of the voids by the residual stress buildup around the cavity formed by the explosion. Such flooding by pore water migration has not been

a major problem in the NTS tuff because of the tuff's extremely low permeability.

- The NTS experience cannot be directly translated to proposed deep based facilities because of the unique geologic and hydrologic regime at NTS and because of the distinctive characteristics of the contained burst loadings.

  — The Rainier Mesa tuff with its perched water table, poor hydraulic interconnectivity of fractures, irregular fracture saturation and very low permeability is not characteristic of sites being considered for deep basing.

  — There are important differences between the contained burst NTS loadings and the surface or shallow buried burst threat to deep basing, particularly in the mechanisms resulting in long term residual stress and pore pressure buildups. Despite the differences, however, both types of loadings produce residual stress and pore pressure buildups which will produce pore water migration.

- Both sources of explosion generated water observed at NTS are a serious threat to deep based systems at candidate sites exemplified by the Generic Mountain C hydrologic/geologic setting.

  — At a site where all fractures are generally saturated, explosion mobilized fracture flow could be a more general and serious problem than at NTS.

However, there are little or no data on properties controlling fracture flow at Mountain C, such as fracture storage capacity, hydraulic interconnectivity, and the mechanical and flow properties of the fractures.

— Simplified two phase calculations of flow produced by explosively generated residual stresses and pore pressures indicate that such flow is a very serious potential threat to deep based systems in the Generic Mountain C setting. Even through pore water migration was not a serious threat at NTS, a similar residual stress loading of the much more permeable Generic Mountain C geology can produce flow volumes orders of magnitude greater than those experienced at NTS.

RECOMMENDATIONS

- The magnitude of the threat of explosively generated flooding of deep based systems should be more realistically defined at generic sites of interest. Better threat definition will require analysis of both the fracture water and pore water migration threat mechanisms. It should also include analysis of alternatives for eliminating, reducing and/or handling such flooding.

- Reliable predictions of fracture flow require the development of analytic tools and most importantly data describing the geologic/hydrologic properties and response parameters governing such flow.

— Acquisition of this descriptive data will require both laboratory and field programs designed to measure simulated and actual dynamic and residual pore pressure response and flow, and the development of programs and tests to measure in situ fracture properties governing fracture flow.

— Development of analytic tools should include two phase codes capable of modeling the dynamic response of saturated fractures and the resultant residual pore pressure buildups and flows. These codes should initially be used to conduct parameter studies in which fracture flow parameters are varied over the entire range of interest to deep based systems.

- Additional work to more realistically define the threat from pore water migration should be mostly analytic, since the governing material parameters are much better defined than those controlling fracture flow. It should be noted that nearly all the refinements suggested below will tend to reduce the flows from the preliminary calculations performed in this initial study. Additional analytic calculations using both one and two dimensional two phase codes are required. One dimensional calculations should be used to study:

  — the use of pressure grouting to reduce pore water migration;

  — more realistic material models, including the influence of shock conditioning;

— the influence of partial saturation (as reported for Generic Mountain C) on flow;

— the influence of limited aquifer boundaries on flow and flow volumes.

- Two phase calculations using currently available codes should be used to:

  — perform more realistic modeling of the ONETON experiment;

  — realistically model the response of depressed water tables (phreatic surfaces) in the vicinity of tunnels;

  — simulate more realistic nonsymmetric loading conditions from threat surface and shallow buried bursts on aquifers having locations, properties and boundary conditions representative of actual field conditions.

SECTION 2

GEOLOGIC AND HYDROLOGIC SETTING, RAINIER MESA

GEOLOGIC SETTING

Rainier Mesa, shown in Figure 2.1, is located in the north central region of the Nevada Test Site. The mesa is centered at about 37° 12' N latitude and 116° 13' W longitude; or at about 890,000 ft N and 630,000 ft E in the center zone of the Nevada state coordinate system. Rainier Mesa is overlain by volcanic cap rock with a surface elevation between 7400 and 7680 ft above sea level. The top of the mesa is more than 2500 ft above Yucca Flat in the nearby basin. The mesa runs north-south. Width of the cap rock is approximately 1.5 miles, length about 3 miles and area about 4.4 square miles. According to Thordarson (1965), the average rainfall on the mesa was 7.5 in/yr in the 5 year period between 1959 and 1964.

Rainier Mesa is a remnant of an eroded volcanic plateau. The volcanic tuffs making up the mesa are of moderately recent (Miocene) to very recent (Pliocene) origin. Thordarson (1965) identifies 11 layered tuff units atop the underlying sedimentary and/or metamorphic rocks. The tuff layers, 2000 to 5000 ft in thickness, are relatively flat, with dips of generally less than 25°. These overlie much older sedimentary/metamorphic dolomites, argillites and quartzites of Paleozoic to late Precambrian age. Prior to deposition of the tuff, the underlying rocks had undergone extensive deformation and are highly fractured, folded

and faulted. The volcanic tuff was deposited atop the eroded surface of these older rocks; hence, the tuff beds tend to parallel the predepositional topography. The tuffs tended to fill in the underlying valleys so that the bedding planes in the later deposits are flatter than those in the earlier ones.

Three major types of tuff make up Rainier Mesa, zeolitic-bedded tuff, friable-bedded tuff and partially welded to welded tuff. The Rainier tuff was originally composed primarily of fine grained pumice and glass shards. Tuff is formed by the release of gases in molten lava resulting in expansion and frothing of the lava. As the froth breaks to the surface, the pumice and glass fragments are sometimes ejected high into the air by volcanic explosions and deposited in the form of ash fall tuff. Alternatively, froth may foam down the side of a volcano in a glowing avalanche and be deposited as ash flow tuff. Under certain conditions the tuff welds itself together after deposition. Depending on the weight of overburden and degree of melt in the freshly deposited material, various degrees of welded or partially welded tuff can be formed during cooling.

The tuff units identified by Thordarson (1965) making up Rainier Mesa are listed in Table 2.1. The underground weapons effects tests are conducted in the lowermost or tunnel bed tuffs, members T1 through T4. These overlie the older sedimentary rocks and are made up of zeolitic bedded tuffs. In addition to the tunnel bed tuffs, the overlying lower portion of the Grouse Canyon member of the Indian Trail formation and the lower portion of the Paintbrush formation are also zeolitic tuffs. Thordarson (1965) lists the aggregate thickness of these zeolitic units at between 800 and 1200 ft. The pumice and glass particles of the original ash flow tuffs in these units have been highly altered to form various zeolitic minerals. These minerals form a nearly

impermeable matrix around the remaining non-zeolitic constituents such as quartz, feldspar, biotite, etc. The resultant zeolitic tuff is a highly porous but very impermeable material. As shown in Table 2.1, Thordarson (1965) gives average interstitial porosities of the zeolitic tunnel bed tuffs from the U12e tunnel complex of from 25 to 38%. On the other hand, average interstitial permeabilities range form 9.4×10^{-7} to 1.9×10^{-8} cm/s, in the very low to practically impermeable range. There appears to be no relationship between porosity, permeability and grain size in the zeolitic tuff.

The second major tuff category forming Rainier Mesa is the friable bedded tuff. As shown in Table 2.1, this tuff occurs in the lower portion of the Grouse Canyon member and comprises the bulk of the Paintbrush Tuff formation. The friable tuff is a porous, weak, ash fall tuff in which the pumice and glass shards are largely unaltered. The porosity tends to average somewhat higher than the zeolitic tuff; samples from the U12b tunnel complex averaged 40% porosity. The average interstitial permeability of the friable tuff is much larger than that in the zeolitic tuff. Permeability measurements from Emerick and Houser (1962) average 1.75×10^{-4} cm/s; lower values are given by Bowers (1963) with an average value of 2.4×10^{-5} cm/s. The latter measurements were made using air rather than water. Data from Keller (1960) indicate that permeability to air is 2 to 20 times higher than the permeability to water. The above permeabilities fall in the low permeability range (10^{-3} to 10^{-5} cm/s) according to Lambe and Whitman (1969).

The welded and partially welded tuffs are among the least porous and least permeable rocks within Rainier Mesa. As shown in Table 2.1, these tuffs comprise the Rainier Mesa cap rock, the Tiva Canyon and part of the Stockade Wash members of the

Paintbrush formation and the upper Grouse Canyon and Tub Spring members of the Indian Trail formation. The welded tuffs were deposited as incandescent ash falls which were subsequently self-welded under their own weight and heat. Cooling fractures are abundant in the welded tuff, with the highest density of fractures in the denser more highly welded tuffs. According to Table 2.1, porosity of the Rainier cap rock averaged only 14% while that in the Grouse Canyon welded tuff averaged 19%. Interstitial permeability in the cap rock averaged 4.7×10^{-7} cm/s and the one sample of Grouse Canyon welded tuff reported had a permeability of 2.8×10^{-8} cm/s. These permeabilities are in the very low to practically impermeable range described by Lambe and Whitman (1969).

Beginning in moderately recent Miocene time and continuing into the very recent Pliocene, the Rainier Mesa region has been subjected to normal faulting resulting in the depression of the adjacent Yucca Valley to the east and Fortymile Canyon to the west. In conjunction with this faulting the Rainier Mesa tuff has undergone extensive normal faulting and joint development. Faults are very steep to nearly vertical and exhibit varying amounts of normal displacement. Most faults have stratigraphic normal displacements of inches, though major faults show displacements to tens of feet. Major faults transect all the tuff beds within the mesa, including the cap rock at the surface. Minor faults are much more numerous than major faults, with many extending less than 300 ft. Joint and fault spacing vary dramatically within relatively small local areas, from tens of feet to inches. Openings in faults and joints also vary considerably. Fault openings of up to 6 in are reported by Thordarson (1965), but in most instances faults are relatively tight and may be filled with clay gouge. Joints are also generally closed, but openings of up to several inches are

observed. Thordarson also observes that fracture openings vary irregularly throughout the rock mass, with fractures that are open several inches at one point being tightly closed only a few feet away.

HYDROLOGIC REGIME

Ground water within Rainier Mesa is concentrated in the zeolitic tunnel beds 1 through 4 of Table 2.1. The very low permeability of the tunnel bed tuffs traps water which originated as rain on the mesa surface and which percolates downward, primarily through fractures in the overlying tuffs. The water trapped in the zeolitic tuffs forms a perched water table approximately 2000 ft above the true regional water table which lies well beneath the floor of the surrounding valleys. Thordarson (1965) classes the zeolitic bedded tuff as a fractured aquitard. There is no appreciable flow of water through the interstices of the zeolitic tuff. Migration of water downward through the tunnel bed layers is predominantly through the generally tight and poorly connected fractures.

The top of the perched water table shows considerable variation in elevation due to the poor hydraulic interconnectivity of the fractures. It lies in the top of the zeolitic tunnel beds, generally within a few hundred feet of the 6000 ft elevation. Figure 2.2 shows the location of various wells from which Thordarson (1965) inferred the elevation of the zone of fracture saturation in the vicinity of the E tunnel complex (U12e). The wells, shafts, and exploration holes discussed by Thordarson are listed in Table 2.2. Only two of the holes, Hagestad 1 and U12e.06-1, were drilled from the top of

the mesa. The others were drilled or excavated from within the E or B tunnel complexes. In addition, in no instance was the depth to the top of the fracture saturation surface measured in an unambiguous manner. Of the two holes from the mesa surface, U12e.06-1 was evidently drilled through the water bearing zeolitized tuff beds into the underlying unsaturated dolomite without measuring the perched water table in the tunnel bed tuffs. The Hagestad 1 test hole was cased to its full depth of 1941 ft and cemented. The casing was then perforated at selected depths allowing water to fill the hole. The depth of water in the hole was a function of the location of the casing perforations. The highest elevation of water in the hole was 6039 ft, but Thordarson admits that perforations at other elevations might have filled the hole further.

The remaining holes and shafts listed in Table 2.2 were excavated or drilled from within the E and B tunnel complexes into the underlying tuffs. In the case of holes U12e.03-1 and U12e.M-1, water poured from the hole up into the tunnel. These holes were plugged off and the elevation of the resulting head computed from the pressure in the hole. In all measurements made from within the tunnels, the very presence of the tunnel had influenced the water table elevation in that area as evidenced by the large volumes of water which were produced during excavation (production of water is discussed in Section 3). For the above reasons, the water table elevations of Table 2.2 should be considered minimum elevations. Elevations prior to tunnel construction and elevations in the vicinity of the cased drill holes were probably somewhat higher than indicated in the table. At any rate, in the vicinity of E Tunnel the elevation of the zone of fracture saturation appears to be somewhat in excess of 6000 ft, with considerable variation within the range of at least 6000 ft to 6200 ft elevation.

Thordarson (1965) attributes the large variability in water table to the variations in fracture permeability and hydraulic interconnectivity within the zeolitized tuff. In areas where fracture frequency and permeability are relatively high, one might expect downward seepage of ground water to be enhanced and the water table to be somewhat depressed relative to more impermeable adjacent areas. Winograd and Thordarson (1975) present the simplified cross section shown in Figure 2.3 to schematically illustrate the perched water table in the vicinity of E tunnel. Beneath the eastern two thirds of the mesa, the underlying dolomite (lower carbonate aquifer) is unsaturated and lies well above the regional water table. The water within the tunnel bed tuffs (tuff aquitard) is perched above the unsaturated dolomite. The variable water table in the region of E Tunnel is represented in the triangular shaped fracture zones 1 and 4. At location 1 variable levels of perched water in the fracture zones are represented by the variable black shading of the schematic fracture zones. In this region, the water table lies even with, or below, the level of E Tunnel. At location 4, the perched water table lies well above the tunnel level.

Beneath the western third of the mesa the underlying dolomite dips beneath the regional water table and the tuff aquitard dips to the level of the regional water table. This creates a continuous saturated zone above the regional water table which is termed a semiperched zone. The semiperched water table extends to the base of the overlying welded tuff aquifer which dips below the 6000 ft elevation in this region.

Immediately south of the mesa at the location of Well 87-62 (Test Well 1 in Figure 2.2), the top of the tuff aquitard is at an elevation of 5931 ft, 225 ft beneath the well head

elevation of 6156 ft. The top of the perched water table is at an elevation of 5746 ft, only 410 ft below the well head and 185 ft beneath the top of the aquitard. The perched water table at this location is 1560 ft above the regional water table, which has an elevation of 4186 ft (Winograd and Thordarson, 1975). Thordarson (1965) notes that these water levels from Test Well 1 are the only true unambiguous measurements of the static water level in the region. It is interesting to note that if the top of the perched water table were also about 200 ft beneath the top of the tuff aquitard in the vicinity of E Tunnel, it would be approximately 150 ft above the tunnel elevation.

Thordarson (1965) maintains that the tunnel bed tuffs are fully saturated interstitially, not only within the zone of fracture saturation, but also hundreds of feet above it as well. He notes seeps of water which were found in the U12b tunnel system at an elevation of 6600 ft, some 400 to 600 ft above the level of fracture saturation in this region. Extensive analysis of tunnel bed tuffs since that time have indicated that there is some variability in the degree of interstitial saturation. In some locations, the tunnel bed tuffs appear to contain a few percent air voids, though specification of the exact location of, and amount of, these air voids has been very illusive.

Based on an estimated annual ground water recharge for Rainier Mesa from the measured annual rainfall, and on measured hydraulic gradients from Test Well 1 and Hagestad 1, Thordarson (1965) estimates an average vertical permeability for the tuff aquitard in the 9.43×10^{-8} to 2.36×10^{-8} cm/sec range. Note that this range agrees well with the interstitial permeabilities for the tunnel bed tuffs reported in Table 2.1. Since it agrees with interstitial permeabilities from laboratory samples it would appear that Thordarson's hypothesis that the

effective permeability is governed by the fractures is incorrect. However, experience in mining the tunnels beneath Rainier Mesa, summarized in the following section, shows that the effective permeability is indeed governed by the fracture flow. Several factors may account for the apparent inconsistency between the laboratory permeabilities and Thordarson's derived in situ permeabilities. These factors are:

- The average permeabilities presented in Table 2.1 may not be representative of the tunnel bed tuffs;

- Thordarson's assumed portion of the annual rainfall going into ground water recharge is too low (this was based on data from other sites);

- the measured hydraulic gradients upon which Thordarson's analysis was based are not representative of those in the tuff;

- or some combination of these factors.

Measurement of in situ or effective permeabilities in the tunnel bed tuffs is a subject needing further investigation.

Table 2.1. Rainier Mesa lithology and properties (after Thorda[illegible] [illegible]965).

Hydrologic unit	Geologic name		Lithology	Thickness (feet)	Interstitial permeability (cm/s)			Interstitial porosity (percent)
	Formation	Member			Number of samples	Average	Range	
Welded or partially welded tuff	Timber Mountain Tuff	Rainier Mesa	Welded and partially welded tuff (caprock of Rainier Mesa)	270-550	6 (water) 10 (brine)	4.7 E-7 2.8 E-7	9.4E-9 - 1.4E-6 9.4E-10 - 5.2E-5	14% (37 samples)
Friable-bedded tuff	Paintbrush Tuff	Tiva Canyon	Welded and partially welded tuff	0 - about 80	---	---	---	---
Zeolitic-bedded tuff		Stockade Wash	Nonwelded to partially welded pumiceous tuff, base locally zeolitic	0 - about 230	---	---	---	---
Welded or partially welded tuff		Bedded tuff (informal local units)	Bedded-friable vitric tuff	100 - 1,000	2 5 (gas)	1.7 E-4 2.2 E-5	1.6E-4 - 1.9E-4 1.0E-5 - 4.2E-5	40% (8 samples)
			Zeolitic tuff in lower 150 feet on east side of Rainier Mesa		11 (water) 5 (brine)	9.4 E-6 1.4 E-[illegible]	1.4E-8 - 4.7E-5 9.4E-8 - 2.3E-5	30% (319 samples)
	Indian Trail	Grouse Canyon, upper part	Welded tuff, lenticular and local	0 - 70	1 (water)	2.8 E-8	---	19% (4 samples)
Friable-bedded tuff		Grouse Canyon, lower part	Friable vitric tuff in upper portion, zeolitic tuff in lower portion	45 - 120	9 (brine)	9.9 E-6	3.3E-6 - 5.2E-5	40% (40 samples)
Welded or partially welded tuff		Tub Spring	Welded tuff	0 - about 400	---	---	---	---
Zeolitic-bedded tuff		Informal local units (includes Tunnel Beds 1-4)	Zeolitic-bedded tuff T4	265 - 375	2 (water) 9 (brine)	9.4 E-7 9.4 E-8	1.4E-8 - 1.4E-6 4.2E-9 - 1.4E-5	38% (166 samples)
			Zeolitic-bedded tuff T3	100 - 200	42 (water) 4 (brine)	1.4 E-7 3.3 E-8	3.8E-9 - 1.9E-6 4.7E-10 - 1.9E-7	35% (142 samples)
			Zeolitic-bedded tuff, contains pisolite beds and locally a welded tuff at the top T2	120	12 (water)	1.9 E-8	3.3E-8 - 1.4E-6	32% (28 samples)
			Zeolitic-bedded tuff T1	200 - 210	3 (brine)	4.7 E-8	2.4E-8 - 1.9E-7	25% (31 samples)

Table 2.2. Data on elevation of fracture saturation in the vicinity of E Tunnel (from Thordarson, 1965).

Hole	Total Depth	Hole Elevation	Inferred Elev. of Fracture Saturation
U12e03-1	834 ft deep	El 6150 ft	6167 ft
U12e.M-1	1501 ft deep	El 6158 ft	6184 ft
Hagestad 1	1941 ft deep	El 7485 ft	6039 ft
U12e.06-1	3114 ft deep	El 7573 ft	< 4643 ft
Shaft in U12e.07	not reported	not reported	6033 ft
Shaft in U12b.07	not reported	not reported	6147 ft

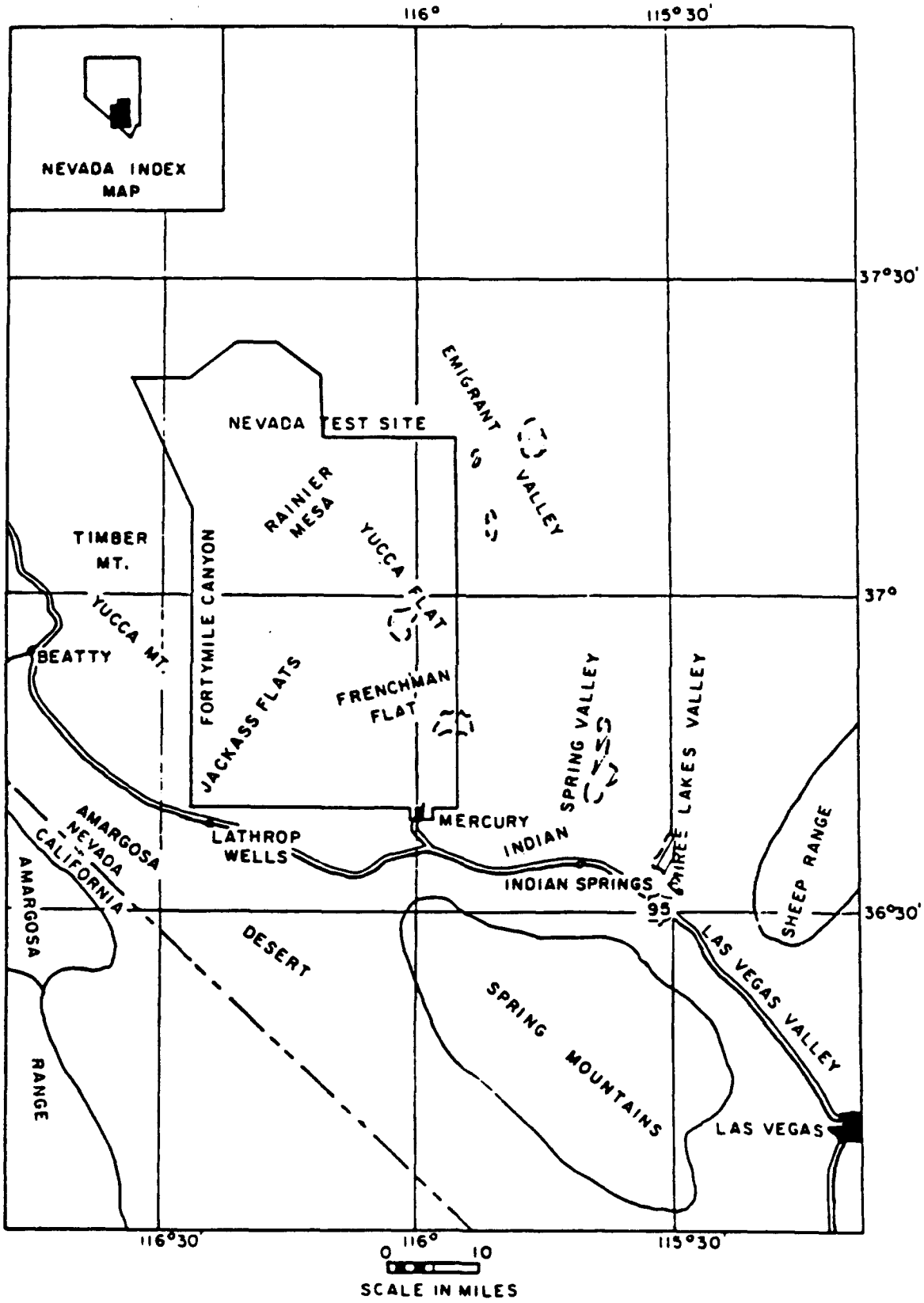

Figure 2.1. Location of Nevada Test Site and Rainier Mesa (from Thordarson, 1965).

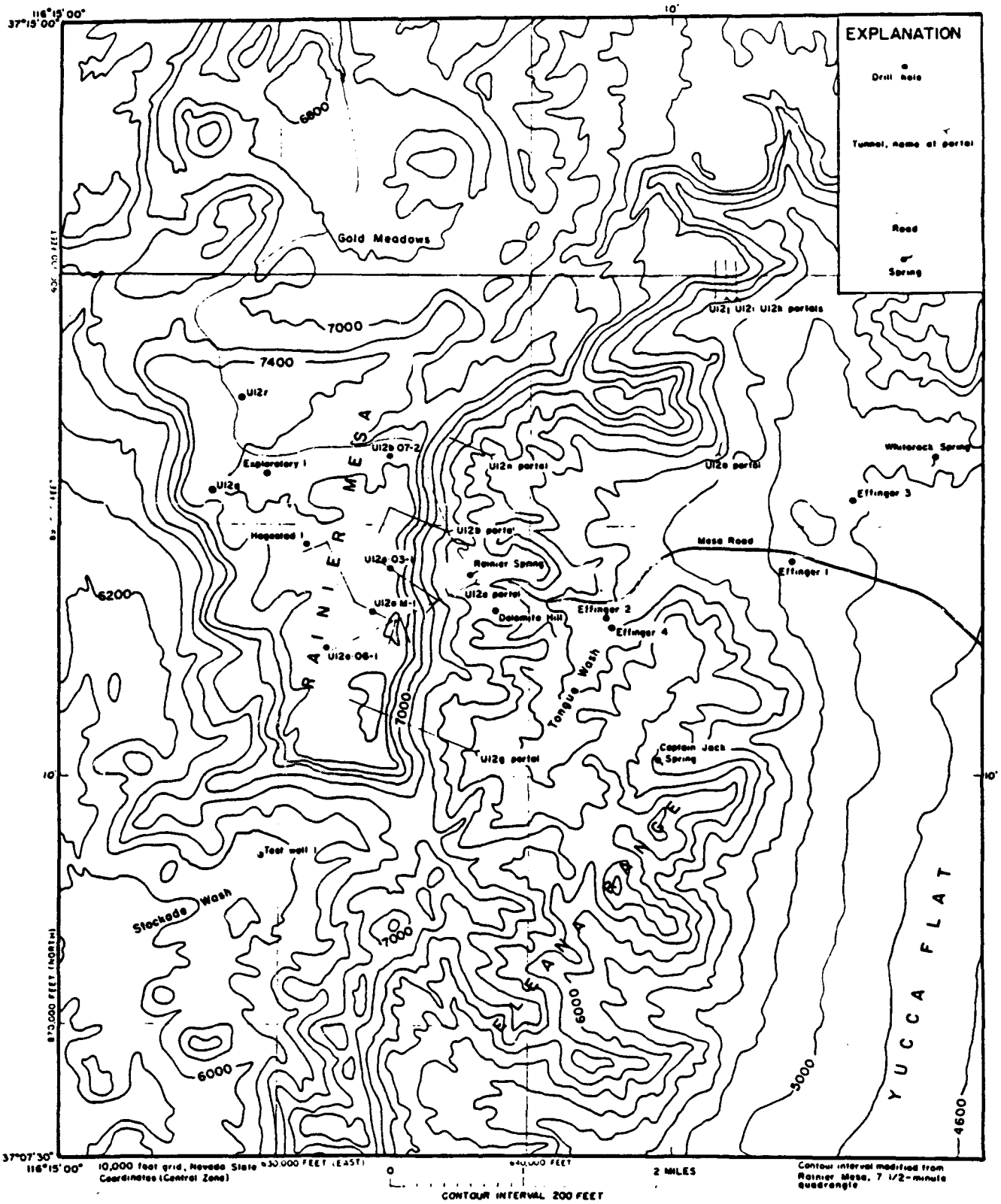

Figure 2.2. Contour map and exploration hole locations, Rainier Mesa (from Thordarson, 1965).

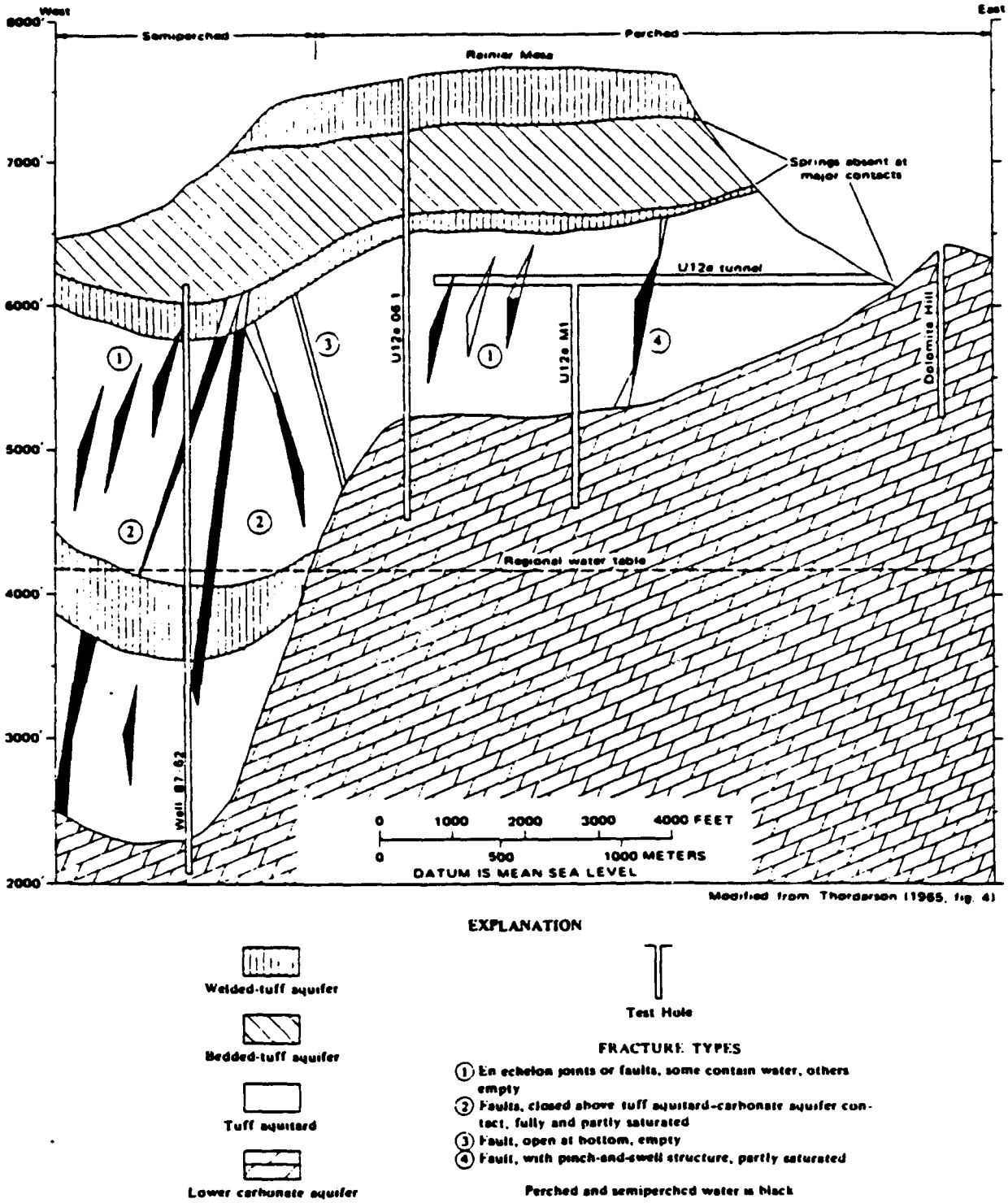

Figure 2.3. Schematic section view of perched and semiperched groundwater in the vicinity of E Tunnel, Rainier Mesa (from Winograd and Thordarson, 1975).

SECTION 3

OCCURRENCE OF WATER DURING AND AFTER MINING

OVERVIEW

Flow of water into the tunnel complexes in the zeolitized tuffs beneath Rainier Mesa has been documented in a piecemeal fashion for many years. A brief look at some of the descriptive and quantitative features of this flow is very helpful in understanding the occurrence and migration of the water in the tunnel bed tuffs. It is also very helpful in formulating hypotheses which explain the tunnel flooding which sometimes has occurred adjacent to underground nuclear and HE detonations.

A plan view of the tunnel complexes beneath Rainier Mesa is shown in Figure 3.1. The major complexes are the F, E, B, N and T tunnel complexes; except for B Tunnel all were mined in the zeolitized tunnel bed tuff units 1 through 4 of Table 2.1. B Tunnel, with a portal elevation of 6606 ft, was mined in the overlying Lower Grouse Canyon member of the Paintbrush Tuff. Significant flows of water from faults and joints were encountered in the E, N, and T complexes during mining. In some instances flow continued well after mining operations had moved elsewhere. In G Tunnel, toward the extreme south end of Rainier Mesa, only a few small seeps were encountered during the mining. In E Tunnel, further into the mesa, but having the same portal elevation (6115 ft) as G Tunnel, numerous seeps and many moderate flows were encountered during mining. Only a few small seeps were encountered in B Tunnel which was mined in the relatively permeable Paintbrush Tuff above the perched water table. In N

and T Tunnels, with portal elevations of 6024 ft and 5600 ft respectively, numerous small seeps and many moderate flows were encountered.

The remainder of this section will highlight features of the flow encountered in the E, N and T complexes as well as observations related to the hydraulic interconnectivity and capacity of the fractures.

E TUNNEL

Thordarson (1965) and Clebsch (1960) provide excellent descriptions of the seeps and flows encountered during the mining of E Tunnel. From August 1958 through December 1963 an estimated 30 to 50 million gallons (90 - 150 acre ft) of water flowed from the E Tunnel portal. This water was discharged from the faults and joints exposed during the mining operations. A detailed layout of the E Tunnel complex is shown in Figure 3.2. Included on this map are the locations of faults intersecting the various drifts. A total of about 110 faults and 5000 joints were mapped during the mining of approximately 19,000 ft of drifts in E Tunnel. Of these, about 50% to 60% of the faults produced most of the water, while about 2% of the joints yielded a minor portion of the water.

Of the total 30 to 50 million gallon flow from E Tunnel, the largest contribution probably came from the U12e.02 LOGAN drift and the U12e.05 BLANCA drift. Between the middle of August and end of October 1958, approximately 10 million gallons of water flowed from these two drifts alone. During the ensuing 3 year period ending in December 1961, about 15 to 30 million additional gallons of water flowed out of the E Tunnel complex as

the main drift was lengthened and adjacent drifts were added. During the final period reported (Thordarson, 1965), between December 1961 and December 1963, another 5 to 10 million gallons was measured, most of this from mining of the U12e.03 and U12e.06 drifts.

Thordarson (1965) reports that about half the occurrences of water were from in or near faults, and that most instances of flows of more than 5 gallons per minute (gpm) were directly out of faults. The larger flows of fracture water from the faults in E Tunnel ranged from 5 gpm to 20 gpm. Typically, after a fracture was penetrated by a tunnel there was a maximum initial discharge which decreased gradually to a small seep within a few days. Within a few weeks or months most of the fractures had drained completely; however, Clebsch (1960) reports that water dripped from some fractures for a period of 2 years or more.

The rapid decrease in flow is indicative of poorly connected fracture surfaces within the tunnel bed tuffs. Both the fact that the fractures drained relatively quickly and that closely spaced fractures flowed strongly following drainage of adjacent fractures attest to this conclusion. There also appeared to be a correlation between flow and the number or density of fractures. Thordarson (1965) notes that the driest drifts in the E Tunnel complex were the U12e.01 and U12e.07 drifts (see Figure 3.2) which also contained the fewest fractures.

The variability in flow and correlation with fracture density is illustrated in the plot of flow vs. time for the U12e.05 BLANCA and U12e.02 LOGAN drifts shown in Figure 3.3. The data record the total flow out of both drifts as reported by Clebsch (1960) during the mining which progressed as shown in the

bottom portion of the figure. Flow varied from a low of about 30 gpm to a high of about 500 gpm during the mining, with considerable variation as flow volumes declined in exposed fractures and were suddenly increased as new fractures were exposed. Within two weeks after the completion of the drifts the total flow had decreased to about 20 gpm. The greatest flow occurred during penetration of intensely jointed and faulted tuff of Tunnel Bed 3 in the U12e.05 BLANCA drift. Subsequent high discharge values were measured during penetration of fractures in the U12e.02 LOGAN drift. At the time of the last measurement most of the flow was from the LOGAN drift.

Thordarson (1965) notes that there were tens of open fractures within the E Tunnel complex which contained no water, despite the fact that fractures on either side were full of water. The presence of these empty fractures is explained as either due to their complete isolation from the surrounding saturated fractures which receive recharge, or due to their being open below and connected through discharge channels to the underlying regional water table.

He also notes that locally there are certain joint orientations which contain all of the fracture water. For instance, at a range of 3000 to 3500 from the portal in the main drift, water occurred only in the NE-SW striking principal joint set. No water flowed from the NW-SE joints forming the minor set. In contrast, water occurred in the NW-SE major joint set in the U12e.03b drift, but there was no discharge from the NE-SW minor joint set. Such contrasts indicate that there is poor hydraulic interconnectivity between the major and minor joint sets in these areas.

Thordarson concludes that production of water in the U12e tunnel complex was governed by the extent, density, opening width and interconnectivity of the steeply dipping faults and joints in the zeolitized tuff surrounding the tunnel. Most of the faults in the area appear to be local, perhaps en echelon faults, limited in extent to less than 100 to 300 ft. For example, note that most of the densely spaced faults along the U12e.05 BLANCA drift in Figure 3.2 don't intersect either the adjacent U12e.03 or U12e.05 drifts. Openness of the faults varies from up to 6 in to closed and nearly sealed by fault gouge. Joints are generally closed, but in some areas are open several inches at one point and are tightly closed within just a few feet.

In order for the fractures to perch the downward migrating fracture water, Thordarson points out that they must be closed or nearly closed at some underlying location(s) along their strike. Evidence from the tunnels suggests that some fractures are irregularly open and pinched shut due to faulting action. Other fractures appear to be open in the massive zeolitic tuff, but closed in the thin underlying beds of clayey tuff. He also notes that clayey gouge or other fine minerals could be deposited by the downward migrating pore water to seal off open faults.

There appears to be no evidence that interstitial water contributes to flow into the tunnels. The only evidence of any interstitial flow are localized moist spots along the tunnel walls. There were no drips or other flow in evidence. These wet spots may have formed due to seepage controlled by particularly impermeable zones within the tuff. In these locations, the rate of evaporation in the ventilated tunnels evidently equalled the

rate of water production. In most areas the tunnel walls were dry, further testimony to the impermeability of the zeolitic tuff.

A final point by Thordarson (1965) concerning flow of interstitial water makes an interesting contrast to the data presented from N Tunnel in the following subsection. As shown in Figure 3.2, there is a syncline, or dip, in the tunnel beds with its trough or axis running NE-SW across the E tunnel complex. Thordarson notes that there was no concentration or flow of water into the base of this prominent syncline at its intersection with any of the three drifts it crosses. Only minor seeps were observed at the intersections with the synclinal axis and these were from fractures, rather than due to flow along bedding planes in the trough.

N TUNNEL

Overall, the N tunnel complex was somewhat drier than E Tunnel during and after mining. However, significant water and mining problems developed during the mining of the U12n.03 drift shown in Figure 3.4. The U12n.03 drift was designed to house a line of site pipe for an underground nuclear test. Mining of the drift began on 18 April 1966 and was completed on 22 May 1967. The drift runs N 26°W from the U12n extension, a distance of 2166 ft. The elevation at the portal end of the drift was 6067 ft and the drift was mined upward at a 0.5% grade. The entire drift is within Tunnel Bed 4 of the zeolitized tuffs shown in the geologic section of Table 2.1. Ege et al. (1980) describe the rock around the U12n.03 drift as an ash fall tuff, interbedded with reworked ash fall tuff and tuffaceous sandstone. The tuff is bedded, zeolitized, and in places altered to a high clay content. The drift crosses the Aqueduct Syncline approximately 1250 ft from

the main drift. The Aqueduct Syncline is a major syncline with its trough oriented nearly perpendicular to the U12n.03 drift.

A section and plan view of the U12n.03 drift in the vicinity of the Aqueduct Syncline is shown in Figure 3.5. The axis of the syncline is near survey station 13+00. Bedded tuff subunits Tt4k, Tt4J and Tt4H, subunits of Tunnel Bed 4, are pictured sloping gently upward on either side of the synclinal axis. The drift is within the Tt4k subunit for approximately 320 ft SE of the synclinal axis and for about 450 ft on the NW side of the axis.

Ege et al. (1980) report that the Tt4k tuff between stations 10+00 and 16+75 ft has been strongly altered to clay by the action of ground water which has collected in the region. X-ray analysis indicated the presence of calcium-montmorillonite and mechanical analyses showed the rock to be highly plastic with a low unconfined compressive strength. Unconfined strengths of core samples from the U12n.03 UG-3 drill hole, shown in Figure 3.5, averaged 1410 psi, with a range in strengths of from 290 psi to 2300 psi and a standard deviation of 670 psi. Ege et al. estimate that maximum stresses in the walls of the U12n.03 drift due to overburden loads and stress concentrations are approximately 2200 psi. As a result of the concentrated overburden stresses exceeding the rock strength, severe construction and support problems developed in the highly plastic rock. Between survey stations 12+00 and 15+25 swelling and squeezing ground deformed steel sets and popped the plates from rockbolts used to stabilize the drift. Within a two week period in the summer of 1966 lateral deformations of the tunnel walls of up to 36 in were monitored.

Also contributing to the instability of the U12n.03 drift in the vicinity of the synclinal axis were a number of normal faults which intersected the drift at a shallow angle as shown in Figure 3.5. The high density of faults in this region, and the fact that they intersected the drift at very shallow angles substantially exacerbated the movement of the squeezing and swelling ground.

A final problem encountered on the NW side of the synclinal axis was heavy water flow. Flow locations are shown in the plan view of Figure 3.5. Minor to moderate flows of water of up to 5 gpm were encountered issuing from joints and faults during mining near the synclinal axis in July and August of 1966. On 21 September 1966 heavy ground water flows of 65 gpm were encountered from the face of the drift near the floor. Ege et al. (1980) report that after ten days of dewatering this flow had decreased to 40 gpm and that after 50 days the flow had dropped to 25 gpm. The water was issuing from three fractures within a fracture zone beneath the drift. These fractures were open from 1 to 3 in and dipped steeply toward the drift portal. A sump was built in the fracture zone and water was pumped from the zone at rates varying between 40 and 60 gpm. In January of 1968, more than two years after excavation, the flow rate was measured at 8 gpm.

Due to the severe water problems and unstable ground, the U12n.03 drift was abandoned. A bulkhead was constructed near the drift portal and for many years the drift was used for a water supply. In 1979 the drift was reentered for a limited distance at both ends in conjunction with site investigations for the MINERS IRON event. In April of that year total flow rate from the U12n.03 drift was 0.35 gpm.

T TUNNEL

An interesting study of water flow and pressure buildup was made in an array of six horizontal drill holes running north and west off the end of the U12t main drift. This array consisted of NX exploration holes ranging in length from 1500 to 3700 ft. The hole layouts are shown in the expanded view of the NW end of the T tunnel complex in Figure 3.6. All holes except U12t.03 UG-1 were drilled from near the end of the U12t main drift. Hole U12t.03 UG-1 was drilled from the end of the U12t.01 Bypass drift on a bearing of approximately N 65°W. This was the longest of the 6 holes and the first to be drilled. It was drilled throughout most of 1972, being completed to a length of 3690 ft in early November. The second hole to be completed was U12t.03 UG-2 completed to a length of 1504 ft in December 1972. The three holes sharing a common terminus near the end of the main drift, U12t.04 UG-1, U12t.05 UG-1 and U12t.06 UG-1, were completed in that order in May, August and October of 1973. Finally hole U12t.03 UG-3 was completed in July of 1974 on a bearing of N 25°W from the the terminus of U12t main drift. The HUSKY PUP line of site drift (U12t.03) was mined along the path of the U12t.03 UG-3 exploration hole. Predictions of ground water flow into the LOS drift during mining were made by Hoover (1974) based on the ground water inflows into the U12t.03 UG-3 exploration hole. An overall description of water production in all the U12t tunnel drill holes is given in a memorandum by Hoover (1975).

A summary of the peak flows and pressures measured in the 6 U12t drill holes is shown in Table 3.1. In all but two of the holes, peak flow occurred after completion of the drilling. Examination of the flow logs in Hoover (1975) indicates that

flow originated in fracture zones within each hole. The drilling and flow logs from hole U12t.04 UG-1 are plotted in Figure 3.7 to illustrate the variability in flow with hole length. Water was first encountered at a hole length of 320 ft on 31 April 1973. The cumulative flow built slowly to 10 gpm on 17 May at a length of 1209 ft. Flow suddenly increased to 25 gpm as the hole length was extended from 1209 ft to 1245 ft on the 18th, the increase being attributed to water bearing fractures between these ranges. Flow then remained steady until the 21st, when a major water bearing fracture zone was penetrated between 1280 and 1400 ft. Over this interval the total flow increased to 200 gpm. Total flow then decreased over the next week as the water in this zone was depleted. Near the end of the hole another major fracture zone was encountered. On the 1st of June flow increased from 80 to 240 gpm as the hole was advanced from 1880 ft to its 1900 ft final length. Over the next 6 days flow decreased slowly to 225 gpm.

A series of flow and shut in experiments was conducted on hole U12t.04 UG-1 during the summer and fall of 1973. With the flow blocked off, pressure in the hole built to a maximum of 127 psi on 26 October. This corresponds to a pressure head of 293 ft of water. The hole was pressure grouted on the 15th of November. Prior to grouting, the flow was generally in the 100 - 125 gpm range.

The flow and pressure data presented in Table 3.1 indicate a range of peak flows in the various exploration holes of from 100 to 240 gpm, with the U12t.04 UG-1 drill hole producing the greatest flow. Peak shut in pressures varied from 42 to 165 psi corresponding to heads of between 97 and 381 ft. This large head variation supports the earlier conclusions of Thordarson (1965) that the elevation of fracture saturation varies

significantly within a limited area due to the generally poor hydraulic interconnectivity of the fracture zones.

Indications of limited hydraulic interconnectivity were provided by pressure measurements in the U12t.03 UG-1 hole during drilling of the U12t.05 UG-1 hole and by pressure measurements in the U12t.04 UG-1 hole during drilling of U12t.06 UG-1. Upon completion of the U12t.03 UG-1 hole the flow was blocked off and pressure monitored during drilling of the UG12t.05 UG-1 hole. The latter crossed but did not intersect the U12t.03 UG-1 hole at a length of 1020 ft in U12t.05 UG-1. As shown in Table 3.2 (from Hoover, 1975), as the length of U12t.05 UG-1 advanced from 790 to 1070 ft, the pressure in the U12t.03 UG-1 hole decreased from 160 to about 130 psi. Flow out of the U12t.05 UG-1 hole increased from 1 gpm to about 100 gpm. Hoover concluded that hydraulic communication between the two holes was established along two faults which intersected each hole near the crossing point.

Following completion of U12t.05 UG-1, a packer was inserted into U12t.03 UG-1 just beyond the intersection of the two holes to prevent the large flows of water from faults and fractures at the 1800 to 2360 ft depth in U12t.03 UG-1 from reaching the intersection with U12t.05 UG-1. Total flow of water out of U12t.05 UG-1 promptly diminished from 150 to about 10 gpm, indicating that the bulk of the flow from U12t.05 UG-1 was actually produced by the water bearing fractures intersected by U12t.03 UG-1.

Pressure was also monitored in the U12t.04 UG-1 hole during drilling of the adjacent U12t.06 UG-1 hole. Hoover (1975) reports that there was some correlation between activity in the

06 hole and pressure in the 04 hole. A stabilized pressure of 120-122 psi was reached in the 04 hole during drilling of 06. During a four day period the pressure in U12t.04 UG-1 dropped to 106 psi while hole 06 was allowed to drain freely. Hole 06 had been drilled to a length of 1400 ft and the flow rate from hole 06 dropped from 142 gpm to 123 gpm during this interval. The pressure in hole 04 took two days to restabilize at 120 - 122 psi once drilling was resumed in hole 06.

In a 1974 memorandum, Hoover (1974) predicted initial inflows of water into the U12t.03 HUSKY PUP main drift based on flow measurements made in the U12t.03 UG-3 exploration hole. The U12t.03 drift followed essentially the same path as the U12t.03 UG-3 drill hole. Hoover predicted initial flows of approximately 60 and 125 gpm through fracture zones at locations in the U12t.03 drift corresponding to the 860 and 965 ft ranges in the U12t.03 UG-3 drill hole. In his 1975 memorandum he notes that neither of these anticipated fracture zones were encountered in the U12t.03 drift. No explanation is offered for this discrepancy.

The most significant inflow into the U12t.03 HUSKY PUP drift occurred at the terminus of the drift, about 65 ft short of a fracture zone which was predicted to flow at 310 gpm had the drift been extended that far. Hoover believes that the 60 gpm flow which occurred at the end of the drift came from interconnecting fractures into this zone. He also notes that inflow from relatively short rockbolt holes attests to the poor hydraulic interconnectivity in this area. In a final observation, Hoover mentions that there was a 30 - 35 gpm flow into the HUSKY PUP Bypass Drift extension from a fracture zone which was dry in an adjacent drift only 10 ft away. This fracture zone had produced a similar initial flow rate when

penetrated by the adjacent drift. This is further testimony to zones of very poor hydraulic interconnectivity.

Hoover (1975) makes the following conclusions with regard to water in the T tunnel complex:

- Most of the water flowing from the exploratory drill holes is evidently from poorly connected reservoirs in fault and fracture zones;

- The pressure response in the U12t.03 UG-1 and U12t.04 UG-1 drill holes to activities in the U12t.05 UG-1 and U12t.06 UG-1 drill holes indicates that some individual fracture or fault zones are interconnected and open to water flow over distances of at least several hundred feet;

- Maximum pressures in the drill holes indicate that the pressure head in the fractures varies significantly within this relatively small area. Maximum pressures indicate fracture saturation from slightly below to well below the top of the zeolitized tunnel bed tuffs.

Table 3.1. Peak flows and pressures in the U12t exploration holes.

HOLE	COMPLETION DATE	LENGTH ft	MAXIMUM FLOW gpm	MAXIMUM PRESSURE AND HEAD psi (ft)
U12t.03 UG-1	NOV 1972	3690.	200. 7 NOV 1972 @ 3690 ft 37.5 16 NOV 1972	165. (381) 17 MAY 1973
U12t.03 UG-2	DEC 1972	1504.	35. 14 DEC 1972 @ 1504 ft	Not Measured
U12t.03 UG-3	JUL 1974	1600.	100. 3 JUL 1974 @ 1379 ft	42. (97.) 15 JUL 1974
U12t.04 UG-1	APR-MAY 1973	1900.	240. 1 JUN 1973 @ 1900 ft 225. 7 JUN 1973 124. 13 SEP 1973	127. (293.) 26 OCT 1973
U12t.05 UG-1	JUN-AUG 1973	2402.	≈200. 24 JUL 1973 @ 1331 ft ≈200. 9 AUG 1973 @ 1610 ft ≈200. 14 AUG 1973 @ 1910 ft	125. (288.) NOV 1973
U12t.06 UG-1	SEP-OCT 1973	2001.	192. 26 OCT 1973 @ 2001 ft 160. 30 OCT 1973 @ 2001 ft	≈70. (162.) NOV 1973

Table 3.2. Pressure response in U12t.03 UG-1 drill hole to drilling in U12t.05 UG-1 drill hole (from Hoover, 1975).

Date	U12t.03 UG-1 pressure (psi)	U12t.05 UG-1 depth (feet)	U12t.05 UG-1 waterflow (gpm)	Remarks
1973				
May 17- to June 11	165	---	---	Maximum pressure U12t.05 UG-1 not drilled.
13	162	100.5	---	----------
18	160	417.5	---	----------
19	160+	537.5	---	----------
22	160+	711.5	---	----------
25		790	1±	----------
27	160+	852	27-40	Open tools.
29	150	919	120	Open tools. Water flow increased from 20 gpm at 895.5 ft to 100 gpm at 911 ft while drilling.
July 3	140	1,031.5	45	Open tools.
16	140	1,068.5	85	Open tools.
16	135	1,068.5	102	Open tools at 588.5.
17	125	1,068.5	100	Open hole.
17	130	1,068.5	?	Open tools partly in.
18	140	1,130.5	?	Drilling.
20	135	1,230±	?	Drilling.
24	120	?	200±	Open hole.
25	130	1,340±	?	Drilling.
26	133	1,359±	90	Drilling.
27	137	1,375±	?	Drilling.

Table 3.2 continued. Pressure response in U12t.03 UG-1 drill hole to drilling in U12t.05 UG-1 drill hole.

Date	U12t.03 UG-1 pressure (psi)	U12t.05 UG-1 depth (feet)	U12t.05 UG-1 waterflow (gpm)	Remarks
1973				
July 30 to Aug. 6	137	1,382	30-32	All tools in hole.
7	137	1,509.5	80	Drilling.
8	135	1,610	?	Open tools ?
8	120	1,610	200	Open hole.
13	133	1,810	?	Drilling.
14	136	1,850	?	Drilling.
15	117	1,910	200	Open hole.
15	130	1,970	?	Drilling. 70 gpm at 1,962 ft.
16	135	1,982	?	Drilling. 60 gpm at 2,022 ft.
17	137	2,052	60	Drilling. Flow measured 1 1/2 hrs. prior to pressure.
17	138	2,095	?	Drilling. 60 gpm at 2,112 ft.
20	129	2,155	60	Drilling.
21	139	2,240	?	Drilling. 60 gpm at 2,232 ft.
22	138	2,252	?	Drilling. 55 gpm at 2,272 ft.
22	139	2,272	34	Open tools?
23	139	2,315	?	Drilling. 45 gpm at 2,312 ft.
24	139	2,392	50	Drilling.
24	139	2,352	70	Open tools.

Table 3.2 continued. Pressure response in U12t.03 UG-1 drill hole to drilling in U12t.05 UG-1 drill hole.

Date	U12t.03 UG-1 pressure (psi)	U12t.05 UG-1 depth (feet)	U12t.05 UG-1 waterflow (gpm)	Remarks
1973				
Aug. 27	127	2,352	220	Open tools at 200 ft.
27	120	2,352	195	Open tools at 1,100 ft.
28	118	2,352	240	Open hole.
28	120	2,352	90	All tools in at 240 ft.
30-Sept. 4	Set packer in U12t.03 UG-1 at 1,026 ft.			
4	142	2,352	54	Open tools at 240 ft. Swing shift.
5	142-145	2,352	42	Open tools at 240 ft. Graveyard shift.
5	142	2,352	3	Open tools at 240 ft. Day shift.
5	147	2,352	3	Open tools at 240 ft. Swing shift.
6	147	2,352	10	Open tools at 240 ft. Graveyard shift.
6	143	2,352	12	Open tools at 240 ft. Day shift.
6	150	2,352	10	Open tools at 240 ft. Swing shift.
6	Packer in U12t.03 UG-1 blew up at 2130 hrs.			
Sept. 7 to Nov. 12	U12t.03 UG-1 open or drilling on packer. Flow in U12t.05 UG-1 used for drilling.			
9	U12t.03 UG-1 shut-in after drilling out packer. 75 psi U12t.03 UG-1 shut in.			
12	90	2,352	---	U12t.05 shut-in at 120 psi.
13	90	2,352		U12t.05 shut-in at 125 psi.
Both drill holes grouted November 13, 1973				

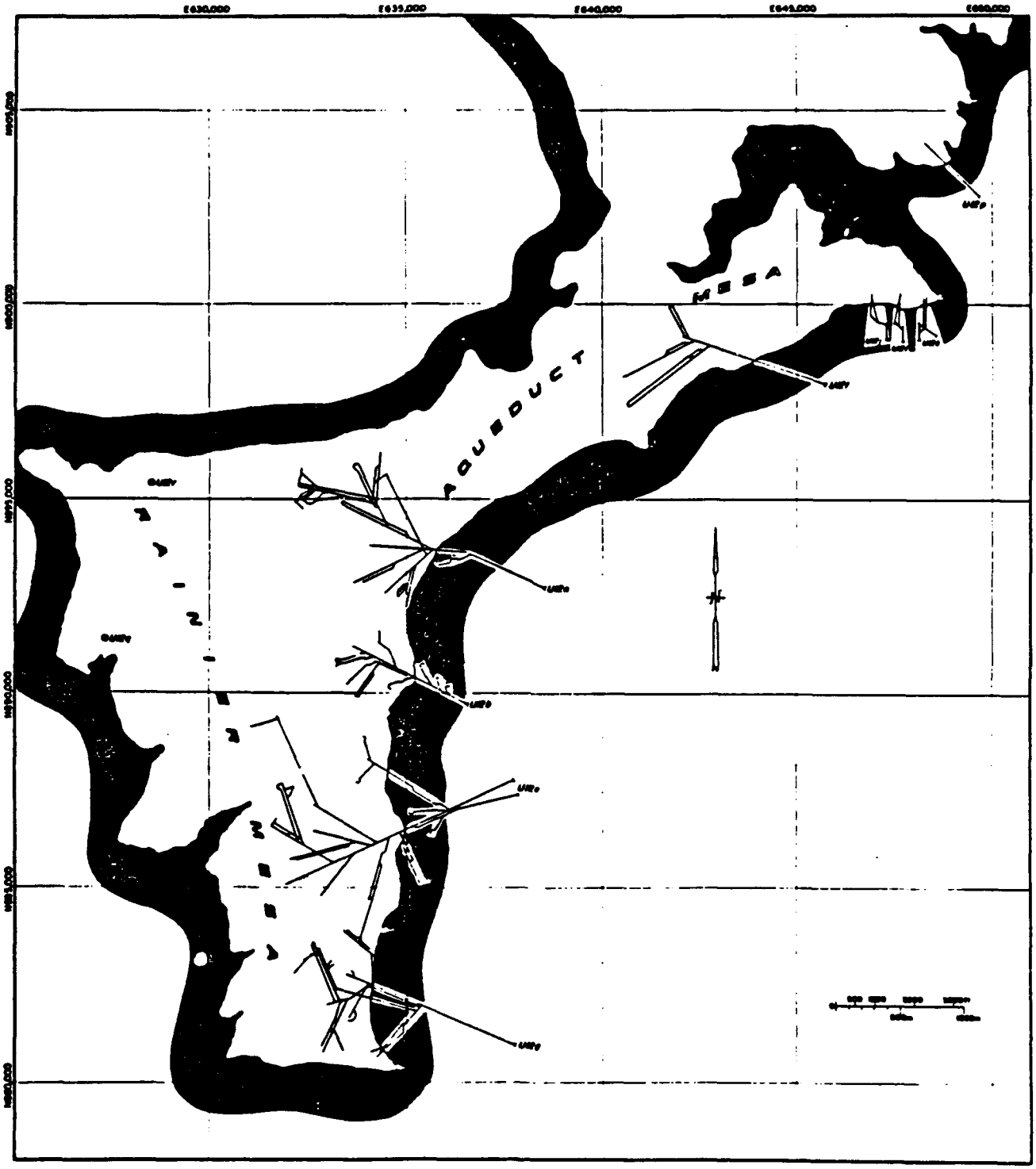

Figure 3.1. Locations of major tunnel complexes, Rainier Mesa (courtesy of Dean R. Townsend, Fenix and Scisson, Inc.).

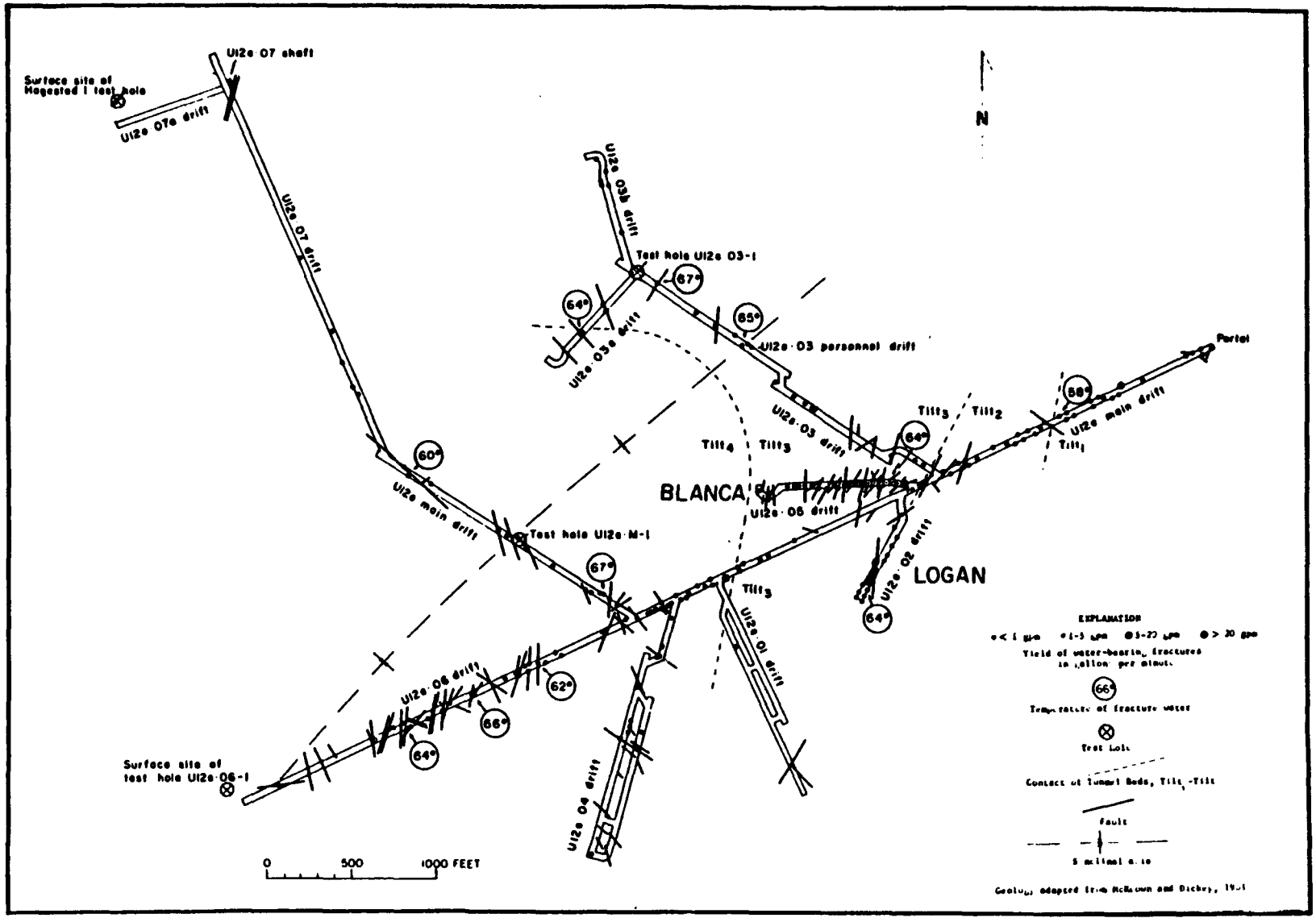

Figure 3.2. Fault locations and occurrence of fracture water in E Tunnel, Rainier Mesa (from Thordarson, 1965).

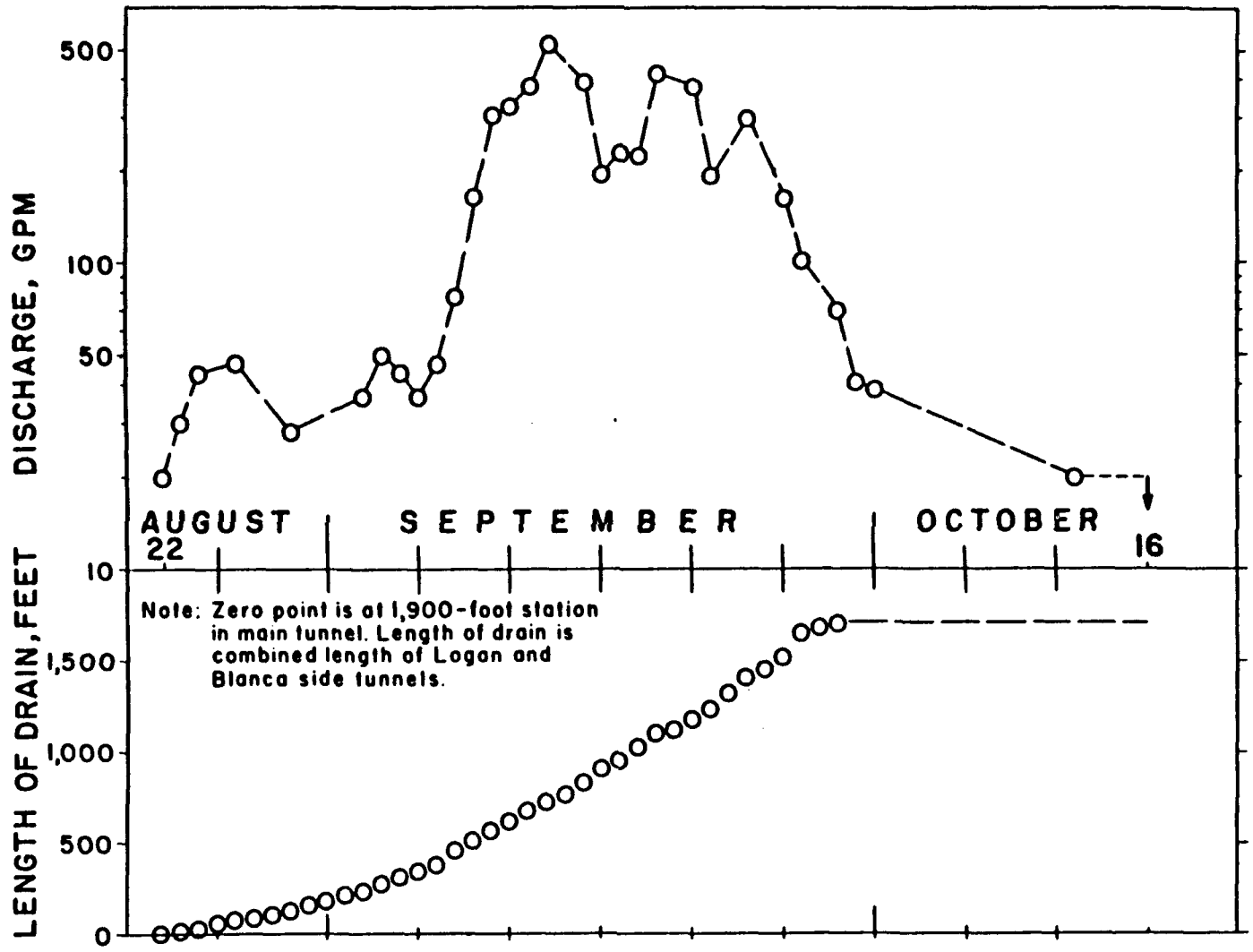

Figure 3.3. Tunneling progress and total flow from LOGAN and BLANCA Drifts (from Thordarson, 1965).

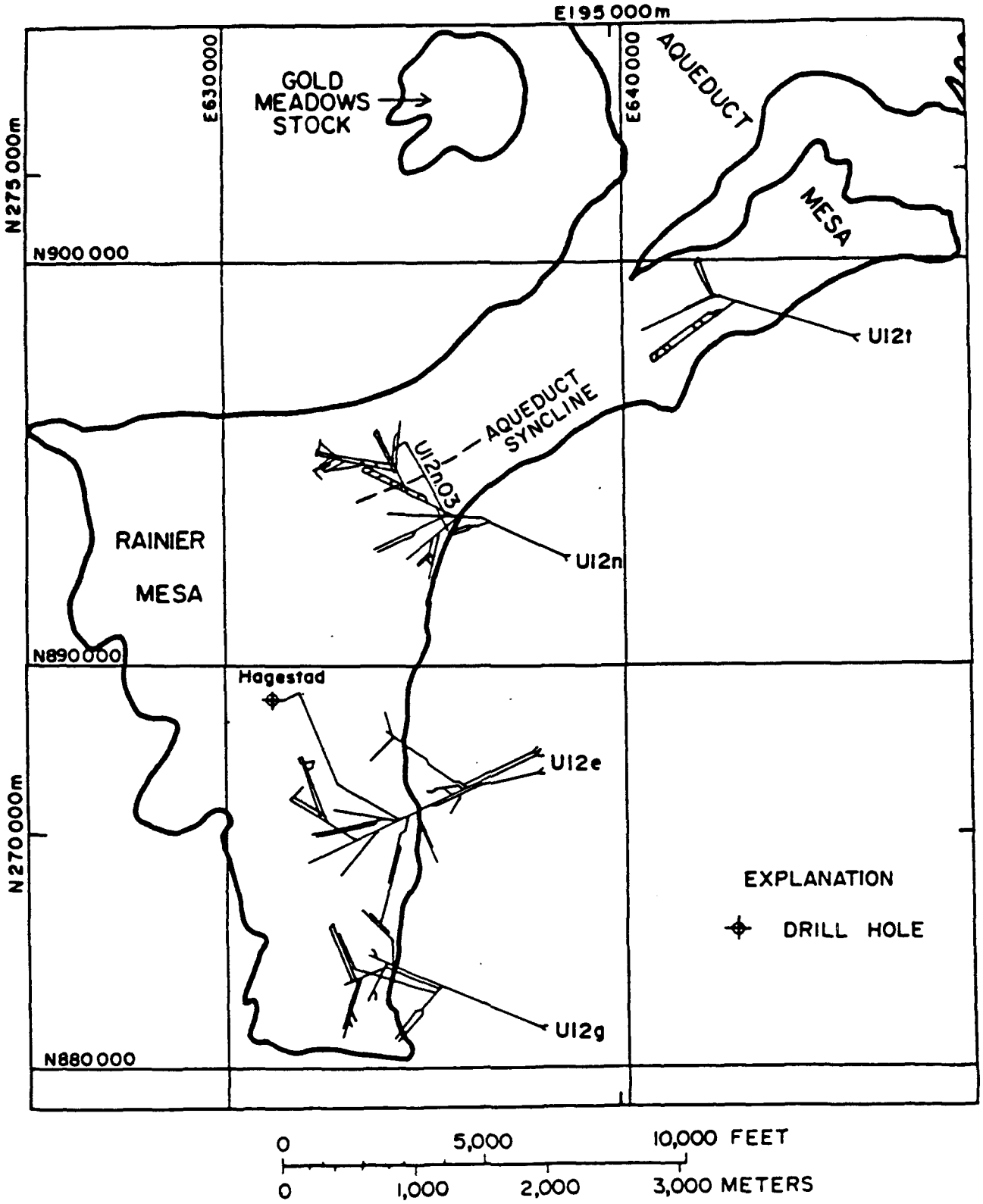

Figure 3.4. Location of U12n.03 Drift (from Ege et al., 1980).

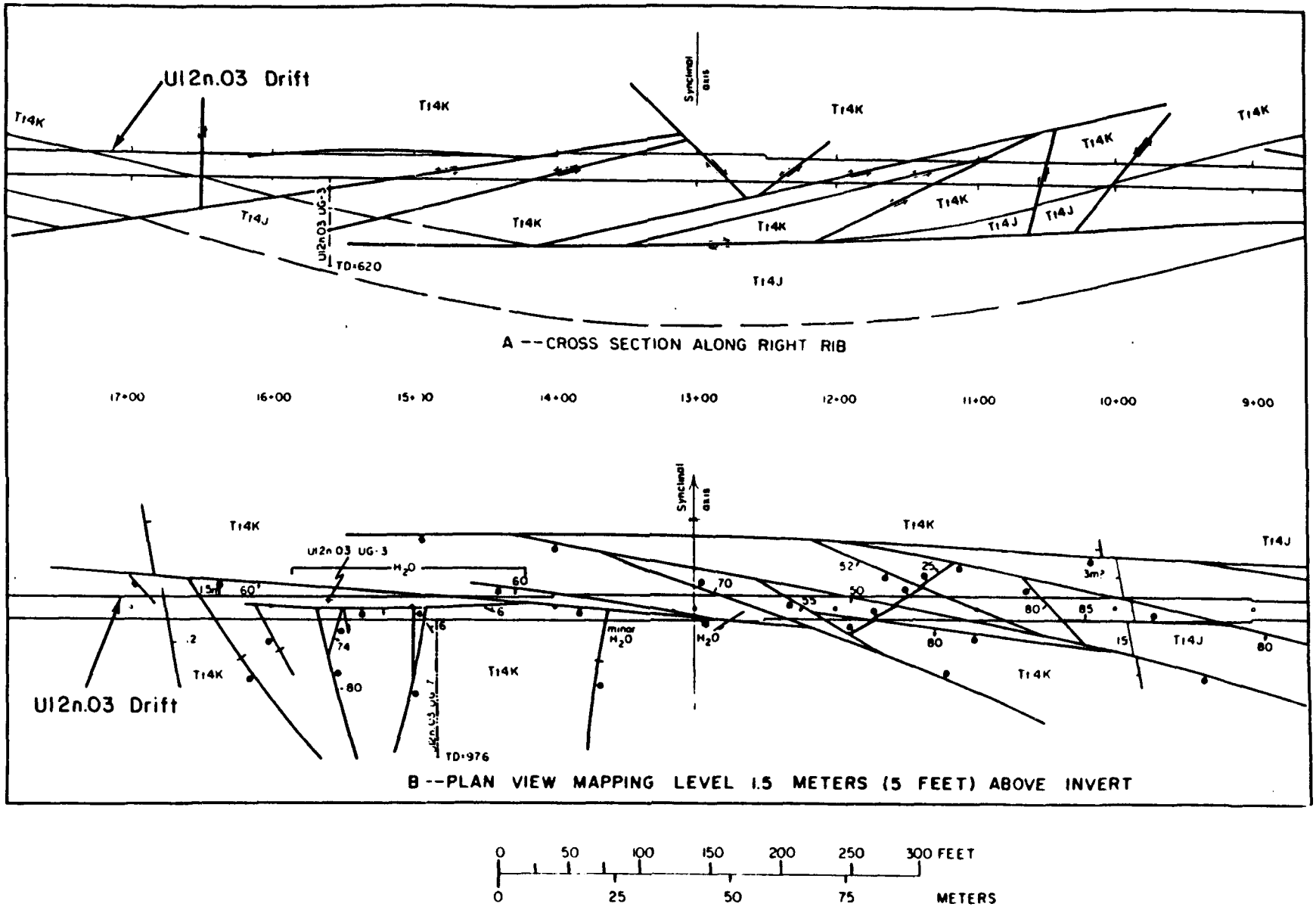

Figure 3.5. Geology of the U12n.03 drift in the vicinity of the Aqueduct Syncline (from Ege et al., 1980).

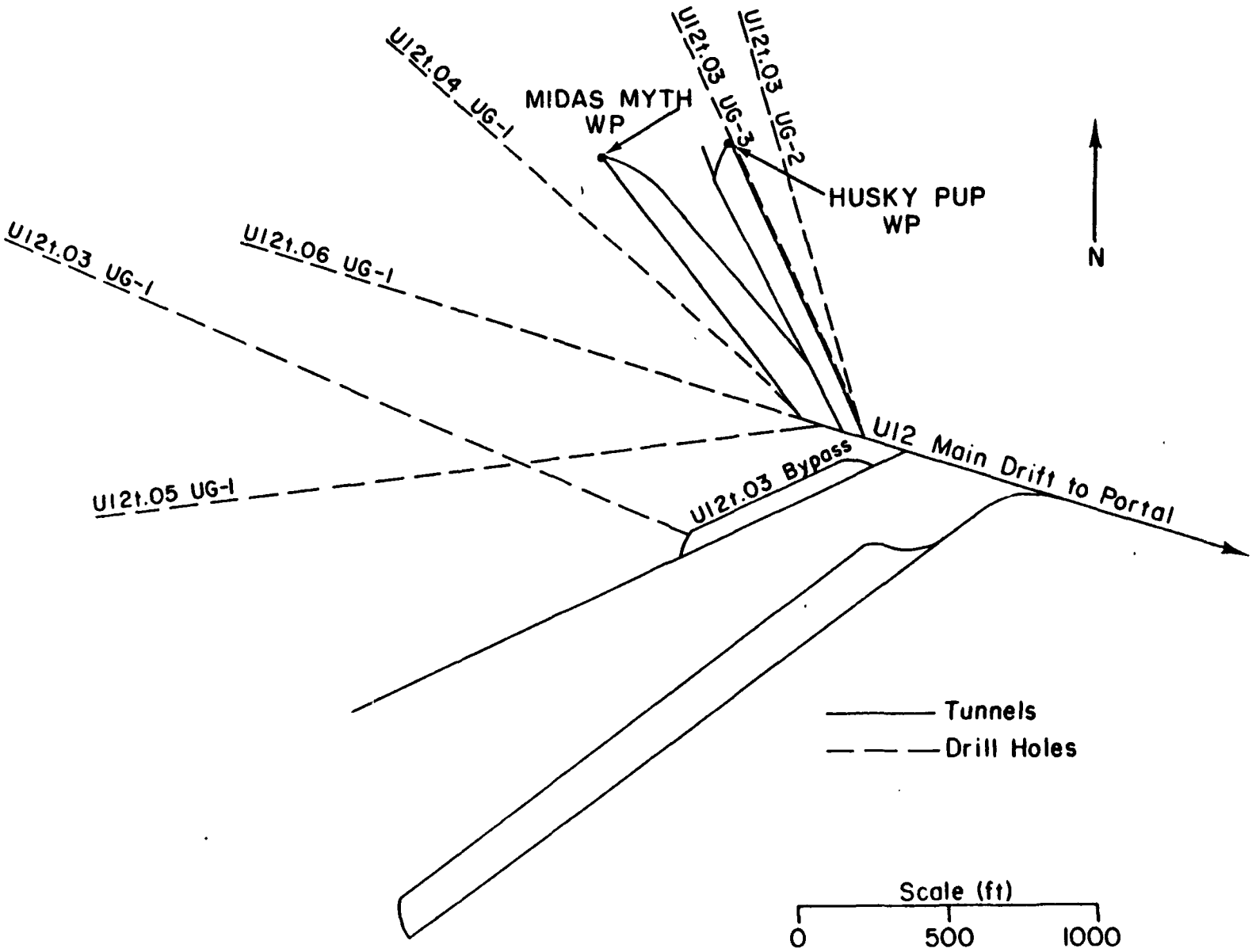

Figure 3.6. Locations of T Tunnel exploratory drill holes.

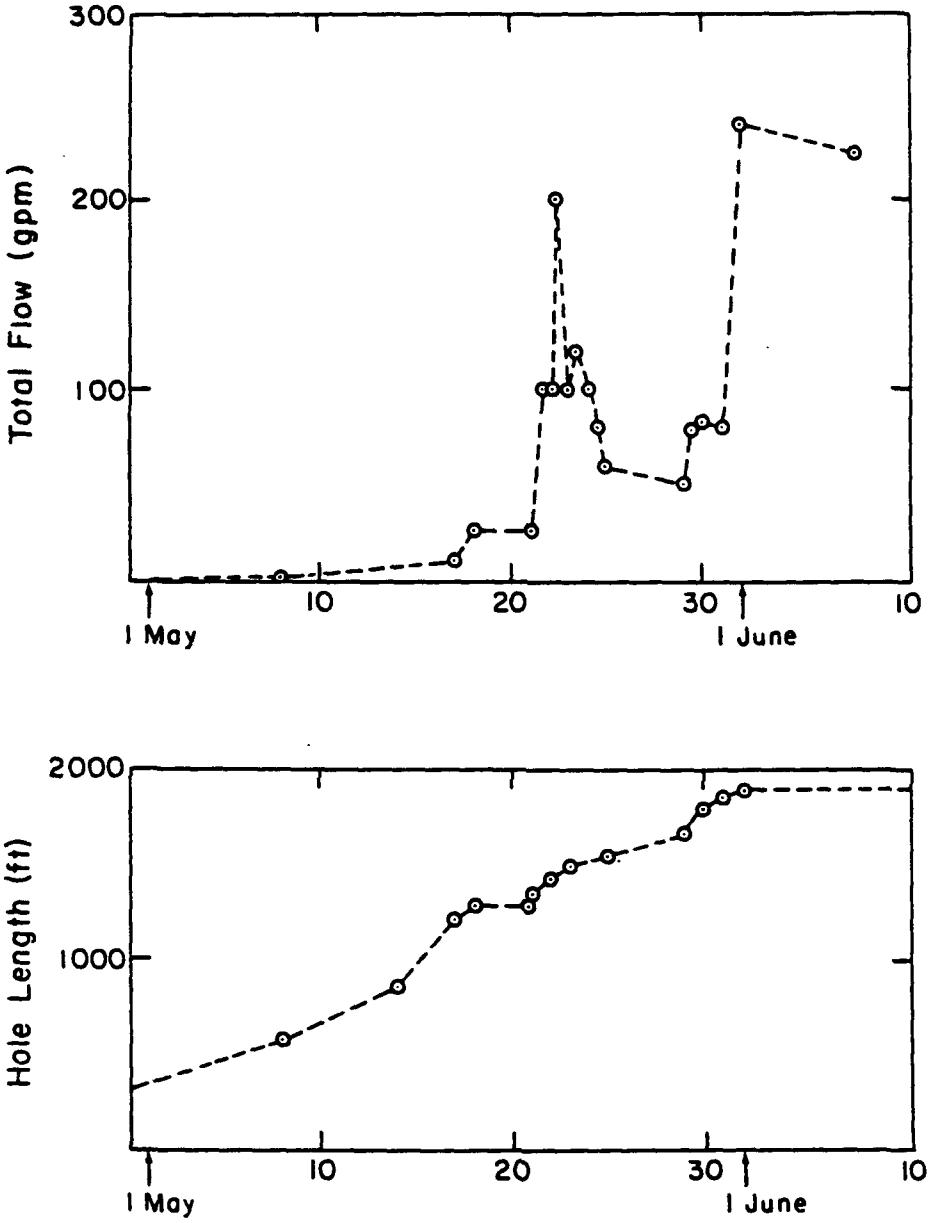

Figure 3.7. Drilling and flow logs - hole U12t.04 UG-1.

SECTION 4

INFLOW OF WATER FOLLOWING UNDERGROUND TESTS

INTRODUCTION

Inflow of water following underground nuclear detonations in the tunnel bed tuffs of Rainier Mesa has not been a major problem. However, following the MIGHTY EPIC event in the U12n tunnel complex, there was flooding of access drifts and severe flooding of hardened test structures in the vicinity of the detonation.

There are a number of possible explanations as to why such flooding has not been a more common occurrence. Most obvious is the location of many of the underground tests in areas where the level of fracture saturation, i.e. the easily mobilized ground water, is below the level of the shot. In general, tests in the G and B tunnel complexes fall into this category.

A second explanation for lack of flooding is that the level of fracture saturation varies significantly within the tunnel complexes which generally lie beneath the water table. As described in previous sections, there are apparently "dry" areas within these complexes which are either within a zone of depressed fracture saturation or are in an area where the fractures drain to the underlying unsaturated and more permeable rock. Tests within such areas have not flooded because there is little or no fracture water to mobilize.

A third explanation for the low incidence of flooding is the possibility that the underground nuclear detonations may actually induce drainage of saturated fractures into the underlying unsaturated rock. Extensive zones of block motion occur to substantial ranges, in some instances to peak dynamic stress levels as low as 0.1 to 0.25 Kbar, surrounding the underground events. Block motions are permanent displacements along pre-existing planes of weakness such as faults and bedding planes. These have been well documented on several events, e.g. Short and Kennedy (1982), Blouin (1980). Such motions surrounding and beneath a shot may provide drainage paths to the underlying more permeable rock, thus tending to dewater rather than flood a particular site. A case in point may be the MIGHTY EPIC event in T Tunnel adjacent to the HUSKY PUP event. Prior to the test many of the faults and bedding planes were wet or seeping water. Following the test there was little or no water evident. In addition, the presence of fracture water may enhance the occurrence and extent of block motion by lubrication of fracture surfaces and/or by preventing mobilization of frictional resistance during dynamic loading.

A final factor contributing to the low flooding incidence is the fact that most of the underground nuclear tests are detonated in close proximity to previous tests which have often already loaded the surrounding rock to very significant stress levels and may have already mobilized fracture water in the area and/or drained the site.

For whatever reasons, flooding on the Rainier events has not been widespread. The flooding on MIGHTY EPIC, however, stands as a warning that the problem cannot be ignored. In fact, in a

different geologic setting where rock permeability is higher than that in the tuffs and where the water table is not perched, as at Rainier Mesa, flooding similar to that experienced on MIGHTY EPIC might be the rule rather than the exception.

Two mechanisms are often put forth to explain the generation of water from underground explosions in the NTS tuffs. In the first, water stored in fracture zones above and adjacent to the underground works is released by explosive disturbance of previously impermeable fracture zones leading to the tunnels. Such disturbances may be in the form of block motion or rebound, whereby there is dilatency in the fractures allowing the water to flow rapidly into the tunnels.

The second mechanism is akin to the consolidation process in soil mechanics. In this process a residual stress field resulting from the explosive detonations is imposed on the saturated rock. The residual stresses squeeze both the interstitial water and fracture water from the surrounding rock into the underground works. In this process the amount of water produced and the rate of flow are dependent on the permeability of both the interstitial rock and fractures, the magnitude of the residual stresses, and the net porosity and mechanical properties of the rock.

There is solid experimental evidence for both of the above water production mechanisms on underground nuclear and HE tests beneath Rainier Mesa. Following reentry to MIGHTY EPIC extensive flooding was observed, with water still flowing from several faults which had been dry prior to the test and other evidence of flow from faults which had been displaced by the shot. On the HE shot ONETON, conducted in G Tunnel, generally considered to be above the level of fracture

saturation, a substantial amount of water was produced from the walls and floor of an open drift located at a range where the peak dynamic stress was only 0.12 Kbar. This appeared to be interstitial water squeezed from the intact rock by the elevated residual stresses generated by the explosion. Water flowed for hundreds of hours following the detonation and was accompanied by continually decreasing residual stresses within the rock mass adjacent to the drift.

The following subsections describe available details on the MIGHTY EPIC and ONETON water production.

MIGHTY EPIC

MIGHTY EPIC was a low yield (i.e. less than 20 KT) contained nuclear event fielded in the U12n.10 drift beneath Rainier Mesa. The location of MIGHTY EPIC is shown on the plan view of Figure 4.1. The working point was located in Tunnel Bed 3 while most of the test structures and the line of site pipe were primarily in the zeolitized tuffs of Tunnel Bed 4. According to Townsend (1984) there was virtually no water inflow during mining of the MIGHTY EPIC line of site and bypass drifts. The only signs of water were a few damp fracture surfaces. Also, unlike the majority of tests, the MIGHTY EPIC works were in virgin ground which had not been subjected to high previous stresses from adjacent shots.

A plan view of the MIGHTY EPIC event is shown in Figure 4.2. The working point is at the west end of the U12n.10 main drift. This drift houses the line of site (LOS) pipe which contained targets for exposure to radiation from the MIGHTY EPIC device. The LOS pipe is simply a large diameter tapered steel

tube with mounts for the targets located at prescribed ranges. These targets are shielded from blast and debris by two large gas driven sliding doors at locations labeled DAC 1 and DAC 2. Beyond the DACs is a third closure, called the Tunnel and Pipe Seal, or TAPS, which was located approximately 100 ft east of the DAC 2. The radiation targets are located to the east of the TAPS at various ranges along the LOS pipe.

The Bypass Drift runs parallel to the LOS Drift and provides access to the working point room and Interface Drift during construction of the LOS pipe. Prior to the test the Bypass Drift is grouted closed to the range indicated by the end of stemming between the B and C Structures Drifts. Beyond the end of stemming the Bypass drift is open and is reinforced with a standard rockbolt, wire mesh and gunite lining.

Running SW off the Bypass Drift are the A, B, and C Structures Drifts. These contained horizontal cylindrical hardened structures at ranges of 290, 400 and 600 ft from the working point. Various structural concepts, sizes and strengths were tested in these drifts.

The Interface Drift running north from the working point provided access to instrumentation holes drilled vertically downward through the tunnel bed tuff to the underlying quartzite. Instrumentation in these holes was designed to measure block motion between the tuff and underlying quartzite. The Interface Drift was also grouted shut prior to the test.

The post-shot observations of water on the MIGHTY EPIC event are based on two memos from Dean R. Townsend (1976, 1977) and on informal interviews with him (1984) in which he supplied additional details from memory. He reentered the MIGHTY EPIC

Bypass Drift approximately 2 days after the event through the overburden plug. This is an additional safety plug to keep any radiation which might escape near the source region from entering the tunnel complex. It is located just beyond the end of the MIGHTY EPIC Bypass Drift at a range of about 2000 ft from the working point. On reentry the Bypass Drift was flooded from the end of stemming all the way to the overburden plug, a distance of approximately 1600 ft. There was approximately 6 inches of water on the floor of the drift, the water being somewhat deeper near the overburden plug and shallower near the end of stemming due to the gradient of the tunnel. Taking the average tunnel width as 11 ft, it is estimated that there was probably in excess of 50,000 gal of water in the Bypass Drift. A similar amount was probably contained in the LOS Drift.

Water flowing from two faults appears to have been the primary source of this flooding. A small reverse fault in the Bypass Drift at a range of 870 ft from the working point was flowing at 3 - 5 gpm several days after the event. A larger normal fault in the LOS Drift at a range of 940 ft from the working point was emitting 5 to 10 gpm at this time. There was no evidence of significant block motion on these faults, though the gunite lining had been spalled from the walls, evidently by the flowing water. These faults continued to flow for approximately 20 days after reentry. Since there was no flow from these faults during mining, the MIGHTY EPIC detonation must have either opened drainage to these faults (if they were already open), or opened these faults sufficiently to allow drainage from saturated zones within them and/or from within other saturated fractures connected to them.

During the initial reentry, water was observed in the LOS pipe between the DAC 1 closure and the TAPS and water was

observed leaking from around DAC 1. The source of this water was believed to be inflow from Fault 5, which ran NS and intersected the LOS Pipe between the two DACs. Block motion occurred along Fault 5, with about 1.5 ft of lateral motion in the area of its intersection with the Bypass and LOS Drifts. Figure 4.3 shows the location of major faults and bedding planes within the MIGHTY EPIC structures region with the direction and magnitudes of block motion indicated on the planes of weakness which were activated by the detonation. Townsend (1977) reports that post-test mining eventually provided access to the LOS Pipe between the two DACs. The LOS Pipe was partially crushed and torn open at its intersection with Fault 5 adjacent to the DAC 2 closure. A view of the pipe at this location is shown in Figure 4.4. The interior of the LOS pipe between the two DACs appeared to have been full of water shortly after the test, as evidenced by mud and water marks within the pipe. This water slowly leaked out past the DAC 1 over a period of days following the test.

Several centimeters of pink mud were deposited in the LOS pipe between the DACs. This mud consisted of finely powdered zeolitized tuff which appeared to be identical to a 1 cm wide seam of pale pink fault gouge lining Fault 5 in this region. Based on this evidence Townsend (1977) concludes that movement along Fault 5 provided a channel for post-test flow into the LOS Pipe. The actual source of this water was probably fracture water trapped in Fault 5 or in other fractures connected to Fault 5.

Post-test mining and reentry to the hardened experimental structures in drifts A and B revealed that these structures were full of water. As shown in Figure 4.3, the block motion along Fault 5 also intersected the B Structures Drift at which point there was a relative lateral displacement of 1.3 ft. This motion

heavily damaged the structure at the intersection, buckling and tearing the steel liner and evidently allowing water from Fault 5 to completely flood the structure. Views of the damage from the Fault 5 relative displacement are shown in Figure 4.5.

Reentry to the A Structures Drift revealed that one of the structures had been torn open in the vicinity of Fault 7, thus providing an entry point for the water which flooded that drift. No significant block motion was indicated on Fault 7; however, so the path and source of the water filling A Drift is uncertain.

In summary, many tens of thousands of gallons of water flooded the MIGHTY EPIC works at a number of locations following the detonation. The sources of most of this water were probably saturated faults and fracture zones which were tapped or mobilized by the stresses and motions generated by the explosion. In several locations flow evidently occurred along faults which were displaced more than a foot by the test. Steel lined hardened structures were completely flooded by water entering through tears in the liners. Significant flows of water were observed from faults at great ranges (nearly 1000 ft) from the working point. Stress levels and motions at these ranges are very low, well below levels normally associated with damage to even minimally lined tunnels. The MIGHTY EPIC drifts were dry during and after mining; the substantial flooding which occurred resulted solely from disturbance by the explosion.

ONETON

The ONETON HE event in G Tunnel produced water in a manner which contrasts with that described previously on MIGHTY

EPIC. Instead of mobilizing fracture water, the ONETON event forced interstitial water out of the voids in the saturated tuff. The residual stresses and stress gradients produced by the detonation apparently generated pore pressures within the rock which caused the pore water to migrate away from the higher stressed regions near the shot point and to flow into an open drift some distance away.

The layout of the ONETON event is shown in the plan view of Figure 4.6. A 2000 lb TNT sphere was detonated at the end of a fully stemmed dogleg drift. Stress and motion gages to actively monitor total dynamic and residual stresses and ground motions were placed at locations 1 through 12. Instrumentation cables were fed into the open drift adjacent to the bulkhead at the end of stemming. Smith (1984) described the ONETON setting in G Tunnel as saturated (about 98%) and free of faults and joints. No water was encountered during the ONETON mining.

Peak dynamic radial stress as a function of range is plotted in Figure 4.7. The ONETON data are a good match to the scaled peak stress attenuation from a previous series of 64 lb HE shots in this material. The ONETON peak stress data are also in reasonably good agreement with scaled peak stress data from the contained nuclear events.

Smith's (1983) plot of residual radial stress as a function of range for 6 HE shots in nearly saturated tuff is shown in Figure 4.8. The PUFF TOO 1000 lb data and the ONETON 2000 lb data have been scaled by the cube root of their yields to be consistent with the 64 lb data. There is considerable scatter in the residual stress data, though deletion of the two low data points from the RS 14 event, which Smith notes are in an unusually soft tuff layer, considerably improves the picture.

Note that residual stresses are considerably less than the peak stresses at any given range and that they tend to decay less rapidly than the peak stresses.

The residual stress field primarily results from formation of a permanent cavity by the detonation. Close to the explosion the high amplitude dynamic stresses cause severe plastic deformation of the rock and a strong outward thrust of material as the cavity around the detonation expands dynamically. Following the maximum dynamic expansion of the cavity there is a rebound caused by the high imbalanced stresses in the surrounding material. The cavity undergoes a partial compression, finally coming into equilibrium with stresses in the surrounding rock. The resulting equilibrium stresses are very high in the severely deformed rock surrounding the cavity, dropping monotonically to lower values in the less severely distorted rock further from the cavity. Smith notes that the ONETON cavity, measured after reentry, was quite uniform, with an average radius of 4.4 ft.

The decay of residual stress with time on the ONETON event is shown in Figure 4.9 for a period of about 17 hours after the event. Residual stresses decayed to approximately half their immediate post-test values over this time span. Similar data were recorded on the 64 lb events. Smith suggests that the decay of residual stress with time is related to migration of pore water induced by the residual stress gradient. He sites seepage of water into the open drift pictured in Figure 4.6 as evidence of this migration.

Following the ONETON detonation, water was observed seeping out of the face, ceiling, walls, and floor of the open drift (Smith, 1984). The face was located at a range of 55 ft from the working point. Following the detonation damp zones

appeared on the walls and ceiling. These became increasingly moist until finally water began running off the ceiling and down the walls and collected on the floor of the drift. During the first 121 hours after the shot, 215 gallons of water seeped out. During the following 116 hours, an additional 335 gallons seeped from the face and sides of the drift. Smith notes that during the reentry mining, no distinct fracture zones or other water bearing aquifers were encountered, suggesting that pore water was migrating away from the high residual stress gradients. As the pore water migrates out of the higher stressed rock, pore compression or partial collapse will occur accompanied by a relaxation of both pore pressures and total stresses in this region. This mechanism, which is similar to the consolidation process in saturated fine grained soils, would account for the decaying residual stresses recorded in Figure 4.9. A preliminary two phase calculation of the ONETON experiment is described in Section 7.

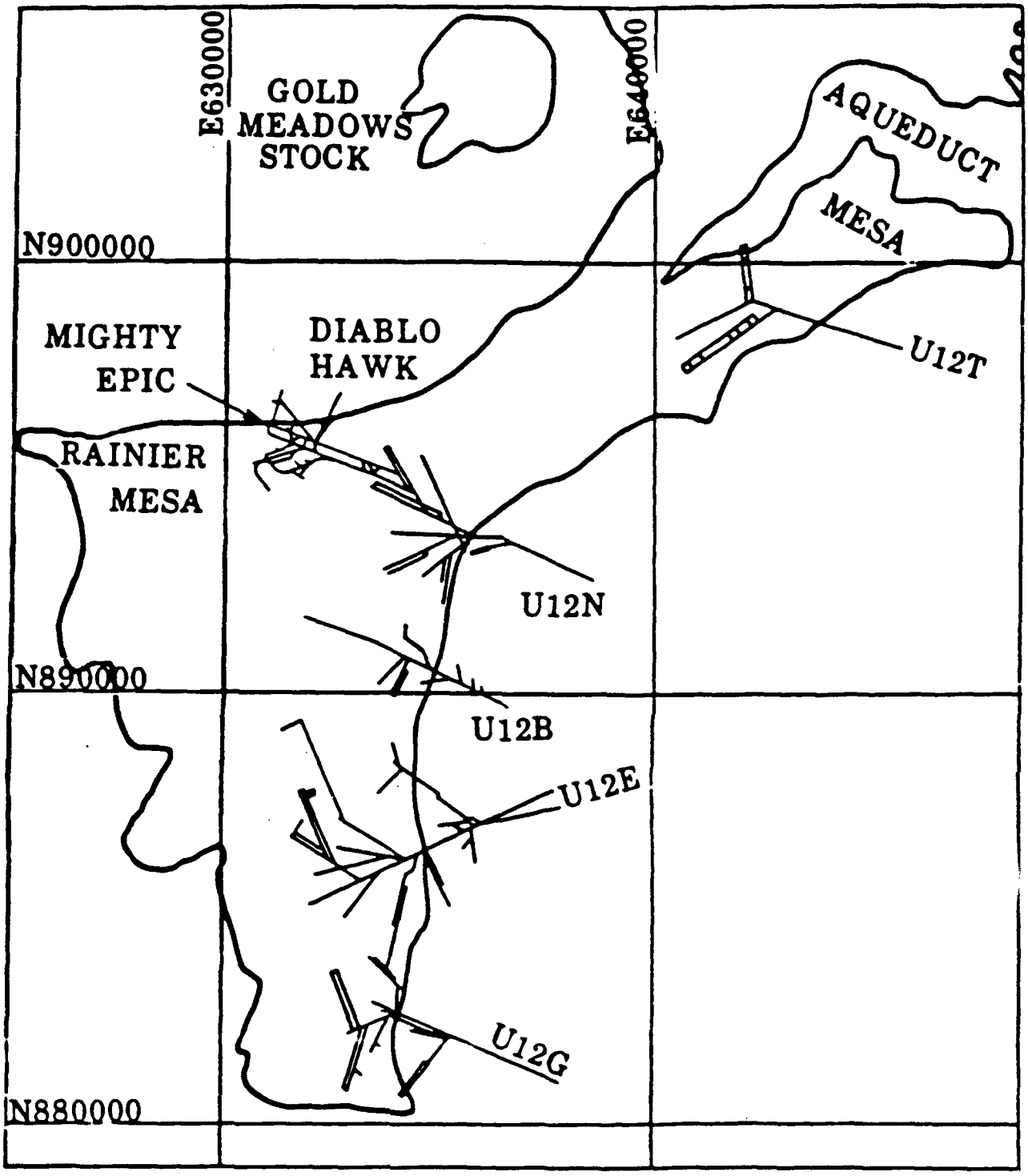

Figure 4.1. Location of MIGHTY EPIC event (from Short and Kennedy, 1982).

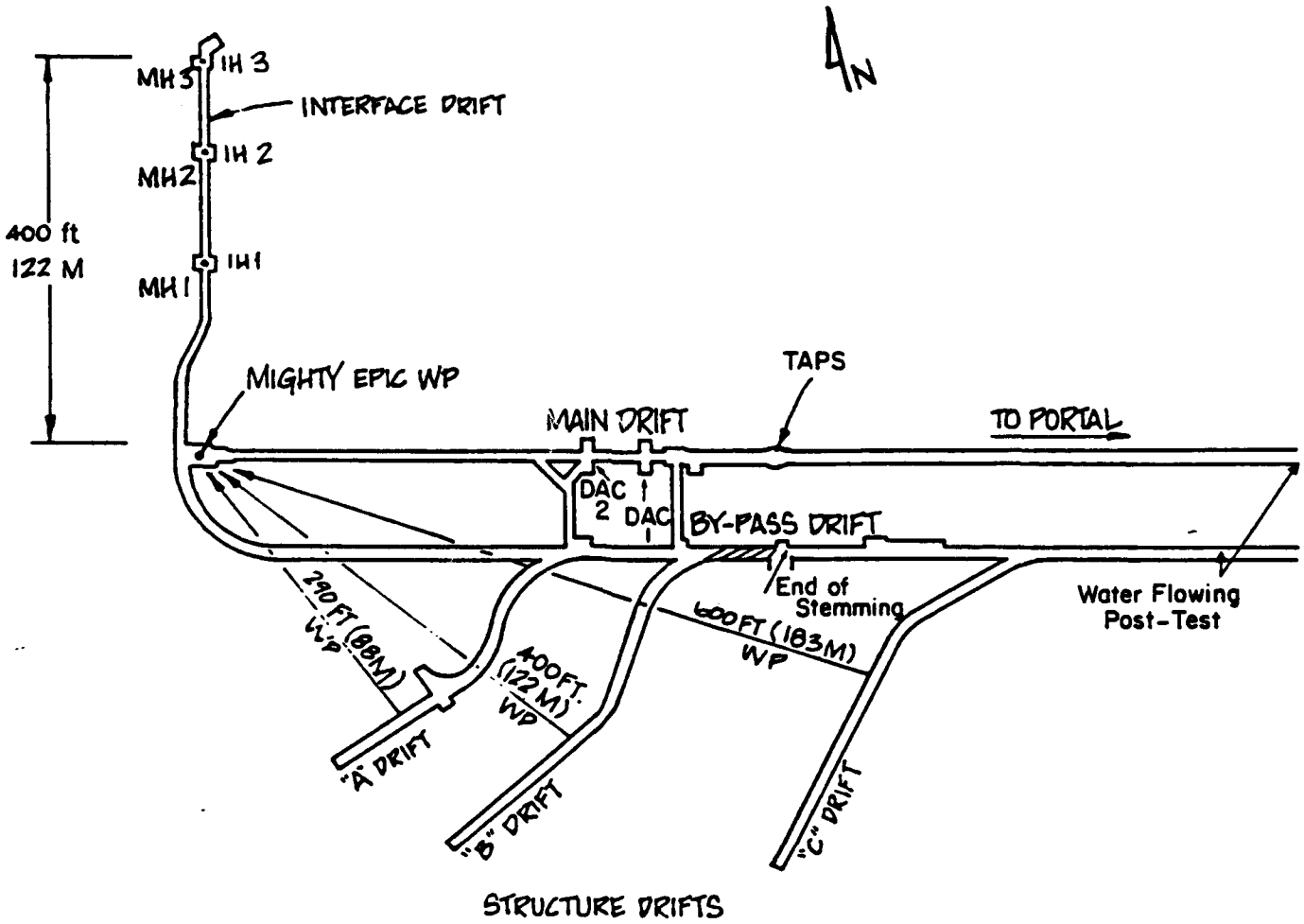

Figure 4.2. Plan view of MIGHTY EPIC Drifts (from Short and Kennedy, 1982).

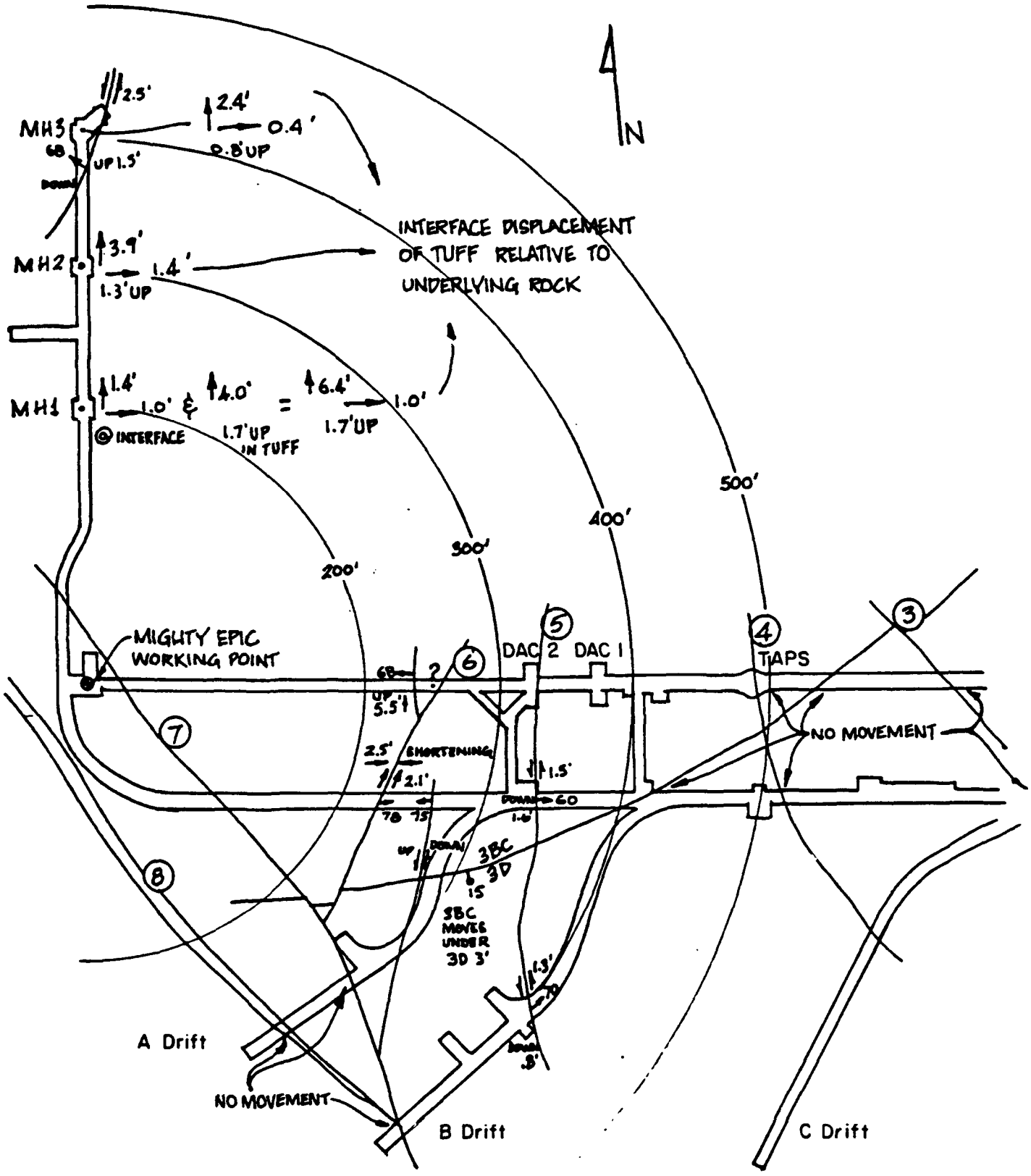

Figure 4.3. Location and magnitude of MIGHTY EPIC block motion (from Short and Kennedy, 1982).

Figure 4.4. Damage to LOS pipe from relative displacement on Fault 5 (from Short and Kennedy, 1982).

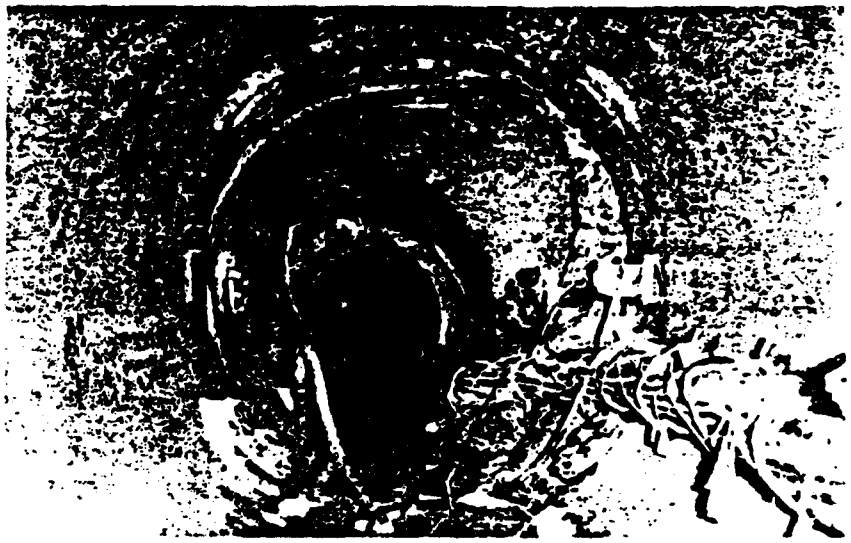

a) Water and damage due to movement along fault #5 looking southwest.

b) Damage due to movement along fault #5 looking northeast.

Figure 4.5. Damage to B Structures Drift from relative displacement along Fault 5 (from Short and Kennedy, 1982).

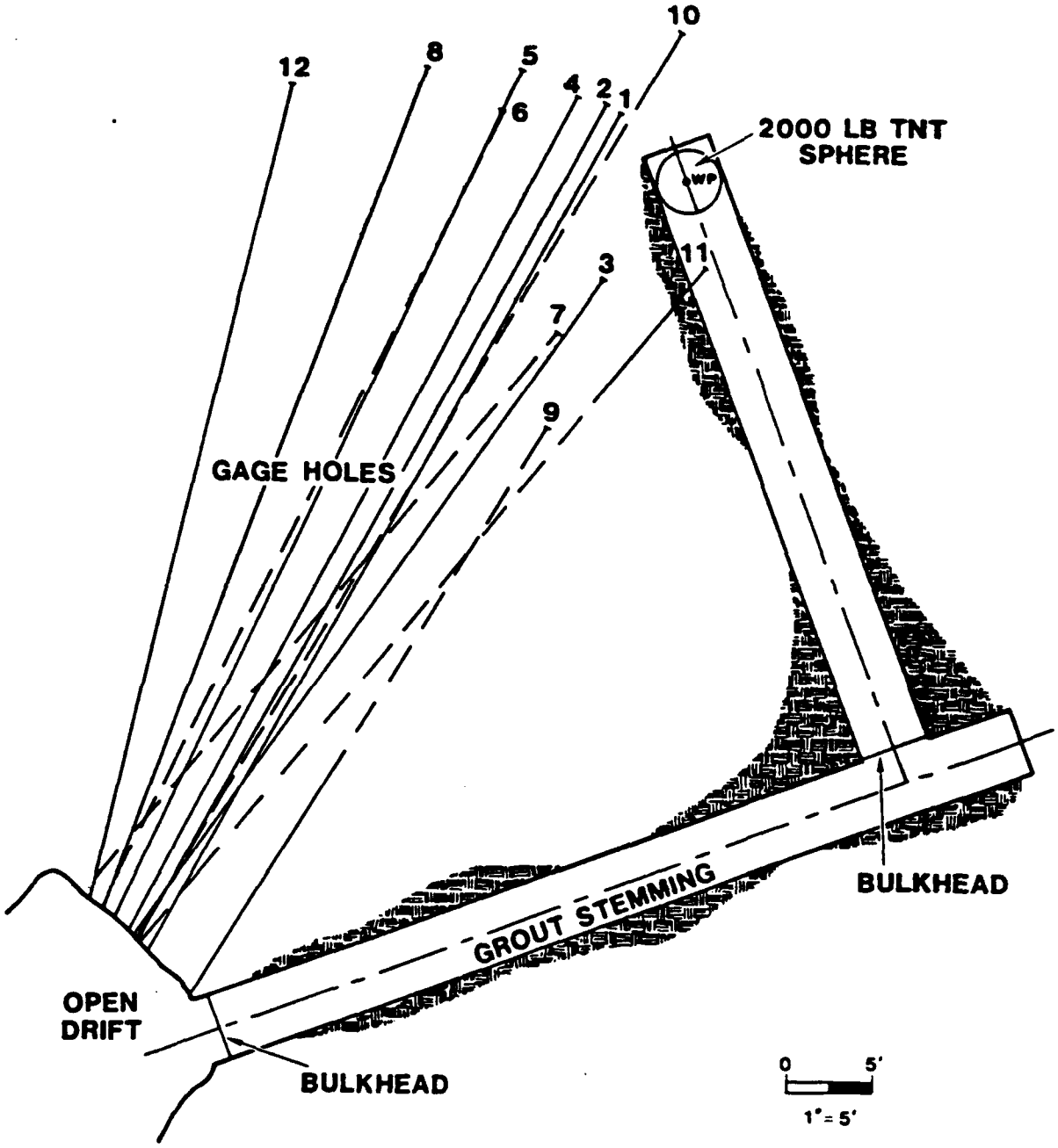

Figure 4.6. ONETON test layout - plan view (from Smith, 1983).

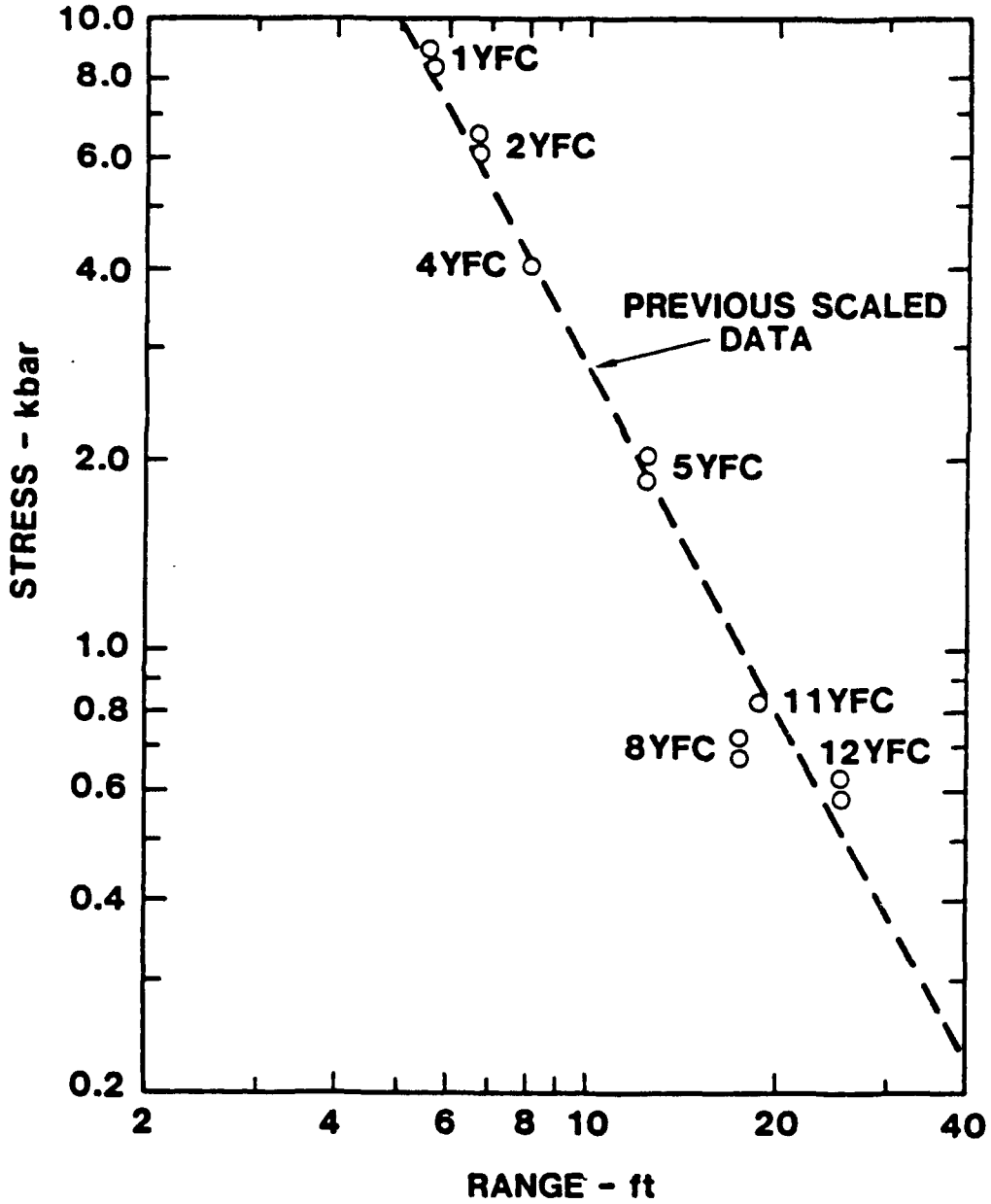

Figure 4.7. ONETON peak dynamic radial stresses (from Smith, 1983).

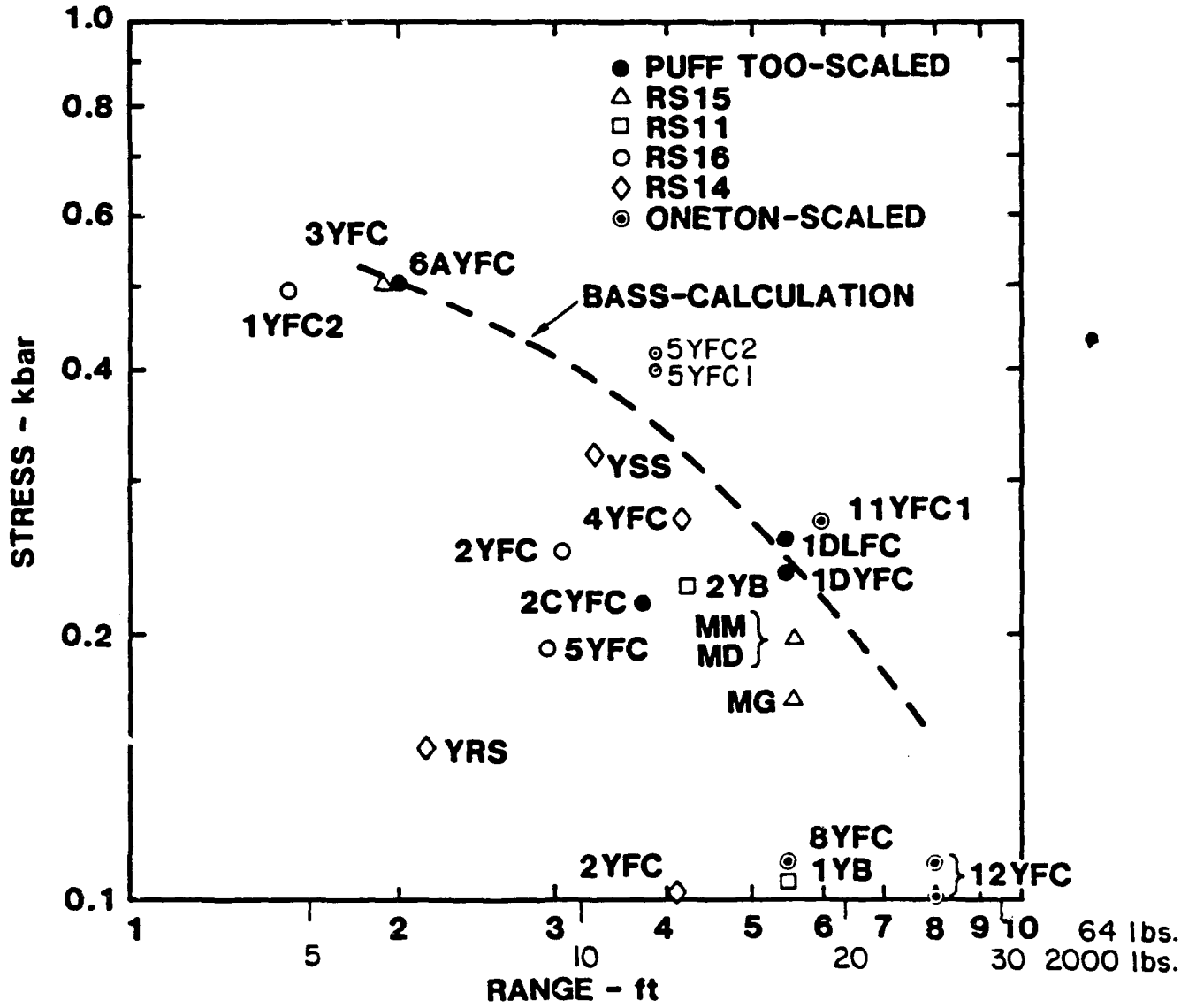

Figure 4.8. Residual stress amplitudes from six HE events, scaled to 64 lbs (from Smith, 1983).

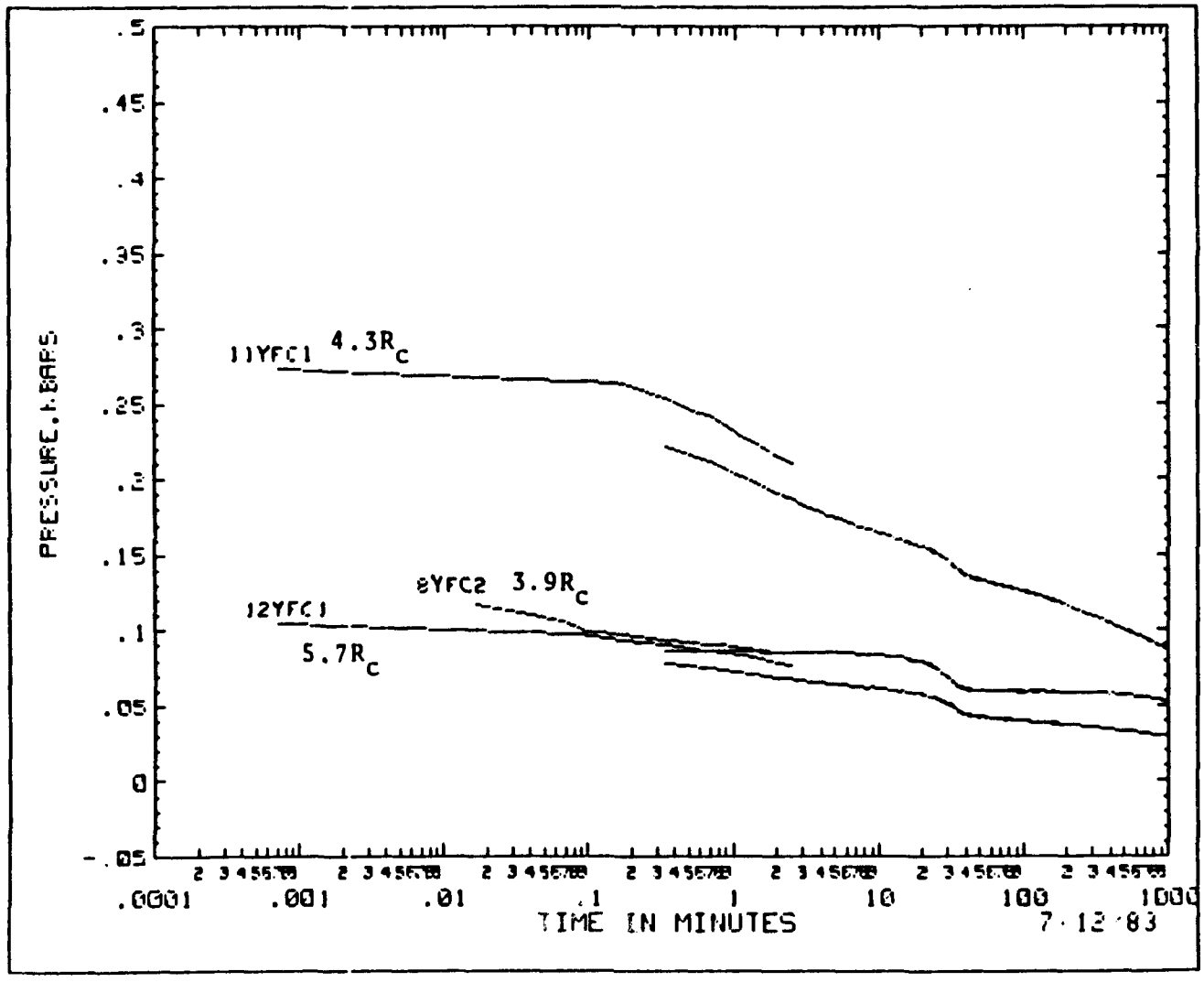

Figure 4.9. Decay of ONETON residual stresses (from Smith, 1984).

SECTION 5

CONSL CODE DESCRIPTION

INTRODUCTION

The numerical parametric calculations in this initial study were conducted using the one dimensional, axisymmetric, two or three phase, quasi-static finite element code CONSL. CONSL is an adaption of the general two dimensional quasi-static analysis program QSAP written and described by Kim (1982). CONSL can be used to solve both uniaxial strain and axisymmetric flow and consolidation problems. It was written in standard FORTRAN and can even be run on microcomputers using the CP/M operating system. CONSL can model nonlinear material behavior and calculate flow rates and consolidation in multilayered media. Imposed loading conditions can include specified total stresses, pore pressures and skeleton displacements. CONSL can also solve three phase problems in which the degree of saturation is over 85%. CONSL was checked against Terzaghi's closed form solution for one dimensional consolidation. There was excellent agreement between the closed form solution and the CONSL results. A copy of CONSL is included in Appendix D. This version is written in FORTRAN 77 for an HP1000 system.

In the next subsection a description of the input to the CONSL program is given which serves to briefly describe the features of the program as well as to provide a guide to its use. The mathematical finite element formulations used in CONSL are described in Appendix C. Appendix A presents derivations of

the undrained properties of saturated media in plane strain. These were used to check the initial loading conditions computed using CONSL. Appendix B is a derivation of one of the two flow algorithms used in CONSL.

DESCRIPTION OF INPUT DATA

Input must be in terms of consistent units such as SI, English, etc.

Card 1

Problem Title (80 characters)

Card 2

RI, RO, AP, NUMEL, NKF, NEF, NTF, IPLANE, NVF, NDF (3E10.0,7I5)

RI = radius of the tunnel
RO = radius of remote boundary
AP = mesh growth factor
If AP = 0.5, element sizes are constant
If AP < 0.5, element sizes become larger toward the remote boundary
If AP > 0.5, element sizes becomes smaller toward the remote boundary
For AP = 0.25, half of the total elements are located within the first 25% of the total distance to the remote boundary

NUMEL = total number of elements

The size of the first element a_1, is given by

$$a_1 = \frac{RO - RI}{NUMEL} \left[1 + \frac{NUMEL - 1}{NUMEL} (4AP - 2) \right] \quad (5\text{-}1)$$

NKF = 0 linear elastic skeleton
= 1 nonlinear skeleton

NEF = 0 saturated skeleton
= 1 partially saturated skeleton

NTF = 0 constant time steps
= 1 variable time steps

IPLANE = 0 1-D cylindrical symmetry
= 1 1-D plane strain

NVF = 0 flow volume calculated from pore pressure gradient on first element
= 1 flow volume based on Equation B-19 as described in Appendix B

NDF = 0 decoupled two phase material model as described in Appendix A
= 1 fully coupled two phase material model as described in Appendices A and C.

Card 3

CM, V, POR, PK, (E10.0,2F10.0,E10.0)

CM = constrained skeleton modulus

V = Poisson's ratio of skeleton

POR = porosity

PK = coefficient of permeability

Card 4 (for NEF = 1)

SO, STAW (2E10.0)

SO = degree of saturation

STAW = pressure difference between pore water and pore air (see Kim, 1982)

Card 5

TEND (E10.0)

TEND = maximum calculation time

Card 6 (for NTF = 0)

DT (E10.0)

DT = constant time step

Card Group 6 (for NTS = 1)

```
NDT(I5)
NCL(1), DTT(1)
NCL(2), DTT(2)
 .
 .
 .
 .
 .
NCL(NDT), DTT(NDT)
```

} NDT Cards with (I5, E10.0)

NDT = number of different time steps
NCL = number of cycles having a given time step DTT
DTT = duration of the given time step

Card 7

SRI, STI, PI (3E10.0)

SRI = initial effective radial stress (compression is negative)
STI = initial effective tangential stress
PI = initial pore fluid pressure

Card 8 (left end boundary conditions, see Figure 7.1)

JSDL, JDCL, TNFL, BPPL, SSDL (2I5, 3E10.0)

JSDL = 0 free skeleton boundary
= 1 fixed or specified skeleton boundary

JDCL = 0 permeable boundary
= 1 impermeable boundary

TNFL = applied total stress on boundary

BPPL = applied pore pressure at boundary

SSDL = specified boundary displacement (for JSDL = 1)

Card 9 right end boundary conditions)

JSDR, JDCR, TNFR, BPPR, SSDR (2I5,3E10.0)

JSDR = 0 free skeleton boundary
= 1 fixed or specified skeleton boundary

JDCR = 0 permeable boundary
= 1 impermeable boundary

TNFR = applied total stress on boundary

BPPR = applied pore pressure at boundary

SSDR = specified boundary displacement (for JSDL = 1)

SECTION 6

DEVELOPMENT OF RESIDUAL STRESSES

INTRODUCTION

Blast loadings will cause significant flow of interstitial pore water from in situ rock masses only if the dynamic stresses produce long term residual stresses and/or pore pressures. Significant pore water flow cannot develop during the dynamic portion of the loading because the dynamic loading is of extremely short duration with respect to the rock permeability.

Two mechanisms for development of residual stresses and pore pressures are described in this section. The first is the primary cause of residual stresses surrounding underground explosions. The second is the cause of residual pore pressures beneath near surface explosions.

It is well known that the underground nuclear shots in Rainier Mesa tuff produce an extensive zone of residual stresses around the cavities formed by the detonations. These have been calculated by Patch (1984), Rimer and Friedman (1978) and others. In addition, measurements of long term residual stresses surrounding a nuclear detonation in Rainier Tuff have been reported by Ellis and Kibler (1983). While these do not precisely match the calculations, similar stress patterns were measured and development of the residual stress field was documented. Finally, the contained HE tuff experiments described by Smith (1983) produced residual stress fields similar to those formed by the nuclear detonations.

As described in Section 4, the residual stress field surrounding an explosively formed underground cavity results from the severe plastic distortion of the rock in the immediate vicinity of the cavity. The rock surrounding the cavity undergoes severe plastic deformations as it is thrust outward by the force of the explosion. The permanent cavity expansion locks very high compressive stresses into this rock and produces residual equilibrium stresses extending many radii outward from the cavity.

The second residual stress/pore pressure formation mechanism is due to the hysteretic nature of the saturated rock skeleton. Nonrecoverable skeleton strain produced by the dynamic loading generates excess residual pore pressures. In essence, a portion of the in situ stress carried by the rock skeleton before the dynamic loading is transferred to the pore water following the hysteretic unloading. This second mechanism would be expected to occur following detonation of a nuclear surface burst.

RESIDUAL STRESS FROM CAVITY EXPANSION

Essoglow and Rogich (1965) presented a simple method for computing the residual displacements and strains surrounding a contained detonation. In their formulation a spherical chamber surrounding the explosive device is expanded outward to form a spherical cavity of final radius r_c. The volume of material between the initial spherical shell and the final cavity shell is assumed to be redistributed throughout the surrounding rock. This redistribution of material is assumed to occur with no volume reduction (noncompressibility) and with no loss of

material from vaporization. In reality, both the pre-shot cavity volume and vaporization volume are negligible with respect to the final cavity volume for an underground nuclear explosion. Based on the above assumptions, the permanent displacement, δ, at range r is given by

$$\delta = (r^3 + r_c^{\ 3})^{1/3} - r \qquad (6\text{-}1)$$

For ranges of two cavity radii and beyond, Equation 6-1 is closely approximated by

$$\delta = \frac{r_c^{\ 3}}{3r^2} \qquad (6\text{-}2)$$

The permanent radial strain ε_r, is given by

$$\varepsilon_r = \frac{r^2}{(r^3 + r_c^{\ 3})^{2/3}} + 1 \qquad (6\text{-}3)$$

For ranges beyond two cavity radii this can be approximated by

$$\varepsilon_r = \frac{2r_c^{\ 3}}{3r^3} \qquad (6\text{-}4)$$

Even though the assumptions governing the derivation of the above equations are quite simplified, they appear to be in good agreement with test data. Figure 6.1 is a plot of Equation

6-2 compared to the permanent displacement data on the Rainier event presented by Diment et al. (1959). Using material models for appropriate rock types, it is possible to compute residual stresses from Equations 6-3 or 6-4.

More sophisticated residual stress calculations have become available in recent years based on finite difference calculations which model the entire ground motion and stress time response surrounding underground tests. Examples of such calculations are given in Rimer and Friedman (1978) and Patch (1984). Figure 6.2, from Patch, shows computed radial and tangential residual stresses as a function of range normalized by the cavity radius for four recent underground nuclear events in Rainier Mesa tuff. Significant radial and tangential stresses are induced to ranges of many cavity radii. In the calculations of Section 7 a residual stress of 1000 psi (6.9 MPa) was assumed which corresponds to the radial residual stress at between 5 and 6 cavity radii for the calculations shown in Figure 6.2.

RESIDUAL EXCESS PORE PRESSURE FROM SURFACE BURST LOADING

Residual excess pore pressures can be induced by nonrecoverable skeleton deformation in saturated materials. While the skeleton tends to only partially recover from a dynamic loading, the pore water is essentially elastic and tends to rebound fully. The result is that some of the initial effective stress originally carried by the skeleton is taken by the pore water. In the limit, all of the effective skeleton stress is transferred to the pore water and a state of liquefaction is achieved (see Kim and Blouin, 1984).

In this subsection the residual excess pore pressures generated by simple one dimensional uniaxial loadings are derived. In the case of a nuclear surface burst the actual loadings are considerably more complex than the one dimensional analog discussed here.

To simplify the complicated two phase response, the following assumptions have been made:

- Motions are vertically one dimensional. In practice, uniaxial one dimensional loadings adequately simulate the response of the underlying geology to airblast loadings.

- The skeleton uniaxial stress-strain curve is approximated by two linear slopes consisting of a loading constrained modulus (M_s^L) and an unloading constrained modulus (M_s^U). This bilinear hysteretic skeleton model is shown in Figure 6.3.

- The solid grains and pore water are linearly elastic.

- Drainage is not permitted during the dynamic loading and unloading.

Partially Coupled Model

If volume change in the soil-water mixture due to effective stress on the individual grains is neglected, the undrained constrained modulus of the bulk mixture, M_p, is given by

$$M_p = M_s - \frac{K_m K_s}{K_g} + K_m \qquad (6\text{-}5)$$

where M_s = constrained modulus of solid skeleton

K_s = bulk modulus of solid skeleton

$K_m = \dfrac{K_g K_w}{K_w + n(K_g - K_w)}$; mixture modulus

K_g = bulk modulus of solid grains

K_w = bulk modulus of pore water

n = porosity

The undrained partially coupled modulus was derived by Blouin and Kim (1984) and is included in Table A.1. Due to the hysteretic nature of the solid skeleton, the unloading modulus is greater than the loading modulus. The loading undrained constrained modulus of the bulk mixture is given by

$$M_p^L = M_s^L - \frac{K_m K_s^L}{K_g} + K_m \qquad (6\text{-}6)$$

where M_s^L and K_s^L are the loading constrained and bulk moduli of the solid skeleton respectively. The unloading undrained constrained modulus of the bulk mixture is given by

$$M_p^U = M_s^U - \frac{K_m K_s^U}{K_g} + K_m \qquad (6\text{-}7)$$

where M_s^U and K_s^U are the unloading constrained and bulk moduli of the solid skeleton respectively.

Figure 6.4 shows volumetric strain change during the dynamic loading and unloading. Volumetric strain at the end of the loading is calculated by

$$\Delta\varepsilon_v^L = \frac{\Delta\sigma_{vD}}{M_p^L} \tag{6-8}$$

where $\Delta\sigma_{vD}$ is the dynamic total vertical stress increment. The recovered volumetric strain at the end of the unloading is calculated by

$$\Delta\varepsilon_v^U = \frac{\Delta\sigma_{vD}}{M_p^U} \tag{6-9}$$

The pore pressure increment at the end of the loading is related to the volumetric strain increment by

$$\Delta\pi_D^L = K_m \, \Delta\varepsilon_v^L \tag{6-10}$$

and the pore pressure drop at the end of the unloading is related to the recovered volumetric strain by

$$\Delta\pi_D^U = K_m \, \Delta\varepsilon_v^U \tag{6-11}$$

The residual excess pore pressure is defined as

$$\Delta\pi_e = \Delta\pi_D^{\ L} - \Delta\pi_D^{\ U} \tag{6-12}$$

Substitution of Equations 6-10 and 6-11 into Equation 6-12 gives

$$\Delta\pi_e = \left(\Delta\varepsilon_v^{\ L} - \Delta\varepsilon_v^{\ U}\right) K_m \tag{6-13}$$

Using Equations 6-8 and 6-9, the volumetric terms in Equation 6-13 can be expressed in terms of stresses and moduli.

$$\Delta\pi_e = \left(\frac{1}{M_p^{\ L}} - \frac{1}{M_p^{\ U}}\right) K_m \, \Delta\sigma_{vD} \tag{6-14}$$

Or, the ratio of excess pore pressure to the dynamic total vertical stress increment can be given by

$$\boxed{\frac{\Delta\pi_e}{\Delta\sigma_{vD}} = \left(\frac{1}{M_p^{\ L}} - \frac{1}{M_p^{\ U}}\right) K_m} \tag{6-15}$$

Substituting Equations 6-6 and 6-7 into Equation 6-15,

$$\frac{\Delta\pi_e}{\Delta\sigma_{vD}} = \frac{\left(M_s^{\ U} - \frac{K_s^{\ U}}{K_g} K_m + K_m\right) - \left(M_s^{\ L} - \frac{K_s^{\ L}}{K_g} K_m + K_m\right)}{\left(M_s^{\ L} - \frac{K_s^{\ L}}{K_g} K_m + K_m\right) \left(M_s^{\ U} - \frac{K_s^{\ U}}{K_g} K_m + K_m\right)} K_m \tag{6-16}$$

Let

$$\bar{M}_s^{\,L} = M_s^{\,L} - \frac{K_m}{K_g} K_s^{\,L} \tag{6-17}$$

and

$$\bar{M}_s^{\,U} = M_s^{\,U} - \frac{K_m}{K_g} K_s^{\,U} \tag{6-18}$$

Substituting Equations 6-17 and 6-18 into Equation 6-15 gives

$$\frac{\Delta\pi_e}{\Delta\sigma_{vD}} = \frac{(\bar{M}_s^{\,U} - \bar{M}_s^{\,L})}{(\bar{M}_s^{\,L} + K_m)\ (\bar{M}_s^{\,U} + K_m)} K_m \tag{6-19}$$

Defining the following nondimensional quantities;

$$\bar{r} = \frac{\bar{M}_s^{\,L}}{\bar{M}_s^{\,U}} \tag{6-20}$$

$$\bar{a} = \frac{\bar{M}_s^{\,L}}{K_m} \tag{6-21}$$

Equation 6-19 can be expressed in the following form

$$\boxed{\frac{\Delta\pi_e}{\Delta\sigma_{vD}} = \frac{(1 - \bar{r})}{(1 + \bar{a})\ (1 + \frac{\bar{r}}{\bar{a}})}} \tag{6-22}$$

Partially Coupled Model With Constant Poisson's Ratio

As a special case, assume Poisson's ratio (μ) remains constant during the dynamic loading and unloading. Then,

$$K_s^{\,L} = \frac{(1 + \mu)}{3(1 - \mu)} \; M_s^{\,L} \qquad (6\text{-}23)$$

$$K_s^{\,U} = \frac{(1 + \mu)}{3(1 - \mu)} \; M_s^{\,U} \qquad (6\text{-}24)$$

Substitution of Equations 6-23 and 6-24 into Equation 6-20 gives

$$\bar{r} = \frac{\bar{M}_s^{\,L}}{\bar{M}_s^{\,U}} = \frac{M_s^{\,L}}{M_s^{\,U}} = r \qquad (6\text{-}25)$$

That is, $\bar{r}$ is equal to the strain recovery ratio, r, in a one phase material. Substitution of Equation 6-23 into Equation 6-21 gives

$$\bar{a} = \frac{M_s^{\,L}}{K_m} \left(1 - \frac{(1 + \mu)}{3(1 - \mu)} \; \frac{K_m}{K_g} \right) \qquad (6\text{-}26)$$

Let

$$a = \frac{M_s^{\,L}}{K_m} \qquad (6\text{-}27)$$

$$\eta = 1 - \frac{(1 + \mu)}{3(1 - \mu)} \frac{K_m}{K_g} \qquad (6\text{-}28)$$

Then

$$\bar{a} = a \cdot \eta \qquad (6\text{-}29)$$

Substituting Equations 6-26 and 6-29 into Equation 6-22 gives

$$\boxed{\frac{\Delta \pi_e}{\Delta \sigma_{vD}} = \frac{(1 - r)}{(1 + a\eta)\ (1 + \frac{r}{a\eta})}} \qquad (6\text{-}30)$$

Decoupled Model

Residual pore pressure response can be obtained in a similar manner for the simpler decoupled model described by Blouin and Kim (1984). In the decoupled model the compressibility of the solid grains by the pore water is neglected. The undrained decoupled loading and unloading constrained moduli are given by

$$M_D^L = M_s^L + K_m \qquad (6\text{-}31)$$

$$M_D^U = M_D^U + K_m \qquad (6\text{-}32)$$

Using the same procedure as employed in the partially coupled case, the following stress ratio is obtained for the decoupled case:

$$\boxed{\frac{\Delta\pi_e}{\Delta\sigma_{vD}} = \frac{(1 - r)}{(1 + a)\ (1 + \frac{r}{a})}} \qquad (6\text{-}33)$$

Equation 6-33 has the same form as Equation 6-22 except that $\bar{r}$ and $\bar{a}$ in Equation 6-22 are replaced by r and a respectively.

Post Shot Effective Stress and Pore Pressure

Once residual excess pore pressure ($\Delta\pi_e$) is obtained, the pore pressure (π) and effective vertical stress (σ_v') at the end of the dynamic unloading are calculated as follows:

$$\pi = \pi_i + \Delta\pi_e \qquad (6\text{-}34)$$

$$\sigma_v' = \sigma_{vi}' - \Delta\pi_e \qquad (6\text{-}35)$$

where π_i and σ_{vi}' are the pre-shot in situ pore pressure and effective vertical stress respectively. It should be noted that if the post-shot effective vertical stress (σ_v') reaches the tensile strength of the material, the material would be liquefied. In such a liquefied material, the effective stress is

zero and the post-shot pore pressure (π) reaches a maximum which is equal to the in situ total vertical stress (σ_{vi}).

Parametric Analysis

A parametric study was conducted to examine the influence of the strain recovery ratio (r) and the ratio of the skeleton loading constrained modulus to the mixture modulus (a) on the residual excess pore pressure ($\Delta\pi_e$).

Equation 6-30, which represents the partially decoupled model with constant Poisson's ratio, was used in this parameter study. Typical material parameters representative of Generic Mountain C are summarized below.

Porosity	$n = 20\%$
Poisson's ratio	$\mu = 0.2$
Bulk Modulus	
Pore Water	$K_w = 0.29 \times 10^6$ psi
Solid Grain	$K_g = 5 \times 10^6$ psi
Mixture	$K_m = 1.177 \times 10^6$ psi
$\eta = 0.8823$	

Figure 6.5 summarizes the results of the parametric study. Residual excess pore pressure normalized by the dynamic total vertical stress increment is plotted as a function of strain recovery ratio at 5 different values of a ranging from 0.5 to 2.5. For the case where the skeleton loading constrained modulus (M_s^L) is equal to the mixture modulus (K_m), the residual excess pore pressure is 20% of the dynamic total vertical stress increment for a strain recovery ratio of 0.46.

The normalized excess pore pressure is 10% for a recovery ratio of 0.67.

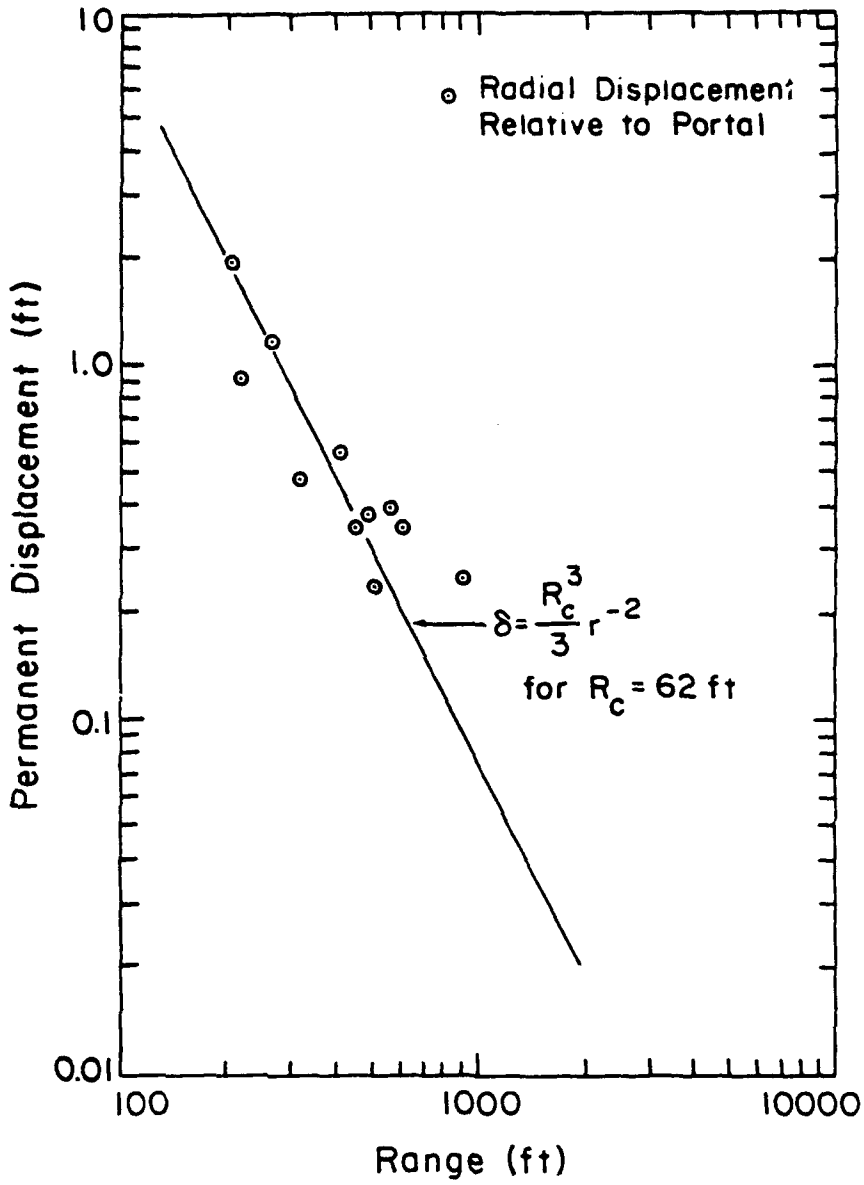

Figure 6.1. Comparison of Rainier radial permanent displacements to theoretical approximation.

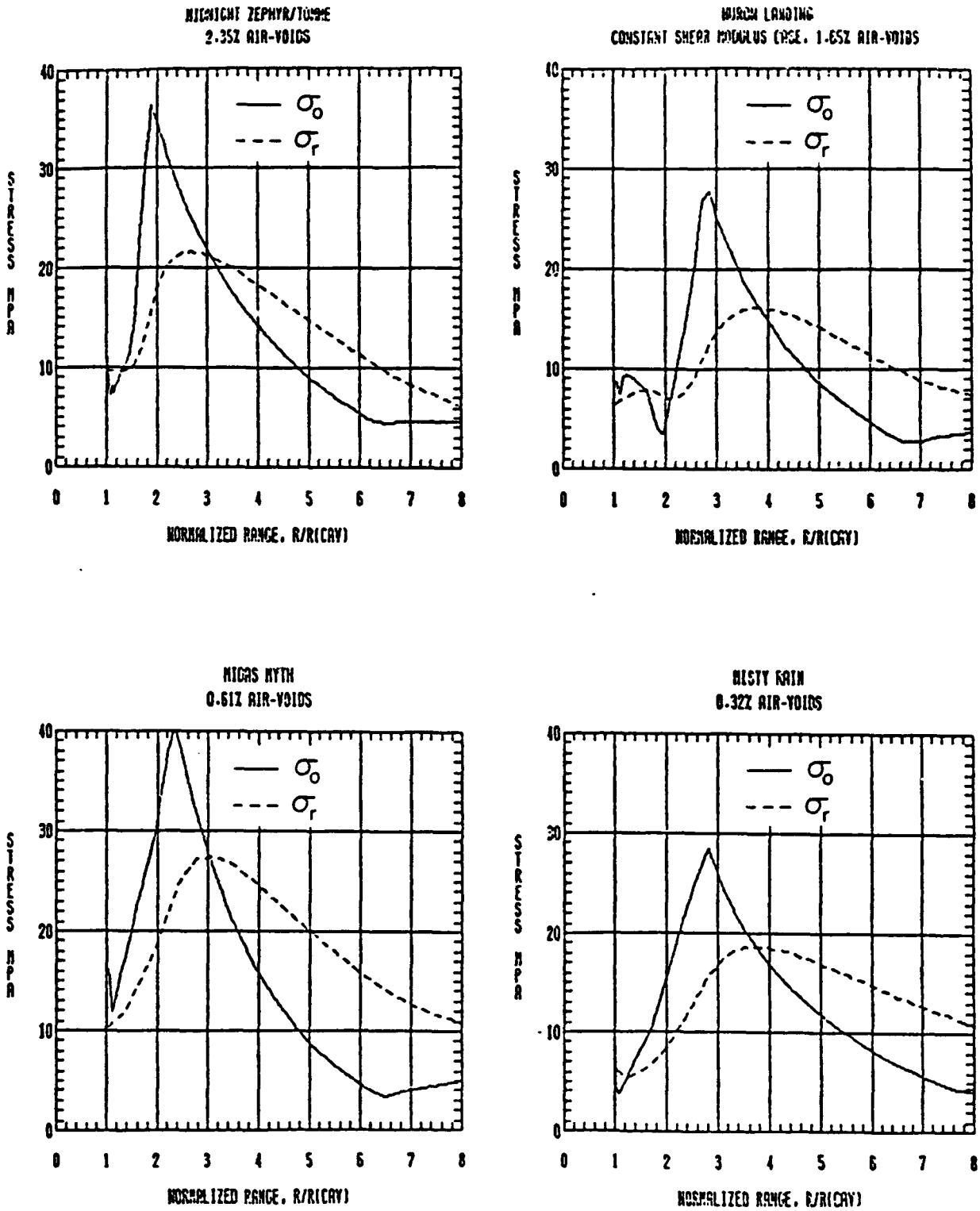

Figure 6.2. Residual stress fields for nearly saturated tuff events normalized by the final cavity radius size (from Patch, 1984).

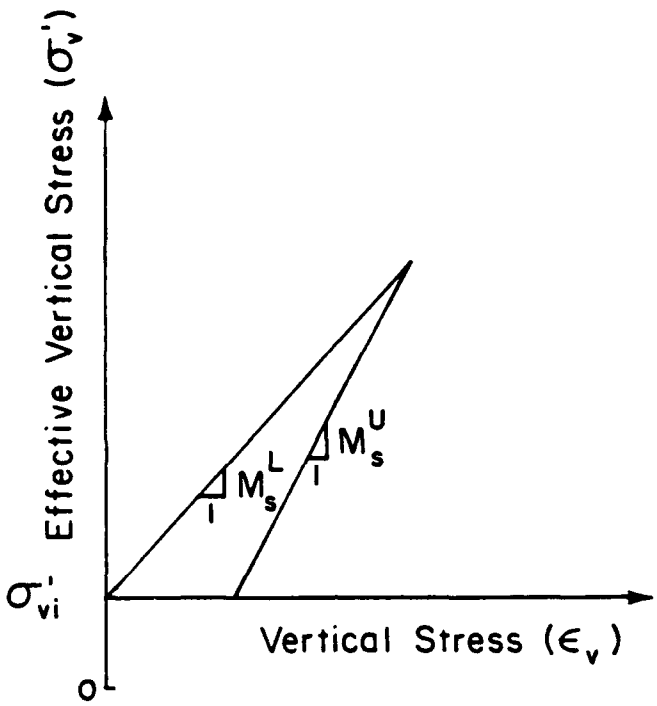

σ_{vi}' = In Situ Effective Vertical Stress

M_s^L = Loading Constrained Modulus of Solid Skeleton

M_s^U = Unloading Constrained Modulus of Solid Skeleton

Figure 6.3. Bilinear stress-strain curve for solid skeleton.

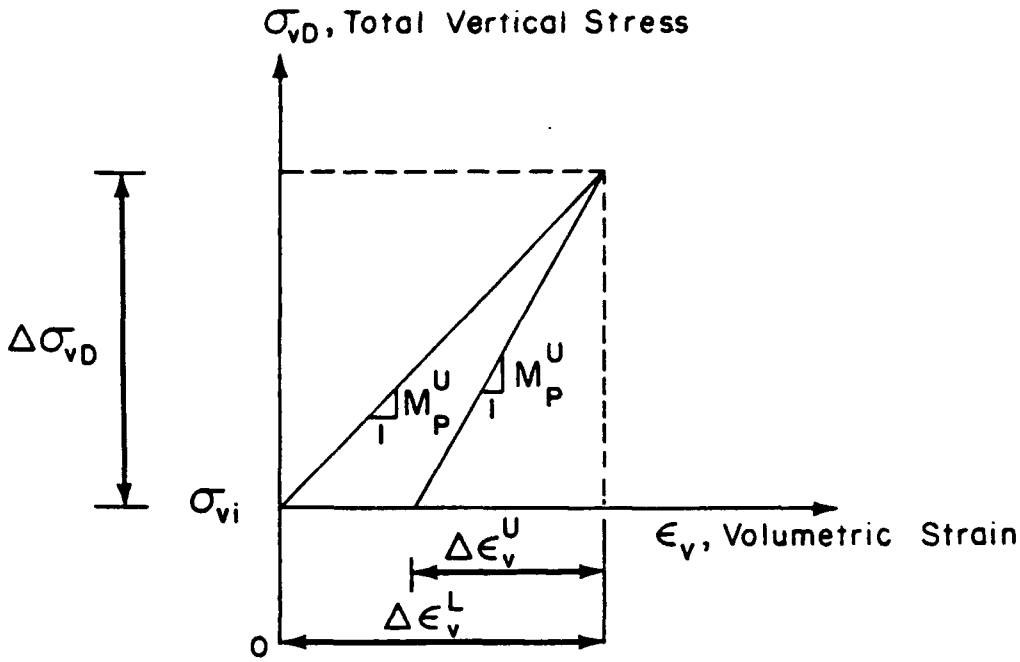

σ_{vi} = In Situ Total Vertical Stress

$\Delta\sigma_{vD}$ = Dynamic Total Vertical Stress Increment

$\Delta\varepsilon_v^L$ = Volumetric Strain at the end of Loading

$\Delta\varepsilon_v^U$ = Recovered Volumetric Strain at the end of Unloading

M_p^L = Loading Undrained Constrained Modulus of Bulk Mixture

M_p^U = Unloading Undrained Constrained Modulus of Bulk Mixture

Figure 6.4. Bilinear stress-strain curve for partially coupled undrained bulk mixture.

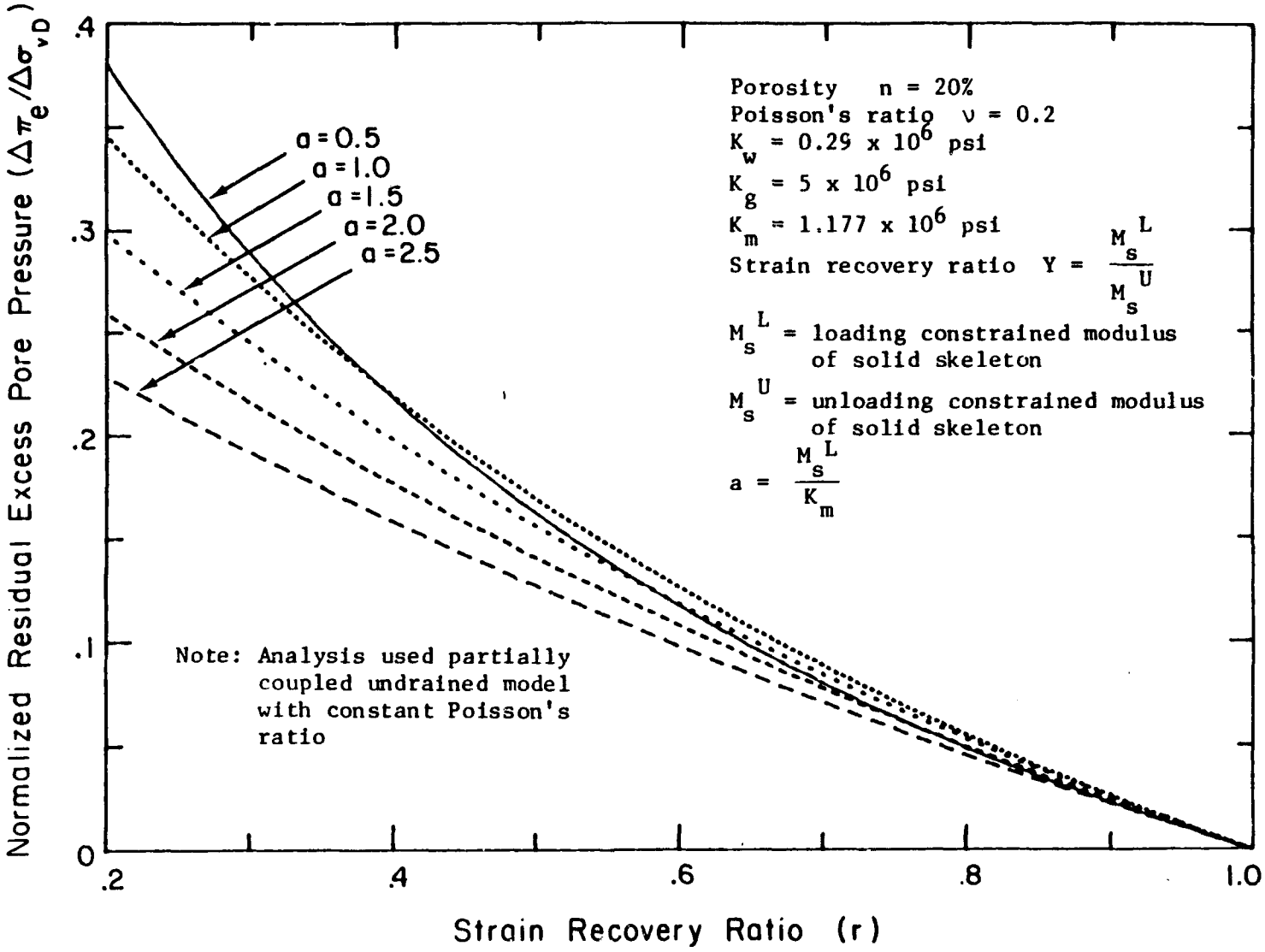

Figure 6.5. Normalized residual excess pore pressure as a function of strain recovery ratio.

SECTION 7

PARAMETRIC EVALUATION OF FLOW AND PRESSURE DISSIPATION

CALCULATIONAL AND MATERIAL PARAMETERS

A matrix of calculations was performed to determine potential flow into tunnels from residual loadings similar to those developed from underground nuclear detonations and similar to those which might be expected from surface or shallow buried nuclear detonations. Material properties of the host rock were varied over a broad range which encompassed nearly the entire range of properties listed for Generic Mountain C as well as the range of properties of Rainier Mesa Tuff. These calculations are primarily meant to identify potential flow problems and the magnitude of these problems in a broad range of geologies; they are not meant to analyze the response of a specific target in a specific geology.

In each of the parametric calculations a segment of tunnel in fully saturated rock is subjected to a uniform long term loading. This loading either involves imposition of a total stress on the grid boundary or imposition of a fixed boundary displacement. The former is similar to the residual stress loading which would develop from the dynamic loading of a hysteretic saturated rock mass, as described in Section 5. Imposition of a fixed displacement is akin to the loading from an underground test, where the rock mass is subjected to a fixed displacement at the cavity boundary. Since these are axisymmetric calculations, however, they cannot accurately replicate the loading from the underground test conditions.

Figure 7.1 shows a schematic section view of the axisymmetric loading conditions imposed on the tunnel throughout this series of calculations. A 20 ft diameter tunnel was used in all calculations. Water is assumed to drain freely from the tunnel and does not build up therein. The tunnel walls are free to displace inward under the imposed loads and there is assumed to be no lining or grout in the vicinity of the tunnel to inhibit flow into the tunnel.

In all but the initial calculations, the loading boundary is assumed to be impermeable and free to displace. In the initial calculations, a fixed displacement was imposed on the boundary which was held throughout the entire time span of the calculations. As shown in Figure 7.2, flow was slightly lower in the fixed boundary calculation. This is expected because the boundary does not move inward during the calculation to accommodate the consolidation near the tunnel wall. Thus, pore pressures are somewhat lower and total stresses dissipate during the fixed boundary calculation. In the fixed boundary calculation the imposed displacement is equal to the initial displacement under the 1000 psi loading. Thus, effective stresses and pore pressures are initially the same in both calculations. Even though the loading boundary is free to displace inward during the fixed stress calculation, there was so little difference between the two calculations that for convenience the fixed displacement loadings were not used in this initial study.

The range to the loaded boundary was varied as necessary in each calculation to insure that pore pressure at the boundary did not decrease significantly during the 30 day total time span of the calculation. In other words, in more permeable material,

where pore pressures dissipated more rapidly and further into the host rock, the loaded boundary was located at a greater range. The range to the loaded boundary was adjusted so that at 30 days the pore pressure drop at the boundary was less than 5% of the initial pore pressure. A boundary radius of 7000 ft was used in most calculations, though this was increased to accommodate the higher permeability materials.

The number of grid elements varied in proportion to the distance to the loaded boundary. For most calculations, there were 120 elements between the tunnel wall and the loaded boundary. However, as many as 400 elements were used in the highest permeability calculations. The element sizes increased with increasing range from the tunnel. In all cases half of the elements were within one quarter of the distance from the tunnel to the loaded boundary. The element closest to the tunnel was 0.83/n percent of the total grid length (where n is the total number of elements), with each successive element increasing in length. Thus, for the standard 120 element 7000 ft grid, the first element was 0.49 ft long and there were 60 elements making up the initial 1750 ft of material adjacent to the tunnel.

A total stress of 1000 psi was applied in all calculations of the parametric matrix. This is representative of residual stresses in the vicinity of tunnels at ranges of interest in the underground nuclear shots. It is also a reasonable approximation of the residual stresses which might develop around a deep based system from nonrecoverable deformation of the surrounding rock due to surface burst loadings as discussed in Section 5. A series of check runs was performed in which the applied stress was varied between 100 and 10,000 psi. For all material properties used in this parametric analysis, the flow and pressure dissipation were found to be in

direct proportion to the applied stress. For the 100 psi loading, flow and pressures were one tenth those in the 1000 psi loading, while flows and pressures were ten times as large in the 10,000 psi calculation. Thus, flows and pressures for loading stresses other than 1000 psi can be easily calculated by multiplying the calculated results by the ratio between the desired applied stress and the 1000 psi load.

A suite of rock properties encompassing nearly the entire range of properties found in the Rainier Mesa tuffs and in the various rocks of Generic Mountain C were included in the parametric calculations. For purposes of this initial study, both the rock skeleton and pore water were assumed to be linear and elastic. Material properties used in the calculations are summarized in Table 7.1. Properties held constant throughout all the various parameter studies included the 100% degree of saturation, the bulk modulus of water with a value of 0.29 x 10^6 psi, and the bulk modulus of the solid grains with a value of 5 x 10^6 psi. Material parameters which were varied in the calculations include the permeability, Poisson's ratio, constrained modulus and porosity of the rock skeleton.

Values of permeability had the widest range of any parameter investigated in this study. Permeability ranged from a low value of 6.7 x 10^{-6} ft/day (9.3 x 10^{-10} in/s), representative of the lower values reported for the zeolitized Rainier Mesa tuffs, to 100 ft/day (1.39 x 10^{-2} in/s) representative of the very permeable Generic Mountain C sandstones. Intermediate values represent more permeable or fractured tuffs and the various other formations of Mountain C. A standard intermediate permeability of 0.1 ft/day (1.39 x 10^{-5} in/s) was used in the parametric evaluations of the

influence of Poisson's ratio, porosity, and skeleton modulus on flow and pore pressure dissipation.

The constrained modulus of the rock skeleton was varied between 0.5×10^6 and 5×10^6 psi. The lowest value is representative of soft altered tuff while the highest is representative of the hardest most competent rocks of Mountain C. A standard value of 2.5×10^6 psi was used in the studies of variation in porosity and Poisson's ratio, while a value of 1.9×10^6 psi was used in the permeability study. Either value is a reasonable representation of the average properties of Generic Mountain C.

Poisson's ratio of the rock skeleton was varied from 0.1 to 0.4, with a standard value of 0.2 used in the other parameter studies. The lower value represents the harder more competent Mountain C rocks while the upper limit approximates that in the weaker zeolitized tuffs. The standard value is representative of Generic Mountain C.

The final parameter varied in this study was the skeleton porosity. A value of 0.2 was used as the standard. This is representative of average values for Generic Mountain C. Other values ranged from 0.05, representative of dense well consolidated sedimentary rock to 0.4, representative of very porous tuff.

The influences of the above parameter variations on flow and pore pressure dissipation are discussed in the following subsections.

INFLUENCE OF PERMEABILITY

The influence of permeability on cumulative flow and flow rate under the 1000 psi total stress loading is summarized in Figures 7.3 and 7.4. These figures show cumulative flow and flow rate per foot of tunnel as a function of permeability at fixed times of 1 hr and 4 hr, and 1, 7 and 30 days. The most striking feature of these plots is the large flows and flow rates which develop in the medium to high permeability rock. Topi et al. (1984) indicate a typical range of permeabilities for rock in Generic Mountain C as 0.5 to 50 ft/day (6.944×10^{-5} to 6.944×10^{-3} in/s). Initial flows during the first day of between 5000 gallons and 400,000 gallons per foot of tunnel would be expected for this permeability range. Since it takes only 2350 gallons per foot to completely fill the tunnel, under these assumed conditions there appears to be a very serious potential flow problem for a deep based system at such a site. This range in cumulative flows equates to an average first day flow rate of from 3.5 to 278 gpm per foot of tunnel.

Contrast these values to the one day flows expected in the saturated zeolitized tuffs. In the tuff, first day flows of between 1.2 to 10 gallons per foot of tunnel would be expected for the typical range of tuff permeabilities of Table 2.1. These equate to flow rates of only 8×10^{-4} to 7×10^{-3} gpm per foot of tunnel. At the lower end of the tuff permeabilities, the incoming water would likely evaporate as fast as it entered the tunnel, and toward the upper end of the permeability range the water would probably pose only a slight inconvenience rather than a problem. Minimal inflow, as indicated by these calculations, has been experienced in Rainier Mesa, except where fracture water has been mobilized. The only measurements of nonfracture inflow,

i.e. squeezing of interstitial water from the rock pores, were made on ONETON. These measurements compare favorably with calculated flows as demonstrated in Section 8.

Examples of calculated flow, flow rate and pore pressure dissipation in the lowest permeability rock examined in this parameter study ($k = 9.3 \times 10^{-10}$ in/s) are shown in Figures 7.5 through 7.7. Accumulated flow and flow rate per foot of tunnel are shown as functions of time for the full 30 days in the first two figures, while pore pressures as a function of range are shown at various times from 10 sec to 30 days in Figure 7.7. In this low permeability rock only about 12 gallons of water accumulate per foot of tunnel over the entire 30 day time span. The relatively high initial flow rates decrease very rapidly within the first several hours to a very low, slowly decaying rate during the bulk of the time span. Pore pressure dissipation advances very slowly into the host rock. At 30 days pore pressures have begun to decay only to a range of 65 ft from the tunnel wall.

Similar plots for an intermediate permeability rock ($k = 1.39 \times 10^{-5}$ in/s) are shown in Figures 7.8 through 7.10. This intermediate permeability is near the lower bound value assumed for Generic Mountain C. Even in this intermediate permeability rock, flows and flow rates are reaching rather alarming proportions in terms of a deep based facility. Accumulated flow exceeds 30,000 gallons per foot of tunnel over the 30 day time span. Flow rate is initially about 3 gpm per foot of tunnel, but drops only modestly to about 0.6 gpm at the end of 30 days. The pore pressure dissipation front advances very rapidly into the host rock, reaching a range of about 1600 ft from the tunnel at the end of the first day and 6000 ft at the end of 30 days. This rapid dissipation suggests that finite

geologic and geometric parameters in an actual deep based system will themselves limit flow into the tunnels; i.e. factors such as finite depths of cover and limited aquifers will somewhat restrict the high accumulated flows and flow rates indicated at later times in these calculations. Boundary limitations which might replicate such restrictions were not used in this analysis so as not to confuse the comparisons with the more impermeable rocks.

Figures 7.11 through 7.13 present the accumulated flows, flow rates and pore pressure dissipations in the highest permeability rock ($k = 1.39 \times 10^{-2}$ in/s). Exceptionally high flows and flow rates occur in this highly permeable rock, with pore pressure dissipation extending for tens of thousands of feet. Again, these calculations do not have realistic boundary conditions, so the large flows indicate only that a substantial problem exists. They should not be used to estimate actual expected flow magnitudes.

INFLUENCE OF SKELETON MODULUS

The influence of varying skeleton constrained modulus between 0.5×10^6 psi and 5×10^6 psi on accumulated flow, flow rate and pore pressure dissipation is shown in Figures 7.14 through 7.16. In this set of calculations, the intermediate permeability of 1.39×10^{-5} in/s was used. Other material properties are listed in Table 7.1. As would be expected, in the stiffer rocks, the skeleton assumes a greater percentage of the imposed load. Thus, the generated pore pressures and resultant flows are lower in the stiffer rocks. Accumulated flow at 30 days in the softest rock is about 4.7 times greater than flow in the stiffest rock. The large differences in initial pore

pressure are evident in Figure 7.16a, where the initial pore pressure in the softest rock is about 4.3 times that in the hardest rock. These initial pore pressures can be calculated directly from Equation A-54 for the undrained loading condition. Figure 7.17 is a plot of pore pressure as a function of skeleton modulus for an undrained loading of 1000 psi. This plot was generated from Equation A-54 using the material properties from Table 7.1.

INFLUENCE OF POISSON'S RATIO

Poisson's ratio of the rock skeleton was found to have only a modest influence on flow and flow rate. Figures 7.18 through 7.20 show accumulated flow, flow rate and pore pressure dissipation for skeletons having Poisson's ratios ranging from 0.1 to 0.4. As indicated in Table 7.1, the constrained moduli and permeabilities were assumed constant at 2.5×10^6 and 1.39×10^{-5} in/s respectively in these calculations. The accumulated flow at 30 days in the rock with a Poisson's ratio of 0.1 is about 50% greater than flow in the rock having a Poisson's ratio of 0.4. The corresponding flow rates and initial pore pressures are also higher in the low Poisson's ratio rock. The initial undrained pore pressures can be calculated directly from Equation A-54. Note, however, that Equation A-54 uses the skeleton bulk modulus which is a function of the constrained modulus and Poisson's ratio according to

$$K_s = M_s \frac{(1 + \mu)}{3(1 - \mu)} \qquad (7\text{-}1)$$

Thus, for a constant constrained modulus, the bulk modulus increases with increasing Poisson's ratio. The combined effect of the increasing bulk modulus and increasing Poisson's ratio is a moderate decrease in initial pore pressure with increasing Poisson's ratio. This effect is shown in Figure 7.21 where pore pressure is plotted as a function of Poisson's ratio for a constant value of constrained modulus. In contrast, for a constant skeleton bulk modulus, initial pore pressure increases slightly with increasing Poisson's ratio. The initial pore pressure as a function of Poisson's ratio for a constant skeleton bulk modulus of 1.25×10^6 psi is plotted for comparison in Figure 7.21.

INFLUENCE OF POROSITY

The final property examined in this parameter study was the influence of porosity on flow. These results gave relationships which seemed opposite to those one would intuitively expect. As shown in Table 7.1, porosity was varied from 5% to 50% while permeability, skeleton constrained modulus and Poisson's ratio were held constant at values of 1.39×10^{-5} in/s, 2.5×10^6 psi and 0.2 respectively. The resulting plots of accumulated flow, flow rate and pore pressure dissipation in Figures 7.22 through 7.24 show that pore pressures and the resulting flows are highest when porosities are lowest. This nonintuitive behavior arises because porosity is varied independently of the other material parameters. Realistically, this could not occur over such a great a range in porosity.

The initial pore pressure response as a function of porosity is governed by the Wood equation (Equation A-13). As

porosity increases, the bulk modulus of the solid-water mixture decreases because there are less very stiff solid grains in the mixture. The pore pressure response of Equation A-54 is in turn directly proportional to the mixture modulus, i.e. the higher the porosity, the lower the mixture modulus and the lower the resultant pore pressure under the undrained loading. Therefore, with all other properties held constant, the pore pressures and flows are highest when permeabilities are lowest. The accumulated flow at 30 days in the lowest porosity rock is 2.9 times that in the highest porosity rock. As shown in Figure 7.24a, this is because the initial pore pressure in the low porosity rock is about 3 times that in the high porosity rock. The influence of porosity on the initial pore pressure is shown in Figure 7.25. This plot was computed from Equation A-54 with material constants taken from Table 7.1.

SUMMARY

From the series of axisymmetric calculations used to study the influence of material property variations on flow and pore pressure dissipation in this section we conclude the following:

- Flow of interstitial pore water generated by explosively induced residual stresses in permeable saturated or nearly saturated rocks such as those in Generic Mountain C is a serious potential threat to deep based systems;

- Interstitial flow generated by similar loadings in non-permeable rock such as the zeolitized tuffs of Rainier Mesa is minimal and both experience and calculations indicate that this type of flow would not be a major problem to a deep based system in similar rock;

- Interstitial pore water flow is extremely sensitive to large changes in permeability, is somewhat sensitive to skeleton modulus and porosity, and is relatively insensitive to skeleton Poisson's ratio and to whether residual stresses are constant or result from a fixed boundary displacement.

Table 7.1. Material properties used in parametric calculations.

PROPERTY	STANDARD VALUE	RANGE OF VALUES
Skeleton Constrained Modulus	2.56×10^6 psi or 1.9×10^6 psi	0.56×10^6 to 5.0×10^6 psi
Bulk Modulus of Pore Water	0.29×10^6 psi	
Skeleton Porosity	0.2	0.05 to 0.5
Skeleton Permeability	0.1 ft/day	6.7×10^{-6} to 100 ft/day
	1.39×10^{-5} in/s	9.28×10^{-10} to 1.39×10^{-2} in/s
Degree of Saturation	100%	
Skeleton Poisson's Ratio	0.2	0.1 to 0.4
Bulk Modulus of Solid Grains	5×10^6 psi	

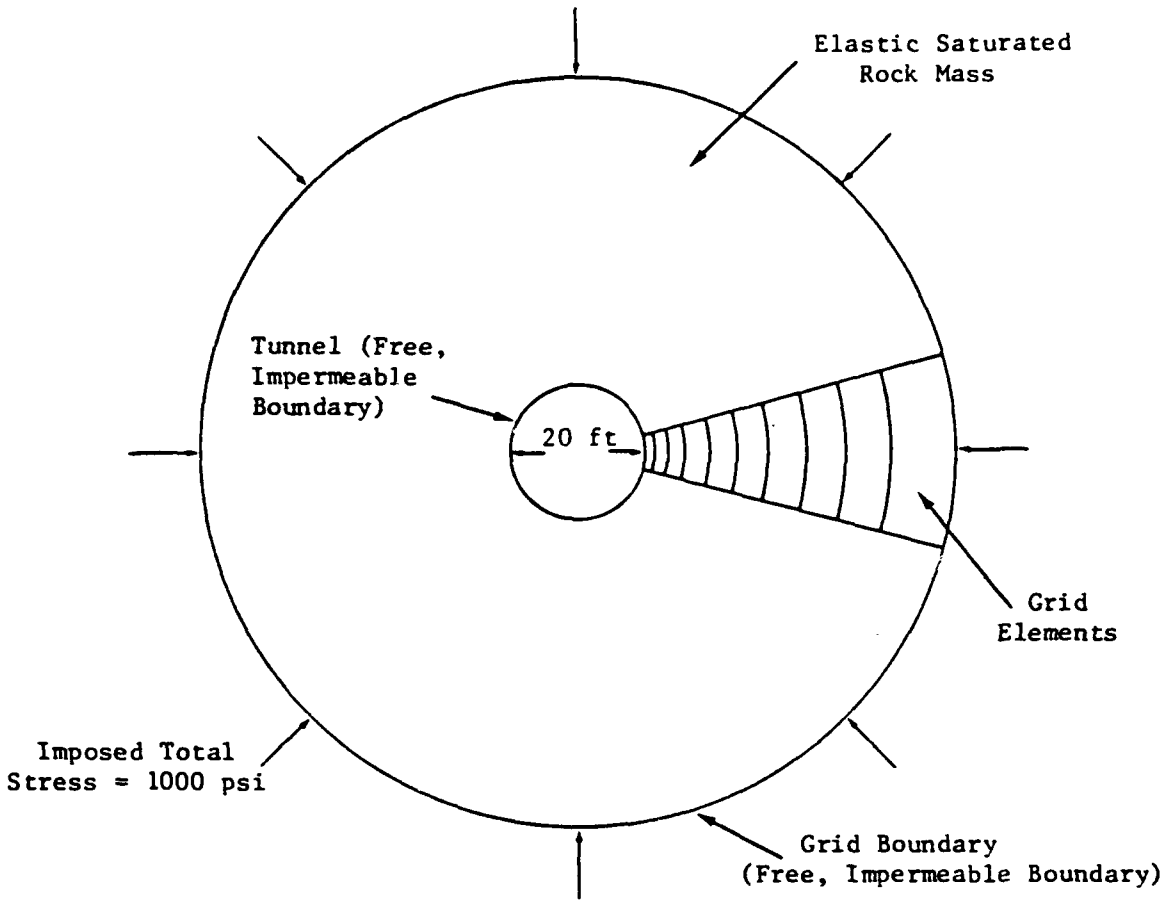

Figure 7.1. Parametric loading conditions, schematic section view.

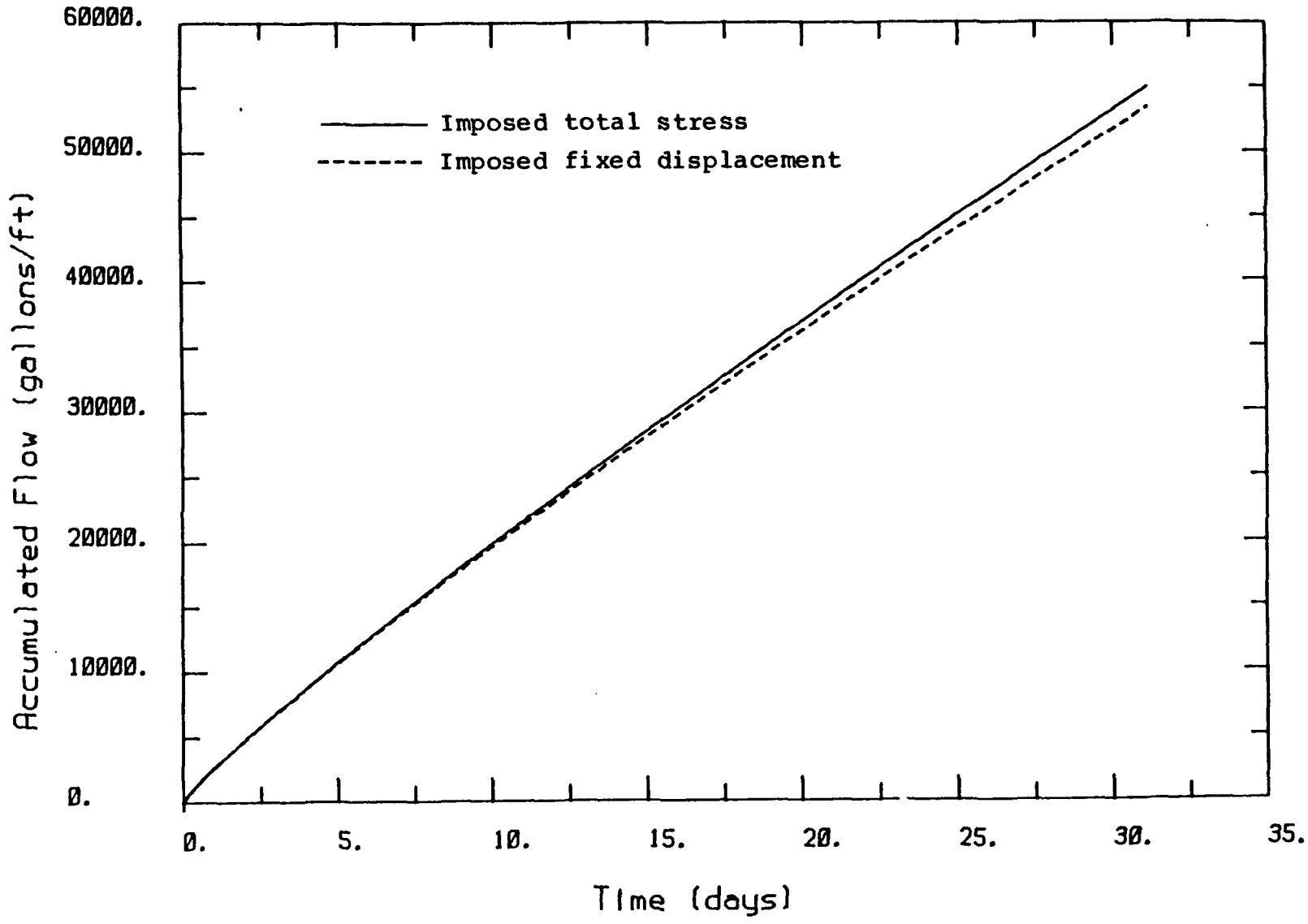

Figure 7.2. Comparison of cumulative stress from total stress and fixed displacement loadings.

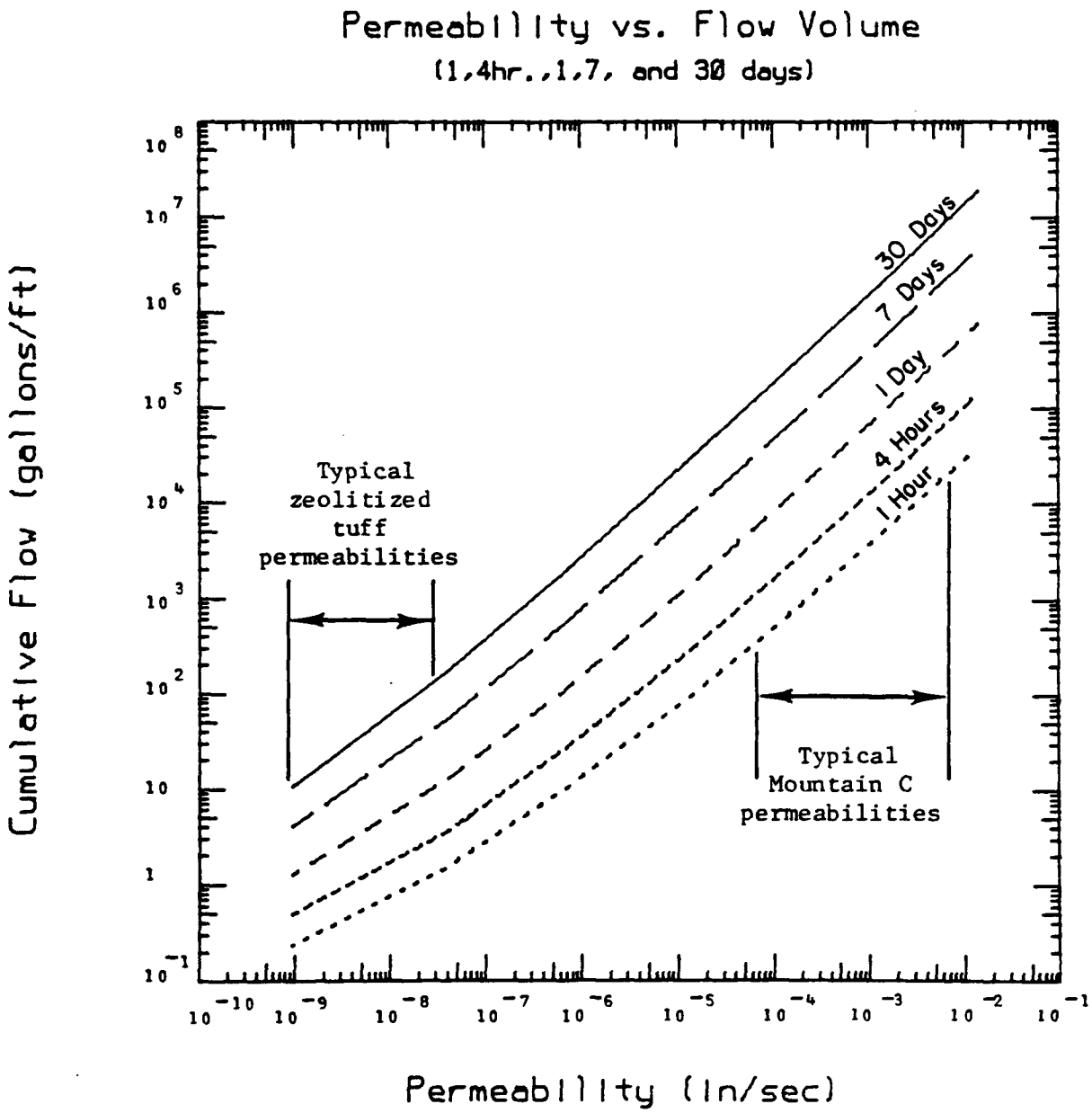

Figure 7.3. Cumulative flow as a function of permeability.

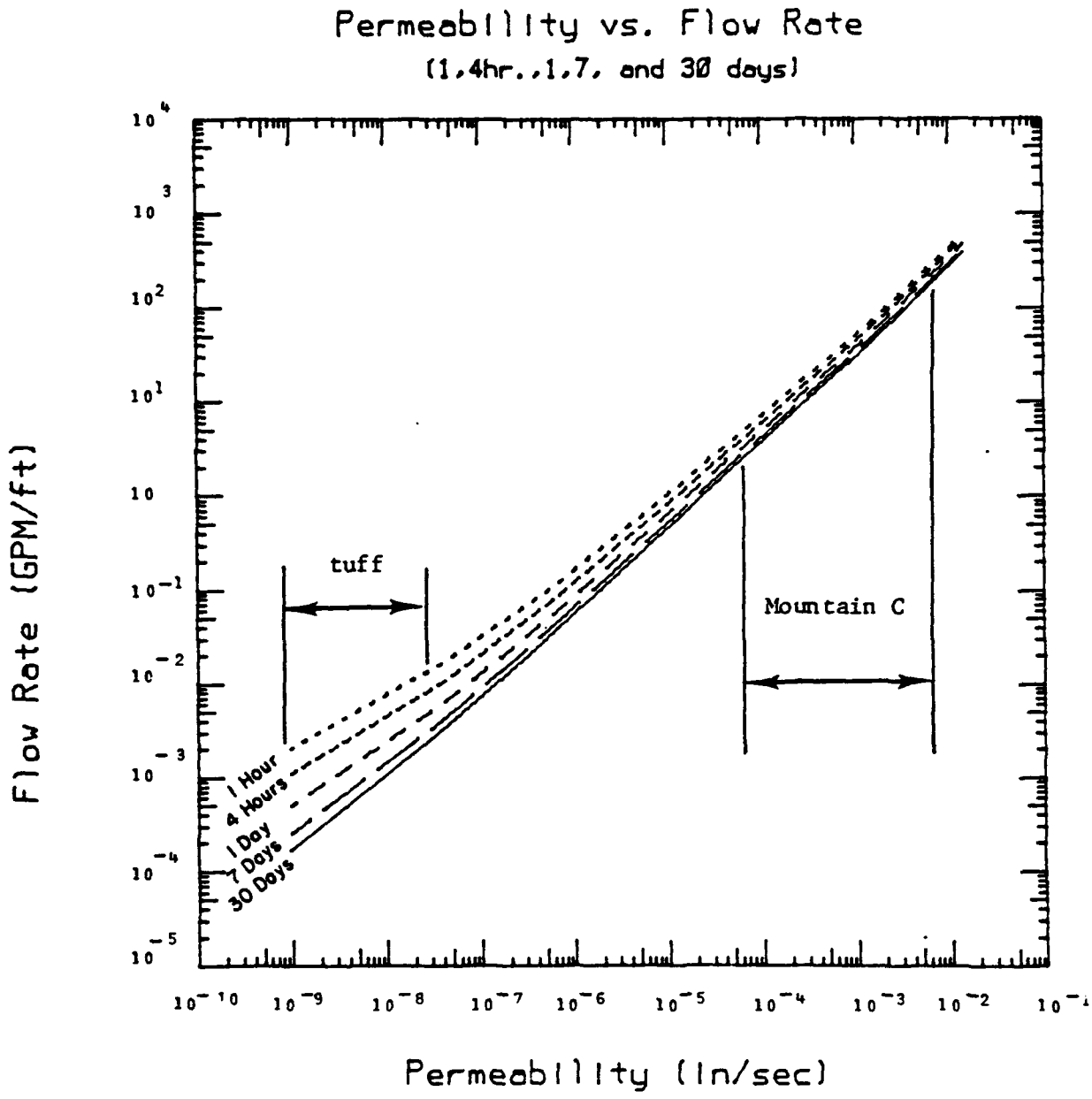

Figure 7.4. Flow rate as a function of permeability.

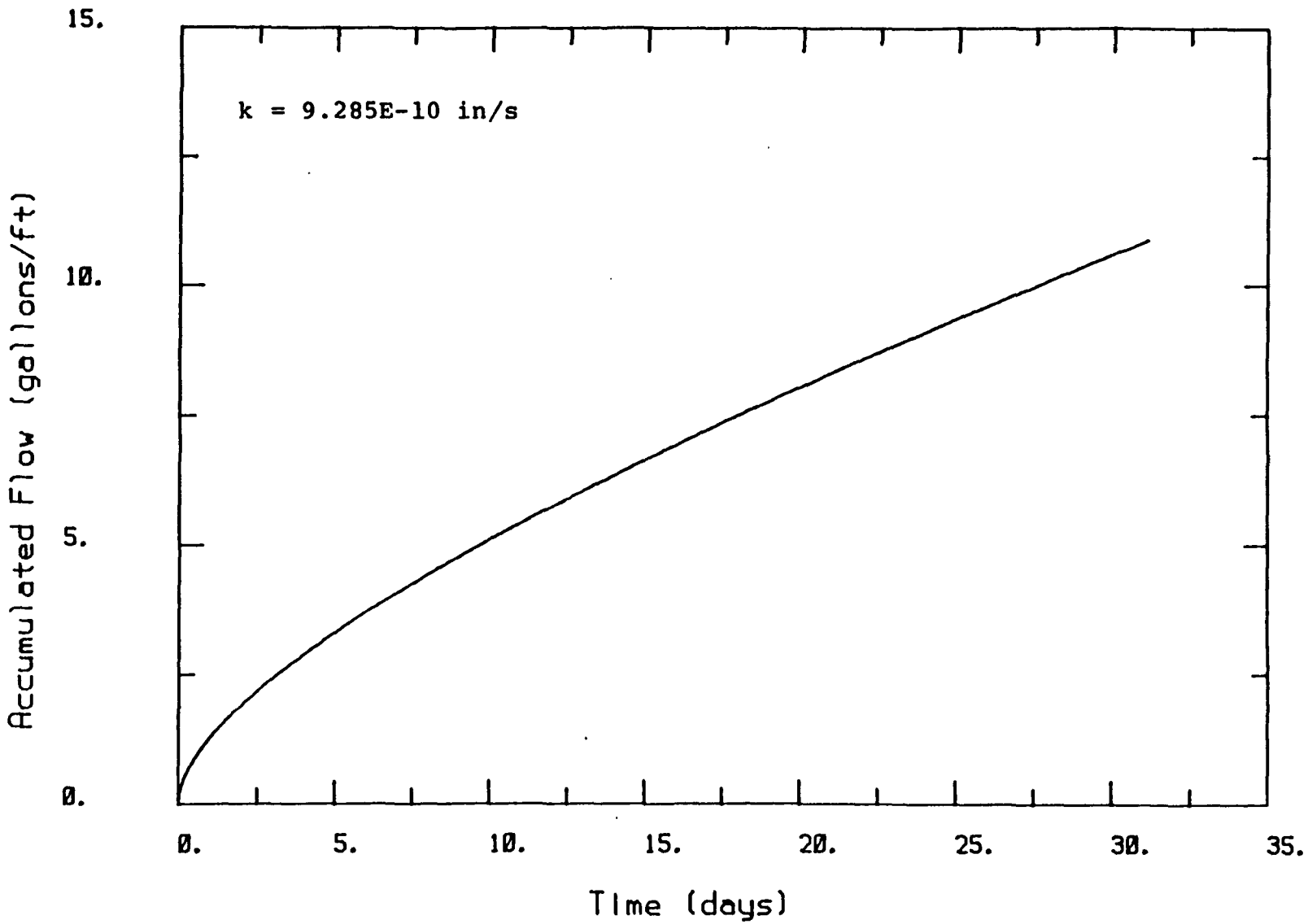

Figure 7.5. Cumulative flow in low permeability rock.

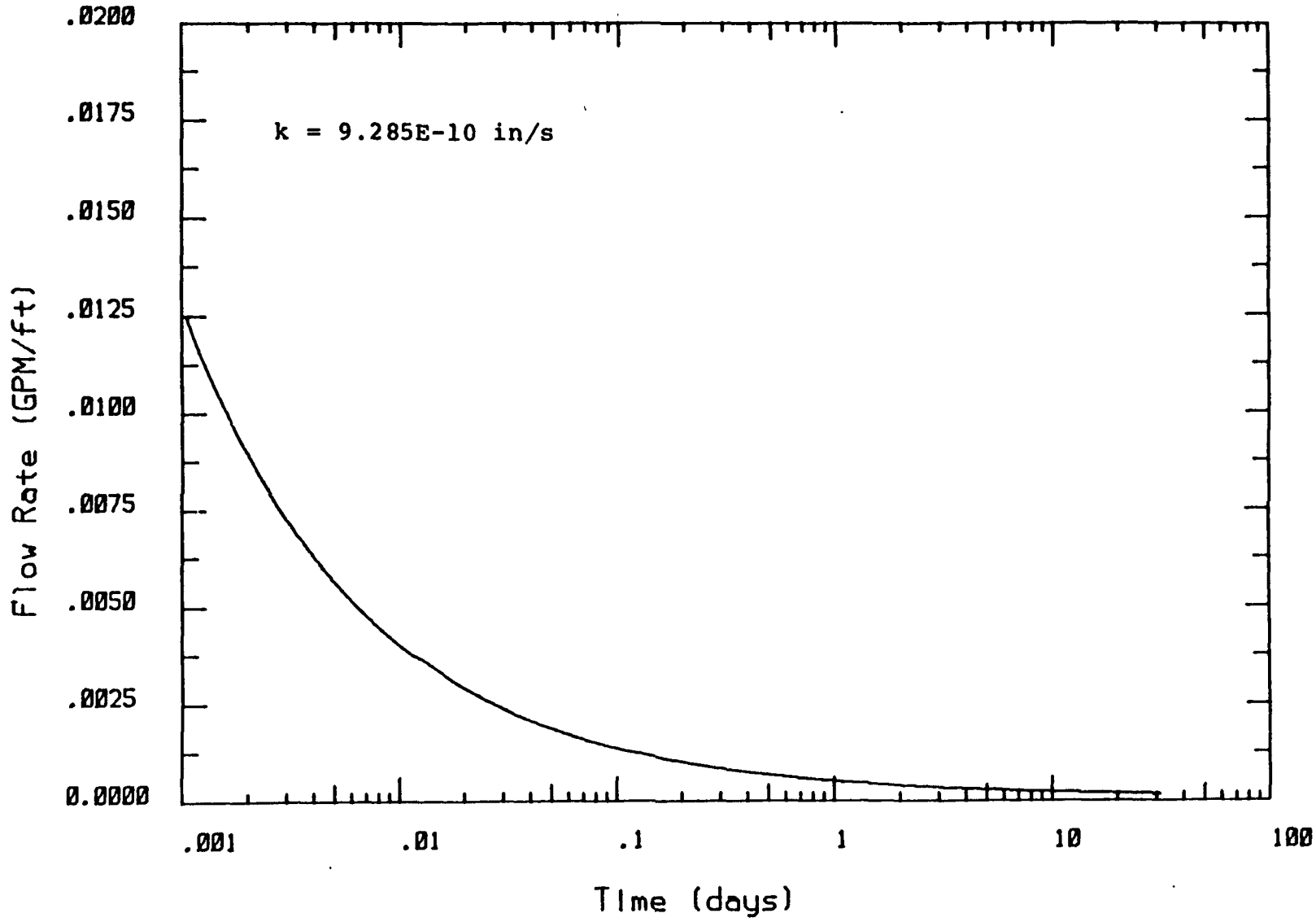

Figure 7.6. Flow rate in low permeability rock.

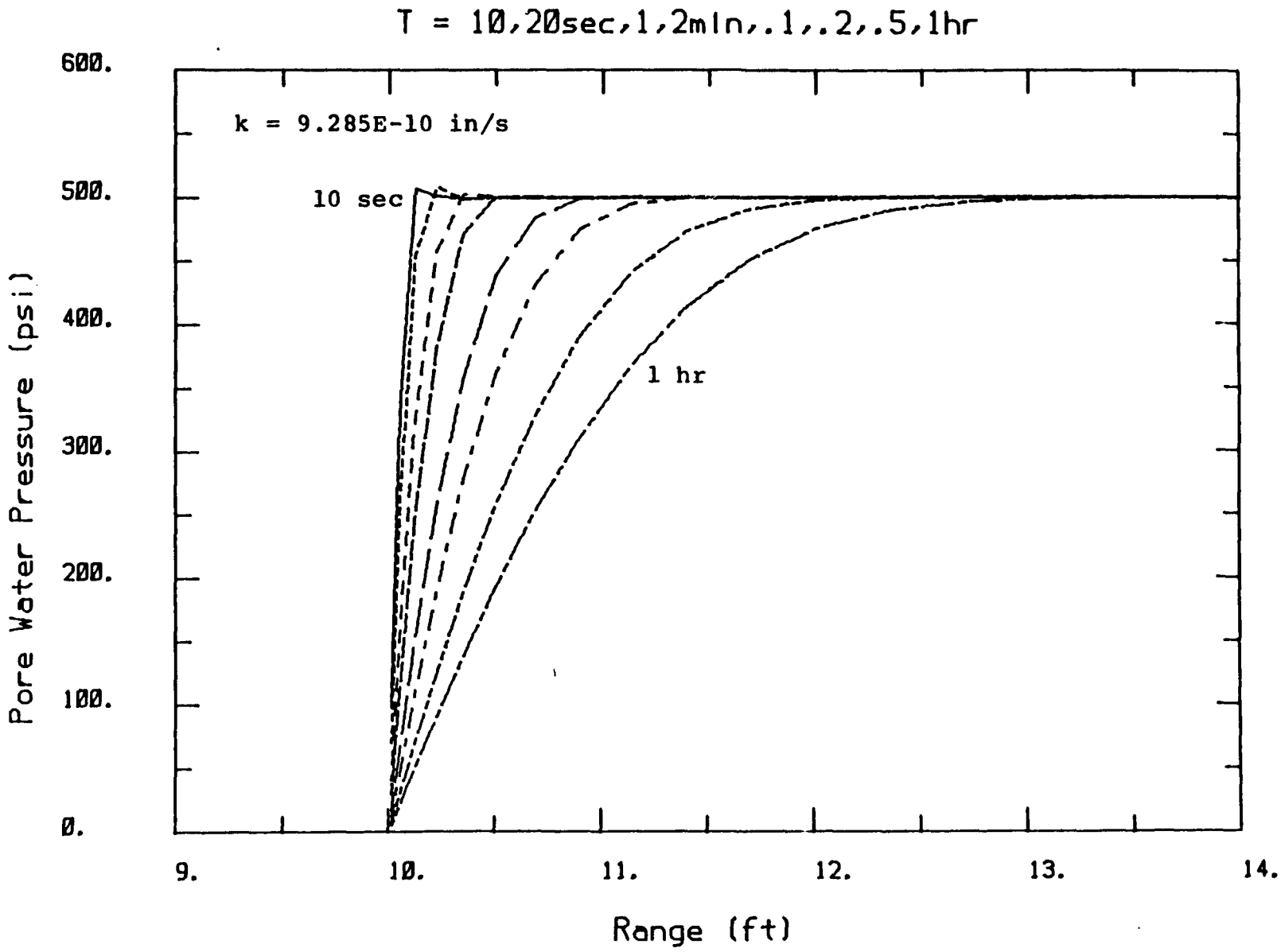

Figure 7.7a. Pore pressure dissipation in low permeability rock.

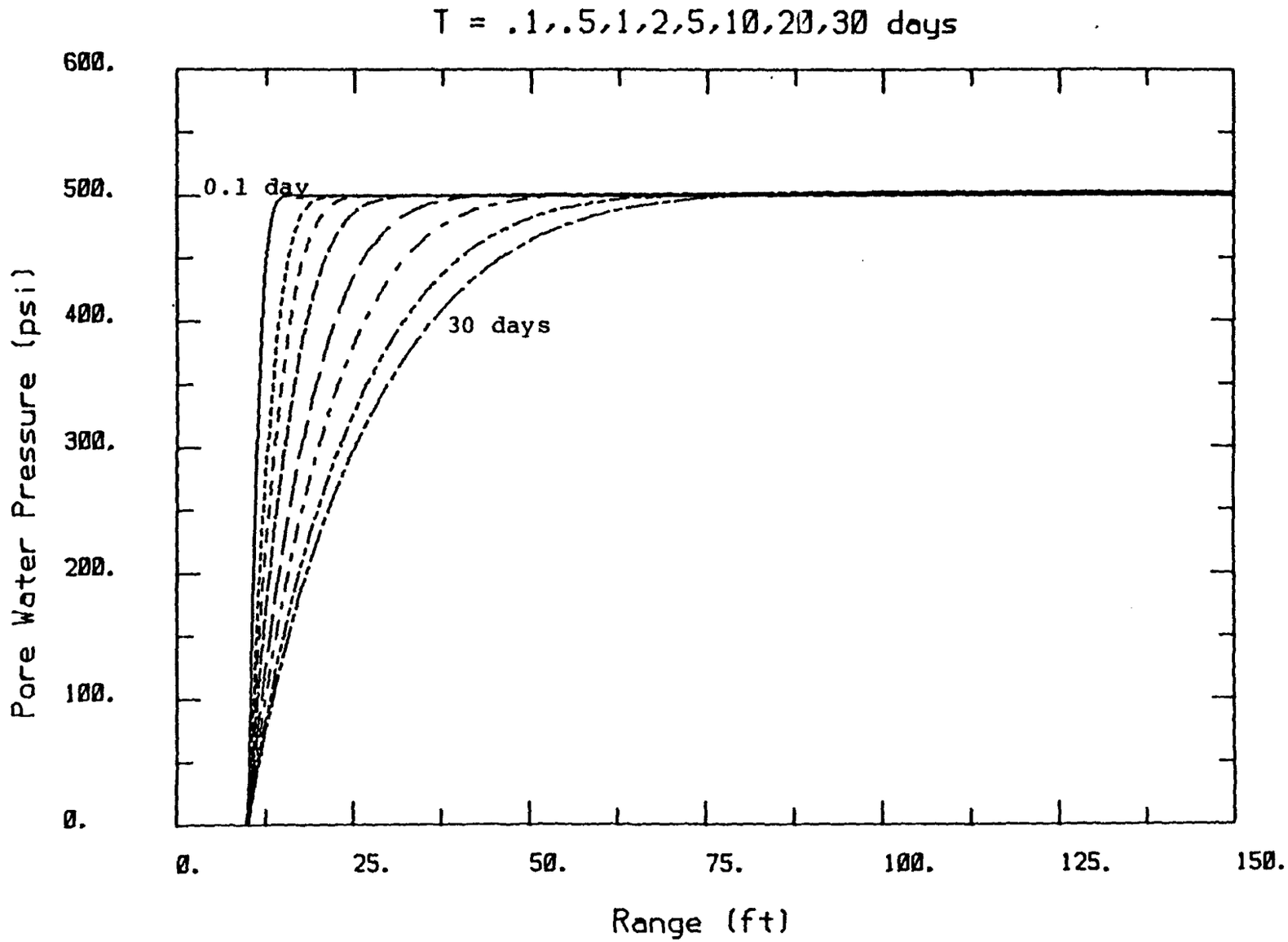
T = .1,.5,1,2,5,10,20,30 days
600.
500.
400.
300.
200.
100.
0.
Pore Water Pressure (psi)
0.1 day
30 days
0.
25.
50.
75.
100.
125.
150.
Range (ft)

Figure 7.7b.

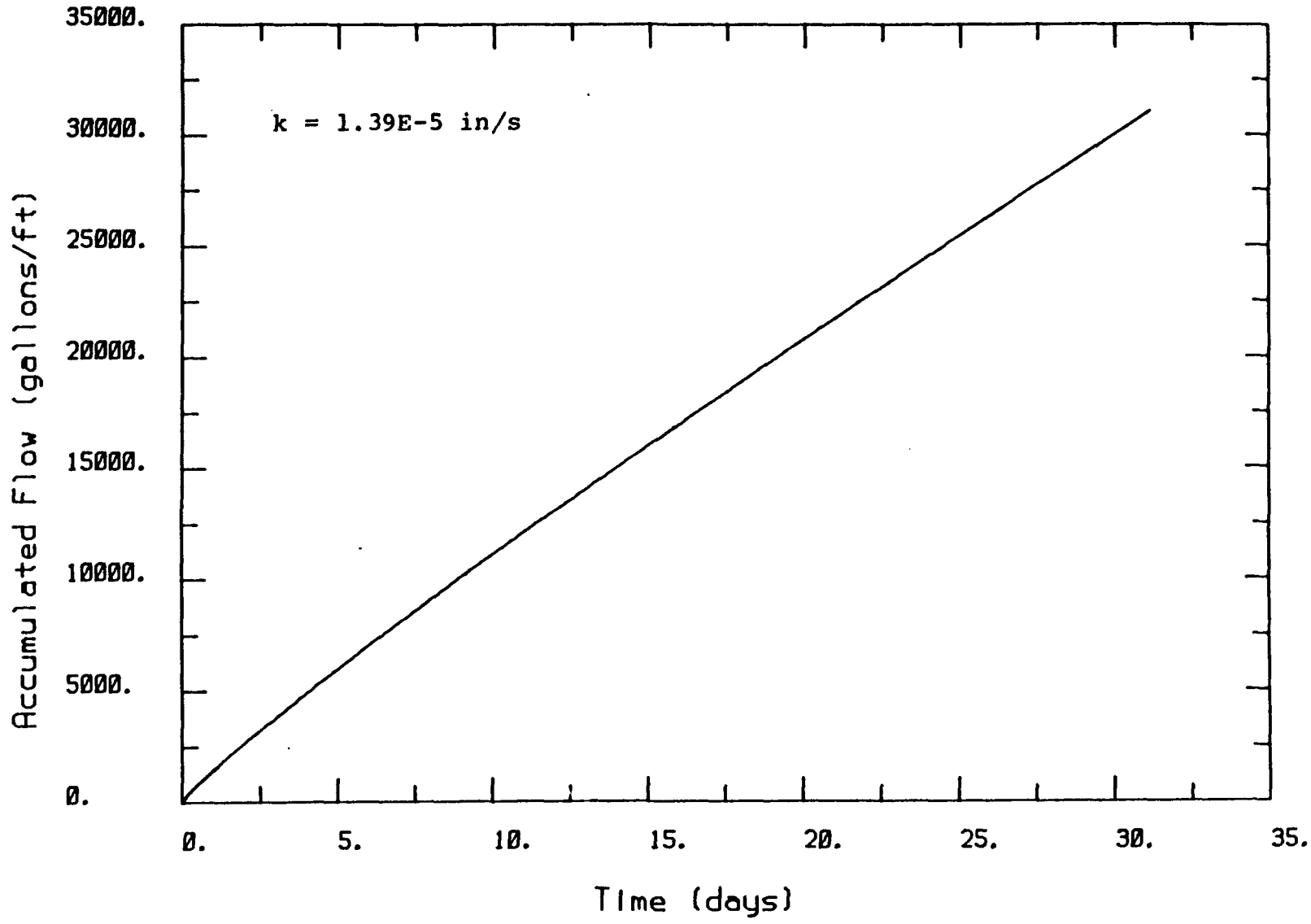

Figure 7.8. Cumulative flow in medium permeability rock.

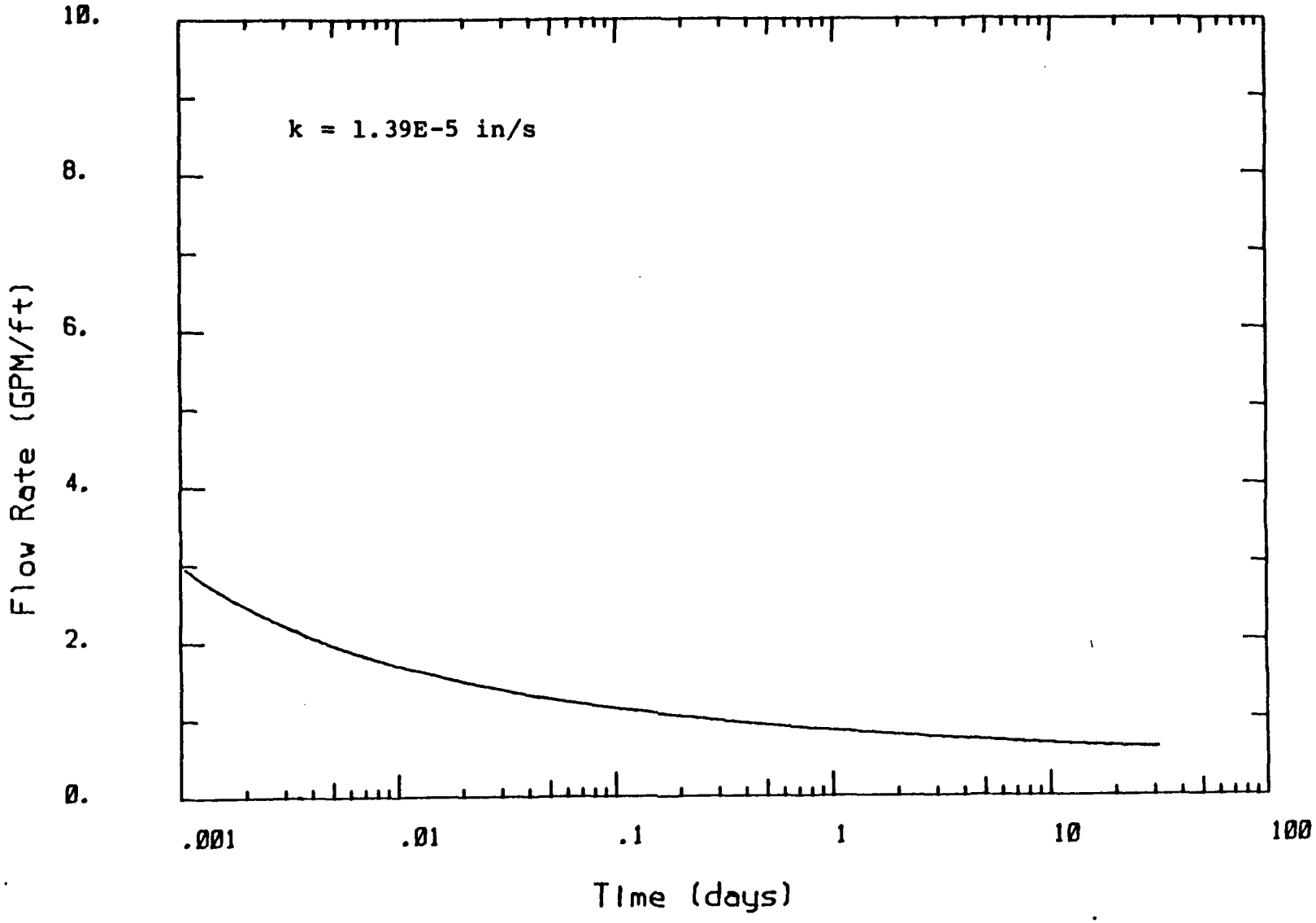

Figure 7.9. Flow rate in medium permeability rock.

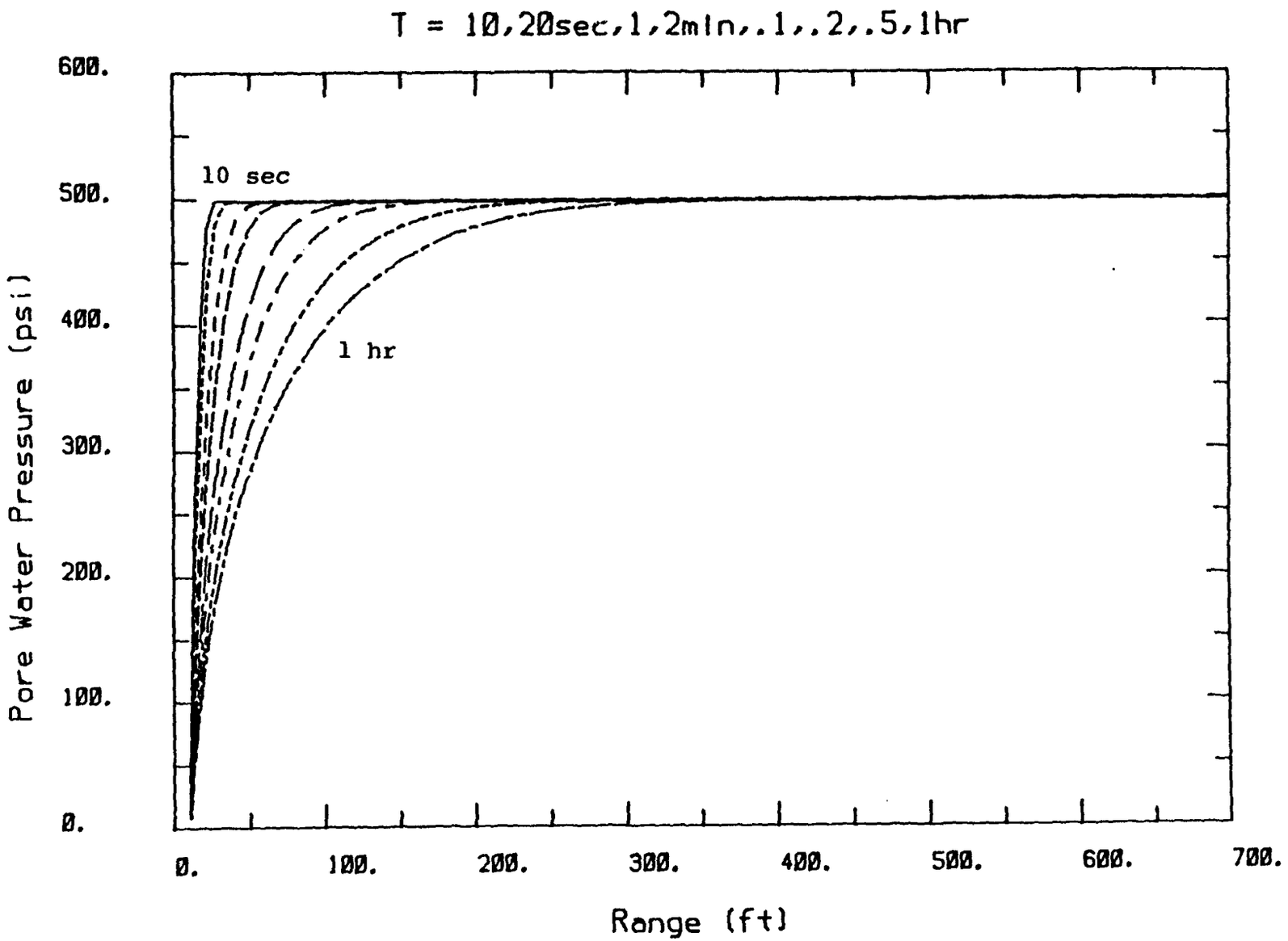

Figure 7.10a. Pore pressure dissipation in medium permeability rock.

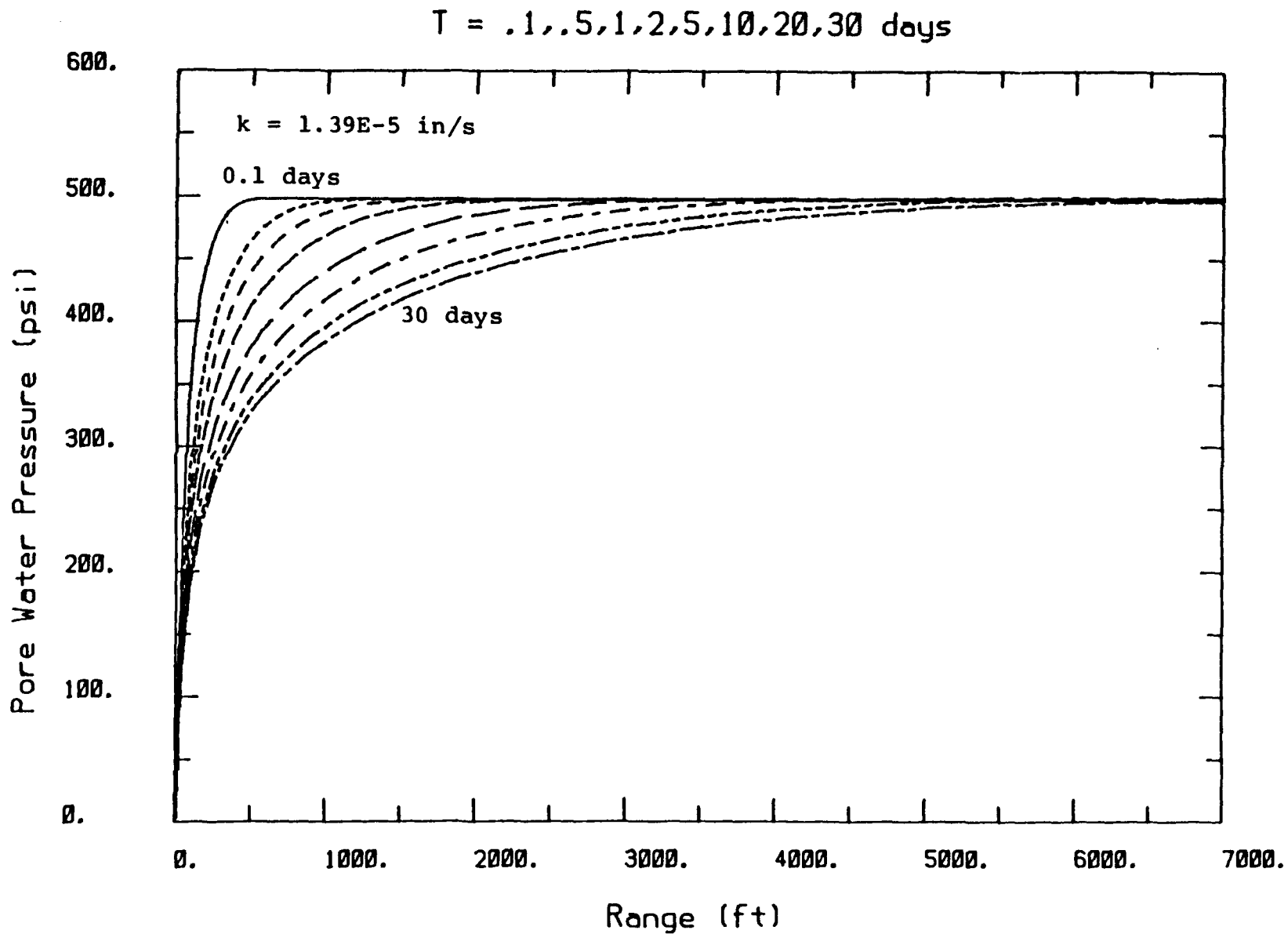
T = .1,.5,1,2,5,10,20,30 days
k = 1.39E-5 in/s
0.1 days
30 days
Pore Water Pressure (psi)
600.
500.
400.
300.
200.
100.
0.
0.
1000.
2000.
3000.
4000.
5000.
6000.
7000.
Range (ft)

Figure 7.10b.

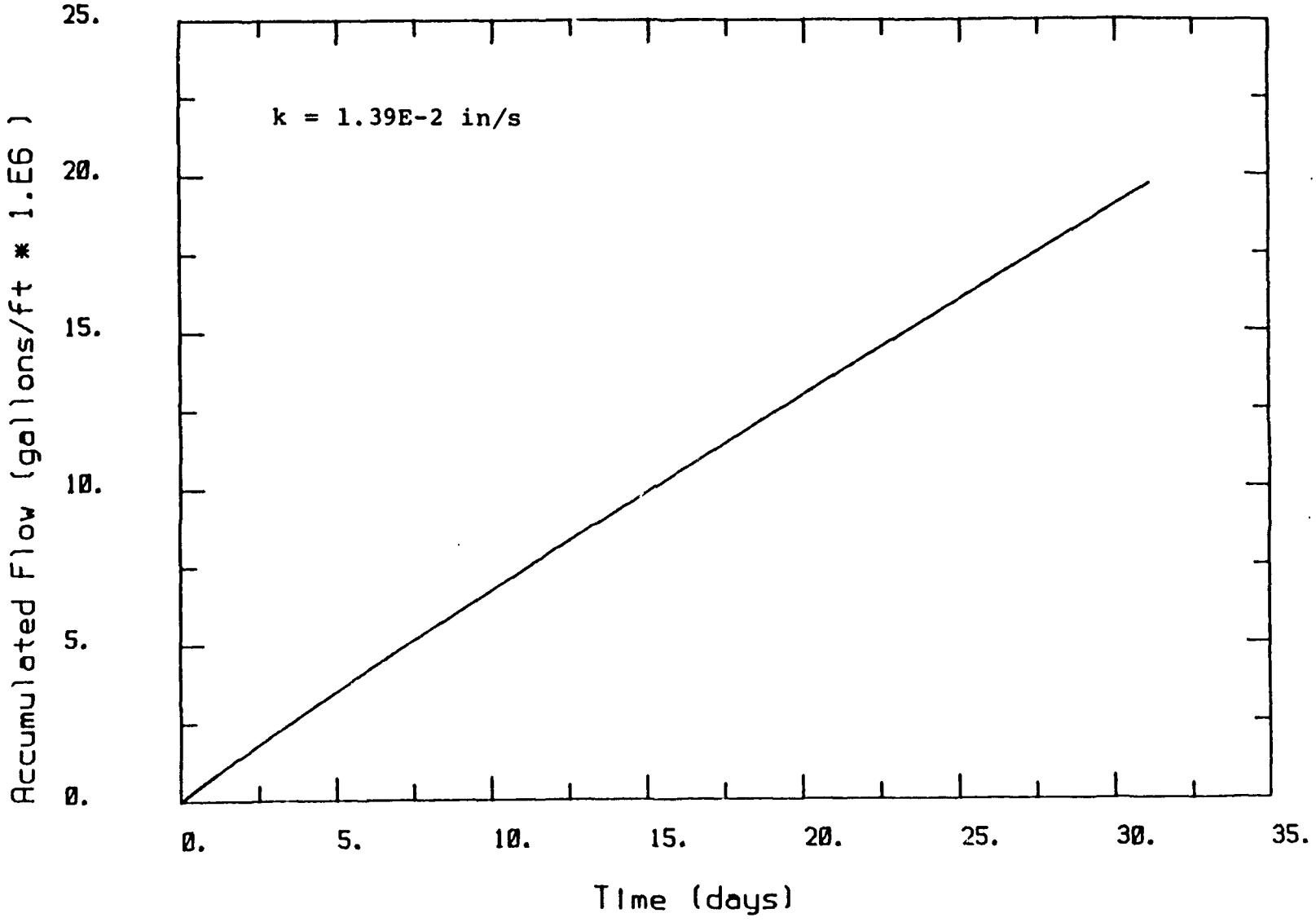

Figure 7.11. Cumulative flow in high permeability rock.

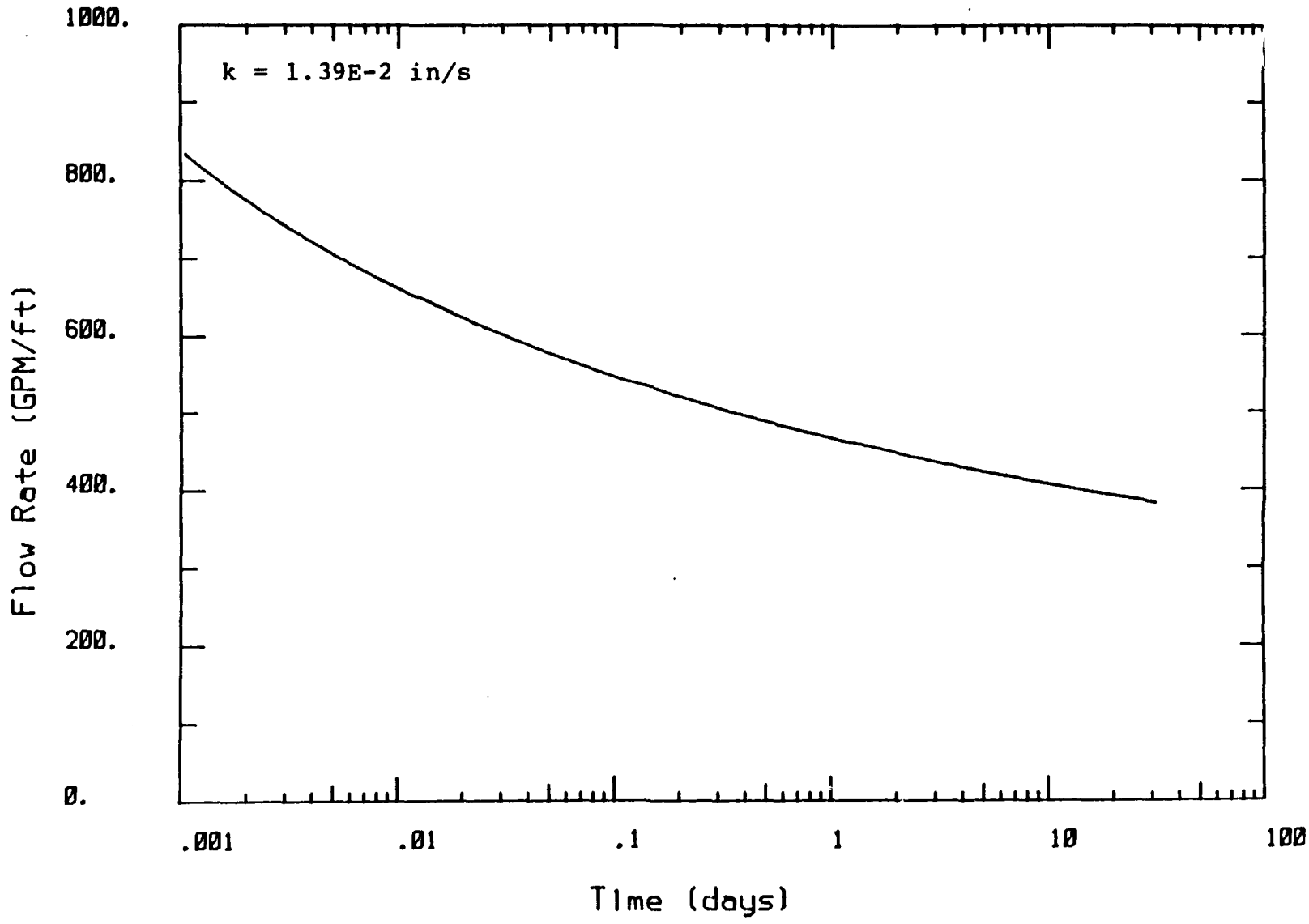

Figure 7.12. Flow rate in high permeability rock.

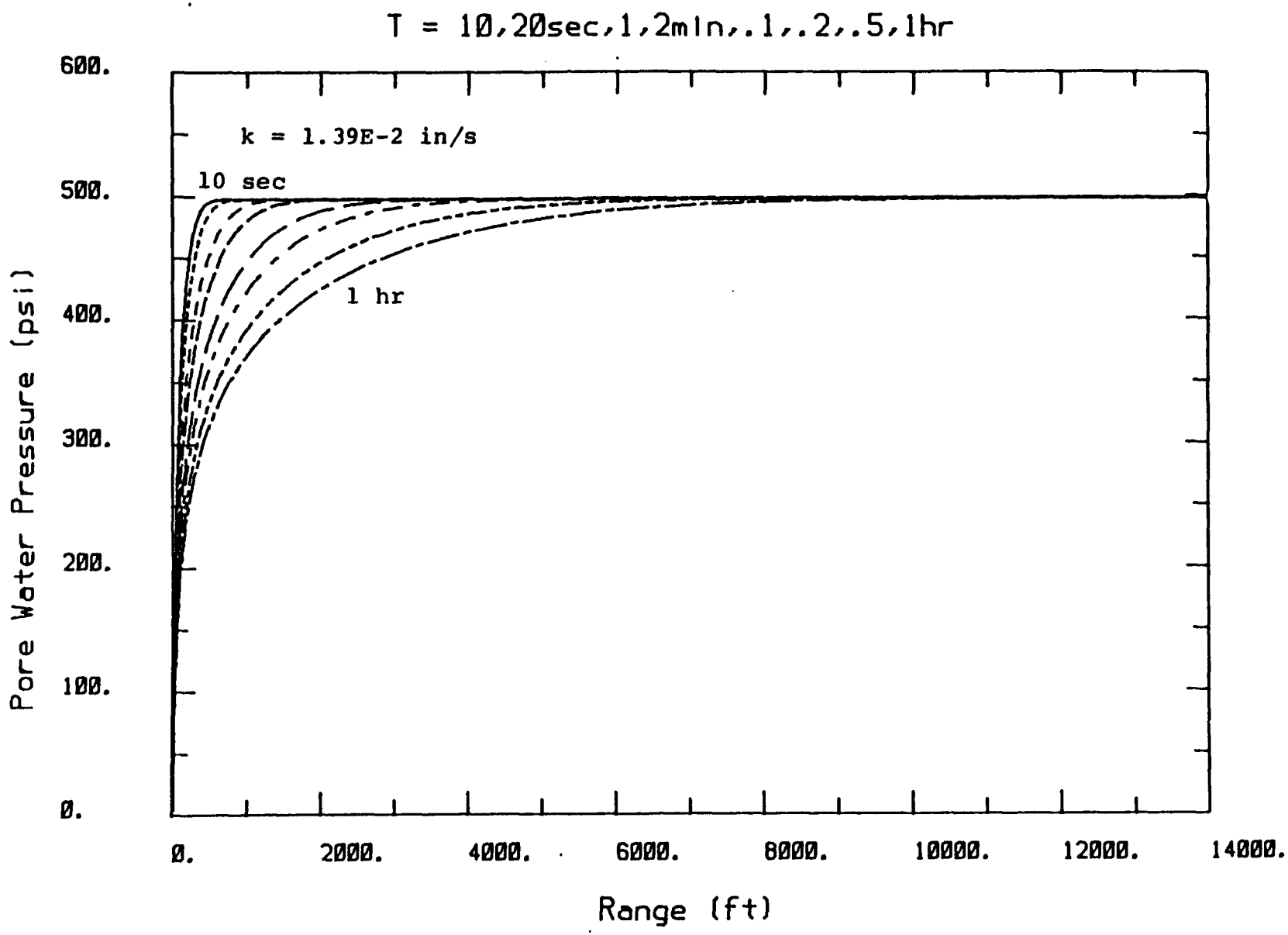

Figure 7.13a. Pore pressure dissipation in high permeability rock.

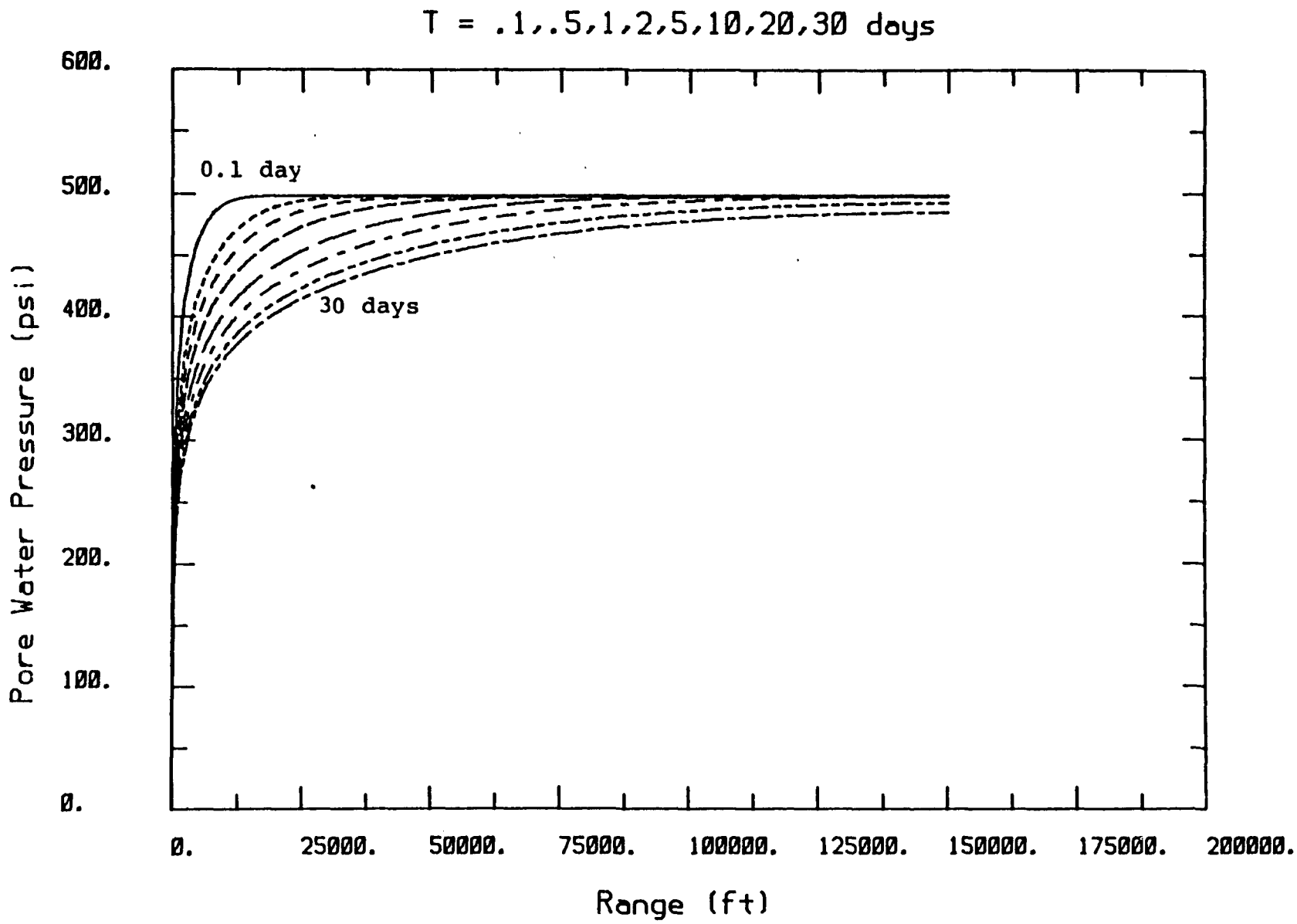
T = .1,.5,1,2,5,10,20,30 days
0.1 day
30 days
Pore Water Pressure (psi)
600.
500.
400.
300.
200.
100.
0.
0.
25000.
50000.
75000.
100000.
125000.
150000.
175000.
200000.
Range (ft)

Figure 7.13b.

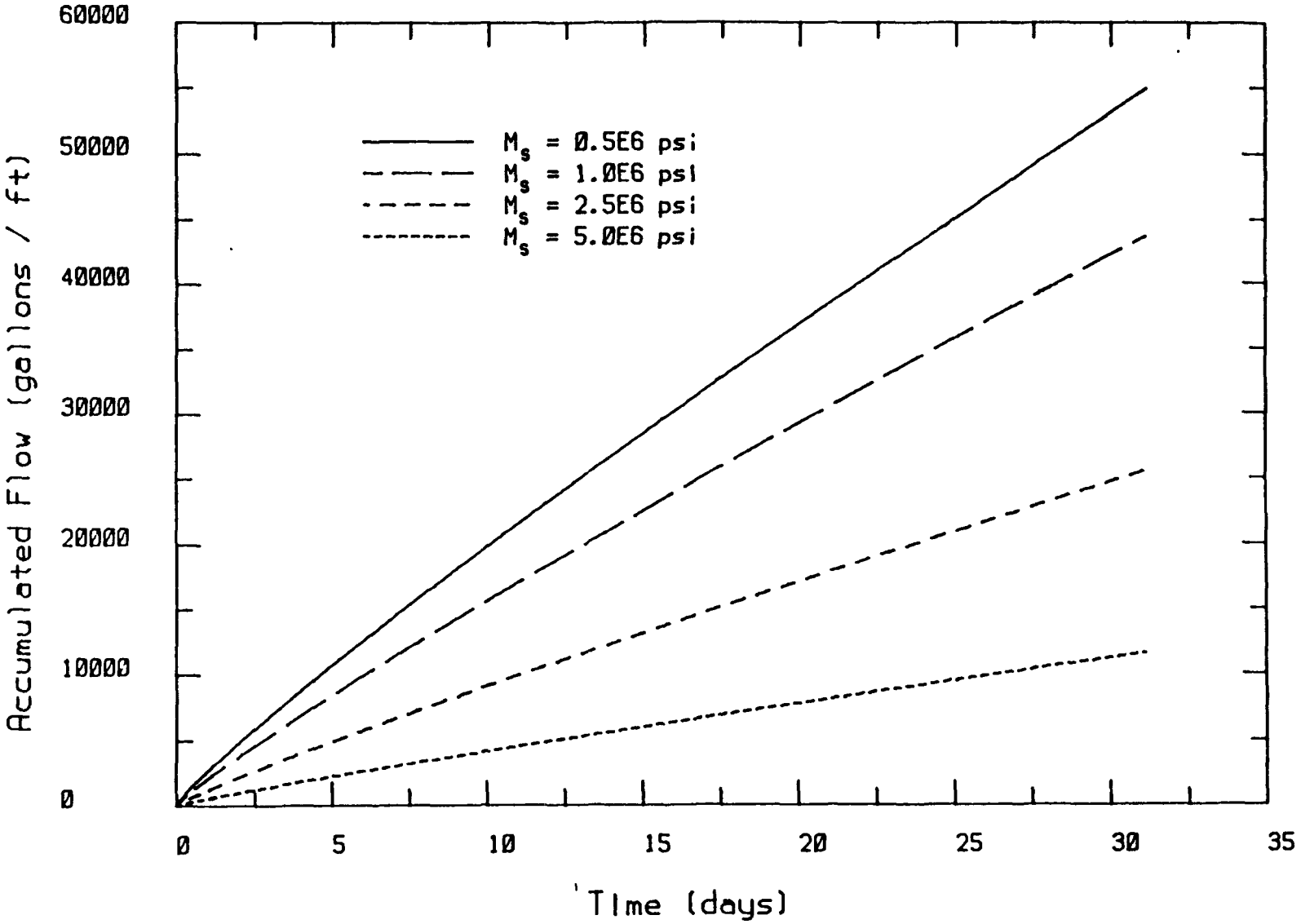

Figure 7.14. Influence of skeleton modulus on flow volume.

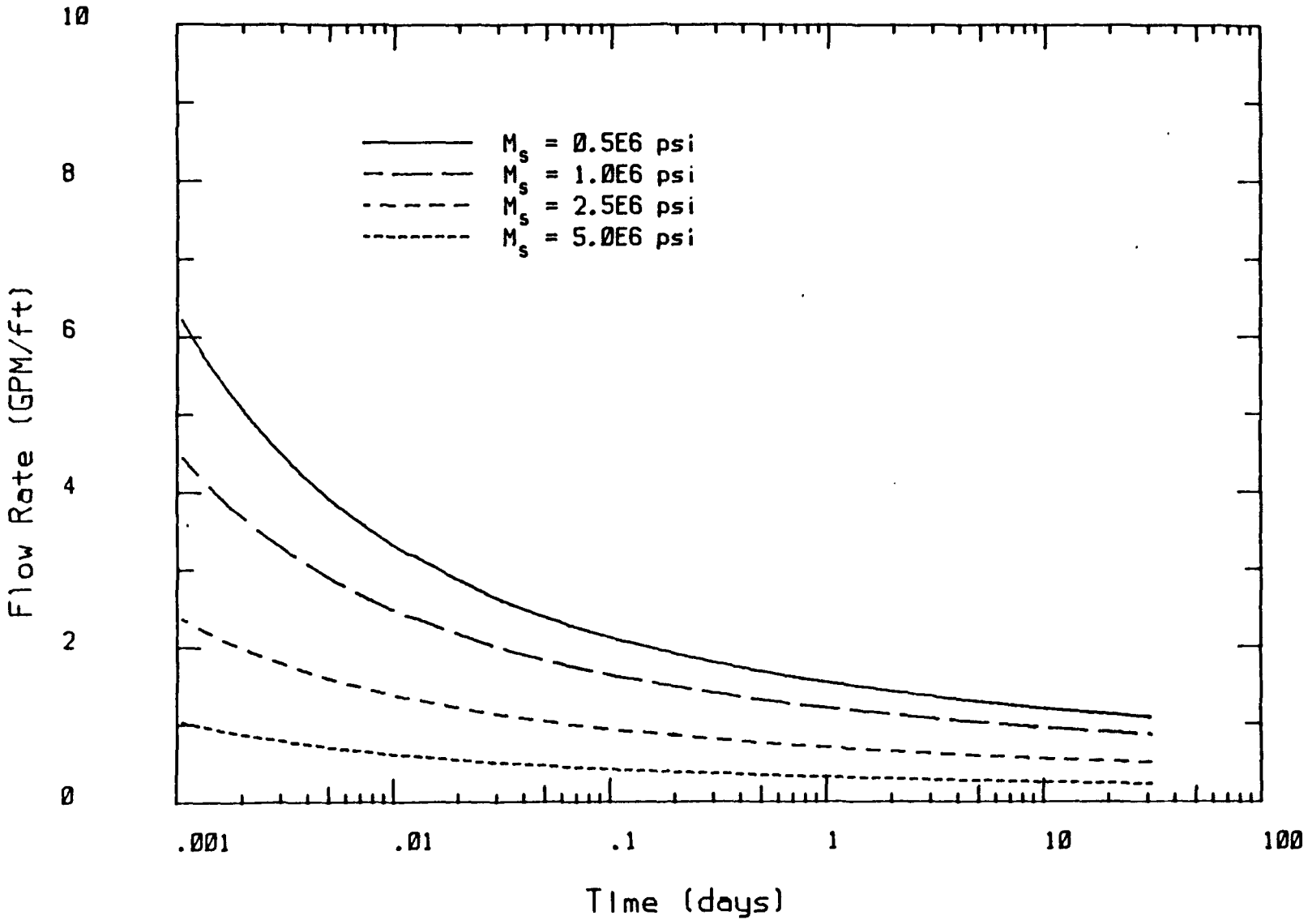

Figure 7.15. Influence of skeleton modulus on flow rate.

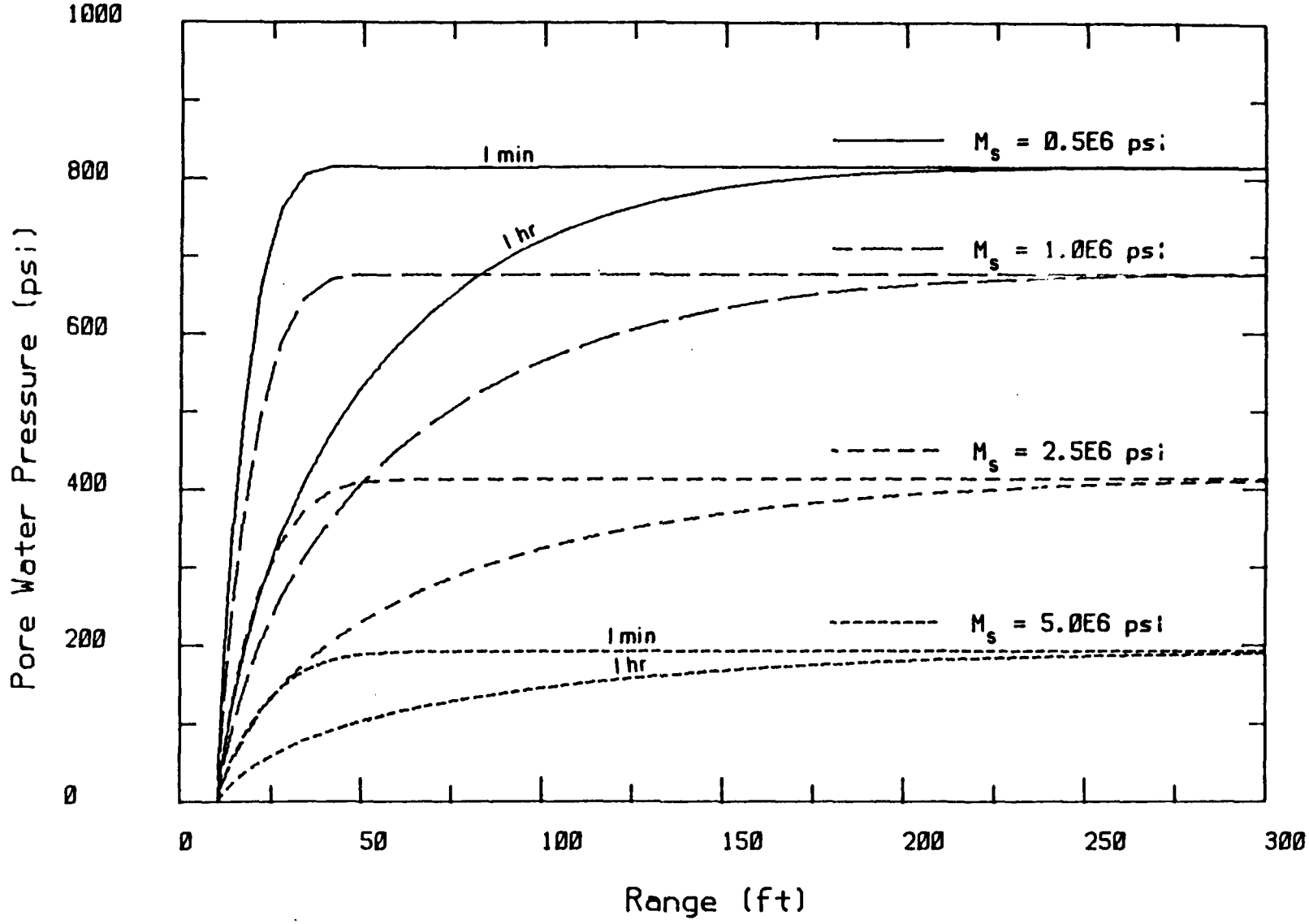

Figure 7.16a. Influence of skeleton modulus on pore pressure.

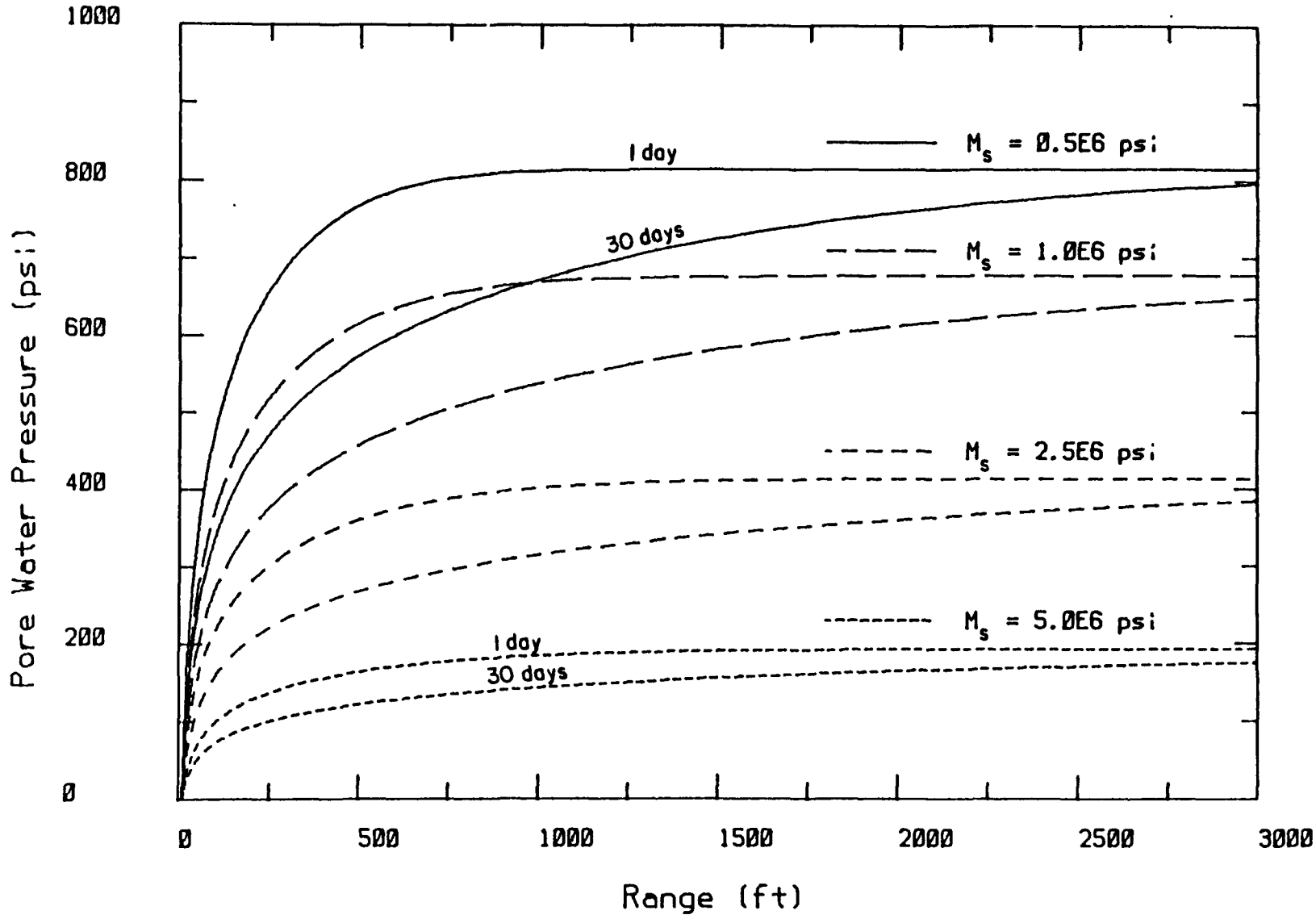
1000
800
600
400
200
0
Pore Water Pressure (psi)
0
500
1000
1500
2000
2500
3000
Range (ft)
1 day
30 days
1 day
30 days
M_s = 0.5E6 psi
M_s = 1.0E6 psi
M_s = 2.5E6 psi
M_s = 5.0E6 psi

Figure 7.16b.

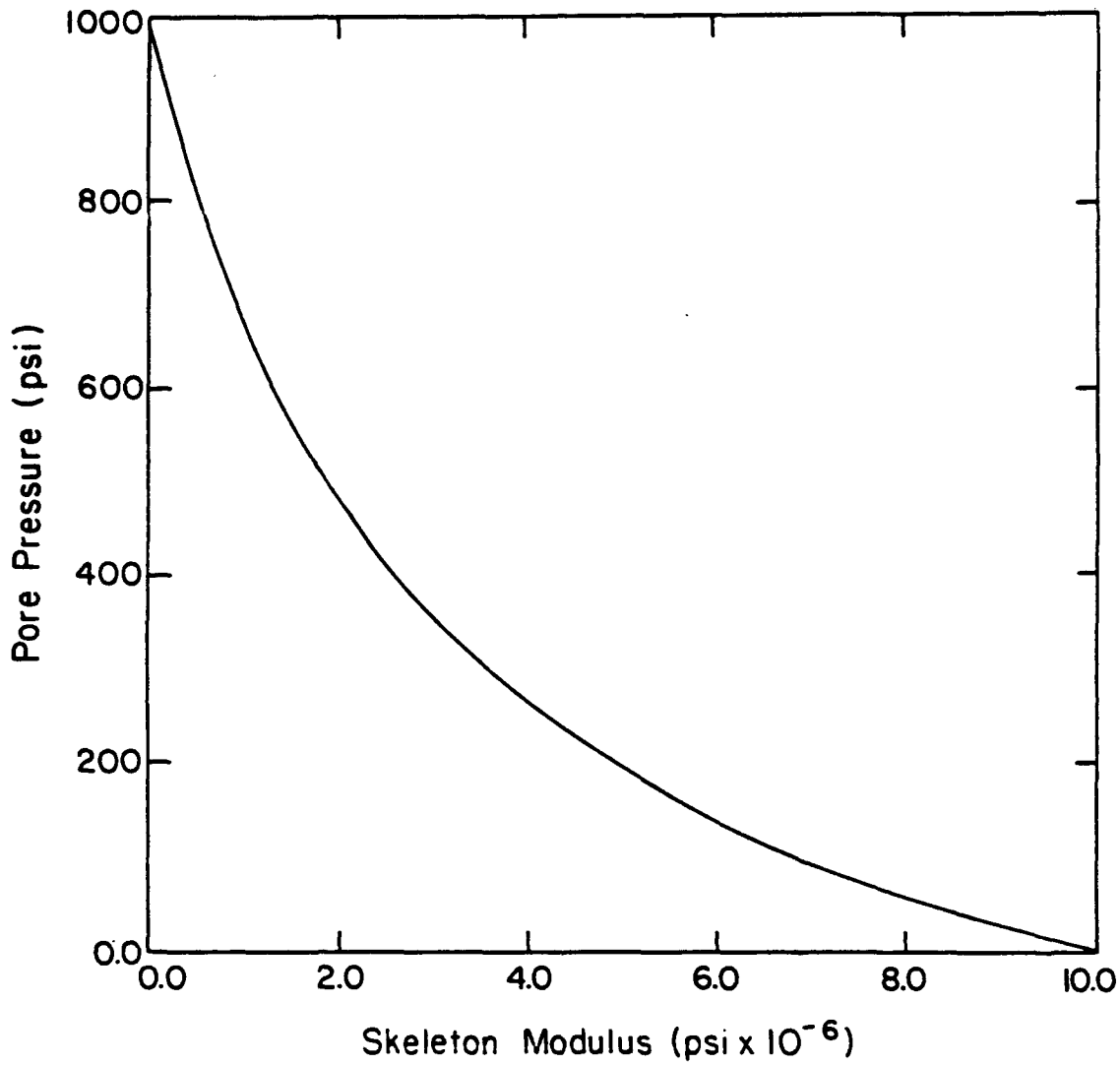

Figure 7.17. Initial pore pressure as a function of skeleton modulus.

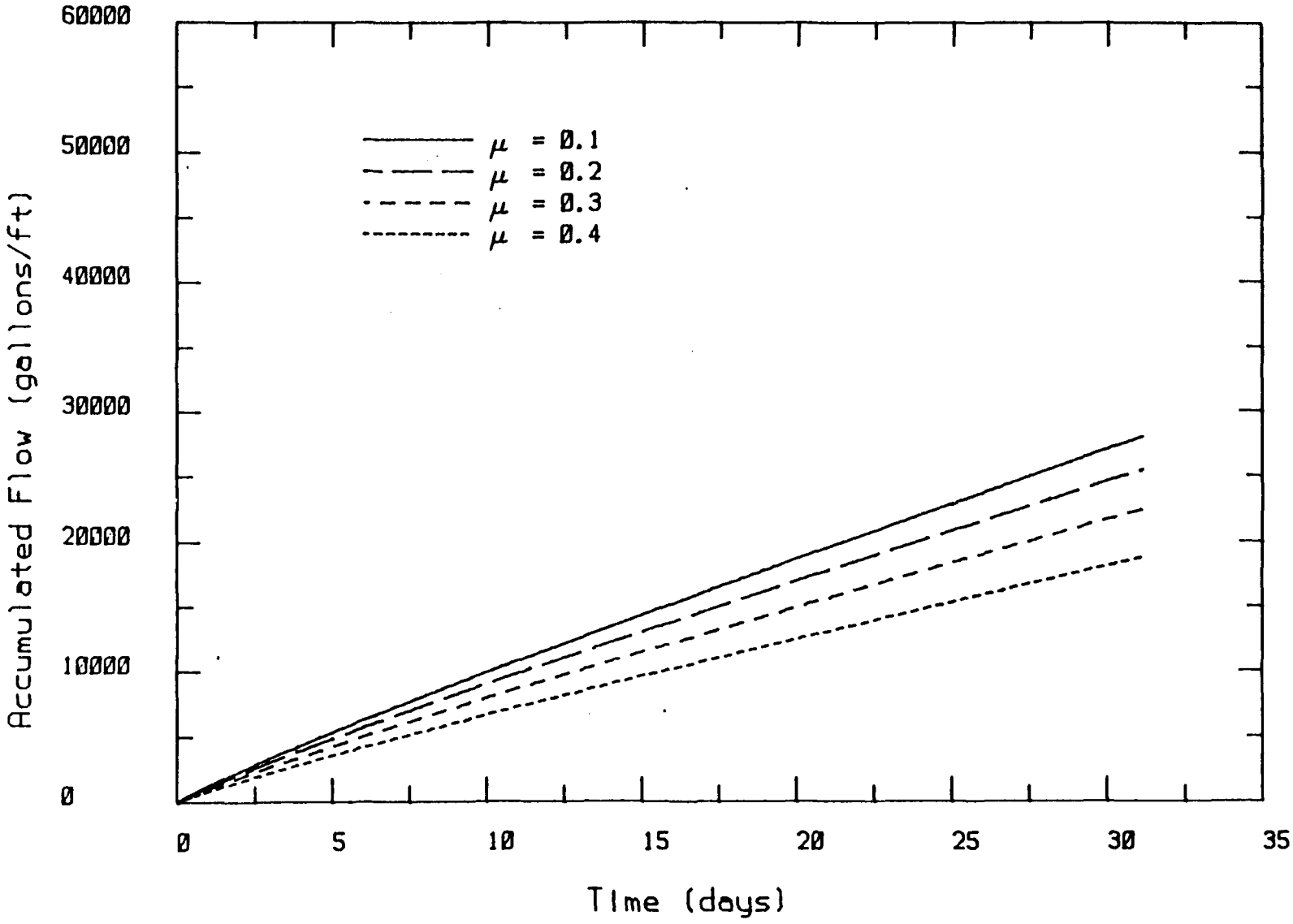

Figure 7.18. Influence of Poisson's ratio on flow volume in plane strain simulation.

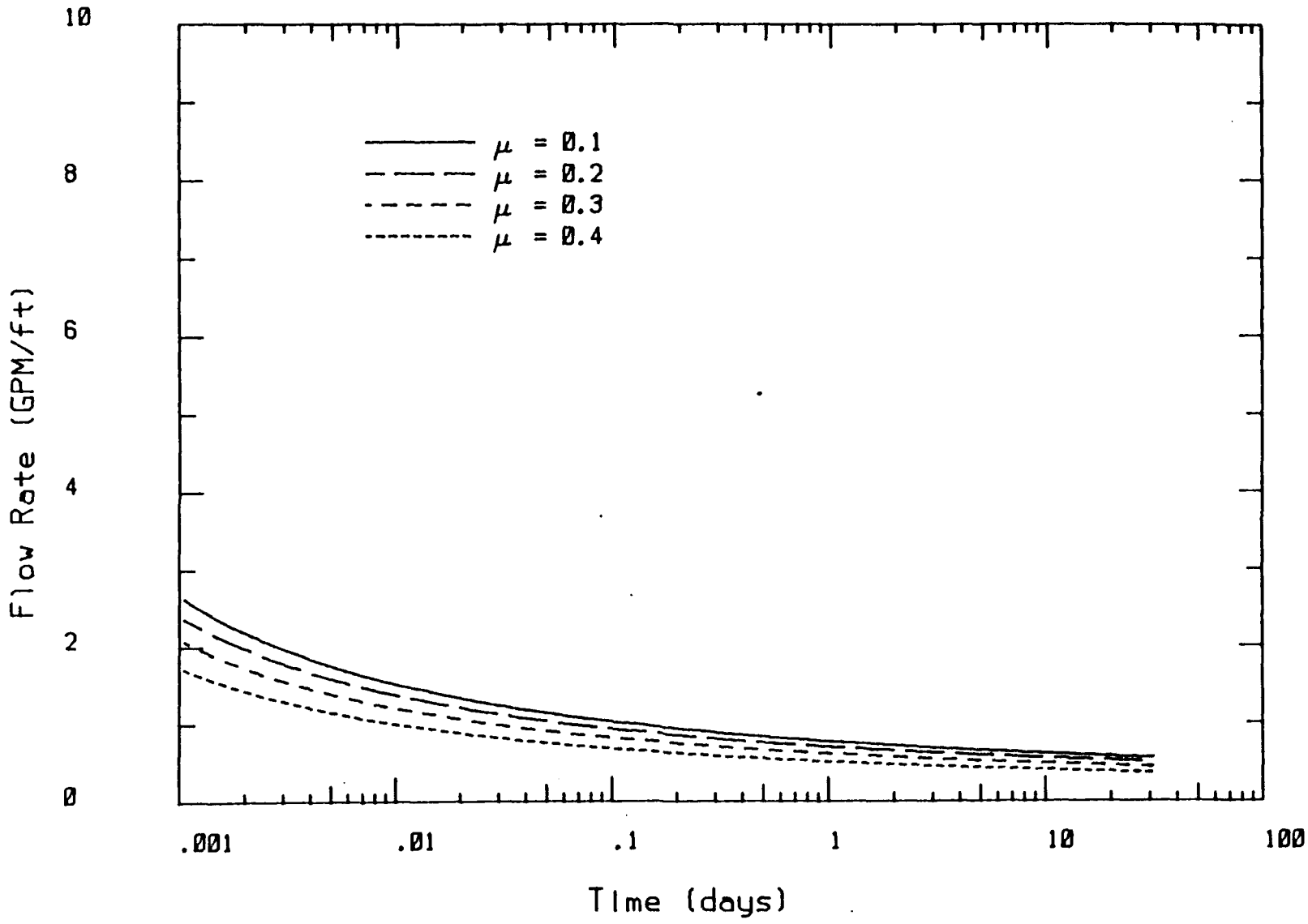

Figure 7.19. Influence of Poisson's ratio on flow rate in plane strain simulation.

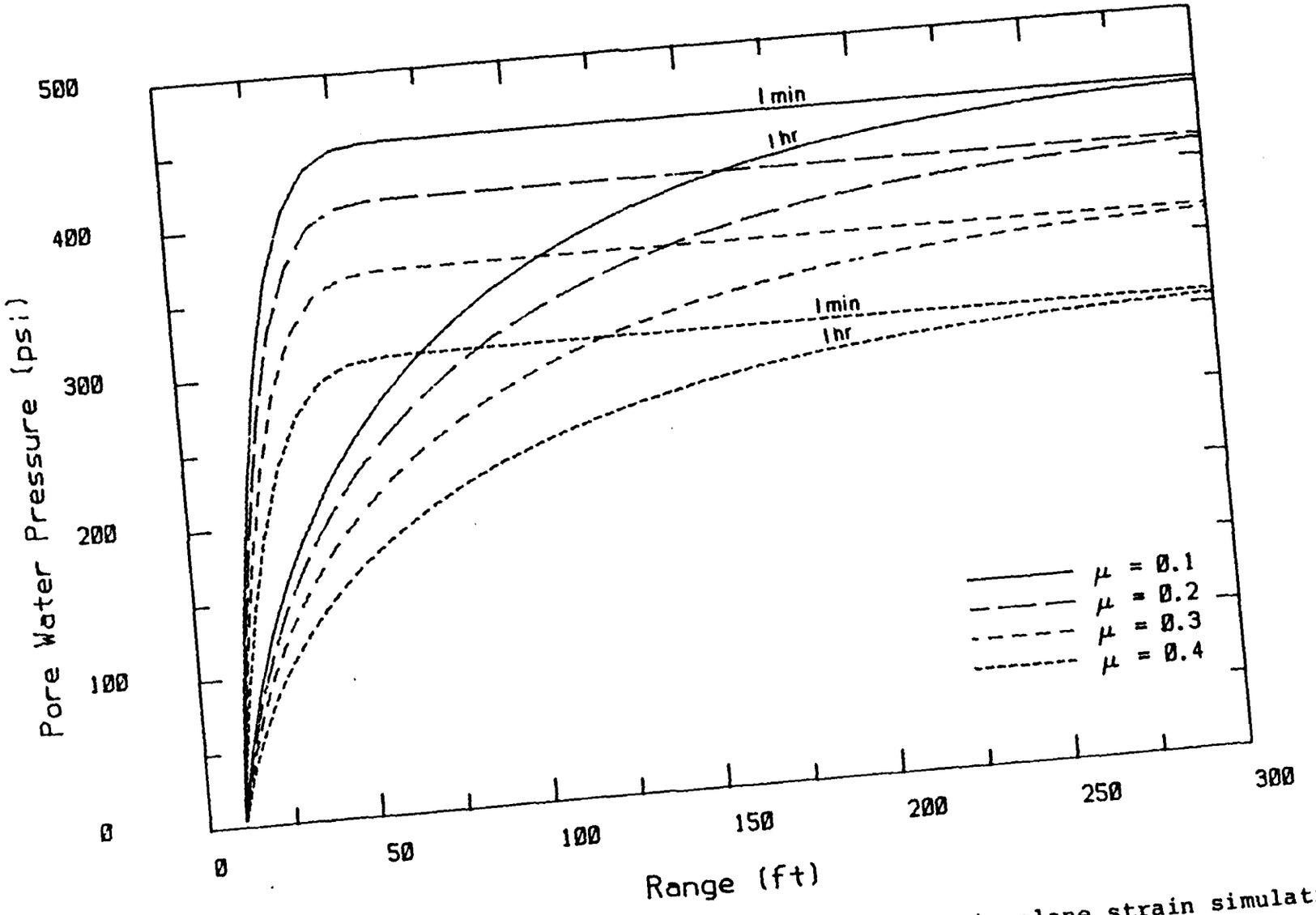

Figure 7.20a. Influence of Poisson's ratio on pore pressure in plane strain simulation.

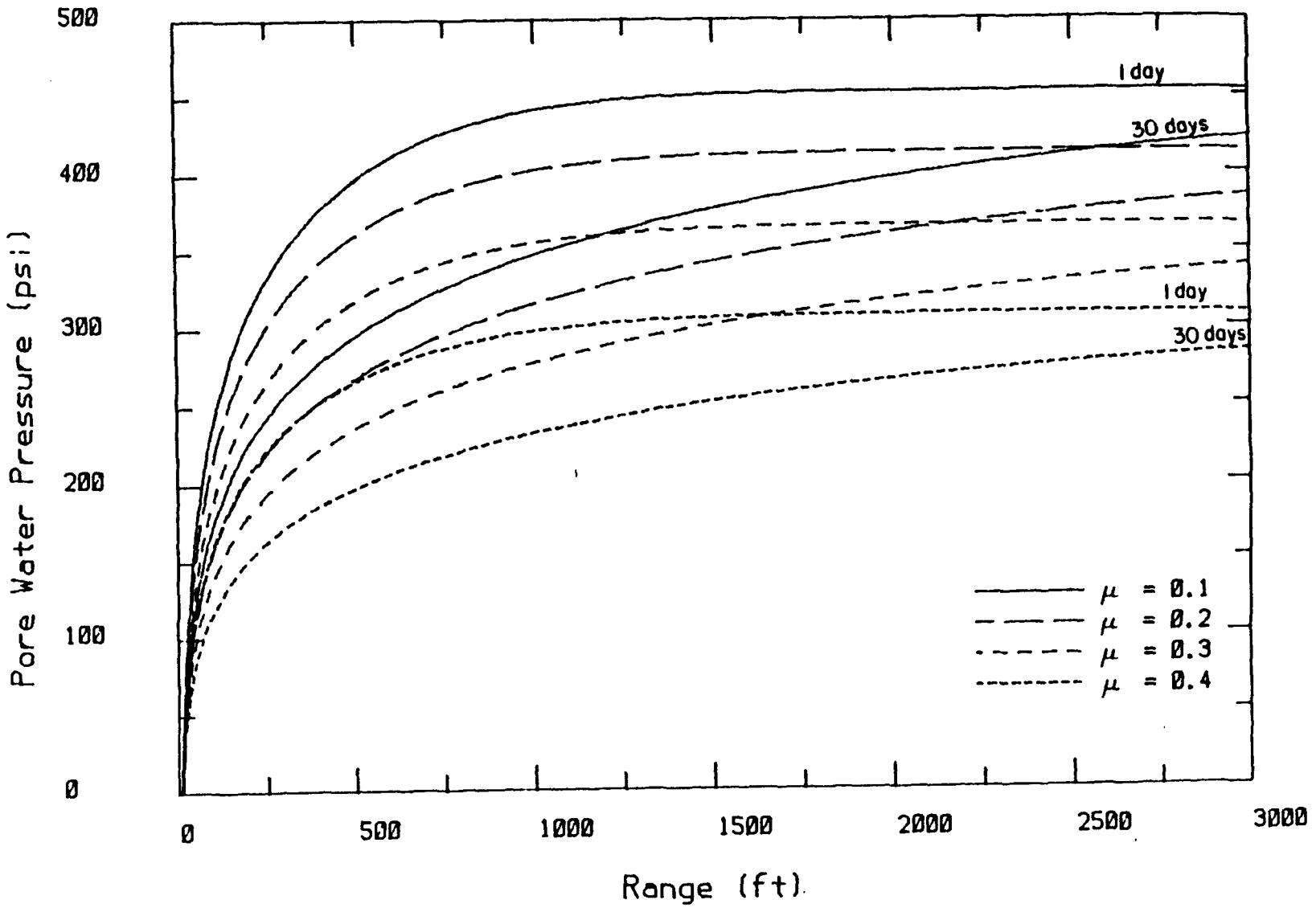
500
400
300
200
100
0
Pore Water Pressure (psi)
0
500
1000
1500
2000
2500
3000
Range (ft)
1 day
30 days
1 day
30 days
μ = 0.1
μ = 0.2
μ = 0.3
μ = 0.4

Figure 7.20b.

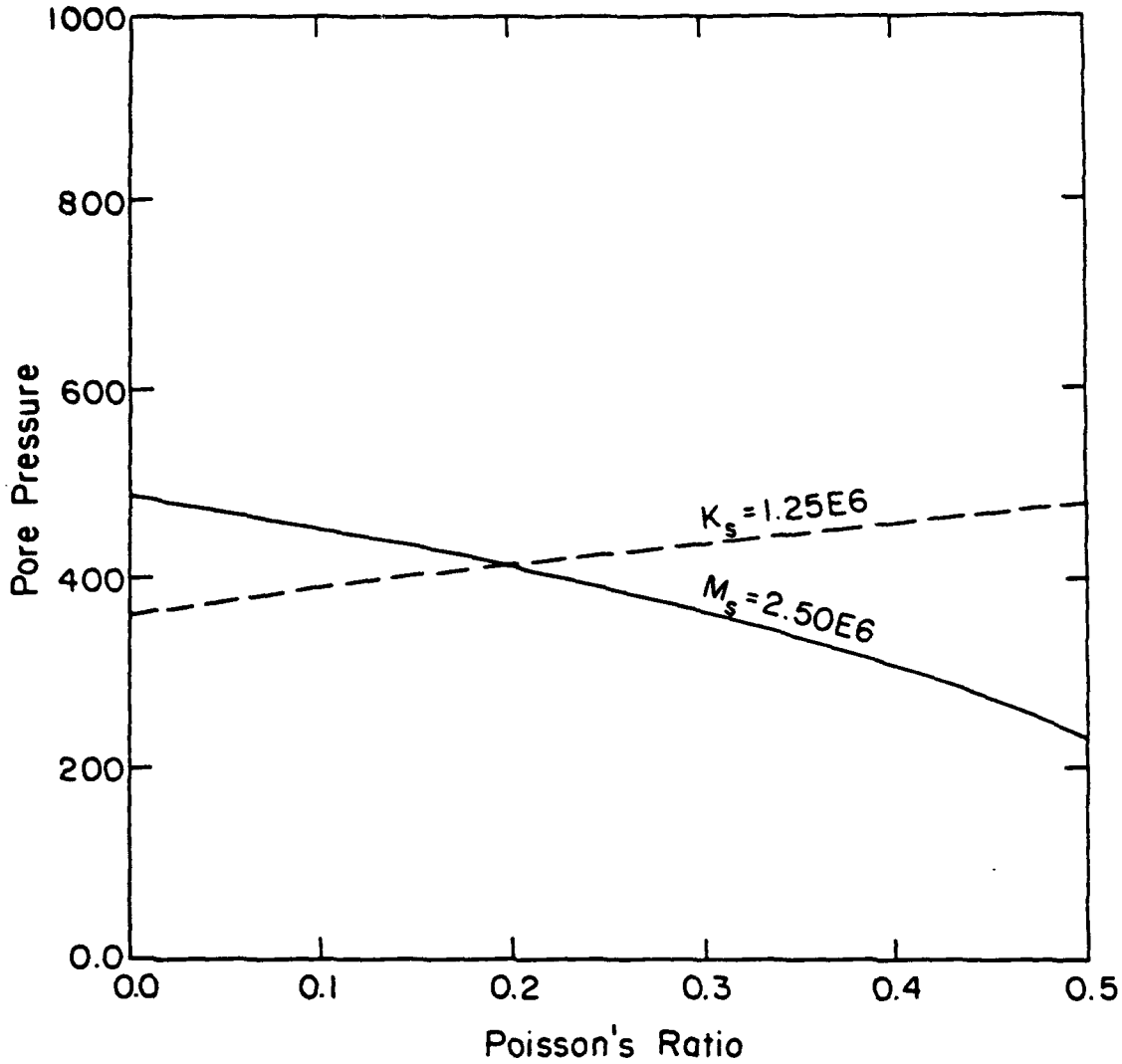

Figure 7.21. Initial pore pressure as a function of Poisson's ratio.

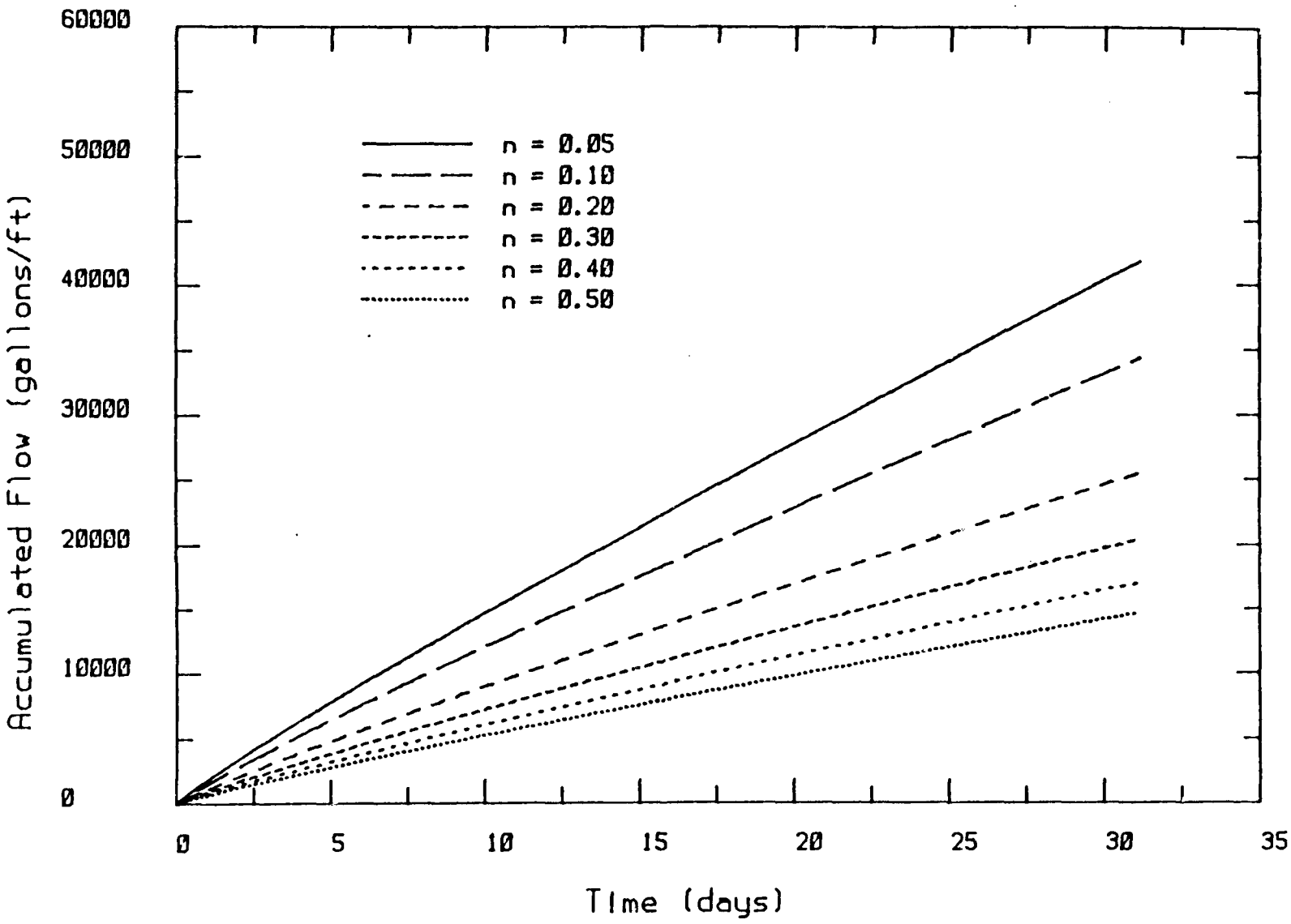

Figure 7.22. Influence of porosity on flow volume.

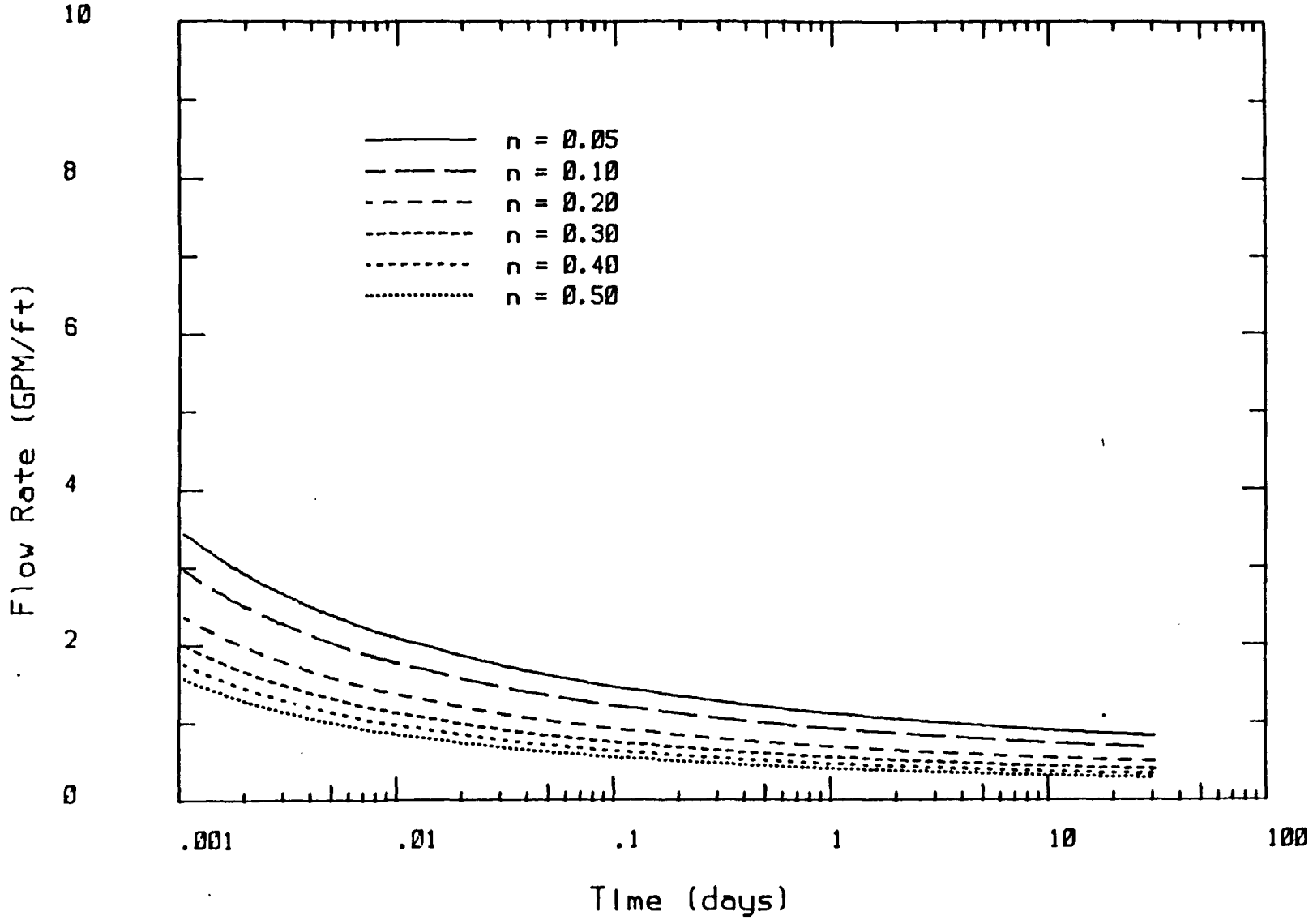

Figure 7.23. Influence of porosity on flow rate.

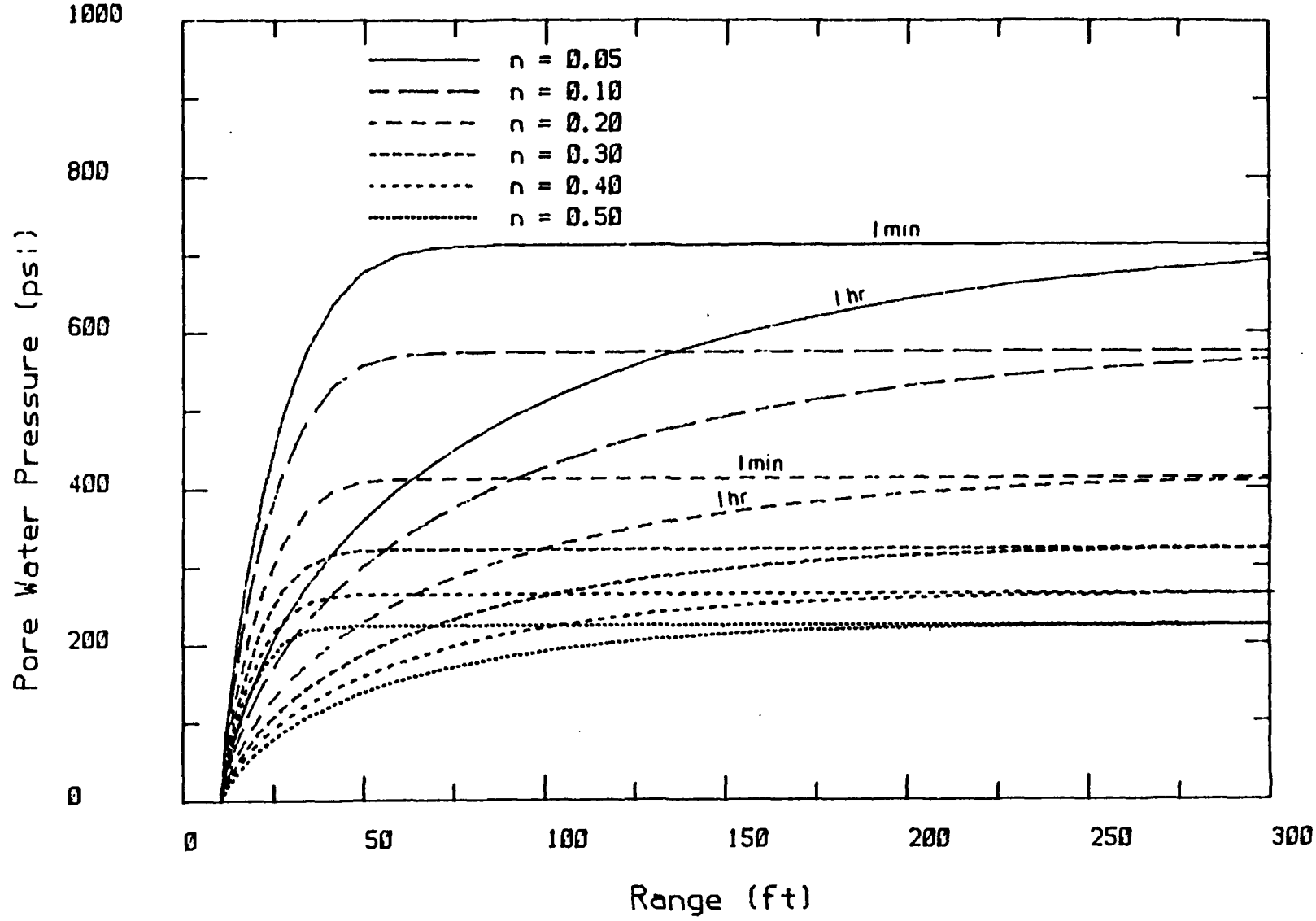

Figure 7.24a. Influence of porosity on pore pressure.

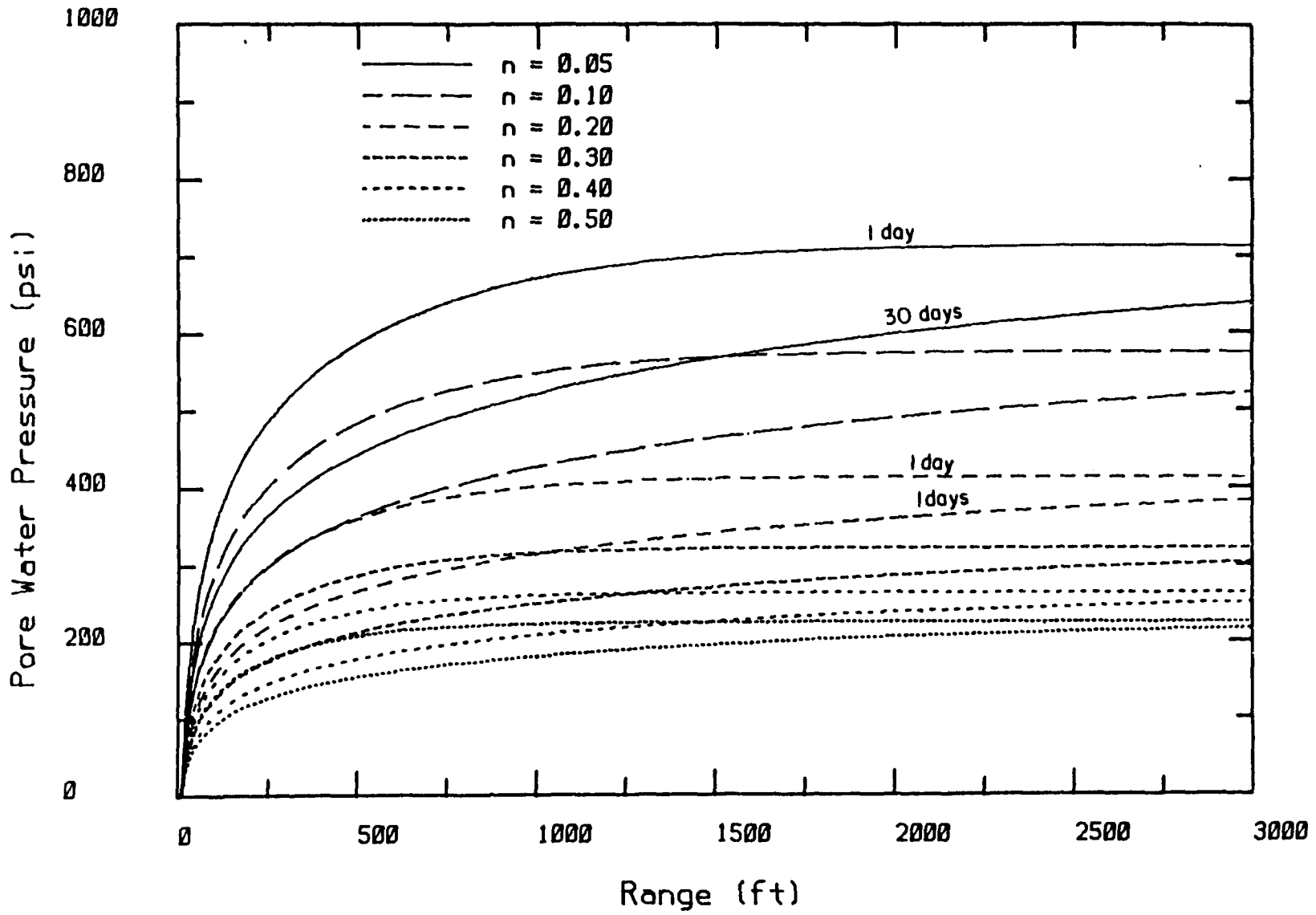
n = 0.05
n = 0.10
n = 0.20
n = 0.30
n = 0.40
n = 0.50
1 day
30 days
1 day
1days
1000
800
600
400
200
0
Pore Water Pressure (psi)
0
500
1000
1500
2000
2500
3000
Range (ft)

Figure 7.24b.

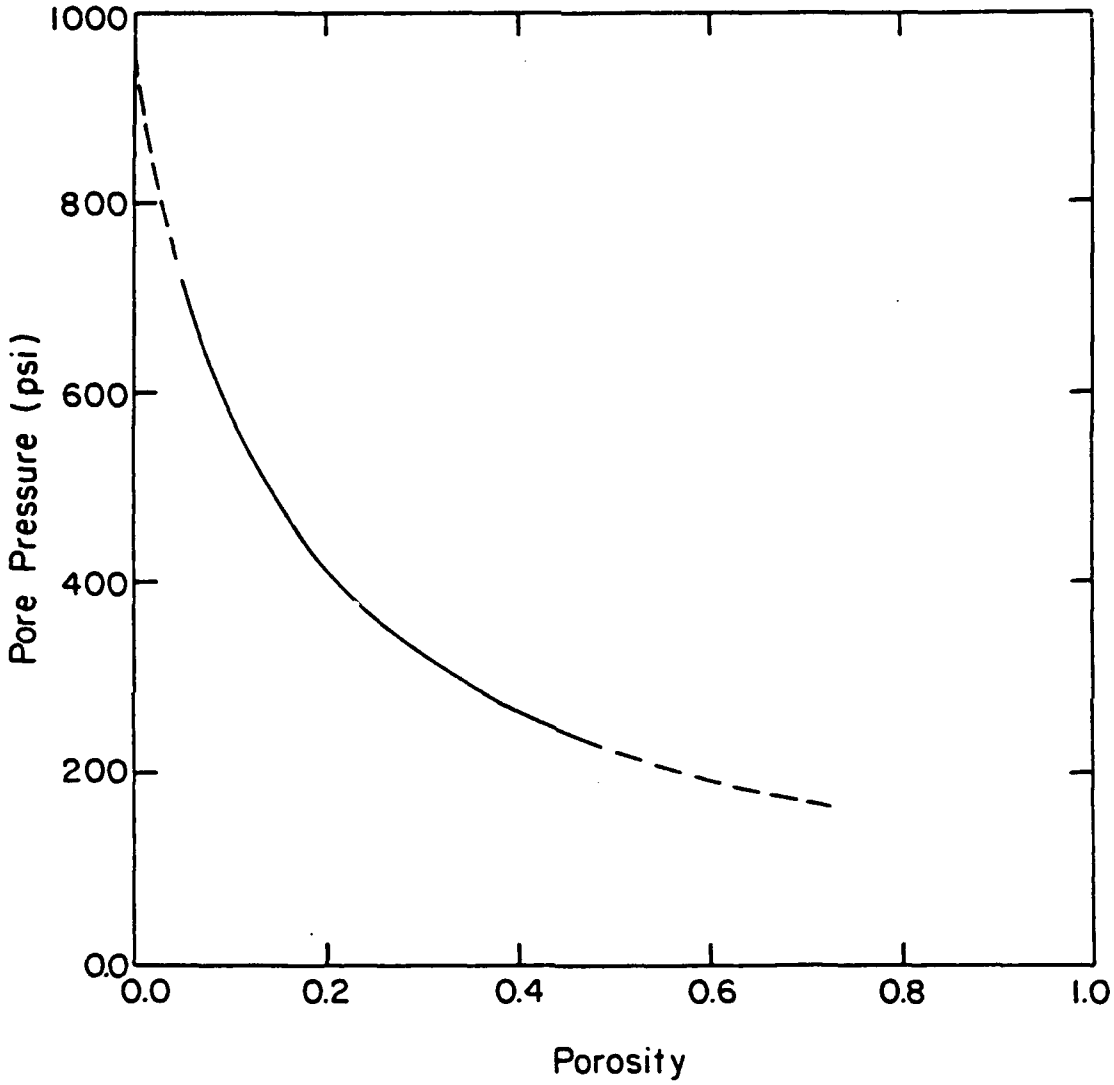

Figure 7.25. Initial pore pressure as a function of porosity.

SECTION 8

ONETON NUMERICAL SIMULATION

INTRODUCTION

Calculations in Section 7 indicated that flow of interstitial pore water due to blast induced residual stresses in the permeable rocks of Generic Mountain C poses a serious potential threat to deep based systems. However, in the much less permeable tuffs of Rainier mesa, flow of interstitial pore water has only been a minor problem. Pore water flow in the Rainier Mesa tuff has only been well documented on one event, the ONETON HE experiment, the data from which is summarized in Section 4. In order to give credibility to the Generic Mountain C calculations, the CONSL axisymmetric code was used to calculate the flow of water on the ONETON event. If the ONETON results could be replicated using measured residual stresses and actual tuff properties, it was felt that the trends toward very high flows in the Generic Mountain C calculations become much more credible. The results of the ONETON calculations are presented in this section.

PROBLEM CHARACTERIZATION AND RESULTS

Since the CONSL code is only a one dimensional axisymmetric code, some simplifying assumptions with regard to the problem geometry and residual stress loading had to be made. Plan and section views of the idealized problem geometry are

shown in Figure 8.1. The drift into which the ONETON instrumentation cables were strung, pictured in Figure 4.6, was approximated as a vertical right circular cylinder. The 16 ft diameter and 8 ft height approximated the actual dimensions of the drift. The center of the drift was at a range of 63 ft from the working point, which placed the closest face at the actual range of 55 ft.

A symmetric total residual stress of 630 psi was applied to the remote grid boundary. This approximated the residual stress at the 63 ft range of the drift centroid. The 630 psi residual stress loading was obtained from a linear fit to, and extrapolation of, the HE residual stress data presented in Figure 4.8. This data fit is shown in Figure 8.2. In the actual case the loading would be considerably more complex, with stresses on the working point side being considerably in excess of those assumed here and with stresses on the far side of the drift being considerably less.

The ONETON calculational parameters and material properties used in the CONSL calculation are listed in Table 8.1. A calculational grid containing 60 elements extended to a range of 200 ft from the tunnel wall. The 630 psi total stress was applied to this impermeable remote boundary. The material properties of the tuff were typical zeolitized tuff properties extracted from a report by Blouin and Kim (1983). The permeability was iteratively varied until the pore water flow matched the measured ONETON flows reported by Smith (1983). Flow per unit area was computed for a circular section of drift and was then multiplied by the total area of the idealized cylindrical drift to give the total accumulated flow. The permeability of 2.8×10^{-8} in/s, which gave the best match to the ONETON flow data, was near the upper end of the range of the

tuff permeabilities reported by Thordarson (1965) and shown in Figure 7.3.

The calculated cumulative flow and pore pressure dissipation profiles for the ONETON event are shown in Figures 8.3 and 8.4 respectively. The flows reported by Smith are superimposed on the calculation. The first flow measurement is somewhat low because some drying out of the pore water near the drift walls probably occurred prior to the detonation. This was not modeled in the calculation. No additional flow measurements were obtained following the second measurement 10 days after the event.

Even though rather crude simplifying assumptions had to be made in order to calculate the ONETON flow using the CONSL one dimensional code, the calculated flows were a good match to the actual flows. The fact that this agreement was achieved using material properties that are within the best estimates of the tuff properties and applied loads which were obtained from test data is strong validation of the calculational procedure. We believe this agreement supports Smith's hypothesis that ONETON pore water flow was caused by the residual stress field forcing the pore water from the voids. The agreement between the calculations and the field data gives real credibility to the conclusion that residual stress induced flow is a serious potential problem for deep based sites in permeable rocks such those of Generic Mountain C.

Table 8.1. ONETON calculational parameters and material properties.

Tunnel Radius	8. ft
Radius of Remote Boundary	208. ft
Number of Elements	60
Mesh Growth Factor	0.25
Applied Total Stress	630 psi
Permeable Tunnel Boundary	
Impermeable Remote Boundary	
Skeleton Constrained Modulus	1.07×10^{6} psi
Skeleton Poisson's Ratio	0.36
Porosity	0.34
Permeability	2.8×10^{-8} in/s
Bulk Modulus of Pore Water	0.29×10^{6} psi
Bulk Modulus of Solid Grains	$5. \times 10^{6}$ psi

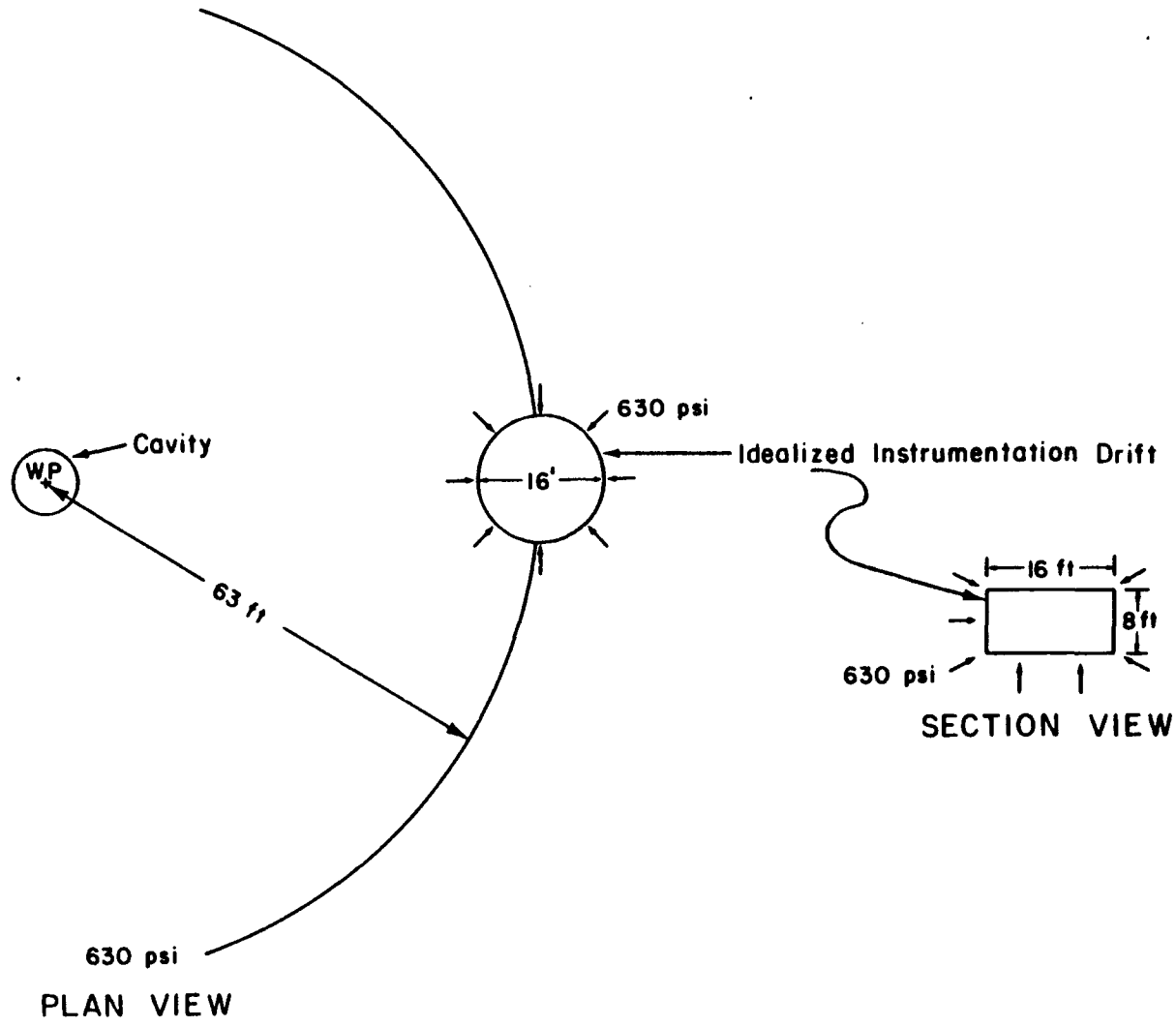

Figure 8.1. Schematic views of idealized ONETON layout.

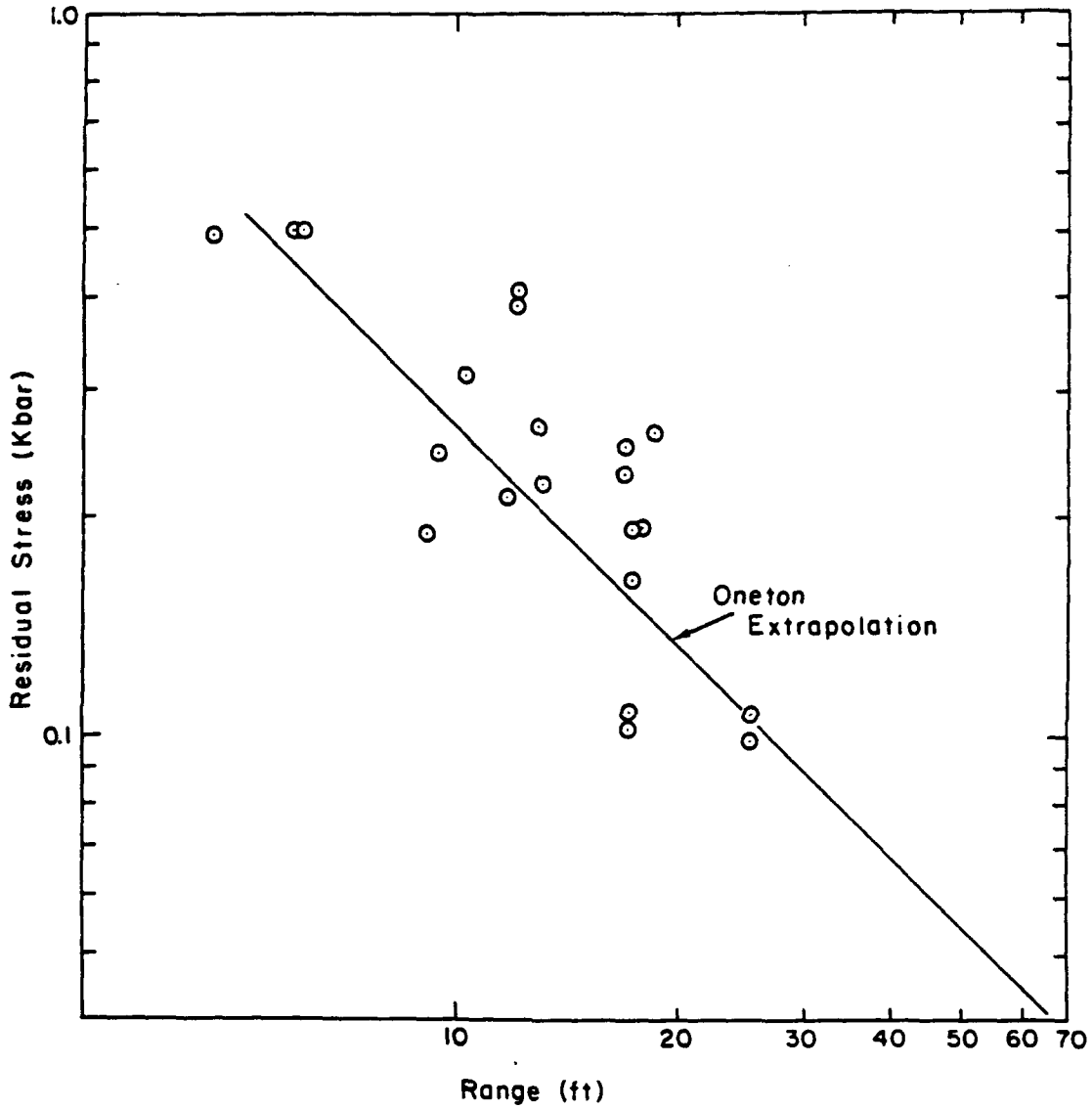

Figure 8.2. Fit to HE residual stress data.

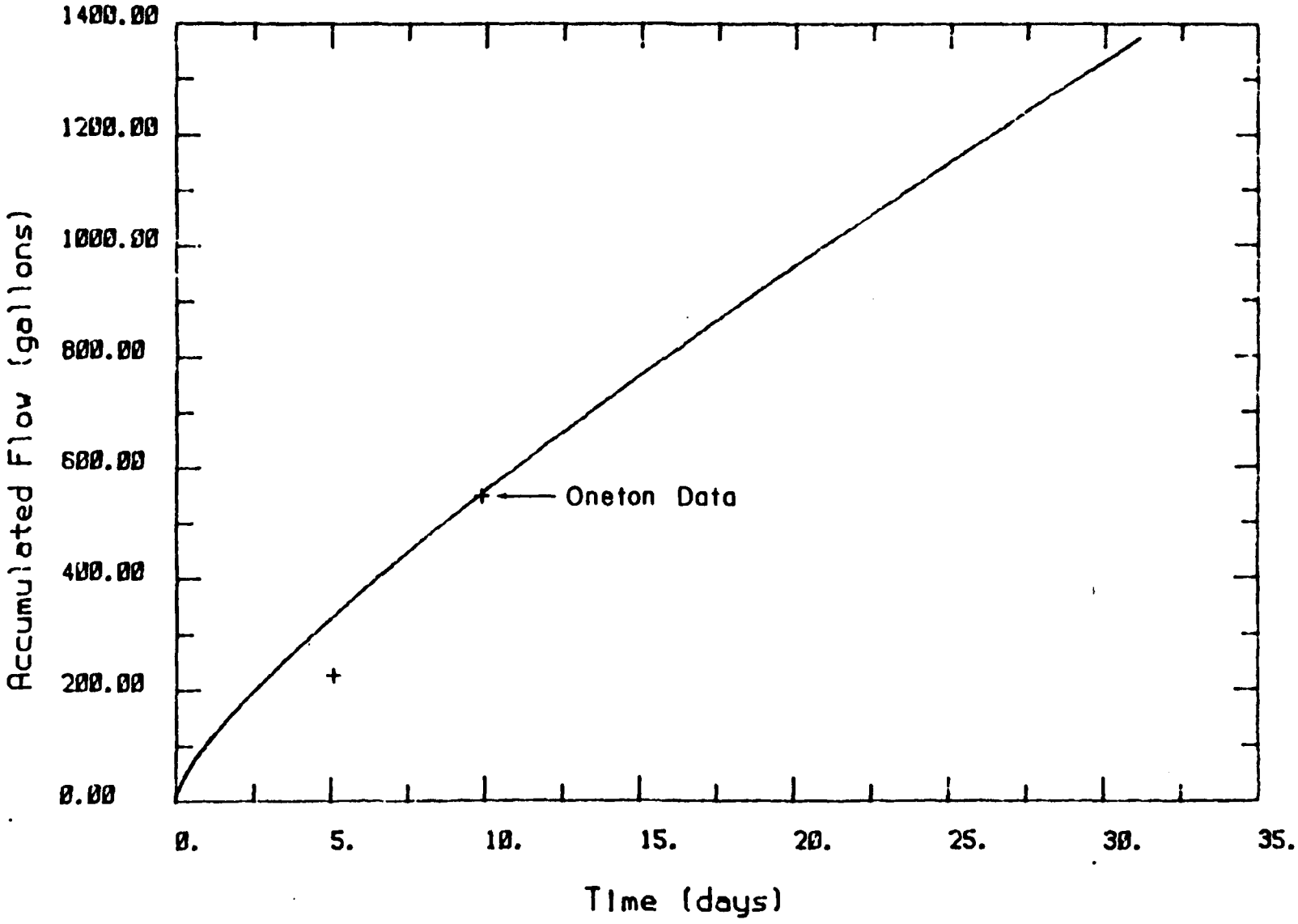

Figure 8.3. Calculated ONETON flow using permeability of 2.8 x 10^{-8} in/s.

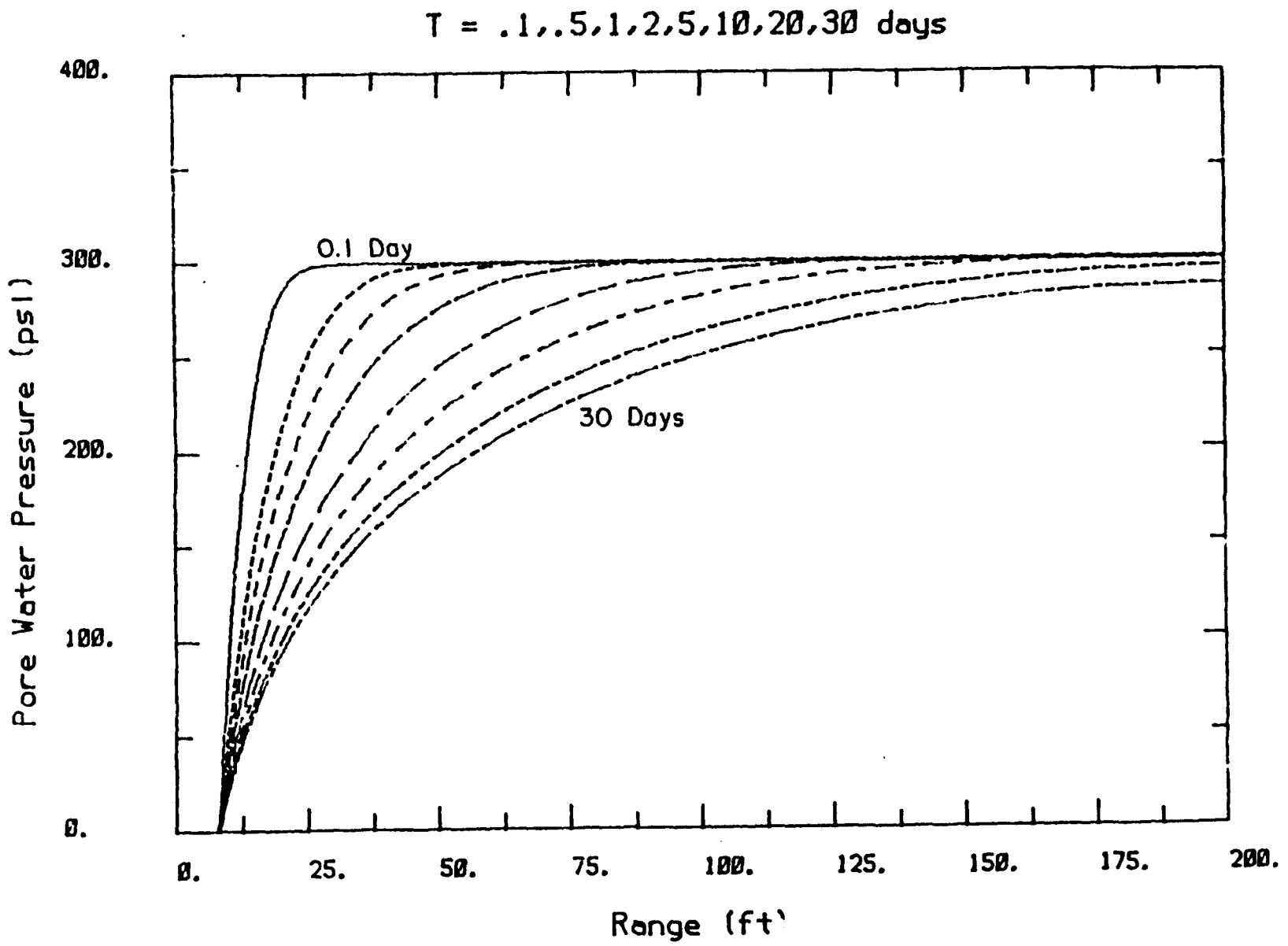

Figure 8.4. Calculated ONETON pore pressure dissipation profiles.

REFERENCES

Blouin, S. E., "Some Aspects of Relative Displacements Produced by Nuclear Detonations," Draft report to DNA, Higgins, Auld and Associates, Inc., July 1980.

Blouin, S. E., and Kim, K. J., "Use of Frozen Backfill as a Combination Egress/Heat Sink System for Deep Basing," Draft Report to Bureau of Mines, Applied Research Associates, Inc., October 1983.

Blouin, S. E., and Kim, K. J., "Undrained Compressibility of Saturated Soil," Draft Report to Defense Nuclear Agency, Applied Research Associates, Inc., February 1984.

Bowers, W. E., "Outline of the Geology of the U12i and U12i.01 Tunnels and Lithology of the U12i.01 drill hole, Nevada Test Site: TEI-842, U.S. Geological Survey, 1963.

Clebsch, A., "Ground Water in the Oak Spring Formation and Hydrologic Effects of Underground Nuclear Explosions at the Nevada Test Site," TEI-759, U.S. Geological Survey, 1960.

Diment, W. H., et al., "Geologic Effects of the Rainier Underground Nuclear Explosion," Trace Elements Investigation Report 355, U.S. Geological Survey, January 1959.

Ege, J. R., Carroll, R. D., Magner, J. E., and D. R. Cunningham, "U.S. Geological Survey Investigations in the U12n.03 Drift, Rainier Mesa, Area 12, Nevada Test Site," Open File Report 80-1074, U.S. Dept. of the Interior Geological Survey, 1980.

Ellis, W. L., and Kibler, J. D., "Explosion Induced Stress Changes Estimated from Vibrating-Wire Stressmeter Measurements Near the MIGHTY EPIC Event, Nevada Test Site," USGS-OFR-83-642, U. S. Geological Survey, 1983.

Emerick, W. L. and Houser, F. N., "Interim Geological Investigations in the U12b.08 tunnel, Nevada Test Site, Nye County, Nevada," TEI-814, U.S. Geological Survey, 1962.

Essoglou, M. E., and Rogich, D. G., "A Simplified Method for Predicting Free-Field Radial Displacements and Strains," NVO-1163-43, Roland F. Beers, Inc., May 1965.

Hoover, D. L., "Possible Water Inflow in U12t.03 Tunnel," Memorandum to Paul P. Orkild, U.S. Geological Survey, August 1974.

Hoover, D. L., "Water Production in the U12t Tunnel Drill Holes," Memorandum to J. Lacomb, U.S. Geological Survey, January 1975.

Keller, G. V., "Physical Properties of the Oak Spring Formation, Nevada," Paper 400-B, U.S. Geological Survey, P. B396-B400, 1960.

Kim, K. J., "Finite Element Analysis of Nonlinear Consolidation," Ph.D. thesis, University of Illinois at Urbana-Champaign, 1982.

Kim, K. J. and Blouin, S. E., "Response of Saturated Porous Nonlinear Materials to Dynamic Loadings," Draft report to Air Force Office of Scientific Research, Applied Research Associates, Inc., May 1984.

Lambe, T. W. and Whitman, R. V., "Soil Mechanics," John Wiley and Sons, Inc., 1969.

Patch, D., personal communication, Pacifica Technology, August, 1984.

Rimer, N. and Friedman, M., "Residual Stress and Coupling from Nuclear Shots in a Cavity," SSS-R-78-3596, Systems, Science and Software, April 1978.

Short, S. A., and Kennedy, R. P., "MIGHTY EPIC/DIABLO HAWK BLOCK MOTION PROGRAM, Volume II-Block Motion Prediction," DNA 6230F-2, Engineering Decision Analysis Company, Inc., December 1982.

Smith, C. W., "Residual Stress Fields - Results from High Explosive Field Tests," Proceedings of 2nd Symposium on Containment of Underground Nuclear Explosions, CONF-830882, August 1983.

Smith, C. W., personal communication, Sandia National Laboratory, 1984.

Thordarson, W. "Perched Ground Water in Zeolitized-Bedded Tuff, Rainier Mesa and Vicinity, Nevada Test Site, Nevada," TEI-862, U.S. Department of the Interior Geological Survey, September, 1965.

Topi, J. E., Lindsey, P. D., and Hokens, D. E., "ICBM Deep Basing Construction Planning Study - Geology Report," Corps of Engineers, Omaha District, July 1984.

Townsend, D. R., "Interim Geologic Report," Memorandum to D. L. Hoover, U. S. Geological Survey, October 1976.

Townsend, D. R., "Probable Cause of Postshot Water Within the MIGHTY EPIC LOS pipe," Memorandum to D. L. Hoover, U. S. Geological Survey, January, 1977.

Townsend, D. R., personal communication, Fenix and Scisson, Inc., July 1984.

Winograd, I. J. and Thordarson, W., "Hydrogeologic and Hydrochemical Framework, South-Central Great Basin, Nevada-California, with Special Reference to the Nevada Test Site," Geologic Survey Professional Paper 712-C, U.S. Government Printing Office, 1965.

Wood, A. B., "A Textbook of Sound," G. Bell and Sons, 1930.

APPENDIX A

UNDRAINED ISOTROPIC COMPRESSION OF SATURATED POROUS MEDIA IN PLANE STRAIN

INTRODUCTION

Relationships between effective stresses, total stresses and pore pressure during undrained isotropic and constrained (uniaxial strain) loadings of saturated porous elastic materials were derived by Blouin and Kim (1984). These relationships are fundamental to the development of sophisticated multiphase computer codes used to model the behavior of saturated soil and rock. Three coupling relationships between the material skeleton and pore water were postulated. The first, termed the decoupled model, is the simplest and generally the least accurate of the three. In the decoupled model the compressibility of the material skeleton and that of the pore water are assumed to act in parallel, but completely independent of one another. That is, the material skeleton is compressed solely by the intergranular or effective stresses and the mixture of pore water and solid grains is compressed solely by the pore pressure. The volume compression of each phase is equal to, but independent of, the compression of the other phase.

In the second more sophisticated model, termed the partially coupled model, the compressibility of the skeleton is linked to that of the pore water in that the pore water pressure compresses the solid grains comprising the skeleton. This

results in a contraction of the skeleton in addition to the skeleton volume reduction caused by the effective stresses.

The third and most sophisticated model, termed the fully coupled model, utilizes the features of the partially coupled model, but also further links the skeleton and pore water response by taking into account the compression of the solid grains by the effective stresses in the soil skeleton. This compression is in addition to the volume change due to the compression of the solid grains and pore water by the pore pressure. The latter is a feature of the solid grain/pore water mixture compressibility of all three models.

The isotropic and uniaxial loading conditions treated by Blouin and Kim (1984) are not applicable to many problems including plane strain loading conditions. Plane strain conditions are often used in the analysis of long structures and loadings such as those around tunnels and footings where there is assumed to be no strain in the axial direction. Also, two dimensional computer codes often approximate three dimensional problems using plane strain loading conditions. Because of the plane strain restriction, the results from these calculations may differ significantly from those expected in the actual problems of interest. In this Appendix, relationships between stresses, pore pressures and volume strains are derived for undrained isotropic loading conditions in plane strain. Sets of equations for each of the three coupling models are presented along with comparisons to the corresponding equations for pure isotropic loadings. These equations were used to check pore pressures and effective stresses under the initial loading conditions in all the CONSL calculations.

DECOUPLED MODEL

The assumed plane strain loading conditions and notation are shown in Figure A.1. An element of saturated porous material is loaded in plane strain by a symmetric stress denoted by σ_r. Since strain in the axial direction is restricted to zero, a resultant total stress in the axial direction, σ_a, develops which satisfies the zero strain restriction. Each of the total stresses is composed of an intergranular or effective stress component, denoted by σ_r' and σ_a', and a pore pressure u. The pore pressure is hydrostatic and acts in all directions within the element. According to the effective stress law the total stresses equal the effective stresses plus the pore pressure according to

$$\sigma_r = \sigma_r' + u \qquad \text{(A-1)}$$

$$\sigma_a = \sigma_a' + u \qquad \text{(A-2)}$$

The total volume change in the element due to application of the total stresses can be expressed individually in terms of both the pore pressure u and the effective stresses, σ_r' and σ_a'. An increase in pore pressure compresses both the water within the granular matrix and the grains themselves. The strain in the water due to application of the pore pressure u is given by

$$\frac{\Delta V_w}{V_w} = \frac{u}{K_w} \qquad \text{(A-3)}$$

where V_w is the total volume of pore water in the element and K_w is the bulk modulus of the pore water. The total volume of water in an element of material having a porosity n and a volume V is

$$V_w = nV \qquad \text{(A-4)}$$

The volume change of the water within the element is obtained by combining A-3 and A-4

$$\Delta V_w = n \frac{u}{K_w} V \qquad \text{(A-5)}$$

Assuming a unit initial volume, volume strain and volume change are both expressed as

$$\Delta V_w = n \frac{u}{K_w} \qquad \text{(A-6)}$$

The pore pressure subjects each of the grains making up the material skeleton to a hydrostatic pressure, u. Each grain undergoes a volume strain of

$$\frac{\Delta V_{sg}}{V_{sg}} = \frac{u}{K_g} \qquad \text{(A-7)}$$

where ΔV_{sg} and V_{sg} are the volume change and total volume of a single grain and K_g is the bulk modulus of the solid grains. The total volume change of the grains within the element is given by

$$\Delta V_g = (1 - n) \frac{u}{K_g} V \qquad \text{(A-8)}$$

The quantity $(1 - n)V$ is the initial volume of the solid grains. For a unit initial element volume, the volume change and volume strain in the solid grains are given by

$$\Delta V_g = (1 - n) \frac{u}{K_g} \qquad \text{(A-9)}$$

The total volume change in the saturated element, ΔV, must equal the sum of the volume changes in the pore water and the solid grains according to

$$\Delta V = \Delta V_w + \Delta V_g \qquad \text{(A-10)}$$

The total volume change in an element of unit volume can also be expressed as

$$\Delta V = \frac{u}{K_m} \qquad \text{(A-11)}$$

where K_m is the bulk modulus of the solid grain/pore water

mixture. Substitution of Equations A-6, A-9 and A-11 into Equation A-10 gives

$$\frac{u}{K_m} = n \frac{u}{K_w} + (1 - n) \frac{u}{K_g} \qquad \text{(A-12)}$$

Solution of A-12 gives the bulk modulus of the solid grain/pore water mixture as

$$K_m = \frac{K_g K_w}{K_w + n(K_g - K_w)} \qquad \text{(A-13)}$$

which is equivalent to the derivation by Wood (1930) for a soil water suspension.

The volume change can also be expressed in terms of the effective stresses acting on the material skeleton as depicted in Figure A-2. The plane strain loading conditions are simulated by summing a true isotropic loading under the effective stress σ_r' and a uniaxial tensile stress loading of $\sigma_a' - \sigma_r'$ in the axial direction. The volume change from the isotropic loading on an element of unit volume is given by

$$\Delta V_i = \frac{\sigma_r'}{K_s} \qquad \text{(A-14)}$$

where K_s is the bulk modulus of the skeleton. K_s is the modulus that would be obtained from a fully drained hydrostatic loading of the material element. The volume change of the skeleton under the axial loading is given by

$$\Delta V_a = \frac{\sigma_a' - \sigma_r'}{E_s} - 2u \frac{\sigma_a' - \sigma_r'}{E_s} \qquad \text{(A-15)}$$

where E_s is the Young's modulus of the skeleton and μ is Poisson's ratio of the skeleton. The first term in A-15 is the axial extension of the element and the second term represents the sum of the two components of radial and circumferential contraction. Equation A-15 is simplified as

$$\Delta V_a = \frac{\sigma_a - \sigma_r'}{E_s} (1 - 2\mu) \qquad \text{(A-16)}$$

Using the elastic relationship between bulk modulus and Young's modulus of

$$E_s = 3K_s (1 - 2\mu) \qquad \text{(A-17)}$$

Equation A-17 can be expressed in terms of bulk modulus as

$$\Delta V_a = \frac{\sigma_a' - \sigma_r'}{3K_s} \qquad \text{(A-18)}$$

The total volume change of the skeleton is the sum of the volume changes due to the isotropic and axial loadings given by Equations A-14 and A-18.

$$\Delta V = \Delta V_i + \Delta V_a \qquad \text{(A-19)}$$

or

$$\Delta V = \frac{2\sigma_r' + \sigma_a'}{3K_s} \qquad \text{(A-20)}$$

The mean effective stress σ_m', is given by

$$\sigma_m' = \frac{2\sigma_r' + \sigma_a'}{3} \qquad \text{(A-21)}$$

and Equation A-20 in terms of the mean effective stress is simply

$$\Delta V = \frac{\sigma_m'}{K_s} \qquad \text{(A-22)}$$

Since the axial strain is zero, the volume change is the sum of the two strain components under the isotropic stress components, σ_r';

$$\Delta V = 2\varepsilon_r \qquad \text{(A-23)}$$

where ε_r is the resultant strain from each of the components of effective stress, σ_r'.

The final compatibility equation is obtained from the zero strain requirement in the axial direction. From Figure A.2, the axial skeleton strain, ε_a, equals one third of the volume

strain under the isotropic loading plus the axial strain from the axial loading;

$$\varepsilon_a = \frac{\sigma_r'}{3K_s} + \frac{\sigma_a' - \sigma_r'}{E_s} \qquad \text{(A-24)}$$

With axial strain set to zero and E_s expressed in terms of K_s according to Equation A-17, the axial effective stress is obtained as a function of the radial effective stress according to

$$\sigma_a' = 2\mu\sigma_r' \qquad \text{(A-25)}$$

The five equations representing the decoupled compatibility conditions for the isotropic loading in plane strain are summarized below.

$$\sigma_r = \sigma_r' + u \qquad \text{(A-1)}$$

$$\sigma_a = \sigma_a' + u \qquad \text{(A-2)}$$

$$\Delta V = \frac{u}{K_m} \qquad \text{(A-11)}$$

$$\Delta V = \frac{2\sigma_r' + \sigma_a'}{3K_s} \qquad \text{(A-20)}$$

$$\sigma_a' = 2\mu\sigma_r' \qquad \text{(A-25)}$$

These are solved for the unknown effective stresses σ_r' and σ_a', the pore pressure, u, volume change ΔV, and the total axial stress, σ_a, all as a function of the prescribed isotropic total stress, σ_r.

Equating equations A-11 and A-20 gives

$$u = K_m \frac{2\sigma_r' + \sigma_a'}{3K_s} \qquad \text{(A-26)}$$

Substitution of Equation A-25 into A-26 yields

$$u = \frac{2K_m}{3K_s} \sigma_r' \ (1 + \mu) \qquad \text{(A-27)}$$

and substitution of A-27 into A-1 gives the isotropic effective stress as

$$\boxed{\sigma_r' = \sigma_r \frac{3K_s}{2K_m(1 + \mu) + 3K_s}} \qquad \text{(A-28)}$$

Further substitution of Equation A-28 into Equation A-1 gives the pore pressure as

$$u = \sigma_r \frac{2K_m(1 + \mu)}{2K_m(1 + \mu) + 3K_s} \qquad \text{(A-29)}$$

The effective axial stress is obtained by substitution of Equation A-28 into A-25 giving

$$\sigma_a' = \sigma_r \frac{6\mu K_s}{2K_m(1 + \mu) + 3K_s} \qquad \text{(A-30)}$$

The total axial stress is found by substitution of A-29 and A-30 into Equation A-2;

$$\sigma_a = \sigma_r \frac{2K_m(1 + \mu) + 6\mu K_s}{2K_m(1 + \mu) + 3K_s} \qquad \text{(A-31)}$$

Finally, the volume change is obtained by plugging Equation A-29 into A-11;

$$\Delta V = \sigma_r \frac{2(1 + \mu)}{2K_m(1 + \mu) + 3K_s} \qquad \text{(A-32)}$$

Note that according to Equation A-23, the isotropic strain, ε_r, equals half the volume change, ΔV.

Equations A-28 through A-32 are included in the summary of Table A-1. They are also compared to the equations for true isotropic loading derived from the relationships given by Blouin and Kim (1984).

PARTIALLY COUPLED MODEL

In the partially coupled model an additional component of skeleton volume strain due to compression of the solid grains by the pore pressure is considered. This alters the last two compatibility equations (Equations A-20 and A-25) used in the derivation of the decoupled models. In addition to the skeleton volume change due to the mean effective stress given by Equation A-20, there is a volume change component due to the pore pressure applied to the solid grains. This component, ΔV_u, is given by

$$\Delta V_u = \frac{u}{K_g} \qquad \text{(A-33)}$$

for an original skeleton volume of unity. Thus, the skeleton component of volume strain equals the volume strain in the individual solid grains given by Equation A-7. In other words, the total skeleton volume contracts in proportion to the contraction in the individual grains. Assuming an isotropic skeleton, the total volume strain due to the pore pressure loading will equal the volume strain in the individual grains.

The overall volume strain is obtained by combining Equation A-33 with A-20;

$$\Delta V = \frac{2\sigma_r' + \sigma_a'}{3K_s} + \frac{u}{K_g} \qquad \text{(A-34)}$$

The compatibility equation for zero axial strain is also affected by the skeleton strain due to the pore pressure. A third term must be added to Equation A-24 to account for the additional axial strain in the skeleton from the pore pressure. Since the volume strain is isotropic, the axial strain will equal one third of the volume strain from Equation A-33, or

$$\varepsilon_a = \frac{u}{3K_g} \qquad \text{(A-35)}$$

Combining equations A-35 and A-24 gives

$$\varepsilon_a = \frac{\sigma_r'}{3K_s} + \frac{\sigma_a' - \sigma_r'}{E_s} + \frac{u}{3K_g} \qquad \text{(A-36)}$$

Setting the axial strain to zero and putting E_s in terms of K_s according to Equation A-17 gives the effective axial stress as

$$\sigma_a' = 2\mu\sigma_r' - u\,\frac{K_s(1 - 2\mu)}{K_g} \qquad \text{(A-37)}$$

Thus, the five compatibility equations for the partially coupled isotropic loading in plane strain are

$$\sigma_r = \sigma_r' + u \qquad \text{(A-1)}$$

$$\sigma_a = \sigma_a' + u \qquad \text{(A-2)}$$

$$\Delta V = \frac{u}{K_m} \qquad \text{(A-11)}$$

$$\Delta V = \frac{2\sigma_r' + \sigma_a'}{3K_s} + \frac{u}{K_g} \qquad \text{(A-34)}$$

$$\sigma_a' = 2\mu\sigma_r' - u\,\frac{K_s(1 - 2\mu)}{K_g} \qquad \text{(A-37)}$$

Solution of the compatibility conditions proceeds as follows. Equating A-34 and A-11 gives the pore pressure as a function of the effective stresses

$$u = (2\sigma_r' + \sigma_a')\,\frac{K_m K_g}{3K_s(K_g - K_m)} \qquad \text{(A-38)}$$

Substitution of Equation A-37 into A-38 gives the pore pressure in terms of the radial effective stress as

$$u = 2\sigma_r' \frac{(1 + \mu)K_m K_g}{3K_s K_g - 2(1 + \mu)K_m K_s} \qquad \text{(A-39)}$$

Finally, substitution of Equation A-39 into A-1 yields the isotropic effective stress in terms of the applied total stress as

$$\boxed{\sigma_r' = \sigma_r \frac{3K_s K_g - 2(1 + \mu)K_m K_s}{2(1 + \mu)K_m(K_g - K_s) + 3K_s K_g}} \qquad \text{(A-40)}$$

Further substitution of Equation A-40 into Equation A-1 gives the pore pressure as a function of the applied total stress

$$\boxed{u = \sigma_r \frac{2(1 + \mu)\ K_m K_g}{2(1 + \mu)K_m(K_g - K_s) + 3K_s K_g}} \qquad \text{(A-41)}$$

The effective axial stress is obtained by substituting Equations A-40 and A-41 into compatibility condition A-37 giving

$$\boxed{\sigma_a' = \sigma_r \frac{6\mu K_s K_g - 2(1 + \mu)K_m K_s}{2(1 + \mu)K_m(K_g - K_s) + 3K_s K_g}} \qquad \text{(A-42)}$$

Total axial stress is obtained by substitution of A-41 and A-42 into Equation A-2,

$$\sigma_a = \sigma_r \frac{6\mu K_s K_g + 2(1 + \mu)K_m(K_g - K_s)}{2(1 + \mu)K_m(K_g - K_s) + 3K_s K_g} \qquad \text{(A-43)}$$

Lastly, the volume change per unit volume is found by substitution of A-41 into A-11,

$$\Delta V = \sigma_r \frac{2(1 + \mu)K_g}{2(1 + \mu)K_m(K_g - K_s) + 3K_s K_g} \qquad \text{(A-44)}$$

Recall that from Equation A-23, the isotropic strain, ε_r, simply equals half the volume strain given by Equation A-44.

The stress, pore pressure and volume strain relationships from Equations A-40 through A-44 for the partially coupled model are summarized in Table A-1. They are compared to the Equations for a true isotropic loading derived using the partially coupled model by Blouin and Kim (1984).

FULLY COUPLED MODEL

The fully coupled model utilizes all the assumptions of the partially coupled model and in addition takes into account the volume change in the solid grains due to application of the effective stresses in the skeleton. Of the five compatibility equations listed in the previous subsection (Equations A-1, A-2, A-11, A-34 and A-37) only Equation A-11 is modified by this added compatibility condition. The other volume change equation, A-34, is not modified because the definition of the skeleton bulk

modulus, K_s, automatically takes account of the solid grain strains resulting from the effective stresses.

The effective stresses are defined in terms of the total cross sectional area of a given material element. Because only a portion of the cross sectional area is made up of solid grains, the actual stress in the solid grains, termed the intragranular stress, is higher than the effective stress. The intragranular stresses are obtained by dividing the effective stresses by (1 - n), the fraction of the total volume occupied by the solid grains. Thus, the intragranular isotropic stresses, σ_{ri}', and the intragranular axial stress, σ_{ai}', are given by,

$$\sigma_{ri}' = \frac{\sigma_r'}{1 - n} \tag{A-45}$$

and

$$\sigma_{ai}' = \frac{\sigma_a'}{1 - n}$$

The mean intragranular stress, σ_{mi}', is the average of the sum of the two components of isotropic stress and the axial stress, given by

$$\sigma_{mi}' = \frac{2\sigma_r' + \sigma_a'}{3(1 - n)} \tag{A-46}$$

The volume strain in a unit volume of saturated porous material due to the intragranular stress is obtained by dividing the mean stress by the bulk modulus of the solid grains and multiplying by the volume of the solid grains in the unit element, (1 - n).

Thus, the volume strain due to the intragranular stress, ΔV_i, is given by

$$\Delta V_i = \frac{2\sigma_r' + \sigma_a'}{3(1 - n)K_g} (1 - n) \qquad \text{(A-47)}$$

or simply

$$\Delta V_i = \frac{2\sigma_r' + \sigma_a'}{3K_g} \qquad \text{(A-48)}$$

The total volume change in the saturated unit element is obtained by combining the volume change due to the intragranular stress given by Equations A-48 with the volume change due to the pore pressure in the pore fluid and on the solid grains given by Equation A-11. The total volume change is thus given by

$$\Delta V = \frac{u}{K_m} + \frac{2\sigma_r' + \sigma_a'}{3K_g} \qquad \text{(A-49)}$$

The five compatibility equations for the fully coupled plane strain loading are given by

$$\sigma_r = \sigma_r' + u \qquad \text{(A-1)}$$

$$\sigma_a = \sigma_a' + u \qquad \text{(A-2)}$$

$$\Delta V = \frac{u}{K_m} + \frac{2\sigma_r' + \sigma_a'}{3K_g} \qquad \text{(A-49)}$$

$$\Delta V = \frac{2\sigma_r' + \sigma_a'}{3K_s} + \frac{u}{K_g} \qquad \text{(A-34)}$$

$$\sigma_a' = 2\mu\sigma_r' - u\,\frac{K_s(1 - 2\mu)}{K_g} \qquad \text{(A-37)}$$

Equating Equations A-49 and A-34 gives the pore pressure in terms of the effective stresses as

$$u = \frac{2\sigma_r' + \sigma_a'}{3}\,\frac{K_m(K_g - K_s)}{K_s(K_g - K_m)} \qquad \text{(A-50)}$$

For simplicity Equation A-50 is reexpressed as

$$u = \frac{2\sigma_r' + \sigma_a'}{3}\,R_k \qquad \text{(A-51)}$$

Where R_k is the modulus ratio given by

$$R_k = \frac{K_m(K_g - K_s)}{K_s(K_g - K_m)} \qquad \text{(A-52)}$$

Substitution of Equation A-37 into A-51 the effective isotropic stress, σ_r', as a function of the pore pressure,

$$\sigma_r' = u \frac{3K_g + (1 - 2\mu)K_s R_k}{2(1 + \mu)K_g R_k} \qquad \text{(A-53)}$$

Substitution of A-53 into Equation A-1 gives the pore pressure in terms of the applied total isotropic stress as

$$\boxed{u = \sigma_r \frac{2(1 + \mu)K_g R_k}{D_f}} \qquad \text{(A-54)}$$

where the denominator D_f is given by

$$D_f = R_k \left(2(1 + \mu)K_g + (1 - 2\mu)K_s \right) + 3K_g \qquad \text{(A-55)}$$

Substitution of Equation A-54 into A-53 gives the isotropic effective stress as

$$\boxed{\sigma_r' = \sigma_r \frac{3K_g + (1 - 2\mu)K_s R_k}{D_f}} \qquad \text{(A-56)}$$

The axial effective stress is obtained by substituting Equations A-54 and A-56 into A-39 to give

$$\boxed{\sigma_a' = \sigma_r \frac{6\mu K_g - 2(1 - 2\mu)K_s R_k}{D_f}} \qquad \text{(A-57)}$$

The total axial stress is obtained by substituting Equations A-54 and A-57 into A-2 to give

$$\sigma_a = \sigma_r \frac{2R_k \left((1 + \mu)K_g - (1 - 2\mu)K_s \right) + 6\mu K_g}{D_f} \qquad \text{(A-58)}$$

Finally, the volume strain in the unit element is found by substitution of Equations A-54, A-56 and A-57 into Equation A-34 giving

$$\Delta V = \sigma_r \frac{2(1 + \mu)(K_g + R_k K_s)}{K_s D_f} \qquad \text{(A-59)}$$

The fully coupled plane strain relationships between effective stresses, pore pressure, volume strain and the applied total isotropic stress are summarized in Table A-1. They are compared to corresponding relationships for a true isotropic loading derived from the report by Blouin and Kim (1984).

NUMERICAL EXAMPLE

A numerical example illustrating the differences between the various models of Table A-1 is listed in Table A-2. Material properties of a typical saturated sandstone having a porosity of 20% were assumed; these properties are listed in Table A-2. The axial symmetric loading in plane strain is compared to the isotropic loading for each of the three models. There are significant differences between the plane strain and isotropic loadings as well as significant differences between the various models.

For each model, the volume change computed for the isotropic loading is significantly (14.0% to 17.7%) higher than the volume change under the plane strain loading. The pore pressures developed under the isotropic loading are also correspondingly higher than those from the plane strain loading. The effective isotropic stresses, however, are about 10% to 14% less than the corresponding effective stresses in the plane strain loading.

There are also significant differences between the various models. For the plane strain loading, the volume change for the fully coupled model is 22.3% larger than that for the decoupled model and 8.2% larger than that for the partially coupled model. A similar trend, with even larger differences, holds for the isotropic loading. In general, the pore pressures computed using the partially coupled model are higher than those from the fully coupled model, while the pressures from the decoupled model are lower than those from the fully coupled model. The effective stresses from both the decoupled and partially coupled models are less than those from the fully coupled model, though the decoupled effective stresses are in closer agreement than are the partially coupled effective stresses.

Table A.1. Comparison of axisymmetric and isotropic loadings.

MODEL	AXIAL SYMMETRIC LOADING IN PLANE STRAIN	ISOTROPIC LOADING
DECOUPLED MODEL		
Pore Pressure	$u = \sigma_r \frac{2K_m(1+\mu)}{2K_m(1+\mu)+3K_s}$	$u = \sigma_r \frac{K_m}{K_m+K_s}$
Effective Stress	$\sigma_r' = \sigma_r \frac{3K_s}{2K_m(1+\mu)+3K_s}$	$\sigma_r' = \sigma_r \frac{K_s}{K_m+K_s}$
Total Axial Stress	$\sigma_a = \sigma_r \frac{2K_m(1+\mu)+6\mu K_s}{2K_m(1+\mu)+3K_s}$	
Effective Axial Stress	$\sigma_a' = \sigma_r \frac{6\mu K_s}{2K_m(1+\mu)+3K_s}$	
Volume Change	$\Delta V = 2\epsilon_r = \sigma_r \frac{2(1+\mu)}{2K_m(1+\mu)+3K_s}$	$\Delta V = \sigma_r \frac{1}{K_m+K_s}$
PARTIALLY COUPLED MODEL		
Pore Pressure	$u = \sigma_r \frac{2(1+\mu)K_mK_g}{2(1+\mu)K_m(K_g-K_s)+3K_sK_g}$	$u = \sigma_r \frac{K_mK_g}{K_mK_g+K_sK_g-K_mK_s}$
Effective Stress	$\sigma_r' = \sigma_r \frac{3K_sK_g-2(1+\mu)K_mK_s}{2(1+\mu)K_m(K_g-K_s)+3K_sK_g}$	$\sigma_r' = \sigma_r \frac{K_s(K_g-K_m)}{K_mK_g+K_sK_g-K_mK_s}$
Total Axial Stress	$\sigma_a = \sigma_r \frac{6\mu K_sK_g+2(1+\mu)K_m(K_g-K_s)}{2(1+\mu)K_m(K_g-K_s)+3K_sK_g}$	
Effective Axial Stress	$\sigma_a' = \sigma_r \frac{6\mu K_sK_g-2(1+\mu)K_mK_s}{2(1+\mu)K_m(K_g-K_s)+3K_sK_g}$	
Volume Change	$\Delta V = 2\epsilon_r = \sigma_r \frac{2(1+\mu)K_g}{2(1+\mu)K_m(K_g-K_s)+3K_sK_g}$	$\Delta V = \sigma_r \frac{K_g}{K_mK_g+K_sK_g-K_mK_s}$
FULLY COUPLED MODEL		
Pore Pressure	$u = \sigma_r \frac{2(1+\mu)K_gR_k}{D_f}$	$u = \sigma_r \frac{R_k}{1+R_k}$
Effective Stress	$\sigma_r' = \sigma_r \frac{3K_g+(1-2\mu)K_sR_k}{D_f}$	$\sigma_r' = \sigma_r \frac{1}{1+R_k}$
Total Axial Stress	$\sigma_a = \sigma_r \frac{2R_k\left((1+\mu)K_g-(1-2\mu)K_s\right)+6\mu K_g}{D_f}$	
Effective Axial Stress	$\sigma_a' = \sigma_r \frac{6\mu K_g-2(1-2\mu)K_sR_k}{D_f}$	
Volume Change	$\Delta V = 2\epsilon_r = \sigma_r \frac{2(1+\mu)(K_g+R_kK_s)}{K_sD_f}$	$\Delta V = \sigma_r \frac{K_gR_k+K_m}{K_mK_g(1+R_k)}$
	where $D_f = R_k\left(2(1+\mu)K_g+(1-2\mu)K_s\right)+3K_g$	
	$R_k = \frac{K_m(K_g-K_s)}{K_s(K_g-K_m)}$	

Table A.2. Numerical comparison between undrained axial symmetric (plane strain) and isotropic loadings.

Material:	Saturated Sandstone	
Properties:	Bulk Modulus of Water	K_w = 0.29 E6 psi
	Bulk Modulus of Solid Grains	K_g = 5 E6 psi
	Bulk Modulus of Skeleton	K_s = 1.5 E6 psi
	Porosity	n = 0.2
	Poisson's Ratio	μ = 0.2
	Mixture Modulus (Eq. A-13)	K_m = 1.177 E6 psi

MODEL	AXIAL SYMMETRIC LOADING IN PLANE STRAIN	ISOTROPIC LOADING
Decoupled Model		
Pore Pressure	$u = 0.386\ \sigma_r$	$u = 0.440\ \sigma_r$
Effective Stress	$\sigma_r' = 0.614\ \sigma_r$	$\sigma_r' = 0.560\ \sigma_r$
Total Axial Stress	$\sigma_a = 0.631\ \sigma_r$	
Effective Axial Stress	$\sigma_a' = 0.246\ \sigma_r$	
Volume Change	$\Delta V = 3.277\ E{-7}\ \sigma_r$	$\Delta V = 3.736\ E{-7}\ \sigma_r$
Partially Coupled Model		
Pore Pressure	$u = 0.436\ \sigma_r$	$u = 0.506\ \sigma_r$
Effective Stress	$\sigma_r' = 0.564\ \sigma_r$	$\sigma_r' = 0.494\ \sigma_r$
Total Axial Stress	$\sigma_a = 0.583\ \sigma_r$	
Effective Axial Stress	$\sigma_a' = 0.147\ \sigma_r$	
Volume Change	$\Delta V = 3.705\ E{-7}\ \sigma_r$	$\Delta V = 4.303\ E{-7}\ \sigma_r$
Fully Coupled Model		
Pore Pressure	$u = 0.355\ \sigma_r$	$u = 0.418\ \sigma_r$
Effective Stress	$\sigma_r' = 0.645\ \sigma_r$	$\sigma_r' = 0.582\ \sigma_r$
Total Axial Stress	$\sigma_a = 0.549\ \sigma_r$	
Effective Axial Stress	$\sigma_a' = 0.194\ \sigma_r$	
Volume Change	$\Delta V = 4.007\ E{-7}\ \sigma_r$	$\Delta V = 4.716\ E{-7}\ \sigma_r$

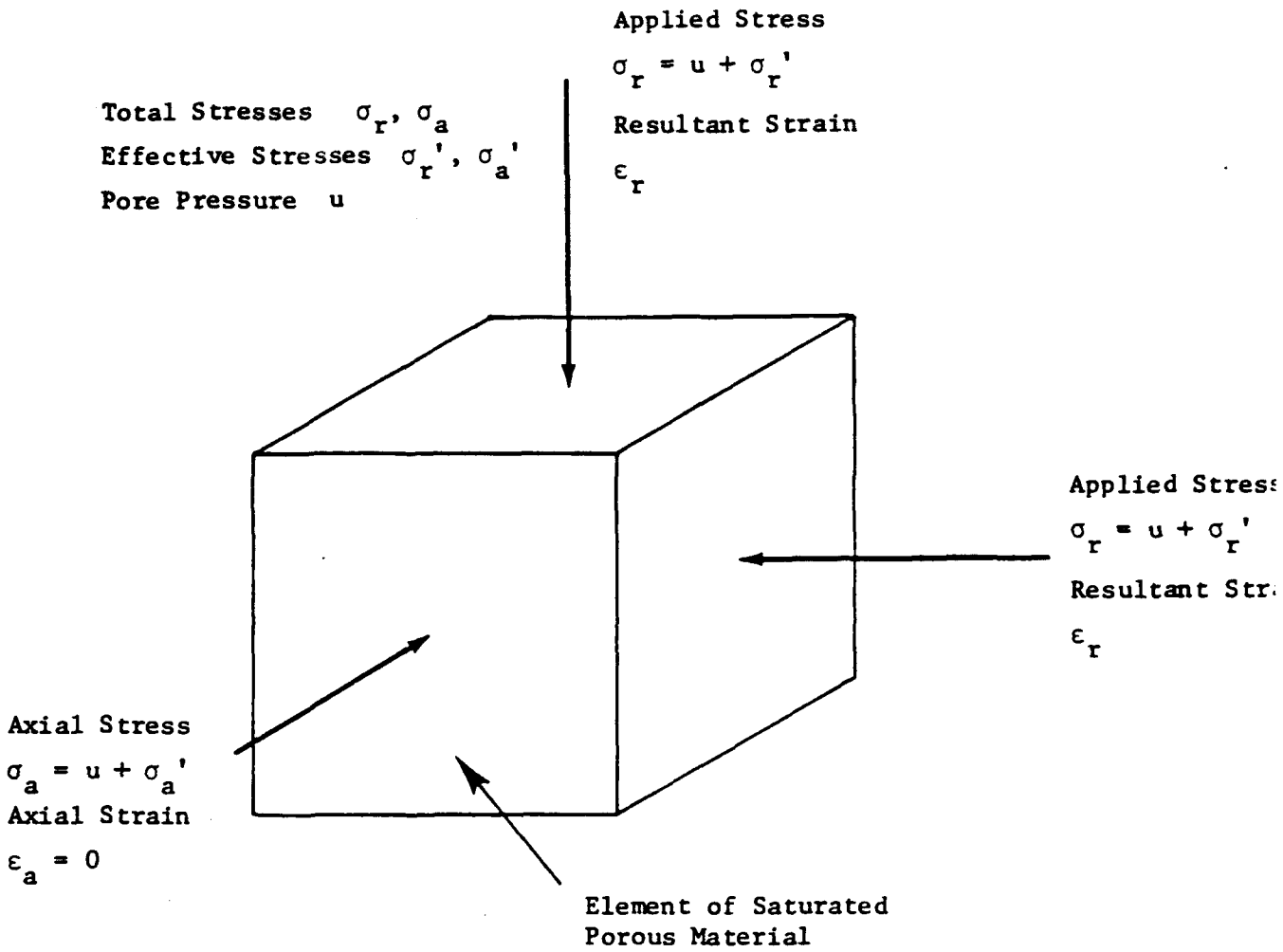

Figure A.1. Definition of symmetric plane strain loading and strains.

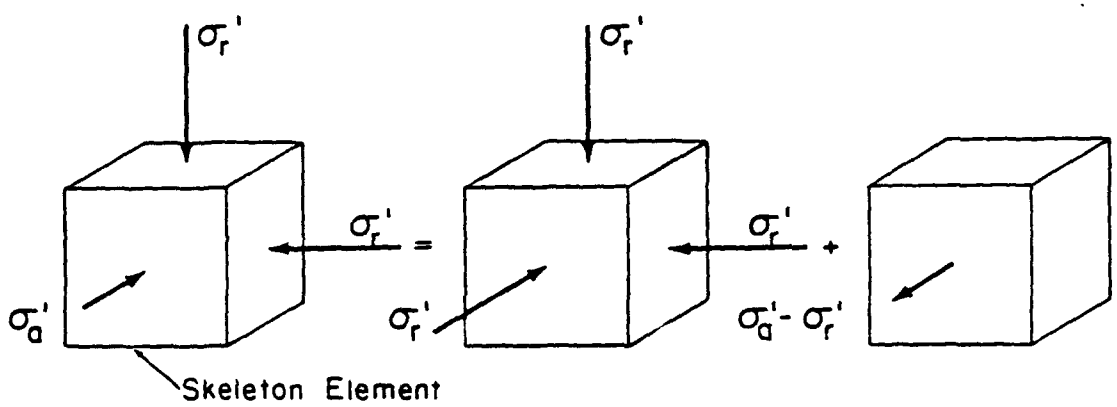

Figure A.2. Equivalent effective stress skeleton loading conditions.

APPENDIX B

FLOW DUE TO VOLUME CHANGE IN SATURATED POROUS MATERIALS

A fundamental aspect of flow in saturated porous media is the relationship between pore water flow and volume change. This relationship is the basis for accurate flow calculations in multi-phase computational models and is used in CONSL as one method of calculating flow (see Section 5). For porous fully saturated materials which obey the effective stress law, i.e. the total stress on an element of material equals the pressure in the pore water throughout the material plus the intergranular or effective stress in the material skeleton, the flow of pore water into or out of any element of material due to an increase or decrease of stress and/or pore water pressure in the element equals

— the change in volume of the element, as measured by change in skeleton volume,

— plus pore water flow into or out of the element due to compression or expansion of the pore water and solid grains within the element.

The total flow of pore water, ΔV_f, is given by

$$\Delta V_f = \Delta V_s - \Delta V_g - \Delta V_w \qquad \text{(B-1)}$$

where ΔV_s is the change in skeleton volume of the element,

ΔV_g is the change in volume of the solid grains in the element due to an increase or decrease in pore pressure, and ΔV_w is the change in volume of the pore water in the element due to an increase or decrease in pore pressure. The signs indicate that flow due to change in skeleton volume is opposite to flow due to volume changes within the skeleton. For example, an increase in total stress results in compression of the skeleton with flow of pore water out of the matrix, while the corresponding increase in pore pressure within the element compresses the pore water and solid grains requiring a component of flow into the element.

Pore water flow, as computed from Equation B-1, will depend on the coupling relationships assumed in the material models. Blouin and Kim (1984) describe three coupling relationships between the material skeleton and pore water having varying degrees of accuracy depending on the level of sophistication desired. These are also described in Appendix A. Flow equations for each of the three models are developed in the following sections.

DECOUPLED MODEL

The decoupled model is the simplest, though least accurate, of the three models.

The decoupled model includes compressible pore water and solid grains, but the skeleton and pore water are assumed to act in parallel, with no coupling between the two. The skeleton volume strain is given by

$$\Delta V_{sd} = \frac{\Delta \sigma_m'}{K_s} \qquad \text{(B-2)}$$

where $\Delta\sigma_m'$ is the change in mean effective stress and K_s the bulk modulus of the material skeleton. The change in volume of the solid grains within the soil element due to compression by the pore water is given by

$$\Delta V_{gd} = (1 - n) \frac{\Delta u}{K_g} \qquad \text{(B-3)}$$

where n is the porosity, Δu the change in pore pressure, and K_g the bulk modulus of the solid grains. The term (1 - n) represents the volume fraction of solid grains. The change in volume of the pore water in the element due to the change in pore water pressure is given by

$$\Delta V_w = n \frac{\Delta u}{K_w} \qquad \text{(B-4)}$$

where K_w is the bulk modulus of the pore water. Substitution of Equations B-2, B-3 and B-4 into Equation B-1 gives the flow volume for the decoupled model as

$$\Delta V_{fd} = \frac{\Delta\sigma_m'}{K_s} - \Delta u \left(\frac{1}{K_g} + \frac{n}{K_g} - \frac{n}{K_w} \right) \qquad \text{(B-5)}$$

This can be rewritten as

$$\Delta V_{fd} = \frac{\Delta\sigma_m'}{K_s} - \Delta u \left(\frac{K_w + nK_w - nK_g}{K_g K_w} \right) \qquad \text{(B-6)}$$

The term in the parentheses is the compressibility of the solid grain/pore water mixture derived in Appendix A and given in Equation A-13. Equation B-6 can be reexpressed as

$$\boxed{\Delta V_{fd} = \frac{\Delta\sigma_m'}{K_s} - \frac{\Delta u}{K_m}} \qquad \text{(B-7)}$$

where K_m is the bulk modulus of the solid grain/pore water mixture with

$$K_m = \frac{K_g K_w}{K_w + n(K_g - K_w)} \qquad \text{(B-8)}$$

Thus, the flow in the decoupled model simply equals the change in volume of the material skeleton due to a change in effective stress, less the change in volume of the solid grain/pore water mixture due to a change in pore pressure.

PARTIALLY COUPLED MODEL

In the partially coupled model the change in skeleton volume due to compression of the grains by the pore water pressure is included in addition to the relationships in the decoupled formulation. The only change in the volume change compatibility equations in the partially coupled model is in the skeleton volume change equation. In the partially coupled model the skeleton volume is a function of both the applied effective

stress and the compression of the grains making up the skeleton by the applied pore pressure. The partially coupled skeleton volume strain is given by

$$\Delta V_{sp} = \frac{\Delta\sigma_m'}{K_s} + \frac{\Delta u}{K_g} \qquad \text{(B-9)}$$

The last term in Equation B-9 is the skeleton volume strain due to the applied pore pressure increment Δu. As explained in Appendix A, the total skeleton volume strain equals the volume strain in the individual particles (assuming isotropic material). The remaining volume change compatibility equations are identical to those of the decoupled model given in Equations B-3 and B-4. Note that the volume change of the solid grains given by B-3 is included in the decoupled model, even though this influence is not included in the volume change of the skeleton.

Substitution of Equations B-3, B-4 and B-9 into Equation B-1 gives the partially coupled flow volume as

$$\boxed{\Delta V_{fp} = \frac{\Delta\sigma_m'}{K_s} - n\Delta u\left(\frac{1}{K_w} - \frac{1}{K_g}\right)} \qquad \text{(B-10)}$$

In terms of the bulk modulus of the solid grain/pore water mixture, Equation B-10 is expressed as

$$\boxed{\Delta V_{fp} = \Delta V_{sp} - \frac{\Delta u}{K_m}} \qquad \text{(B-11)}$$

where the change in skeleton volume ΔV_{sp} is given by Equation B-9.

FULLY COUPLED MODEL

The fully coupled model described by Blouin and Kim (1984) and in Appendix A is the most sophisticated of the three multi-phase models. The fully coupled model incorporates all the features of the partially coupled model plus it accounts for volume change in the solid grains resulting from the effective stresses in the grains. This additional compatibility condition alters only Equation B-3 of the partially coupled compatibility equations. In the fully coupled model the volume of water flowing in or out of the porous element due to compression of the solid grains is made up of a component due to compression by the pore pressure and a component due to compression of the solid grains by the effective stresses in the skeleton. The overall volume change in the grains is given by

$$\Delta V_{gf} = (1 - n) \frac{\Delta u}{K_g} + \frac{\Delta \sigma_m'}{K_g} \qquad \text{(B-12)}$$

where the first term is the volume compression by the pore water as given in Equation B-3. The last term is the compressive volume strain in the solid grains due to the mean effective stress increment $\Delta \sigma_m'$. The actual stress in the grains is termed the intragranular stress. This is higher than the intergranular or effective stress because the effective stress is an average value. In actuality the total effective loading is carried only in the grain structure, not in the intervening pore spaces. Thus, the mean intragranular stress is given by

$$\sigma_{mi}' = \frac{\sigma_m'}{1 - n} \qquad \text{(B-13)}$$

The volume change due to the intragranular stress, ΔV_{gi} is

$$\Delta V_{gi} = \frac{\Delta\sigma_m'{}_i}{K_g}(1 - n) \qquad \text{(B-14)}$$

Substitution of Equation B-13 into B-14 gives

$$\Delta V_{gi} = \frac{\Delta\sigma_m'}{K_g} \qquad \text{(B-15)}$$

which is the last term of Equation B-12. Note that the intragranular stress does not enter into the volume change relationships for the soil skeleton given by Equation B-9. This is because the intragranular stresses are automatically accounted for in the skeleton bulk modulus, K_s.

Combining the fully coupled volume change components from Equations B-4, B-9 and B-12 into Equation B-1 gives the volume of water flowing into or out of a fully coupled element as

$$\boxed{\Delta V_{ff} = \Delta\sigma_m'\left(\frac{1}{K_s} - \frac{1}{K_g}\right) - n\Delta u\left(\frac{1}{K_w} - \frac{1}{K_g}\right)} \qquad \text{(B-16)}$$

In terms of the mixture bulk modulus, K_m, flow is given as

$$\boxed{\Delta V_{ff} = \Delta V_{sf} - \frac{\Delta u}{K_m} - \frac{\Delta \sigma_m'}{K_g}} \qquad \text{(B-17)}$$

where ΔV_{sf} is the volume change of the skeleton given by Equation B-9.

In numerical two phase calculations output is often in terms of volume change and pore pressure. Flow volume can be calculated directly from these parameters by a slight modification of Equation B-17. Manipulation of Equation B-9 gives the change in mean effective stress as

$$\Delta \sigma_m' = \Delta V_s K_s - \Delta u \frac{K_s}{K_g} \qquad \text{(B-18)}$$

Substitution of Equation B-18 into B-17 yields

$$\boxed{\Delta V_{ff} = \Delta V_{sf} \left(1 - \frac{K_s}{K_g}\right) + \Delta u \left(\frac{K_s}{K_g^2} - \frac{1}{K_m}\right)} \qquad \text{(B-19)}$$

CHECK CASE - UNDRAINED LOADING

As a check on the fully coupled flow Equation B-17, the undrained effective stress and pore pressure relationships derived for the fully coupled model in Appendix A can be used to certify that there is no flow into or out of a saturated element during an undrained loading. Substitution of Equation B-9 into Equation B-17 gives

$$\Delta V_{ff} = \Delta\sigma_m' \left(\frac{1}{K_s} - \frac{1}{K_g}\right) - u\left(\frac{1}{K_m} - \frac{1}{K_g}\right) \qquad \text{(B-20)}$$

For the plane strain hydrostatic loading condition, the mean effective stress is given by

$$\sigma_m' - \frac{2\sigma_r' + \sigma_a'}{3} \qquad \text{(B-21)}$$

where σ_r' is the radial hydrostatic effective stress and σ_a' is the axial effective stress in which direction no strain is allowed. Substitution of the effective stresses from Equations A-56 and A-57 into B-21 gives the mean effective stress

$$\sigma_m' = \sigma_r \frac{2K_g(1 + \mu)}{D_f} \qquad \text{(B-22)}$$

in terms of the total stress, σ_r. Poisson's ratio for the soil skeleton is μ and the denominator D_f is given by

$$D_f = R_k \left(2(1 + \mu)\ K_g + (1 - 2\mu)\ K_s \right) + 3K_g \qquad \text{(B-23)}$$

Substitution of the mean effective stress from Equation B-22 and the pore pressure from Equation A-54 into B-20 gives

$$\Delta V_{ff} = \frac{2\sigma_r(1 + \mu)}{D_f} \left(R_k \left(1 - \frac{K_g}{K_m}\right) + \frac{K_g}{K_s} - 1 \right) \qquad \text{(B-24)}$$

where the ratio, R_k, is

$$R_k = \frac{K_m(K_g - K_s)}{K_s(K_g - K_m)} \qquad \text{(B-25)}$$

Substitution of Equation B-25 into B-24 and further manipulation gives

$$\Delta V_{ff} = \frac{0}{K_m K_s (K_g - K_m)} \qquad \text{(B-26)}$$

Thus, the computed flow is zero, which satisfies undrained loading compatibility conditions.

NOTE OF CAUTION

In applying the flow equations based on the skeleton volume change, care must be taken not to violate the compatibility conditions implicit in the flow equations. In making finite element calculations, it is possible to specify boundary and pore pressure conditions which violate the compatibility conditions used to derive the equations. This occurs when boundary conditions are set so that the deformations of the individual elements of the calculational grid do not correspond to the deformation of the material skeleton. For instance, if grid boundaries are fixed and pore pressure is applied to the saturated porous material, the material skeleton will contract due to grain compression by the pore water. Since the grid boundaries are fixed, however, the element boundaries will not contract with the material skeleton. In this case large errors in any flow calculations across the grid boundaries are introduced.

APPENDIX C

FINITE ELEMENT FORMULATION OF CONSOLIDATION

It is a common assumption in soil mechanics that the solid grains and pore water making up a saturated soil are incompressible. This assumption is a reasonably good approximation for soils whose skeleton moduli are much lower than those of the solid grains and pore water. For most rocks, however, the skeleton modulus is on the same order, or significantly greater than that of the pore water. Thus, the compressibility of the solid grains and pore water plays an important role in the consolidation process of saturated porous rocks.

Presented in this appendix is the finite element formulation of consolidation including the compressibility of solid grains and pore water.

NOTATION

Note that positive signs have been used for elongation and tension. A comma denotes differentiation with respect to the subsequent indices and the superposed dot denotes time rate.

$\{u\}$: solid phase displacement
$\{U\}$: fluid phase displacement
$\{\sigma\}$: total stress
$\{\sigma'\}$: effective stress
π : fluid pressure

$\{\varepsilon\}$: solid phase strain

ε_v : solid phase volumetric strain

ε_F : fluid phase volumetric strain

$\{\bar{u}\}_e$: nodal solid phase displacement vector at the element degrees of freedom

$\{\bar{\pi}\}_e$: nodal fluid pressure at the element degrees of freedom

$\{\bar{u}\}$: nodal solid phase displacement vector at the structural degrees of freedom

$\{\bar{\pi}\}$: nodal fluid pressure at structural degrees of freedom

$\{T\}$: applied boundary traction

$\hat{Q}$: specified boundary flux

$\{b\}$: body force vector

$[k]$: permeability matrix

$[D^{ep}]$: elasto plastic stress-strain matrix

$\{1\}$: unit vector $\{1\}^T = \langle 1\ 1\ 1\ 0\ 0\ 0 \rangle$

n : porosity

C_w : fluid compressibility

C_s : compressibility of solid grains

α : compressibility of soil-water mixture

ρ : bulk mass density of mixture

ρ_f : fluid mass density

δ_{ij} : Kronecker's delta

$[K_T]$: tangent stiffness matrix

$[C]$: coupling matrix between solid skeleton and pore fluid

$[E]$: matrix of compressibility of pore fluid

$[H]$: dissipation resistance matrix

$\{F\}$: vector of nodal forces

$\{R\}$: internal resisting force vector

$\{\bar{Q}\}$: equivalent flow vector

FIELD EQUATIONS

Principle of effective stress

$$\sigma_{ij} = \sigma_{ij}' + \sigma_{ij}\,\pi \qquad \text{(C-1)}$$

Constitutive law for solid skeleton

$$\{d\sigma'\} = [D^{ep}]\left(\{d\varepsilon\} - \frac{C_s}{3}\{1\}\,d\pi\right) \qquad \text{(C-2)}$$

Continuity Equations

The coupled continuity equation of flow has been derived by Kim, 1982a and is given by

$$(1 - n)d\varepsilon_v + nd\varepsilon_F - \alpha d\pi - (1 - n)C_s'\,dp' = 0 \qquad \text{(C-3)}$$

where

$$\alpha = nC_w + (1 - n)\,C_s \qquad \text{(C-4)}$$

and

$$C_s' = \frac{C_s}{(1 - n)} \qquad \text{(C-5)}$$

Substitution of Equation C-5 into Equation C-3 gives

$$n(d\varepsilon_F - d\varepsilon_v) = \alpha d\pi + C_s dp' - d\varepsilon_v \qquad \text{(C-6)}$$

Generalized Darcy's Flow Law

Neglecting inertia term,

$$\dot{w}_i = n(\dot{U}_i - \dot{u}_i) = k_{ij}\ (\pi_{,j} + \rho_f b_j) \qquad \text{(C-7)}$$

FINITE ELEMENT DISCRETIZATION

Two global equilibrium equations are derived, first in terms of field variables and then discretized using the nodal variables.

The total stresses are in equilibrium with the applied boundary tractions. Taking the solid skeleton movement as the virtual displacement, the internal and external virtual work must be equal. At certain time t,

$$\delta W_I = \int_V \{\delta\varepsilon\}^T \{\sigma\}\ dv \qquad \text{(C-8)}$$

$$\delta W_E = \int_V \{\delta u\}^T \rho\ \{b\}\ dv + \int_S \{\delta u\}^T \{T\}\ ds \qquad \text{(C-9)}$$

and

$$\delta W_I = \delta W_E \tag{C-10}$$

The internal fluid movements relative to the solid skeleton are compatible with the specified boundary flux. Taking the fluid pressure field at a certain time t as the complementary virtual stresses, the internal and external complementary virtual work must be equal.

$$\delta W_I{}^* = \left[\int_V \delta\pi \; n\left(\dot{\varepsilon}_F - \dot{\varepsilon}_v\right) dv \right.$$

$$\left. + \int_V \{\delta\pi_{,i}\}^T \; n\left(\{\dot{U}\} - \{\dot{u}\}\right) dv\right] dt \tag{C-11}$$

Substituting Equations C-6, and C-7 into Equation C-11

$$\delta W_I{}^* = \left[\int_V \delta\pi\left(\alpha\dot{\pi} + C_s\dot{p}' - \dot{\varepsilon}_v\right)dv \right.$$

$$\left. + \int_V \{\delta\pi_{,i}\}^T \; [k] \left(\{\pi_{,i}\} + \rho_f \; \{b\}\right) dv\right] \; dt \tag{C-12}$$

$$\delta W_E{}^* = \left[\int_s \delta\pi\hat{Q} \; ds\right] dt \tag{C-13}$$

and

$$\delta W_I{}^* = \delta W_E{}^* \tag{C-14}$$

Discretization of field variables into nodal variables

$$\begin{aligned} \{u\} &= [N]\ \{\bar{u}\}_e \\ \{\varepsilon\} &= [B]\ \{\bar{u}\}_e \\ \pi &= \langle G \rangle\ \{\bar{\pi}\}_e \\ \{\pi_{,i}\} &= [A]\ \{\bar{\pi}\}_e \end{aligned} \tag{C-15}$$

FINITE INCREMENTAL RELATIONSHIPS

Stress vector at time step n can be expressed as

$$\{\sigma_n\} = \{\sigma'_{n-1}\} + \{\Delta\sigma_n{}'\} + \{1\}\ \pi_n \tag{C-16}$$

Substitution of Equation C-2 into Equation C-16 yields

$$\{\sigma_n\} = [D^{ep}]\ \{\Delta\varepsilon_n\} + \left(\{1\} - \frac{C_s}{3}\ [D^{ep}]\ \{1\}\right)\pi_n$$

$$+ \{\sigma'_{n-1}\} + \frac{C_s}{3}\ [D^{ep}]\ \{1\}\pi_{n-1} \qquad \text{(C-17)}$$

Substituting Equation C-17 into Equation C-8 and replacing the field variables in Equations C-8 and C-9 by the nodal values using Equation C-15 gives,

$$\delta W_I = \{\delta u\}^T \left[\left(\Sigma\int_V [B]^T\ [D^{ep}]\ [B]\ dv\right)\{\Delta\bar{u}_n\}\right.$$

$$+ \left(\Sigma\int_V [B]^T\left(\{1\} - \frac{C_s}{3}\ [D^{ep}]\ \{1\}\right) < G >\ dv\right)\{\bar{\pi}_n\}$$

$$\left. + \Sigma\int_V [B]^T\ \{\sigma'_{n-1}\}\ dv + \Sigma\int_V \frac{C_s}{3}\ [B]^T\ [D^{ep}]\ \{1\}\ \pi_{n-1}\ dv\right] \text{(C-18)}$$

$$\delta W_E = \{\delta u\}^T \left[\Sigma\int_V [N]^T \rho\ \{b\}\ dv + \Sigma\int_S [N]^T\ \{T\}\ ds\right] \qquad \text{(C-19)}$$

From Equation C-10

$$\boxed{[K_T]\ \{\Delta\bar{U}_n\} + [C]\ \{\bar{\pi}_n\} = \{F_n\} - \{R_{n-1}\}} \qquad \text{(C-20)}$$

where

$$[K_T] = \Sigma \int_v [B]^T \; [D^{ep}] \; [B] \; dv$$

$$[C] = \Sigma \int_v [B]^T \left(\{1\} - \frac{C_s}{3} [D^{ep}] \{1\} \right) \; \langle G \rangle \; dv$$

$$\{F_n\} = \Sigma \int_v [N]^T \rho \{b\} \; dv + \Sigma \int_s [N]^T \{T\} \; ds$$

$$\{R_{n-1}\} = \Sigma \int_v [B]^T \{\sigma'_{n-1}\} \; dv + \Sigma \int_v \frac{C_s}{3} [B]^T \; [D^{ep}] \{1\} \; \pi_{n-1} \; dv$$

(C-21)

The right hand side of Equation C-6 can be expressed as

$$\alpha d\pi + C_s \, dp' - d\varepsilon_v = \left(\alpha - \frac{C_s^{\,2}}{9} \{1\}^T [D^{ep}] \{1\} \right) d\pi$$

$$- \left(\{1\}^T - \frac{C_s}{3} \{1\}^T [D^{ep}] \right) \{d\varepsilon\} \qquad \text{(C-22)}$$

Substituting Equation C-22 into Equation C-12 and replacing the field variables in Equations C-12 and C-13 by the nodal values using the Equation C-15,

$$\delta W_I{}^* = \{\delta\bar{\pi}\}^T \int_V \langle G\rangle^T \left(\alpha - \frac{C_s{}^2}{9} \{1\}^T [D^{ep}] \{1\}\right) \langle G\rangle dv \Big) \{\dot{\bar{\pi}}\}$$

$$- \left(\Sigma \int_V \langle G\rangle^T \left(\{1\}^T - \frac{C_s}{3} \{1\}^T [D^{ep}] \right) [B] \, dv \right) \{\dot{\bar{u}}\}$$

$$+ \left(\Sigma \int_V [A]^T [k] [A] \, dv \right) \{\bar{\pi}\}$$

$$+ \left(\Sigma \int_V [A]^T [k] \rho_f \{b\} \, dv \right) \Bigg] dt \qquad \text{(C-23)}$$

$$\delta W_E{}^* = \{\delta\bar{\pi}\}^T \left[\Sigma \int_S \langle G\rangle^T \hat{Q} \, ds \right] dt \qquad \text{(C-24)}$$

From Equation C-14

$$[C]^T \{\dot{\bar{u}}\} - [E] \{\dot{\bar{\pi}}\} - [H] \{\bar{\pi}\} = -\{Q\} \qquad \text{(C-25)}$$

where

$$[E] = \Sigma \int_V \langle G\rangle^T \left(\alpha - \frac{C_s{}^2}{9} \{1\}^T [D^{ep}] \{1\}\right) \langle G\rangle \, dv$$

$$[H] = \Sigma \int_V [A]^T [k] [A] \, dv$$

$$\{Q\} = \Sigma \int_S \langle G\rangle^T \hat{Q} \, ds - \Sigma \int_V [A]^T [k] \{b\} \rho_f \, dv \qquad \text{(C-26)}$$

In deriving Equation C-25, the symmetry of $[D^{ep}]$ has been assumed. Assuming the linear variation of skeleton displacements and fluid pressures between t and t + Δt and setting the equilibrium equations at time t + $1/2\Delta t$,

$$\boxed{[C]^T \{\Delta\bar{u}_n\} + \left(-[E] - \frac{\Delta t}{2}[H]\right)\{\bar{\pi}_n\} = \{\bar{Q}_n\}} \quad \text{(C-27)}$$

where

$$\{\bar{Q}_n\} = -\frac{\Delta t}{2}\left(\{Q_n\} + \{Q_{n-1}\}\right) + \left(\frac{\Delta t}{2}[H] - [E]\right)\{\bar{\pi}_{n-1}\} \quad \text{(C-28)}$$

Equations C-20 and C-27 can be solved simultaneously by the incremental step by step procedure. These incremental equations have been implemented in the one-dimensional axisymmetric finite element code "CONSL."

APPENDIX D

CONSL CODE LISTING

```
FTN7X,E
$FILES(0,5)
$EMA /WAREA/
      PROGRAM CONSL
C
C
C REVISION: August 30, 1984
C REVISION: September 1, 1984
C REVISION: September 2, 1984
C REVISION: September 5, 1984
C REVISION: September 6, 1984
C
C
      INTEGER FILE1(6),FILE2(6)
      COMMON/WAREA/A(32767),M(14000)
      COMMON/GINPT/TITLE(20),RI,RO,NUMEL,NKF,NEF,NTF,IPLANE
      COMMON/GPARM/NLNR,NPK,NPE,NPH,NUMNP,NEQ,NEQH,AP,NVF,NDF
      COMMON/BPRES/NMOD,NOD(2),SPR(2)
      COMMON/BFORC/NMOS,NOS(2),TNF(2),NMOU,NOU(2),SPU(2)
      COMMON/PRINT/TPRNT(20),NPRNT
      COMMON/INIST/SRI,STI,PI
C
      WRITE(1) '  TYPE NAME OF INPUT FILE      '
      READ(1,2021) FILE1
      WRITE(1) '  TYPE NAME OF OUTPUT FILE     '
      READ(1,2021) FILE2
 2021 FORMAT(6A2)
      OPEN(6,FILE=FILE1,STATUS='OLD')
      OPEN(7,FILE=FILE2,STATUS='NEW')
      OPEN(8,FILE='CONOUT::-19')
      OPEN(9,FILE='FLOW::-19')
      OPEN(5,FILE='XFLOW::-19')
C
      NTOTL = 32767
      ITOTL = 14000
C
      CALL DREAD
C
      I1 = 1
      I2 = I1+2*NUMNP
      I3 = I2+NUMNP
      I4 = I3+NUMNP
      I5 = I4+2*NUMEL
      I6 = I5+2*NUMEL
      I7 = I6+2*NUMEL
      N1 = 1
      N2 = N1+NUMNP
C
      CALL NODEG(A(N1))
C
```

```
      CALL ELEMT(M(I1),M(I2),M(I3),M(I4),M(I5),M(I6),NUMEL,
     *           NUMNP,NEQ,NEQH,A(N1))
C
      I8 = I7+NEQ
      I9 = I8+2*NEQH
      IF(I9.GT.ITOTL) GO TO 200
      N3 = N2+4*NEQ
      N4 = N3
      IF(NLNR.NE.0) N4 = N3+4*NEQ
      N5 = N4+2*NEQH
      N6 = N5
      IF(NLNR.GT.1.AND.NLNR.LT.6) N6 = N5+2*NEQH
      N7 = N6+NEQH
      N7A=N7
      IF(NVF.EQ.1.AND.PI.NE.0.0) N7A=N7+NEQH
      N8 = N7A+NEQH
      N9 = N8+NEQ
      N10 = N9+NEQ
      N11 = N10+NEQ
      N12 = N11+NEQ
      N12A = N12
      IF(NMOD.EQ.1.OR.NMOU.EQ.1) N12A = N12+NEQ
C
      N13 = N12A+2*2*NUMEL
      N14 = N13
      IF(NKF.EQ.1) N14 = N13+2*NUMEL
      IF(N14.GT.NTOTL) GO TO 200
C
      NEQH2 = 2*NEQH
C
      CALL KSTAR(A(N1),A(N2),A(N3),M(I7),A(N4),A(N5),M(I8),
     *           A(N6),A(N11),M(I4),M(I5),M(I6),A(N12A),
     *           A(N13),NUMEL,NUMNP,NEQ,NEQH,NEQH2,A(N12),A(N7))
C
      CALL SOLVE(M(I3),A(N1),A(N2),A(N3),M(I7),A(N4),A(N5),
     *           M(I8),A(N6),A(N7A),A(N8),A(N9),A(N10),
     *           A(N11),M(I4),M(I5),M(I6),A(N12A),A(N13),
     *           NUMEL,NUMNP,NEQ,NEQH,NEQH2,A(N12),A(N7))
C
  200 CONTINUE
      WRITE(7,2000) ITOTL,I9
 2000 FORMAT('MAX. INTEGER DIMENSION SET IN PROGRAM = ',I5/
     .       'REQUIRED INTEGER DIMENSION ---------- = ',I5//)
C
      WRITE(7,2001) NTOTL,N14
 2001 FORMAT('MAX. REAL DIMENSION SET IN PROGRAM = ',I5/
     .       'REQUIRED REAL DIMENSION ---------- = ',I5//)
C
      CLOSE(5)
      CLOSE(6)
      CLOSE(7)
      CLOSE(8)
```

```
      CLOSE(9)
      STOP
      END
C
$EMA /WAREA/
      BLOCK DATA
      COMMON/WAREA/A(32767),M(14000)
      COMMON/GINPT/TITLE(20),RI,RO,NUMEL,NKF,NEF,NTF,IPLANE
      COMMON/GPARM/NLNR,NPK,NPE,NPH,NUMNP,NEQ,NEQH,AP,NVF,NDF
      COMMON/MTPRT/CM,V,POR,PK,ALPHA,SO,STAW,RSG
      COMMON/TIMEV/DT,TEND,NDT,DTT(10),NCL(10)
      COMMON/INIST/SRI,STI,PI
      COMMON/BFORC/NMOS,NOS(2),TNF(2),NMOU,NOU(2),SPU(2)
      COMMON/BPRES/NMOD,NOD(2),SPR(2)
      COMMON/BCONC/JSDL,JDCL,TNFL,BPPL,JSDR,JDCR,TNFR,BPPR,
     #SSDL,SSDR
      COMMON/PRINT/TPRNT(20),NPRNT
      END
C
      SUBROUTINE DREAD
      COMMON/GINPT/TITLE(20),RI,RO,NUMEL,NKF,NEF,NTF,IPLANE
      COMMON/GPARM/NLNR,NPK,NPE,NPH,NUMNP,NEQ,NEQH,AP,NVF,NDF
      COMMON/MTPRT/CM,V,POR,PK,ALPHA,SO,STAW,RSG
      COMMON/TIMEV/DT,TEND,NDT,DTT(10),NCL(10)
      COMMON/INIST/SRI,STI,PI
      COMMON/BFORC/NMOS,NOS(2),TNF(2),NMOU,NOU(2),SPU(2)
      COMMON/BPRES/NMOD,NOD(2),SPR(2)
      COMMON/BCONC/JSDL,JDCL,TNFL,BPPL,JSDR,JDCR,TNFR,BPPR
     #,SSDL,SSDR
      COMMON/PRINT/TPRNT(20),NPRNT
C
C     PROBLEM SPECIFICATION
C
      READ(6,1001) TITLE
 1001 FORMAT(20A4)
      WRITE(7,2001) TITLE
 2001 FORMAT(/20A4///)
C
C     GLOBAL INPUT
C
      READ(6,1002) RI,RO,AP,NUMEL,NKF,NEF,NTF,IPLANE,NVF,NDF
 1002 FORMAT(3E10.0,7I5)
      WRITE(7,2002) RI,RO,AP,NUMEL,NKF,NEF,NTF,IPLANE,NVF,NDF
 2002 FORMAT('RADIUS OF TUNNEL -------------------- = ',E10.3/
     .       'RADIUS OF REMOTE BOUNDARY ----------- = ',E10.3/
     .       'MESH GROWTH FACTOR ------------------ = ',E10.3/
     .       'NUMBER OF ELEMENTS ------------------ = ',I5   //
     .       '.EQ.0   ELASTIC SKELETON                '      /
     .       '.EQ.1   NONLINEAR SKELETON ---------- = ',I5   //
     .       '.EQ.0   SATURATED FLUID                 '      /
     .       '.EQ.1   PARTIALLY SATURATED FLUID --- = ',I5   //
     .       '.EQ.0   CONSTANT TIME STEPS             '      /
```

```
     .        '.EQ.1   VARIABLE TIME STEPS --------- = ',I5   //
     .        '.EQ.0   1-D CYLINDRICAL SYMMETRY        '      /
     .        '.EQ.1   1-D PLANE STRAIN ------------ = ',I5   //
     .        '.EQ.0   FLOW VOL. BASED ON FIRST ELEM   '      /
     .        '.EQ.1   FLOW VOL. BASED ON ALL ELEM.- = ',I5   //
     .        '.EQ.0   DECOUPLED STORAGE EQUATION      '      /
     .        '.EQ.1   FULLY COUPLED STORAGE EQUATION= ',I5   ///)
C
      NUMNP = NUMEL+1
C
C     INPUT FOR MATERIAL PROPERTIES
C
      READ(6,1003) CM,V,POR,PK
 1003 FORMAT(E10.3,2F10.0,E10.3)
      WRITE(7,2003) CM,V,POR,PK
 2003 FORMAT('SKELETON CONSTRAINED MODULUS -------- = ',E10.3/
     .        'SKELETON POISSONS RATIO ------------- = ',F10.2/
     .        'POROSITY ---------------------------- = ',F10.2/
     .        'COEFFICIENT OF PERMEABILITY --------- = ',E10.3///)
C
      RW = 0.0361
      PK = PK/RW
C
      IF(NEF.EQ.1) GO TO 10
      READ(6,1004) RKW,RKS
 1004 FORMAT(2E10.3)
      WRITE(7,2004) RKW,RKS
 2004 FORMAT('BULK MODULUS OF PORE FLUID ---------- = ',E10.3/
     .        'BULK MODULUS OF SOLID --------------- = ',E10.3///)
      ALPHA = (POR+(1.-POR)*(RKW/RKS))/RKW
      IF(NDF.EQ.0) GOTO 5
      BKS=CM*(1.0+V)/(3.0*(1.0-V))
      ALPHA=ALPHA-BKS/(RKS*RKS)
      RSG=BKS/RKS
 5    CONTINUE
      GO TO 20
   10 CONTINUE
      READ(6,1005) SO,STAW
 1005 FORMAT(2F10.0)
      WRITE(7,2005) SO,STAW
 2005 FORMAT('INITIAL DEGREE OF SATURATION -------- = ',F10.2/
     .        'SURFACE TENSION OF AIR-WATER MIXTURE  = ',F10.2///)
   20 CONTINUE
C
C     INPUT FOR TIME VARIABLES
C
      READ(6,1006) TEND
 1006 FORMAT(E10.3)
      WRITE(7,2006) TEND
 2006 FORMAT('MAXIMUM CALCULATION TIME ------------ = ',E10.3/)
C
      IF(NTF.EQ.1) GO TO 30
```

```
      READ(6,1007) DT
 1007 FORMAT(E10.3)
      WRITE(7,2007) DT
 2007 FORMAT('CONSTANT TIME STEP ------------------ = ',E10.3/)
      GO TO 40
   30 CONTINUE
      READ(6,1008) NDT
 1008 FORMAT(I5)
      WRITE(7,2008) NDT
 2008 FORMAT('NO. OF VARIABLE TIME STEPS ---------- = ',I5   /)
      WRITE(7,2009)
 2009 FORMAT('NO. OF CYCLES    TIME STEP                '       )
      DO 35 I=1,NDT
      READ(6,1010) NCL(I),DTT(I)
 1010 FORMAT(I5,E10.3)
      WRITE(7,2010) NCL(I),DTT(I)
 2010 FORMAT(I5,10X,E10.3)
   35 CONTINUE
   40 CONTINUE
      WRITE(7,2011)
 2011 FORMAT(///)
C
C     INPUT FOR INITIAL STRESSES
C
      READ(6,1012) SRI,STI,PI
 1012 FORMAT(3E10.3)
      WRITE(7,2012) SRI,STI,PI
 2012 FORMAT('INITIAL EFFECTIVE RADIAL STRESS ----- = ',E10.3/
     .       'INITIAL EFFECTIVE CIRCUMF. STRESS --- = ',E10.3/
     .       'INITIAL PORE FLUID PRESSURE --------- = ',E10.3///)
C
C     INPUT FOR BOUNDARY CONDITIONS AT LEFT END
C
      READ(6,1013) JSDL,JDCL,TNFL,BPPL,SSDL
 1013 FORMAT(2I5,3E10.3)
      WRITE(7,2013) JSDL
 2013 FORMAT('SKELETON DISPL. AT LEFT END BOUNDARY     '/
     .       '.EQ.0   FREE                             '/
     .       '.EQ.1   FIXED OR SPECIFIED ---------- = ',I5//)
      IF(JSDL.EQ.0) WRITE(7,2014) TNFL
 2014 FORMAT('APPLIED TOTAL STRESS AT LEFT END     = ',E10.3//)
      IF(JSDL.EQ.1) WRITE(7,2114) SSDL
 2114 FORMAT('SPEC. SKELETON DISP. AT LEFT END     = ',E10.3//)
      WRITE(7,2015) JDCL
 2015 FORMAT('DRAINAGE CONDITION AT LEFT END BOUNDARY '/
     .       '.EQ.0   PERMEABLE                        '/
     .       '.EQ.1   IMPERMEABLE ----------------- = ',I5//)
      IF(JDCL.EQ.0) WRITE(7,2016) BPPL
 2016 FORMAT('SPECIFIED PORE PRESSURE AT LEFT END   = ',E10.3//)
C
C     INPUT FOR BOUNDARY CONDITION AT RIGHT END
C
```

```
      READ(6,1017) JSDR,JDCR,TNFR,BPPR,SSDR
 1017 FORMAT(2I5,3E10.3)
      WRITE(7,2017) JSDR
 2017 FORMAT('SKELETON DISPL. AT RIGHT END BOUNDARY    '/
     .        '.EQ.0   FREE                             '/
     .        '.EQ.1   FIXED OR SPECIFIED ---------- = ',I5//)
      IF(JSDR.EQ.0) WRITE(7,2018) TNFR
 2018 FORMAT('APPLIED TOTAL STRESS AT RIGHT END    = ',E10.3//)
      IF(JSDR.EQ.1) WRITE(7,2118)SSDR
 2118 FORMAT('SPEC. SKELETON DISP. AT RIGHT END    = ',E10.3//)
      WRITE(7,2019) JDCR
 2019 FORMAT('DRAINAGE CONDITION AT RIGHT END          '/
     .        '.EQ.0   PERMEABLE                        '/
     .        '.EQ.1   IMPERMEABLE ---------------- = ',I5//)
      IF(JDCR.EQ.0) WRITE(7,2020) BPPR
 2020 FORMAT('SPECIFIED PORE PRESSURE AT RIGHT END    = ',E10.3///)
C
C        INPUT TIME OF PRINTS
C
      READ(6,*) NPRNT
      READ(6,*) (TPRNT(NJ),NJ=1,NPRNT)
      NPRNT = NPRNT + 1
      TPRNT(NPRNT) = 1.E+0)
      NPRNT = 1
C
C
C     CALCULATE INTERNAL FLAG
      IF(NKF.EQ.0.AND.NEF.EQ.0.AND.NTF.EQ.0) NLNR = 0
      IF(NKF.EQ.1.AND.NEF.EQ.0.AND.NTF.EQ.0) NLNR = 1
      IF(NKF.EQ.0.AND.NEF.EQ.1.AND.NTF.EQ.0) NLNR = 2
      IF(NKF.EQ.0.AND.NEF.EQ.0.AND.NTF.EQ.1) NLNR = 3
      IF(NKF.EQ.1.AND.NEF.EQ.1.AND.NTF.EQ.0) NLNR = 4
      IF(NKF.EQ.1.AND.NEF.EQ.0.AND.NTF.EQ.1) NLNR = 5
      IF(NKF.EQ.0.AND.NEF.EQ.1.AND.NTF.EQ.1) NLNR = 6
      IF(NKF.EQ.1.AND.NEF.EQ.1.AND.NTF.EQ.1) NLNR = 7
C
      NPK = 0
      NPE = 0
      NPH = 0
C
      IF(NLNR.EQ.2.OR.NLNR.EQ.3.OR.NLNR.EQ.6) NPK = 1
      IF(NLNR.EQ.1.OR.NLNR.EQ.3.OR.NLNR.EQ.5) NPE = 1
      IF(NLNR.EQ.1.OR.NLNR.EQ.2.OR.NLNR.EQ.4) NPH = 1
      RETURN
      END
C
      SUBROUTINE NODEG(X)
      REAL N,L
      DIMENSION X(1)
      COMMON/GINPT/TITLE(20),RI,RO,NUMEL,NKF,NEF,NTF,IPLANE
      COMMON/GPARM/MM(7),AP,NVF,NDF
      N = FLOAT(NUMEL)
```

```
      L = RO-RI
      AX = RI
      X(1) = AX
C
      DO 100 I=1,NUMEL
      A1 = L*(1.+(N-1.)*(4.*AP-2.)/N)/N
      B = (2.*L/N-2.*A1)/(N-1.)
      AI = A1+(I-1.)*B
      AX = AX+AI
      X(I+1) = AX
  100 CONTINUE
C
      RETURN
      END
C
C   INSERT ELEMT
C
      SUBROUTINE ELEMT(ID,IDH,IHD,IXS,IXF,IXH,NUMEL,NUMNP,
     *                 NEQ,NEQH,X)
      DIMENSION ID(NUMNP,2),IDH(1),IHD(1),IXS(2,1),IXF(2,1),
     *          IXH(2,1),X(1)
      COMMON/BPRES/NMOD,NOD(2),SPR(2)
      COMMON/BFORC/NMOS,NOS(2),TNF(2),NMOU,NOU(2),SPU(2)
      COMMON/BCONC/JSDL,JDCL,TNFL,BPPL,JSDR,JDCR,TNFR,BPPR
     #,SSDL,SSDR
C
      CALL IZERO(ID,NUMNP*2)
      CALL IZERO(IDH,NUMNP)
C
C     ASSIGN SKELETON DISPL. BOUNDARY CONDITIONS
C
      NMOS = 0
      NMOU = 0
      IF(JSDL.NE.0) GO TO 10
      NMOS = NMOS+1
      ID(1,1) = 0
      NOS(NMOS) = 1
      TNF(NMOS) = -TNFL*X(1)
      GO TO 20
   10 CONTINUE
      NMOU=NMOU+1
      ID(1,1) = 0
      NOU(NMOU)=1
      SPU(NMOU)=SSDL
   20 CONTINUE
      IF(JSDR.NE.0) GO TO 30
      NMOS = NMOS+1
      ID(NUMNP,1) = 0
      NOS(NMOS) = NUMNP
      TNF(NMOS) = TNFR*X(NUMNP)
      GO TO 40
   30 CONTINUE
```

```
      NMOU=NMOU+1
      ID(NUMNP,1) = 0
      NOU(NMOU)=NUMNP
      SPU(NMOU)=SSDR
   40 CONTINUE
C
C     ASSIGN DRAINAGE BOUNDARY CONDITIONS
C
      NMOD = 0
      IF(JDCL.NE.0) GO TO 48
      IF(BPPL.NE.0.0) GO TO 42
      ID(1,2) = 1
      IDH(1) = 1
      GO TO 50
   42 CONTINUE
      NMOD = NMOD+1
      ID(1,2) = 0
      IDH(1) = 0
      NOD(NMOD) = 1
      SPR(NMOD) = BPPL
      GO TO 50
   48 CONTINUE
      ID(1,2) = 0
      IDH(1) = 0
   50 CONTINUE
C
      IF(JDCR.NE.0) GO TO 58
      IF(BPPR.NE.0.0) GO TO 52
      ID(NUMNP,1) = 1
      IDH(NUMNP) = 1
      GO TO 60
   52 CONTINUE
      NMOD = NMOD+1
      ID(NUMNP,2) = 0
      IDH(NUMNP) = 0
      NOD(NMOD) = NUMNP
      SPR(NMOD) = BPPR
      GO TO 60
   58 CONTINUE
      ID(NUMNP,2) = 0
      IDH(NUMNP) = 0
   60 CONTINUE
C
      NEQ = 0
      NEQH = 0
      DO 75 I=1,NUMNP
      DO 70 J=1,2
      IF(ID(I,J)) 68,65,68
   65 NEQ = NEQ+1
      ID(I,J) = NEQ
      IF(J.EQ.2) GO TO 66
      GO TO 70
```

```
   66 NEQH = NEQH+1
      IDH(I) = NEQH
      IHD(NEQH) = NEQ
      GO TO 70
   68 ID(I,J) = -1
      IF(J.EQ.2) IDH(I) = -1
   70 CONTINUE
   75 CONTINUE
C
      DO 100 I=1,NUMEL
      IXS(1,I) = ID(I,1)
      IXS(2,I) = ID(I+1,1)
      IXF(1,I) = ID(I,2)
      IXF(2,I) = ID(I+1,2)
      IXH(1,I) = IDH(I)
      IXH(2,I) = IDH(I+1)
  100 CONTINUE
C
      IF(NMOS.EQ.0) GO TO 106
      DO 104 I=1,NMOS
      II = NOS(I)
  104 NOS(I) = ID(II,1)
  106 CONTINUE
C
      IF(NMOD.EQ.0) GO TO 120
      DO 110 I=1,NMOD
      II = NOD(I)
  110 NOD(I) = ID(II,2)
  120 CONTINUE
      IF(NMOU.EQ.0) GOTO 140
      DO 130 I=1,NMOU
            II=NOU(I)
 130  NOU(I)=ID(II,1)
 140  CONTINUE
C
      RETURN
      END
      SUBROUTINE KSTAR(X,GK,GKO,MB,GH,GHO,MBH,PNO,RS,IXS,IXF,IXH,
     *                 S,STRES,NUMEL,NUMNP,NEQ,NEQH,NEQH2,SHA,PNI)
      DIMENSION X(NUMNP),GK(NEQ,4),GKO(NEQ,4),MB(NEQ),
     * GH(NEQH,2),GHO(NEQH,2),MBH(NEQH2),PNO(NEQH),RS(NEQ),
     * IXS(2,NUMEL),IXF(2,NUMEL),IXH(2,NUMEL),S(2,2,NUMEL),
     * STRES(2,NUMEL),CT(2,2),SHA(NEQ),PP(2),DI(2),PNI(NEQH)
      DIMENSION E(2,2),H(2,2),C(2,2),EHP(2,2),EHM(2,2),R(2)
      COMMON/GINPT/TITLE(20),RI,RO,NUMEX,NKF,NEF,NTF,IPLANE
      COMMON/GPARM/NLNR,NPK,NPE,NPH,NUMNX,NEX,NEQX,AP,NVF,NDF
      COMMON/MTPRT/CM,V,POR,PK,ALPHA,SO,STAW,RSG
      COMMON/TIMEV/DT,TEND,NDT,DTT(10),NCL(10)
      COMMON/INIST/SR,ST,PI
      COMMON/BPRES/NMOD,NOD(2),SPR(2)
      COMMON/BFORC/NMOS,NOS(2),TNF(2),NMOU,NOU(2),SPU(2)
C
```

```
      IF(NTF.EQ.1) DT = DTT(1)
C
C     CALCULATE INITIAL VALUE OF ALPHA
C
      IF(NEF.NE.1) GO TO 50
      PAO = 14.7
      HC = 0.02
      P = PAO+STAW+PI
      P2 = P*P
      ALPHA = POR*(1.0-SO+HS*SO)*PAO/P2
   50 CONTINUE
C
      NEQ4 = NEQ*4
      CALL SZERO(GK,NEQ4)
      CALL SZERO(GH,NEQH2)
      CALL IZERO(MB,NEQ)
      CALL IZERO(MBH,NEQH2)
      CALL SZERO(RS,NEQ)
      IF(NLNR.NE.0) CALL SZERO(GKO,NEQ4)
      IF(NLNR.GT.1.AND.NLNR.LT.6) CALL SZERO(GHO,NEQH2)
C
      DO 200 NN=1,NUMEL
      N = NN
C
C     ASSEMBLE GLOBAL STIFFNESS MATRIX
C
C
      CALL CONST(X,N,A,XL)
C
      CALL ELSTF(CM,V,A,XL,S(1,1,N))
C
      CALL ASMBM(GK,S(1,1,N),IXS(1,N),IXS(1,N),NEQ,4)
      IF(NPK.EQ.1)
     *  CALL ASMBM(GKO,S(1,1,N),IXS(1,N),IXS(1,N),NEQ,4)
C
      CALL ELEMX(ALPHA,A,XL,E)
C
      CALL ELHMX(PK,A,XL,H)
C
      DO 150 I=1,2
      DO 150 J=1,2
      EHP(I,J) =  0.5*DT*H(I,J)+E(I,J)
      EHM(I,J) = -0.5*DT*H(I,J)+E(I,J)
  150 CONTINUE
C
      CALL ASMBM(GK,EHM,IXF(1,N),IXF(1,N),NEQ,4)
      IF(NPE.EQ.1)
     *  CALL ASMBM(GKO,E,IXF(1,N),IXF(1,N),NEQ,4)
C
      CALL ELCMX(A,XL,C,CT)
      IF(NDF.EQ.0) GOTO 157
      DO 155 I=1,2
```

```
      DO 155 J=1,2
            C(I,J)=(1.0-RSG)*C(I,J)
            CT(I,J)=(1.0-RSG)*CT(I,J)
 155  CONTINUE
 157  CONTINUE
C
      CALL ASMBM(GK,C,IXS(1,N),IXF(1,N),NEQ,4)
      IF(NLNR.NE.0)
     *  CALL ASMBM(GKO,C,IXS(1,N),IXF(1,N),NEQ,4)
      IF(NLNR.NE.0)
     *  CALL ASMBM(GKO,CT,IXF(1,N),IXS(1,N),NEQ,4)
C
      CALL ASMBM(GK,CT,IXF(1,N),IXS(1,N),NEQ,4)
C
      IF(NPH.NE.1) GO TO 180
      DO 160 I=1,2
      DO 160 J=1,2
      EHP(I,J) =  0.5*DT*H(I,J)
  160 EHM(I,J) = -0.5*DT*H(I,J)
      CALL ASMBM(GKO,EHM,IXF(1,N),IXF(1,N),NEQ,4)
  180 CONTINUE
C
C
C     ASSEMBLE GLOBAL GH MATRIX
C
      CALL ASMBM(GH,EHP,IXH(1,N),IXH(1,N),NEQH,2)
      IF(NLNR.LE.1.OR.NLNR.GE.6) GO TO 190
      IF(NPE.EQ.1)
     *  CALL ASMBM(GHO,E,IXH(1,N),IXH(1,N),NEQH,2)
      IF(NPH.EQ.1)
     *  CALL ASMBM(GHO,EHP,IXH(1,N),IXH(1,N),NEQH,2)
C
C     RESIDUAL LOAD VECTOR DUE TO INITIAL EFFECTIVE STRESS
C
 190  IF(SR.EQ.0.0.AND.ST.EQ.0.0) GOTO 200
      CALL RESLS(SR,ST,A,XL,R)
C
      CALL ASMBV(RS,R,IXS(1,N),2)
C
  200 CONTINUE
C
C
C     TRIANGLIZE GLOBAL STIFFNESS MATRIX
C
      IF(NMOD.EQ.0.AND.NMOU.EQ.0) GO TO 250
      CALL SZERO(SHA,NEQ)
      IF(NMOD.EQ.0) GOTO 220
      DO 210 I=1,NMOD
210   CALL MODFY(NOD(I),SPR(I),GK,SHA,NEQ,4)
220   IF(NMOU.EQ.0) GOTO 250
      DO 230 I=1,NMOU
  230 CALL MODFY(NOU(I),SPU(I),GK,SHA,NEQ,4)
```

```
  250 CONTINUE
C
      CALL TRIA(NEQ,4,GK,MB)
C
C     PROFILE GLOBAL GH MATRIX
C
      CALL PRFIL(GH,MBH,NEQH,2)
C
C     ASSIGN INITIAL PORE PRESSURE
C
      DO 300 I=1,NEQH
  300 PNO(I) = PI
C
C
C RESIDUAL LOAD VECTOR DUE TO INITIAL PORE PRESSURE
C
C
      IF(NDF.EQ.0.OR.PI.EQ.0) GOTO 348
      DO 346 N=1,NUMEL
            CALL CONST(X,N,A,XL)
            CALL ELCMX(A,XL,C,CT)
      DO 342 I=1,2
      DO 342 J=1,2
342         C(I,J)=RSG*C(I,J)
            CALL EXTRT(PP,IXH(1,N),PNO,2)
            DI(1)=C(1,1)*PP(1)+C(1,2)*PP(2)
            DI(2)=C(2,1)*PP(1)+C(2,2)*PP(2)
            CALL ASMBV(RS,DI,IXS(1,N),2)
346   CONTINUE
348   CONTINUE
      IF(NVF.EQ.1.AND.PI.NE.0.0) GOTO 350
      GOTO 360
 350  CALL COPY(PNI,PNO,NEQH)
 360  CONTINUE
C
C     ASSIGN INITIAL EFFECTIVE STRESSES
C
      DO 400 I=1,NUMEL
      STRES(1,I) = SR
  400 STRES(2,I) = ST
      RETURN
      END
C
C   INSERT SOLVE
C
      SUBROUTINE SOLVE(IHD,X,GK,GKO,MB,GH,GHO,MBH,PNO,PNC,DISP,
     *  UI,RSV,RS,IXS,IXF,IXH,S,STRES,NUMEL,NUMNP,NEQ,NEQH,NEQH2,
     *  SHA,PNI)
      INTEGER BDUMMY
      DIMENSION IHD(1),X(1),GK(NEQ,4),GKO(NEQ,4),MB(1),
     *   GH(NEQH,2),GHO(NEQH,2),MBH(1),PNO(1),PNC(1),DISP(1),
     *   UI(1),RSV(1),RS(1),IXS(2,1),IXF(2,1),IXH(2,1),
```

```
     *   S(2,2,1),STRES(2,1),SHA(1),PNI(1),PPI(2)
      DIMENSION DU(2),E(2,2),H(2,2),R(2),PP(2),DI(2)
      COMMON/GINPT/TITLE(20),RI,RO,NUMEX,NKF,NEF,NTF,IPLANE
      COMMON/GPARM/NLNR,NPK,NPE,NPH,NUMNX,NEX,NEQX,AP,NVF,NDF
      COMMON/MTPRT/CM,V,POR,PK,ALPHA,SO,STAW,RSG
      COMMON/TIMEV/DT,TEND,NDT,DTT(10),NCL(10)
      COMMON/BFORC/NMOS,NOS(2),TNF(2),NMOU,NOU(2),SPU(2)
      COMMON/BPRES/NMOD,NOD(2),SPR(2)
      COMMON/INIST/SRI,STI,PI
C
      NFIRST = 0
      ISTEP = 0
      TIME = 0.0
      Q = 0.0
      VCUR = 0.0
C
      M = 0
      MM = 1
C
      CALL SZERO(PNC,NEQH)
      CALL SZERO(DISP,NEQ)
      CALL SZERO(UI,NEQ)
C
   50 CONTINUE
      VOL=0.0
      NGH = 0
      IF(NTF.NE.1) GO TO 70
      M = M+1
      IF(MM.GT.NDT) GO TO 70
      IF(M.GT.NCL(MM)) GO TO 60
      DT = DTT(MM)
      GO TO 70
   60 MM = MM+1
      DT = DTT(MM)
      M = 1
      NGH = 1
   70 CONTINUE
C
      ISTEP = ISTEP+1
      IF(NMOU.EQ.0) GOTO 73
      IF(ISTEP.NE.2) GOTO 73
      DO 72 I=1,NMOU
72    SPU(I)=0.0
73    CONTINUE
      TIME = TIME+DT
      CALL SZERO(RSV,NEQ)
C
      IF(NMOS.EQ.0) GO TO 78
      DO 74 I=1,NMOS
      II = NOS(I)
   74 RSV(II) = TNF(I)
   78 CONTINUE
```

```
C
      WRITE(1,2000) ISTEP
 2000 FORMAT('  CYCLE NUMBER = ',I5)
C
      IF(NFIRST.EQ.0) GO TO 340
      IF(NLNR.EQ.0) GO TO 80
      IF(NLNR.EQ.3.AND.NGH.EQ.0) GOTO 80
      CALL COPY(GK,GKO,NEQ*4)
      IF(NLNR.GE.6) CALL SZERO(GH,NEQH*2)
      IF(NLNR.GT.1.AND.NLNR.LT.6) CALL COPY(GH,GHO,NEQH*2)
   80 CONTINUE
C
C     ELEMENT PACKAGE
C
      DO 330 N=1,NUMEL
C
      CALL EXTRT(DU,IXS(1,N),UI,2)
      IF(NVF.NE.1) GOTO 90
      CALL EXTRT(DI,IXS(1,N),DISP,2)
      CALL EXTRT(PP,IXH(1,N),PNO,2)
      IF(PI.EQ.0.0) GOTO 85
      CALL EXTRT(PPI,IXH(1,N),PNI,2)
      PP(1)=PP(1)-PPI(1)
      PP(2)=PP(2)-PPI(2)
85    CONTINUE
      CALL CONST(X,N,A,XL)
      CALL FLVOL(DI,PP,POR,ALPHA,A,XL,VOL,IPLANE,RSG,NDF)
C     WRITE(50,*)'N=',N,'  VOL=',VOL
C     WRITE(50,*)'DI(1)=',DI(1),'   DI(2)=',DI(2)
C     WRITE(50,*)'PP(1)=',PP(1),'   PP(2)=',PP(2)
C     WRITE(50,*)'A=',A,'    XL=',XL
C     WRITE(50,475)
C475   FORMAT(/)
 90   CONTINUE
C
      IF(NLNR.EQ.0) GO TO 250
      IF(NLNR.EQ.3.AND.NGH.EQ.0)  GOTO 250
      CALL CONST(X,N,A,XL)
C
C     NONLINEAR IN SOLID SKELETON (NKF = 1)
C
      IF(NKF.NE.1) GO TO 100
C
C     UPDATE CONSTRAINED MODULUS(CM) AND POISSION RATIO(V)
C     BASED ON EFFECTIVE STRESSES
C
      CALL MODEL(CM,V,STRES(1,N),STRES(2,N))
C
C     UPDATE ELEMENT TANGENT STIFFNESS MATRIX
C
      CALL ELSTF(CM,V,A,XL,S(1,1,N))
C
```

```
C     ASSEMBLE ELEMENT TANGENT STIFFNESS MATRIX
C
      CALL ASMBM(GK,S(1,1,N),IXS(1,N),IXS(1,N),NEQ,4)
C
C     UPDATE ELEMENT EFFECTIVE STRESSES
C
      CALL EFFST(DU,A,XL,CM,V,STRES(1,N),STRES(2,N))
C
C     NONLINEAR IN FLUID COMPRESSIBILITY (NEF = 1)
C
  100 IF(NEF.NE.1) GO TO 200
C
C     UPDATE ALPHA BASED ON OLD PORE PRESSURE
C
      CALL VCOMP(PNO,IXH,SO,POR,STAW,ALPHA)
C
C     UPDATE ELEMENT E MATRIX
C
      CALL ELEMX(ALPHA,A,XL,E)
C
C     ASSEMBLE E MATRIX TO GK
C
      CALL ASMBM(GK,E,IXF(1,N),IXF(1,N),NEQ,4)
C
C     ASSEMBLE E MATRIX TO GH
C
      CALL ASMBM(GH,E,IXH(1,N),IXH(1,N),NEQH,2)
C
C     VARIABLE TIME STEPS (NTF = 1)
C
  200 IF(NTF.NE.1) GO TO 250
C
C     CALCULATE ELEMENT H MATRIX
C
      CALL ELHMX(PK,A,XL,H)
C
C     ASSEMBLE -0.5*DT*H TO GK
C
C     CALL FACTR(H,4,-0.5*DT)
      DO 202 I=1,2
      DO 202 J=1,2
 202  H(I,J) = -.5 * DT * H(I,J)
      CALL ASMBM(GK,H,IXF(1,N),IXF(1,N),NEQ,4)
C
C     ASSEMBLE  0.5*DT*H TO GH
C
C     CALL FACTR(H,4,-1.0)
      DO 204 I=1,2
      DO 204 J=1,2
204   H(I,J) = -H(I,J)
      CALL ASMBM(GH,H,IXH(1,N),IXH(1,N),NEQH,2)
C
```

```
C     ASSEMBLE ELEMENT RESIDUAL LOAD VECTOR DUE TO
C     EFFECTIVE STRESSES
C
  250 CONTINUE
      R(1) = S(1,1,N)*DU(1)+S(1,2,N)*DU(2)
      R(2) = S(2,1,N)*DU(1)+S(2,2,N)*DU(2)
      CALL ASMBV(RS,R,IXS(1,N),2)
  330 CONTINUE
C
  340 CONTINUE
C
C
      DO 350 I=1,NEQ
  350 RSV(I) = RSV(I)-RS(I)
C
      CALL MLTPL(GH,PNC,PNO,MBH,NEQH,NEQH2,2)
      CALL ASMBV(RSV,PNC,IHD,NEQH)
C
      IF(NFIRST.EQ.0) GO TO 380
      CALL OUTPT(DISP,X,PNO,STRES,PK,NUMEL,NKF,IPLANE,Q,TIME,DT,
     *   IXH(1,1),NVF,VOL,IXS,VCUR)
  380 CONTINUE
C
      IF(NFIRST.EQ.0) GOTO 386
      IF(NLNR.EQ.0) GO TO 386
      IF(NLNR.EQ.3.AND.NGH.EQ.0) GOTO 386
      IF(NMOD.EQ.0.AND.NMOU.EQ.0) GO TO 385
      CALL SZERO(SHA,NEQ)
      IF(NMOD.EQ.0) GOTO 383
      DO 382 I=1,NMOD
382   CALL MODFY(NOD(I),SPR(I),GK,SHA,NEQ,4)
383   IF(NMOU.EQ.0) GOTO 385
      DO 384 I=1,NMOU
384   CALL MODFY(NOU(I),SPU(I),GK,SHA,NEQ,4)
385   CONTINUE
C
      CALL TRIA(NEQ,4,GK,MB)
C
  386 CONTINUE
C
      IF(NMOD.EQ.0.AND.NMOU.EQ.0) GOTO 395
      DO 387 I=1,NEQ
  387 RSV(I) = RSV(I)+SHA(I)
      IF(NMOD.EQ.0) GOTO 389
      DO 388 I=1,NMOD
      II = NOD(I)
  388 RSV(II) = SPR(I)
  389 CONTINUE
      IF(NMOU.EQ.0) GOTO 395
      DO 392 I=1,NMOU
            II=NOU(I)
  392 RSV(II)=SPU(I)
```

```
395   CONTINUE
C
      CALL BACKS(NEQ,GK,RSV,MB)
C
      CALL SZERO(PNO,NEQH)
      CALL SZERO(PNC,NEQH)
      KK = 1
C
      DO 405 I=1,NEQ
      UI(I) = RSV(I)
      IF(IHD(KK).NE.I) GO TO 400
      DISP(I) = UI(I)
      PNO(KK) = UI(I)
      KK = KK+1
      GO TO 405
  400 DISP(I) = DISP(I)+UI(I)
  405 CONTINUE
C
      IF(NFIRST.EQ.1) GO TO 420
      WRITE(1,2001)
 2001 FORMAT(' INITIAL PORE PRESSURE RESPONSE')
      DO 410 I=1,NEQH
  410 WRITE(1,2002) I,PNO(I)
 2002 FORMAT(I5,E10.3)
C     PAUSE 55
      WRITE(1,*) '  PAUSE 55'
      READ(1,2022) BDUMMY
2022  FORMAT(A2)
      IF(BDUMMY.EQ.84) STOP 84
C
C
  420 NFIRST = 1
      IF(TIME.LT.TEND) GO TO 50
      RETURN
      END
      SUBROUTINE CONST(X,N,A,L)
      REAL L,LL,X(1)
      COMMON/CNSTS/B0,B(12)
      A = X(N)
      L = X(N+1)-X(N)
      AA = A*A
      LL = L*L
      B0 = 0.5*L*(2.*A+L)
      B(1) = L
      B(2) = LOG(1.+L/A)
      B(3) = B(1)-A*B(2)
      B(4) = L/(A*(A+L))
      B(5) = B(2)-A*B(4)
      B(6) = B(1)-2.*A*B(5)-AA*B(4)
      B(7) = 0.5*LL
      B(8) = B0-2.*A*B(3)-AA*B(2)
      B(9) = B0-3.*A*B(6)-3.*AA*B(5)-AA*A*B(4)
```

```
      B(10) = LL*L/3.
      RINSD = L**3+3.*AA*L+3.*A*LL
      B(11) = (RINSD)/3.-3.*A*B(8)-3.*AA*B(3)-AA*A*B(2)
      B(12) = 0.25*(L**4)
      RETURN
      END
C
C     ELEMENT STIFFNESS MATRIX
C
      SUBROUTINE ELSTF(CM,V,A,L,S)
      REAL L,LL,S(2,2)
      COMMON/CNSTS/B0,B1,B2,B3,B4,B5,B6,B7,B8,B9,B10,B11,B12
      D = CM*V/(1.-V)
      G = 0.5*CM*(1.-2.*V)/(1.-V)
      DP = D+2.*G
      LL = L*L
C
      S11 = A*DP*B1/LL-2.*A*D*B2/L+(2.*A*D/LL-2.*D/L)*B3+A*DP*B4
     .      +(DP-2.*A*DP/L)*B5+(A*DP/LL-2.*DP/L)*B6+DP*B7/LL
     .      +2.*D*B8/LL+DP*B9/LL
C
      S12 = -A*DP*B1/LL+A*D*B2/L+(D/L-2.*A*D/LL)*B3+A*DP*B5/L
     .      +(DP/L-A*DP/LL)*B6-DP*B7/LL-2.*D*B8/LL-DP*B9/LL
C
      S22 = A*DP*B1/LL+2.*A*D*B3/LL+A*DP*B6/LL+DP*B7/LL
     .      +2.*D*B8/LL+DP*B9/LL
C
      S(1,1) = S11
      S(1,2) = S12
      S(2,1) = S12
      S(2,2) = S22
      RETURN
      END
C
C     ELEMENT C MATRIX
C
      SUBROUTINE ELCMX(A,L,C,CT)
      REAL L,LL,C(2,2),CT(2,2)
      COMMON/CNSTS/B0,B1,B2,B3,B4,B5,B6,B7,B8,B9,B10,B11,B12
      LL = L*L
C
      C11 = -A*B1/L+(A/LL-1./L)*B7+A*B2+(1.-2.*A/L)*B3
     .      +(A/LL-2./L)*B8+B10/LL+B11/LL
C
      C12 = -A/LL*B7+A*B3/L+(1./L-A/LL)*B8-B10/LL-B11/LL
C
      C21 = A*B1/L+(1./L-A/LL)*B7+A*B3/L+(1./L-A/LL)*B8
     .      -B10/LL-B11/LL
C
      C22 = A*B7/LL+A*B8/LL+B10/LL+B11/LL
C
      C(1,1) = C11
```

```
      C(1,2) = C12
      C(2,1) = C21
      C(2,2) = C22
C
      CT(1,1) = C(1,1)
      CT(1,2) = C(2,1)
      CT(2,1) = C(1,2)
      CT(2,2) = C(2,2)
C
      RETURN
      END
C
C     ELEMENT H MATRIX
C
      SUBROUTINE ELHMX(K,A,L,H)
      REAL L,LL,K,H(2,2)
      COMMON/CNSTS/B0,B1,B2,B3,B4,B5,B6,B7,B8,B9,B10,B11,B12
      LL = L*L
C
      H11 = A*K*B1/LL+K*B7/LL
C
      H12 = -H11
C
      H22 = H11
C
      H(1,1) = H11
      H(1,2) = H12
      H(2,1) = H12
      H(2,2) = H22
      RETURN
      END
C
C     ELEMENT E MATRIX
C
      SUBROUTINE ELEMX(ALPHA,A,L,E)
      REAL L,LL,E(2,2)
      COMMON/CNSTS/B0,B1,B2,B3,B4,B5,B6,B7,B8,B9,B10,B11,B12
      LL = L*L
C
      E11 = A*B1+(1.-2.*A/L)*B7+(A/LL-2./L)*B10+B12/LL
C
      E12 = A*B7/L+(1./L-A/LL)*B10-B12/LL
C
      E22 = A*B10/LL+B12/LL
C
      E(1,1) = -E11*ALPHA
      E(1,2) = -E12*ALPHA
      E(2,1) = -E12*ALPHA
      E(2,2) = -E22*ALPHA
      RETURN
      END
C
```

```
C     ELEMENT RESIDUAL EFFECTIVE STRESS VECTOR
C
      SUBROUTINE RESLS(SR,ST,A,L,R)
      REAL L,R(2)
      COMMON/CNSTS/B0,B1,B2,B3,B4,B5,B6,B7,B8,B9,B10,B11,B12
C
      R1 = SR*(-A*B1/L-B7/L)+ST*(A*B2+(1.-A/L)*B3-B8/L)
C
      R2 = SR*(A*B1/L+B7/L)+ST*(A*B3/L+B8/L)
C
      R(1) = R1
      R(2) = R2
      RETURN
      END
C
C   INSERT ALIB
C
      SUBROUTINE SZERO(A,N)
      DIMENSION A(N)
      DO 100 I=1,N
  100 A(I) = 0.0
      RETURN
      END
      SUBROUTINE IZERO(M,N)
      DIMENSION M(N)
      DO 100 I=1,N
  100 M(I) = 0
      RETURN
      END
      SUBROUTINE COPY(A,B,N)
      DIMENSION A(1),B(1)
      DO 100 I=1,N
  100 A(I) = B(I)
      RETURN
      END
      SUBROUTINE FACTR(A,N,FAC)
      DIMENSION A(N)
      DO 100 I=1,N
  100 A(I) = FAC*A(I)
      RETURN
      END
      SUBROUTINE EXTRT(DU,NA,GU,N)
      DIMENSION DU(1),NA(1),GU(1)
      CALL SZERO(DU,N)
      DO 100 I=1,N
      J = NA(I)
      IF(J.LE.0) GO TO 100
      DU(I) = GU(J)
  100 CONTINUE
      RETURN
      END
      SUBROUTINE VCOMP(PNO,IXH,SO,POR,STAW,ALPHA)
```

```
      DIMENSION PNO(1),IXH(1)
      PAO = 14.7
      HC = 0.02
      P = 0.0
      DO 100 I=1,2
      N = IXH(I)
      IF(N.LE.0) GO TO 100
      P = P-PNO(N)
  100 CONTINUE
      P = PAO+STAW+P/2.
      PP = P*P
      CW = (1.0-SO+HC*SO)*PAO/PP
      ALPHA = POR*CW
C
      RETURN
      END
      SUBROUTINE MODEL(CM,V,SR,ST)
C
C
C
C
C
C
C
      RETURN
      END
      SUBROUTINE EFFST(DU,A,L,CM,V,SR,ST)
      REAL DU(2),L
      U1 = DU(1)
      U2 = DU(2)
      AL = 2.*A+L
      D = CM*V/(1.-V)
      G = 0.5*CM*(1.-2.*V)/(1.-V)
      DP = D+2.*G
      SR = (D/AL-DP/L)*U1+(D/AL+DP/L)*U2
      ST = (DP/AL-D/L)*U1+(DP/AL+D/L)*U2
C
      RETURN
      END
C
      SUBROUTINE OUTPT(DISP,X,PNC,STRES,K,NUMEL,NKF,IPLANE,Q,
     *                 TIME,DT,LF,NVF,VOL,IXS,VCUR)
      REAL DISP(1),X(1),PNC(1),STRES(2,1),L,K
      DIMENSION IXS(2,1)
      COMMON/BCONC/JSDL,JDCL,TNFL,BPPL,JSDR,JDCR,TNFR,BPPR
     #,SSDL,SSDR
      COMMON/PRINT/TPRNT(20),NPRNT
C
      PIE = 3.1415926
      L = X(2)-X(1)
      IF(LF.GT.0) PDF = PNC(2)-PNC(1)
      IF(LF.LE.0) PDF = PNC(1)
```

```
      IF(JDCL.EQ.1) PDF = 0.0
      VR = -K*PDF/L
      VOLD=VCUR
      VCUR=VR
      VAVG=0.5*(VOLD+VCUR)

435   IF(IPLANE.EQ.0) FAC = 2.*PIE*1.0*X(1)
      IF(IPLANE.EQ.1) FAC = 1.0
      IF(NVF.EQ.0)  Q = Q+FAC*VR*DT
      IF(NVF.EQ.1)  Q = VOL
C
       DPL=DISP(1)
       II=IXS(2,NUMEL)
       DPR=DISP(II)
C
      TIMEO = TIME-DT
C
C                OUTPUT TIME(SEC) AND FLOW(GALS PER UNIT FOOT)
C
      WRITE(9,*) TIMEO/86400.,Q/1728. * 7.479 * 12.
      WRITE(5,*) TIMEO/86400.,VAVG *2.0*PIE*X(1)*12*60/231
      NFR=NFR+1
C
C           IF TIMEO LESS THAN PRINT TIME SKIP OUTPUT SECTION
C
      IF(TIMEO.LT.TPRNT(NPRNT))  GOTO 300
      NPRNT = NPRNT + 1
C
      WRITE(7,2001) TIMEO
 2001 FORMAT('TIME = ',E10.3//)
C
      WRITE(7,2002) DPL,DPR,VR,Q
 2002 FORMAT('DISPLACEMENT AT TUNNEL SURFACE ------ = ',E10.3/
     .       'DISPLACEMENT AT REMOTE BNDRY--------- = ',E10.3/
     .       'FLOW VELOCITY AT TUNNEL SURFACE ----- = ',E10.3/
     .       'ACCUMULATED VOLUME OF WATER            '       /
     .       'PER UNIT LENGTH OF TUNNEL ----------- = ',E10.3//)
C
C     IF(NKF.EQ.0) WRITE(7,2003)
 2003 FORMAT('DISTANCE   PORE PRESS.')
C     IF(NKF.EQ.1) WRITE(7,2004)
 2004 FORMAT('DISTANCE  PORE PRESS.  EFF. RAD. S.  EFF. CIR. S.')
      DO 200 I=1,NUMEL
      IF(LF.GT.0) GO TO 100
      P = PNC(I)
      R = X(I+1)
      GO TO 150
  100 P = 0.5*(PNC(I)+PNC(I+1))
      R = 0.5*(X(I)+X(I+1))
  150 CONTINUE
      IF(IPLANE.EQ.1) R = R-X(1)
C     IF(NKF.EQ.0) WRITE(7,2005) R,P
```

```
      IF(NKF.EQ.0) WRITE(8,*) R/12.,-P
 2005 FORMAT(F10.0,5X,F10.0)
C     IF(NKF.EQ.1) WRITE(7,2006) R,P,STRES(1,I),STRES(2,I)
 2006 FORMAT(4(F10.0,5X))
  200 CONTINUE
C     WRITE(7,2007)
 2007 FORMAT(///)
      WRITE(8,*) '   0.0   123456789.    TIME =',TIMEO
 300  CONTINUE
      RETURN
      END
C
C   INSERT MLIB
C
C
C     MATRIX ASSEMBLE
C
      SUBROUTINE ASMBM(ST,EST,NDR,NDC,NEQ,MBAND)
      DIMENSION ST(NEQ,MBAND),EST(2,2),NDR(2),NDC(2)
      DO 200 K=1,2
      IR = NDR(K)
      IF(IR.LE.0) GO TO 200
      DO 100 L=1,2
      IC = NDC(L)
      IF(IC.LE.0) GO TO 100
      IC = IC-IR+1
      IF(IC.LE.0) GO TO 100
      ST(IR,IC) = ST(IR,IC)+EST(K,L)
  100 CONTINUE
  200 CONTINUE
      RETURN
      END
C
C     VECTOR ASSEMBLE
C
      SUBROUTINE ASMBV(VC,EVC,NDR,NA)
      DIMENSION VC(1),EVC(1),NDR(1)
      DO 300 K=1,NA
      IR = NDR(K)
      IF(IR.LE.0) GO TO 300
      VC(IR) = VC(IR)+EVC(K)
  300 CONTINUE
      RETURN
      END
C
C     TRIANGLIZE
C
      SUBROUTINE TRIA(NEQ,M,A,MB)
      DIMENSION A(NEQ,1),MB(NEQ)
      NE = NEQ-1
      MN = M-1
      MM = M
```

```
      MK = NEQ-MN
      DO 300 N=1,NE
      NT = N-MK
      IF(NT.GT.0) MM = MM-1
      MB(N) = 0
      IF(A(N,1).EQ.0.0) GO TO 300
      L = N
      IH = MM
      JB = 0
      IB = 0
      DO 200 I=2,IH
      L = L+1
      J = L
      IB = IB+1
      AI = A(N,I)
      C = AI/A(N,1)
      IF(C.EQ.0.0) GO TO 200
      JC = 1
      DO 100 K=I,IH
      A(J,JC) = A(J,JC)-C*A(N,K)
  100 JC = JC+1
      A(N,I) = C
      JB = IB
  200 CONTINUE
      MB(N) = JB
  300 CONTINUE
      MB(NEQ) = 0
      RETURN
      END
C
C     BACKSUBSTITUTE
C
      SUBROUTINE BACKS(NN,A,B,MB)
      DIMENSION A(NN,1),B(NN),MB(NN)
      N = 0
  270 N = N+1
      C = B(N)
      IF(A(N,1).NE.0.0) B(N) = B(N)/A(N,1)
      IF(N.EQ.NN) GO TO 300
      IL = N+1
      IH = N+MB(N)
      M = 1
      DO 285 I=IL,IH
      M = M+1
  285 B(I) = B(I)-A(N,M)*C
      GO TO 270
  300 IL = N
      N = N-1
      IF(N.EQ.0) RETURN
      IH = N+MB(N)
      M = 1
      C = B(N)
```

```
      DO 400 I=IL,IH
      M = M+1
  400 C = C-A(N,M)*B(I)
      B(N) = C
      GO TO 300
      END
C
C     MATRIX MULTIPLICATION
C
      SUBROUTINE MLTPL(A,B,BO,MB,NEQ,NEQ2,MBAND)
      DIMENSION A(NEQ,MBAND),B(NEQ),BO(NEQ),MB(NEQ2)
      DO 300 N=1,NEQ
      BB = A(N,1)*BO(N)
      L = N
      NI = MB(N)
      IF(NI.GT.1) GO TO 50
      GO TO 120
   50 DO 100 M=2,NI
      L = L+1
  100 BB = BB+A(N,M)*BO(L)
  120 L = N
      NNEQ = N+NEQ
      NJ = MB(NNEQ)
      IF(NJ.GT.1) GO TO 150
      GO TO 250
  150 DO 200 M=2,NJ
      L = L-1
      NM1 = N-M+1
  200 BB = BB+A(NM1,M)*BO(L)
  250 B(N) = B(N)+BB
  300 CONTINUE
      RETURN
      END
C
C     MODIFY GLOBAL STIFFNESS MATRIX
C
      SUBROUTINE MODFY(N,X,A,B,NEQ,MBAND)
      DIMENSION A(NEQ,1),B(1)
      DO 250 M=2,MBAND
      K = N-M+1
      IF(K.LE.0) GO TO 235
      B(K) = B(K)-A(K,M)*X
      A(K,M) = 0.0
  235 L = N+M-1
      IF(NEQ-L) 245,240,240
  240 B(L) = B(L)-A(N,M)*X
  245 A(N,M) = 0.0
  250 CONTINUE
      A(N,1) = 1.0
      RETURN
      END
```

```
C
C     PROFILE MATRIX
C
      SUBROUTINE PRFIL(A,MB,NEQ,MBAND)
      DIMENSION A(NEQ,1),MB(1)
      DO 300 N=1,NEQ
      NI = 1
      NJ = 1
      DO 100 M=2,MBAND
      IF(A(N,M).NE.0.0) NI = M
      IF(N-M) 100,80,80
   80 NM1 = N-M+1
      IF(A(NM1,M).NE.0.0) NJ = M
  100 CONTINUE
      MB(N) = NI
      NNEQ = N+NEQ
      MB(NNEQ) = NJ
  300 CONTINUE
      RETURN
      END
C
C
C
      SUBROUTINE FLVOL(DU,PP,POR,ALPHA,A,XL,VOL,IPLANE,RSG,NDF)
C
      DIMENSION DU(2),PP(2)
      COMMON/CNSTS/B0,B1,B2,B3,B4,B5,B6,B7,B8,B9,B10,B11,B12
C
      AL1=1.0/XL
      AL2=1.0/(2.0*A+XL)
      EV=DU(1)*(AL2-AL1)+DU(2)*(AL2+AL1)
      IF(IPLANE.EQ.0) VEL = (A*B1+B7)*2.0*3.1415926
      IF(IPLANE.EQ.1) VEL =1.0*XL
      P = 0.5*(PP(1)+PP(2))
      IF(NDF.EQ.0) VOL = VOL-(EV-ALPHA*P)*VEL
      IF(NDF.EQ.1) VOL = VOL-(EV*(1.0-RSG)-ALPHA*P)*VEL
C     WRITE(50,*)'VOL IN FLVOL=',VOL,'  EV=',EV,'  P=',P
C     WRITE(50,*)'VEL=',VEL,'  A=',A,'  XL=',XL,'  B1=',B1,' B7=',B7
      RETURN
      END
C
```

REPORT DOCUMENTATION PAGE

Form Approved
OMB No. 0704-0188

Public reporting burden for this collection of information is estimated to average 1 hour per response, including the time for reviewing instructions, searching existing data sources, gathering and maintaining the data needed, and completing and reviewing the collection of information. Send comments regarding this burden estimate or any other aspect of this collection of information, including suggestions for reducing this burden, to Washington Headquarters Services, Directorate for Information Operations and Reports, 1215 Jefferson Davis Highway, Suite 1204, Arlington, VA 22202-4302, and to the Office of Management and Budget, Paperwork Reduction Project (0704-0188), Washington, DC 20503.

1. AGENCY USE ONLY *(Leave blank)*

2. REPORT DATE
September 1994

3. REPORT TYPE AND DATES COVERED
Final report

4. TITLE AND SUBTITLE
Task IV: Groundshock-Induced Hydrogeologic Response; Volume II: Hydrologic Response of Deep Based Systems to Blast Loading

5. FUNDING NUMBERS
DACW45-84-C-0128

6. AUTHOR(S)
Scott E. Blouin, Kwang J. Kim

7. PERFORMING ORGANIZATION NAME(S) AND ADDRESS(ES)
Applied Research Associates, Inc.
New England Division
South Royaltion, VT 05068

8. PERFORMING ORGANIZATION REPORT NUMBER
Miscellaneous Paper
GL-94-49

9. SPONSORING/MONITORING AGENCY NAME(S) AND ADDRESS(ES)
See reverse.

10. SPONSORING/MONITORING AGENCY REPORT NUMBER

11. SUPPLEMENTARY NOTES
The main text was published under separate cover. Available from the National Technical Information Service, 5285 Port Royal Road, Springfield, VA 22161.

12a. DISTRIBUTION/AVAILABILITY STATEMENT
Approved for public release; distribution is unlimited.

12b. DISTRIBUTION CODE

13. ABSTRACT *(Maximum 200 words)*

Mechanisms controlling the hydrologic response of a deep based system to nuclear attack are identified through an analysis of data from underground tunnel complexes at the Nevada Test Site. Two mechanisms are identified, inflow of fracture water mobilized by the dynamic loadings and inflow of pore water due to explosion generated residual stresses and pore pressures. Both mechanisms are serious potential threats to deep based systems located in geologies similar to Generic Mountain C. The magnitude of the fracture water threat is impossible to assess due to nonavailability of sufficient geologic and hydrologic data at Mountain C. The magnitude of the pore water threat at site C is estimated based on flow calculations using the one dimensional axisymmetric code CONSL. Calculations indicate that pore water flow at the Generic Mountain C site will be orders of magnitude greater than similar flow at the Nevada Test Site because of the much more permeable rock at Mountain C. The need for more refined calculations of the Mountain C response is emphasized.

14. SUBJECT TERMS
See reverse.

15. NUMBER OF PAGES
219

16. PRICE CODE

17. SECURITY CLASSIFICATION OF REPORT
UNCLASSIFIED

18. SECURITY CLASSIFICATION OF THIS PAGE
UNCLASSIFIED

19. SECURITY CLASSIFICATION OF ABSTRACT

20. LIMITATION OF ABSTRACT

9. (Continued).

U.S. Army Engineer Waterways Experiment Station
3909 Halls Ferry Road
Vicksburg, MS 39180-6199

U.S. Air Force Ballistic Missile Office
Norton Air Force Base

14. (Continued).

Consolidation	Hydrologic response
Deep basing	Pore pressure dissipation
Explosive loadings	Rock mechanics